APPLICATION OF SLIDING MODE THEORY TO GUIDANCE AND CONTROL OF UNMANNED AERIAL VEHICLES

by

Syed Ussama Ali
PE113009

A thesis submitted to the
Department of Electrical Engineering
in partial fulfillment of the requirements for the degree of
DOCTOR OF PHILOSOPHY IN ELECTRICAL ENGINEERING

Faculty of Engineering
Capital University of Science & Technology
Islamabad

December 2016

APPLICATION OF SLIDING MODE THEORY TO GUIDANCE AND CONTROL OF UNMANNED AERIAL VEHICLES

By
Syed Ussama Ali
(PE113009)

Dr. James F. Whidborne, Professor
School of Aerospace, Transport and Manufacturing
Cranfield University, Bedfordshire, United Kingdom
(Foreign Evaluator)

Dr. Asif Sabanovic, Professor
Faculty of Engineering and Natural Sciences
Sabanci University, Istanbul, Turkey
(Foreign Evaluator)

Dr. Raza Samar, Adjunct Professor
Department of Electrical Engineering
Capital University of Science and Technology
(Thesis Supervisor)

Dr. Noor Muhammad Khan, Professor
HoD, Department of Electrical Engineering
Capital University of Science and Technology

Dr. Imtiaz Ahmed Taj, Professor
Dean, Faculty of Engineering
Capital University of Science and Technology

DEPARTMENT OF ELECTRICAL ENGINEERING
FACULTY OF ENGINEERING
CAPITAL UNIVERSITY OF SCIENCE & TECHNOLOGY
DECEMBER 2016

C.U.S.T.

CAPITAL UNIVERSITY OF SCIENCE & TECHNOLOGY
ISLAMABAD

PhD Thesis Defense Report Form

Student's Name : **Mr. Syed Ussama Ali**   Registration No : **PE- 113009**

Course Work: **18 Cr Hrs**   CGPA : **3.61**   Thesis Credit Hours: **34 Cr Hrs**

Thesis Title : **Application of Sliding Mode Theory to Guidance and Control of Unmanned Aerial Vehicles**

Examining Committee

1	Convener	**Dr. Imtiaz Ahmad Taj, Dean FoE, CUST, Islamabad**
2	External Examiner	**Dr. Abdul Qayyum Khan, PIEAS, Islamabad**
3	External Examiner	**Dr. Ammar Hasan, SEECS, NUST, Islamabad**
4	Internal Examiner	**Dr. Fazal ur Rehman, CUST, Islamabad**
5	Supervisor	**Dr. Raza Samar, CUST, Islamabad**

Recommendation:

The PhD thesis defense of **Mr. Syed Ussama Ali** was held at Capital University of Science & Technology on **Saturday**, **December 10, 2016** at **1100 Hrs**.

The abovementioned committee, unanimously agreed to award PhD degree, to the candidate on his original contribution in the field of **Electrical Engineering**, presented in his thesis entitled, **"Application of Sliding Mode Theory to Guidance and Control of Unmanned Aerial Vehicles"**.

The Supervisor is authorized to verify that changes have been incorporated in the thesis as recommended by the examiners, before its final submission to the University, for award of degree.

Dr. Raza Samar
Supervisor

Dr. Fazal ur Rehman
Internal Examiner

Dr. Abdul Qayyum Khan
External Examiner

Dr. Ammar Hasan
External Examiner

Dr. Noor Muhammad Khan
HoD

Dr. Imtiaz Ahmad Taj
Dean

CAPITAL UNIVERSITY OF SCIENCE & TECHNOLOGY
ISLAMABAD

AUTHOR'S DECLARATION

I, **Mr. Syed Ussama Ali (Registration No. PE-113009)**, hereby state that my PhD thesis titled, '**Application of Sliding Mode Theory to Guidance and Control of Unmanned Aerial Vehicles**' is my own work and has not been submitted previously by me for taking any degree from Capital University of Science and Technology, Islamabad or anywhere else in the country/ world.

At any time, if my statement is found to be incorrect even after my graduation, the University has the right to withdraw my PhD Degree.

(Mr. Syed Ussama Ali)

Dated: January, 2017   Registration No : PE113009

PLAGIARISM UNDERTAKING

I solemnly declare that research work presented in the thesis titled "**Application of Sliding Mode Theory to Guidance and Control of Unmanned Aerial Vehicles**" is solely my research work with no significant contribution from any other person. Small contribution/ help wherever taken has been duly acknowledged and that complete thesis has been written by me.

I understand the zero tolerance policy of the HEC and Capital University of Science and Technology towards plagiarism. Therefore, I as an author of the above titled thesis declare that no portion of my thesis has been plagiarized and any material used as reference is properly referred/ cited.

I undertake that if I am found guilty of any formal plagiarism in the above titled thesis even after award of PhD Degree, the University reserves the right to withdraw/ revoke my PhD degree and that HEC and the University have the right to publish my name on the HEC/ University Website on which names of students are placed who submitted plagiarized thesis.

(Mr. Syed Ussama Ali)
Registration No. PE113009
January, 2017

TO MY PARENTS

ACKNOWLEDGMENT

DECLARATION

It is declared that this is an original piece of my own work, except where otherwise acknowledged in text and references. This work has not been submitted in any form for another degree or diploma at any university or other institution for tertiary education and shall not be submitted by me in future for obtaining any degree from this or any other University or Institution.

Syed Ussama Ali
PE113009

December 2016

ABSTRACT

The main objective of the lateral guidance algorithm is to keep the vehicle on pre-planned desired path by controlling the lateral track errors during flight and to keep them as small as possible by generating suitable reference commands. Cross track (lateral) error control of unmanned aerial vehicles (UAVs) in the presence of uncertainties and disturbances with bounded control input (ϕ_{ref}) is a challenging task. The path following guidance law needs to be devised using generalized kinematic model and by explicitly considering the UAV autopilot dynamics. However, the inclusion of these dynamics into guidance design further complicates the problem by increasing the relative degree, and stability, and control boundedness becomes difficult to analyze. To address these challenges, several studies for inclusion of autopilot dynamics into guidance design are presented in this thesis for lateral path following applications.

Firstly, the guidance and control framework based on sliding mode theory is presented to solve the two dimensional path-following problem. Limitations of the existing nonlinear sliding surface for lateral guidance are indicated and thus two novel stable nonlinear sliding manifolds are proposed for the guidance problem. The two surfaces are then employed to generate two new nonlinear guidance laws for UAV path following. The proposed guidance schemes rely on First Order Sliding Mode Control (FOSMC) algorithm derived at the kinematic level generating reference bank commands. The autopilot based on super twisting algorithm using linear sliding surface forms the inner control loop for control actuation.

The autopilot is involved in the feedback nonlinear sliding mode based guidance law design for path following of UAVs. The major contribution of this work is the dynamics of the autopilot taken into account for guidance law design, along-with saturation constraints on guidance commands for high performance in all scenarios. To solve relative degree two problem, a nonlinear sliding manifold is used with real twisting algorithm for guidance design, the guidance loop generates bank angle commands for executing roll maneuvers. The strategy provides a framework to implement the developed controller on the experimental vehicle without modifying the key structure of the original autopilot controller.

Moreover, an innovative sliding mode based partially integrated lateral guidance and control scheme for UAVs is proposed. Guidance and control framework based on second order sliding modes is presented to solve the problem of two dimensional path-following. The main contribution of the technique presented here is the partial integration of the two loops i.e., a guidance and control system via series interconnection of two stable sliding manifolds. The proposed guidance scheme relies on a nonlinear switching surface with the real twisting algorithm derived at the kinematic level, generating roll error commands. The autopilot based on the super-twisting algorithm using a linear sliding surface forms the autopilot loop.

Finally, a new guidance law for accurate following of flight path to observe tight ground track control is presented. The unique feature is to explicitly account for autopilot constraints by defining a 3-D sliding manifold. The guidance solution described is based on state stabilization of kinematics-dynamics trajectories i.e., the guidance law is evolved based on the knowledge of dynamical characteristics of the UAV. A robust FOSMC guidance algorithm is derived using the nonlinear 3-D sliding manifold to develop the guidance law.

For the proposed schemes, proof of existence of sliding mode, actuation boundedness and performance of the path-following closed-loop system is analyzed. Flight results validate the performance and effectiveness of the proposed framework for guidance and control design.

Keywords: Sliding Mode Control, Unmanned Aerial Vehicles (UAVs), Guidance & Control, Sliding Surface, Cross Track Error, Lateral Guidance.

LIST OF PUBLICATIONS

Journal Publications

1. Syed Ussama Ali, Raza Samar, M. Zamurad Shah, Aamer Iqbal Bhatti and Khalid Munawar. Higher-Order Sliding Mode based Lateral Guidance of Unmanned Aerial Vehicles. Transactions of the Institute of Measurement and Control, Published online, doi:10.1177/0142331215619972, SAGE Publications.

2. Syed Ussama Ali, Raza Samar, M. Zamurad Shah, Aamer Iqbal Bhatti, Khalid Munawar and Ubaid M. Al-Sggaf. Lateral Guidance and Control of UAVs using second-order sliding modes. Journal of Aerospace Science and Technology, vol. 49, pp. 88-100, 2016, doi: http://dx.doi.org/10.1016/j.ast.2015.11.033".

3. Syed Ussama Ali, Raza Samar, M. Zamurad Shah, Aamer Iqbal Bhatti. Nonlinear Manifolds for Lateral Path Following Guidance of Unmanned Aerial Vehicles. Submitted for publication.

4. Syed Ussama Ali, Raza Samar, M. Zamurad Shah, Aamer Iqbal Bhatti. Lateral Path following: Guidance of UAVs with Autopilot Constraint. Submitted for publication.

Conference Publications

1. S. U. Ali, M. Z. Shah, R. Samar, "Sliding Mode Based Roll Control Law Design for a Research UAV and its Flight Validation," 2016 13th International Bhurban Conference on Applied Sciences and Technology (IBCAST), Islamabad, 2016, pp. 118-125 doi: 10.11009/IBCAST.2016.7429865

2. S. U. Ali, M. Z. Shah, R. Samar and A. Waseem, "Wind Estimation for Lateral Path following of UAVs using Higher Order Sliding Mode," 2016 International Conference on Intelligent Systems Engineering (ICISE), Islamabad, pp. 364-371 doi: 10.1109/INTELSE.2016.7475150

3. A. Saeed, S. U. Ali and M. Z. shah, "Linear control techniques application and comparison for a research UAV altitude control," 2016 13th International Bhurban Conference on Applied Sciences and Technology (IBCAST), Islamabad, 2016, pp. 126-133 doi: 10.11009/IBCAST.2016.7429866

4. M. Zamurad shah, Raza Samar & Syed Ussama Ali, "Altitude controller design and flight demonstration for a research UAV," Proceedings of 8th International Aerospace Conference, Sep 10-12, 2015, Ankara, Turkey

5. Syed Ussama Ali, M. Zamurad shah, A.I. Bhatti & Raza Samar, "Robust nonlinear control design for scaled Yak-54 Unmanned Aerial Vehicle," 26th Chinese Control and Decision Conference (2014 CCDC), pp.713,718, May 31 2014-June 2 2014 doi: 10.1109/CCDC.2014.6852258

6. Syed Ussama Ali, M. Zamurad shah, Raza Samar & A.I. Bhatti, "Lateral control of UAVs: Trajectory tracking via Higher-Order Sliding Modes," 9th Asian Control Conference (ASCC), 2013, pp.1,6, 23-26 June 2013 doi: 10.1109/ASCC.2013.6606256

7. M. Zeeshan Babar, Syed Ussama Ali, M. Zamurad shah, Raza Samar, A.I. Bhatti & W. Afzal, "Robust control of UAVs using H_∞ control paradigm,"Proceedings of 9th International Conference on Emerging Technologies, Dec 09-10, 2013, Islamabad, Pakistan

8. Syed Ussama Ali, M. Zamurad shah, Raza Samar & A.I. Bhatti, "Robust level flight control design for scaled Yak-54 unmanned aerial vehicle using single sliding surface.," 24th Chinese Control and Decision Conference (2012 CCDC), pp.1209,1214, 23-25 May 2012 doi: 10.1109/CCDC.2012.6244193

TABLE OF CONTENTS

Chapter 5

Chapter 6

Chapter 7

Chapter A

Chapter B

LIST OF FIGURES

LIST OF TABLES

LIST OF ACRONYMS

LIST OF SYMBOLS

Symbol	Description	Units
S_{ref}	Wing reference area	m^2
b	Wing span	m
c	Chord length	m
m	Mass of The UAV	Kg
g	Acceleration due to gravity	m/s^2
V	Velocity of the UAV	m/s
y	Lateral Track Error	m
χ	Course angle	rad
χ_E	Intercept Course angle	rad
χ_R	Reference Course angle	rad
ϕ	Roll Angle	rad
ϕ_{ref}	Reference Bank Angle	rad
ϕ_E	Angular bank error commands	deg
p, q, r	Body Angular Rates	rad/s
$\delta_a, \delta_e, \delta_r$	Control Surface deflection	deg
I_{xx}, I_{yy}, I_{zz}	Moment of Inertia terms	$kg - m^2$
R	Radius of turn	m
O	Center of turn	m
C_l, C_n	Roll and Yaw moment coefficients	

Chapter 1

INTRODUCTION

1.1 Background and Motivation

Unmanned Aerial Vehicles (UAVs) are operated remotely or autonomously. In last two decades, extensive research has been carried out on the UAVs. The technological advancement in the field of UAVs has gained a lot of momentum. They can carry a variety of payloads depending on their mission objectives, operational characteristics and functionality. UAVs exhibit many remarkable capabilities due to accurate path following, like possibility to accept high risk missions of long endurance. UAVs are increasingly being used in civilian and military applications due to relatively low operational cost and reduced risk to life.

The UAVs have wide range of operational capabilities. Some applications of UAVs are listed below:

- Security: anti-terrorism operations, border control surveillance, rescue, sensitive sites surveillance and law enforcement, policing applications for civil security.

- Military systems: combat search and rescue, destruction/suppression of enemy air defense, intelligent surveillance and reconnaissance, countermeasures, weapon delivery, communication/network node.

- Civil applications: pollution detection, forest fire detection, oil/gas or water pipeline, power line monitoring, agriculture, field spraying, environmental studies, crop dusting, fire monitoring control for the forests.

UAVs have demonstrated numerous potential uses in military, commercial and civil applications and their prospects for broad impact are strong. Their cost

continues to decrease with substantial increase in their functionality. To extend the usefulness of UAVs beyond their current applications, UAVs rely on automation to provide this functionality. The applications such as search, surveillance and rescue operations require UAVs to fly in areas surrounded by buildings or near the surface of abruptly changing mountainous terrain, therefore accurate path following of pre-planned paths is essential. In the last decade, noticeable research is reflected to show UAVs potential as a support tool for wide variety of applications. These platforms are by all means impressive providing low detection probability and high functionality in path planning, obstacle avoidance, artificial vision, environment modeling and decision making. All of these works are aimed to endow UAV with autonomy. The capability of the UAV to fly by itself to complete few mission parts without external control is not an autonomous flight. The autonomous systems perform the desired maneuvers in a predictable environment according to a given set of predefined rules. Classically, autonomy demands for a UAV to perform all its maneuvers without any external control or supervision in a dynamic environment in all uncertain conditions. An autonomous system should be equipped with all sort of functionality level, so that it only needs an initiating instruction from the user to Loiter(city) or explore(area) and perform all of its maneuvers without any supervision.

Autonomy refers to the ability of the vehicle to perform certain task or a mission without any remote involvement by human operator [8]. The autonomy will become more and more important for the future UAV development. The autonomy falls under the following categories: communication, trajectory generation, sensor fusion, path/motion planning, or path following, task allocation and scheduling and cooperative tactics. These categories are about handling communication and coordination between multiple UAVs ground stations in the presence of incomplete and imperfect information. It determines an optimal control maneuver to follow a given path or to go from one location to another. It combines the information from different sensors as measurements and determines an optimal path for the UAV, while meeting certain objectives and constraints. It also determines the
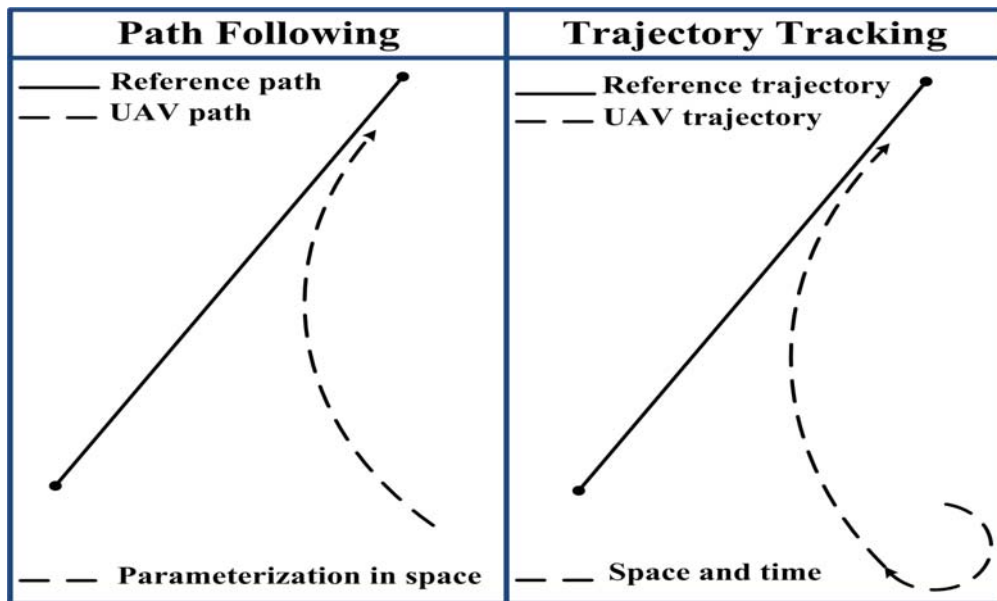
FIGURE 1.1: Path following and trajectory tracking

optimal distribution of tasks amongst a group of agents with time and equipment constraints as well as formulates an optimal sequence and spatial distribution of activities between agents in order to maximize chances of success in any given mission scenario. In autonomy, an important aspect is path following; for high performance control of UAVs, the control design is robust in the presence of disturbing forces and it has the ability of precise path following. For the design of guidance and control, efficient and effective techniques are required. A criterion is presented in [9] for the handling qualities for such vehicles and to access the lateral performance.

The guidance problem in UAVs can be classified in two categories Figure 1.1:

- Path following

    - Reference path given in a time-free parametrization.

    - Path following is of concern with the design of control laws that drive an object (be it UAV, ship, aircraft or a mobile robot) to reach and follow a geometric path.

    - Smooth convergence to the path.

- Trajectory (reference) tracking

  – Reference path is parametrized in space and time.

  – The vehicle may attempt to loiter a while to reach a reference point at a prescribed time.

  – Trajectory tracking problem concerns the design of control laws that force a vehicle to reach and follow a time parametrized reference (i.e., a geometric path with an associated timing law).

Path-following is motivated by applications in which spatial errors are more critical than temporal errors. Steering the UAV along a desired path is of primary importance while the speed or dynamic behavior along the path maybe of secondary. The problem is first solved with respect to the primary objective, leaving the choice of a timing law for it as an additional degree of freedom. The freedom to design guidance algorithms independent of timing laws is a fundamental advantage of path following over trajectory tracking. In case of UAV, trajectory tracking problem becomes more complicated due to varying ground speed and due to unpredictable nature of winds.

Among the uses mentioned above, the current work is more focused on devising guidance and control schemes to provide precise lateral track regulation for UAVs in missions while navigating through waypoints (2-D path following). UAV path following becomes more challenging in conditions where it needs to perform lateral guidance tasks while keeping in mind various parameters, some of them are;

- UAV dynamics (parametric uncertainty)

- Maneuvering capabilities and constraints

- Cruise speed

- External disturbances like winds

UAV Autonomy addresses the challenging topic among the research community i.e., path following. Regardless of the end use given to the UAV, guidance and control system is the key component to make UAV autonomous. The primary motivation is to examine the technologies leading to UAV autonomy and attempt to expand them. Motivated by these considerations, we propose a solution to the path following problem for unmanned vehicles in this thesis for the 2-D (lateral) plane. Inspired by the inherent properties of sliding mode i.e., robustness against uncertainties and disturbances, the proposed guidance and control schemes are based on the sliding mode approach.

1.2 Literature Review

1.2.1 Guidance and control structures

The guidance and control design problems for path following of UAVs are treated separately, designed and implemented in an outer-loop, inner-loop configuration [3, 10, 11, 12, 13]. The outer loop is designed for guidance law, which generates lateral commands for the inner loop to track. These commands are generated on the basis of ground track measurements in the form of reference lateral acceleration or reference bank commands. The inner loop is equipped with tracking controllers that receive these commands and perform necessary control surface deflection. The inner loop is also responsible for stability augmentation tasks. An alternative to inner-outer loop control strategy is the integrated approach also utilized for guidance and control problems [4, 13, 14, 15]. However, due to the coupling between slower guidance and faster control variables this technique is complicated [16, 17, 18]. Contrary to both, a third approach of partially integrated guidance and control utilizes the partial integration of guidance and control (PIGC) structure [19, 20] which exploits the inherent time scale separation property. PIGC aims to generate an angular rate commands by the outer loop and uses control surface actuation to track these signals in the control loop.
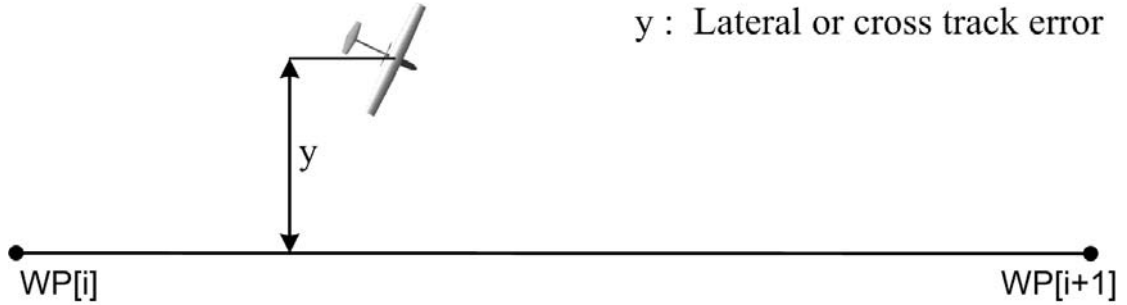
FIGURE 1.2: Lateral error minimization with traditional linear controller [1, 2]

In 3-D guidance, the reference mission is followed in both the longitudinal (vertical) and lateral (horizontal) planes [21, 22]. This involves reference altitude following along with 2-D ground track following. The 3-D guidance algorithm will generate pitch or altitude commands for the longitudinal control system and roll or heading commands for the lateral/directional control system, while taking into account the coupling between the two. In case of 3-D guidance, the challenge arises due to coupling between the longitudinal and lateral dynamics. Designing a guidance law for this multi-input multi-output system is a demanding task. The work presented here is about two-dimensional guidance algorithm design for following the desired ground track of the vehicle with minimum deviation. The objective here is to closely follow the projection of the mission on the ground plane through smooth bank-to-turn maneuvers. In the two loop approach employed here, the outer guidance loop consider kinematics while the dynamics are used in the inner autopilot loop. The existing algorithms on path following can be broadly classified into two categories: geometrical and those based on classical control theory. In this section, we will discuss the existing work in literature related to 2-D lateral guidance problems. The work of [13] and [23] presents the detailed contributions in this area.

For unmanned vehicles, linear controllers based on classical control theory are commonly used for guidance law design [1, 2]. Typically, the guidance commands i.e., desired lateral acceleration or reference bank angular commands are generated using the feedback of UAVs lateral error as shown in Figure 1.2. This strategy

6

provides reasonable results when the desired trajectory for tracking is a straight path. But in the presence of wind disturbance or while following curved paths, the performance of PD control degrades. The second drawback of the scheme is the decision logic for smooth transition from one waypoint to the other when following series of waypoints. To enhance the tracking performance for zero steady state error, the conventional linear proportional and derivative lateral control scheme is modified with addition of a limited integrator along with nonlinear gain scheduling in [10, 24]. Integral action is activated only when the cross-track error becomes less than a certain threshold and gains are scheduled depending on the lateral error. Performance of the scheme is compared to other techniques and found comparable for circular paths. The performance is better for large track errors because of gain scheduling, the solution is informal and no stability analysis is provided.
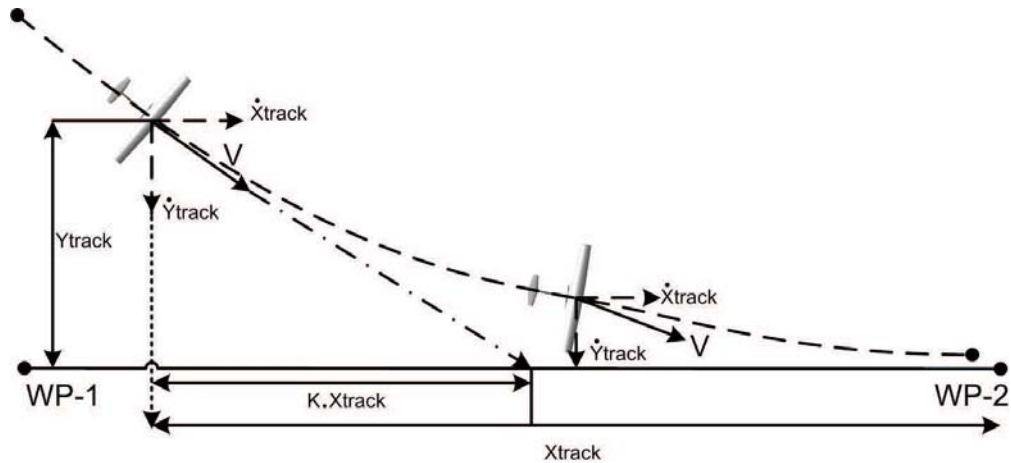
FIGURE 1.3: Lateral track guidance logic based on geometrical concepts [3]

A lateral guidance scheme for UAVs is proposed based on geometrical concepts in [3]. The strategy is based on keeping the objective function equal to zero i.e., longitudinal distance to longitudinal velocity ratio is equal to the ratio of lateral deviation to lateral velocity with the help of proportional feedback control law in the form of yaw-rate commands (see Figure 1.3). A primary limitation comes from the implied assumption that the desired path should be a straight line. Simulation results also indicate that vehicle roll channel is oscillatory due to yaw-rate guidance commands. To overcome the drawbacks of PD control a nonlinear

7

guidance algorithm is suggested in [4, 5] for path following applications with an aim to keep a specified angle in sight towards the desired course (see Figure 1.4). The proposed algorithm provides better performance than the traditional PD logic for both straight and curved paths. However, for large track errors the control output of this nonlinear scheme saturates and perfect knowledge of the vehicle velocity is required for zero steady-state error. No proof of stability and control boundedness are provided. A 'reference point' on the desired point ahead of the current position of the UAV is also required for lateral acceleration commands which in certain cases may cause large control inputs.
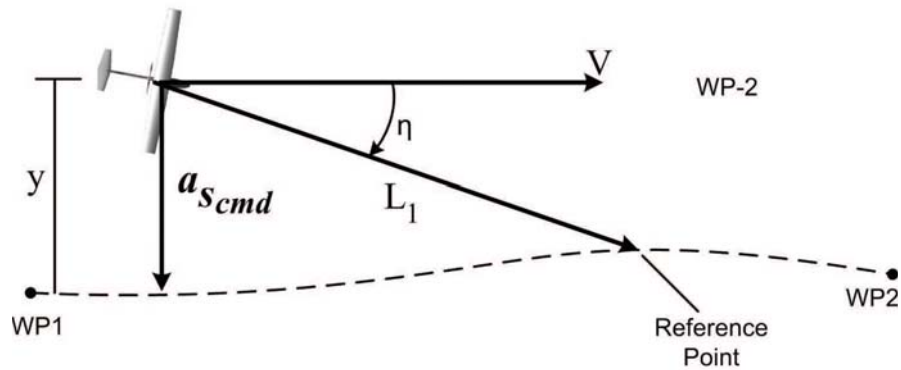
FIGURE 1.4: Nonlinear lateral track guidance logic [4, 5]

A tracking guidance law for a pursuer UAV is considered in [25] for UAV formation flying applications. The UAV tracks a moving target and the guidance law generates lateral acceleration commands for the control system to follow. The main constraint of the problem, i.e., boundedness of the lateral acceleration commands for a fixed-wing vehicle with constant airspeed is analyzed here. The proposed guidance law is based on an oscillatory motion created by a center of oscillation that allows the pursuer UAV to fulfill the requirements of target tracking under the stated constraints. Design of a path following controller for a small UAV is presented in [26]; the cross-track and course angle errors are used to generate heading angle corrections as guidance commands for bank to turn maneuvers. LQR (linear quadratic regulator) based autopilot forms the inner loop. However, the scheme is limited to only simulation results. PID based guidance law utilizing a short time

8

stability approach is designed in [27] by considering the control loop dynamics, it is shown that the stability bound of the proposed scheme is less conservative than PN (proportional navigation), PDN (proportional derivative navigation) and PIN (proportional integral navigation). In [28], a finite-time convergent guidance law is designed based on integral backstepping control by considering the autopilot dynamics. However, only the computer simulation results are presented in [27, 28] and real time actual hardware implementation remains to be addressed.

A lot of extensive research in recent years is conducted in the design of guidance laws with Model Predictive Control (MPC) and Nonlinear Model Predictive Control (NMPC) techniques. For small fixed wing UAVs a high level controller is proposed in [29] with NMPC, the cross track error is averted by the minimization of the designed cost function. It is minimized N steps ahead with an assumption that the entire mission knowledge is available before hand. For the cross track error regulation, an adaptive NMPC based path following scheme for UAVs with variable control horizon is developed in [30]. Non-quadratic cost function is combined with high level control for UAVs in [31]. In [32], the authors discussed an integrated navigation, guidance and control algorithm using NMPC and suggested that for NMPC application to UAVs, promissory advances are first required to be made. Computational complexity of MPC based techniques made these strategies hard to implement in real-time applications, particularly for low cost UAVs. Based on NMPC approach, trajectory tracking problem is discussed in [33]. Using a genetic algorithm an optimal control problem is solved online to track the desired path by the proposed algorithm. However, most of the techniques presented with MPC or NMPC are limited to computer simulation results.

A path following strategy for UAVs that is becoming increasingly popular is the notion of a vector field [34, 35]. A nice extension of [35] is given in [36], which derives general stability conditions for vector field based methods. Vector field based guidance for curved paths is studied in [37]. It is shown using Lyapunov stability criteria that controlling the heading rate and speed in a vector field yields

asymptotic following of straight and circular paths. Vector field indicating directions for course commands is computed as a function of vehicle deviation from the desired path and to drive the error to zero a vector field of heading commands is generated. However in certain cases, the control system of the vehicle is saturated by large heading commands for the control system to follow. An extension to the idea of vector field for general paths on 3-D space is reported in [38]. However, in [36] and [38], the vehicle model used is a single integrator.

A terminal guidance problem based on the integral sliding mode (ISM) control method and nonlinear disturbance observer technique is discussed in [39]. A novel strategy is proposed for the guidance law with first order lag autopilot and constrained impact angle which guarantees the line of sight (LOS) angular rate and LOS angle convergence in finite time. Application of SMC in the outer guidance loop is discussed in [40, 41]. Interesting contribution based on the second order sliding structure for coupled roll and pull-up motions is proposed as a means to develop an integrated guidance and autopilot (IGA) scheme [42]. An Integrated guidance and control approach is proposed in [43], which is based on a sliding surface structure that utilizes the pure pursuit guidance scheme. It is important to select the intermediate control variables carefully for the partial derivatives of the sliding surface during design synthesis phase. The problem with the sliding surface design is that it is difficult to relate the actuator input to the sliding surface, although the structure of the sliding surface is efficient. In [17], an IGA design for a chasing UAV is presented. The scheme used a second order sliding mode (SOSM) to make a smooth bank and turn coupled motion during the path-following. The sliding surface parameters are estimated using a higher order sliding mode differentiator (HOSM). In [44], a scheme is designed in which pitch, roll and yaw channels can be independently controlled using IGA design. Each channel is designed separately by defining a sliding surface and control variables are generated after estimation of unknown variables using a HOSM differentiator. Control boundedness is not considered and magnitude of the bank angle reaches $\pi/2$ in some cases. The convergence of the SOSM controller depends upon correct

estimation of the sliding variables by the differentiator, this causes oscillations in the control channel for the initial few seconds as the differentiator converges towards the true estimate. The paper is only limited to simulation results.

In [45], a distributed cohesive motion control scheme is proposed for autonomous formations in three dimensions. A high level trajectory generation scheme is developed based on geometric and graph theoretical analysis. The lower level of the distributed control scheme is composed of the two individual controllers, first for generating reference path angle based on the trajectory and second for attitude and altitude control. The performance of the designed control schemes is verified via numerical simulations. The tracking problem of dynamical feasible trajectories is discussed in [46] as opposed to following geometric paths, the paper concentrates on applying linear matrix inequalities (LMIs) based control approach that use the $\mathcal{L}_2$-induced norm as the performance measure. This scheme is suited for applications where tracking time parametrized paths are necessary, however in strong wind disturbance case, the performance degrades. Receding horizon (RH) optimization based guidance scheme is proposed in [47]. Spatial value function (SVF) is approximated to plan optimal trajectory which captures the critical interaction between the vehicle dynamics and environment, there by resulting in tighter coupling between planning and control. For autonomous guidance design, performance analysis of practical control laws with an emphasis to precisely track trajectories is given in [48]. Path following controller is designed in combination with a velocity control augmentation and experimental results are addressed for a research platform. In [49], vision-based aerial target tracking problem is discussed, a guidance algorithm is proposed based on nonlinear adaptive observer for fixed wing UAVs. Practical operations of UAVs involve measurement noise and disturbances which can adversely affect the performance of adaptive observer, therefore experimental verifications needs to be addressed. Guidance strategy for autonomous dynamic soaring is proposed in [50]. To extend the flight duration, dynamic soaring is discussed as an effective method to extract energy from wind shear, the drawback is the computational load which is addressed in the guidance

11

algorithm design phase. Numerical simulations are presented to show the efficacy of the proposed approach.

Guidance law with finite time convergence is designed for missiles in [51] accounting for autopilot lag. A similar idea for accounting autopilot constraints while designing the guidance scheme for path following of UAVs is discussed in [34]. A path following scheme is developed in [52], unique feature is that the roll and flight path angle constraints are explicitly considered while deriving the guidance law, which are absolutely necessary for small UAVs. The concept of nested saturation is used to derive explicit flight conditions for straight line and curved arcs which guarantee convergence to the path. Furthermore, the path is precisely followed even in the presence of wind, as explicit condition on magnitude of wind are derived and accounted for in the guidance law design phase. For circular paths, a switching strategy is also introduced for asymptotic convergence and stability. In [53], the trajectory tracking strategy is developed for UAVs where an unmodifiable autopilot is involved in deriving the feedback guidance control law. A novel control structure is proposed that enables an explicit design for a system with an unmodifiable autopilot and a novel controller that augments the existing autopilot law. The law is designed using Lyapunov based backstepping approach, exponential stability and states boundedness is proved. The work is limited to only simulation results. The limitation of the work arises due to an assumption in the convergence proof [54] i.e., the autopilot system is capable of driving the actual UAV states (e.g., roll angle) to exponentially follow its reference states. Implementing a guidance law on UAVs can be problematic when the existing autopilot system is unmodifiable or incompatible with the controller structure. Reference [54] extends the strategy of incorporating pre-existing autopilot system in closed loop architecture in [53]. In this work a strategy is devised to incorporate the unknown autopilot gains using an adaptive control technique. It is also ensured that the tracking error converges to an ultimate bound by the controller. However, this work is limited to only simulation results. In our previous work [55, 56], lateral track guidance scheme for aerial vehicles with a novel nonlinear sliding manifold is

proposed. Stability of the nonlinear surface is proved using Lyapunov theory along with control boundedness to ensure that the controls are not saturated. The proposed guidance framework performance and robustness is validated by presenting the flight test result. However, the guidance scheme is designed with the assumption that the autopilot dynamics of inner loop from ϕ_{ref} to ϕ are fast enough to be neglected (i.e., $\phi_{ref} \approx \phi$).

There has been several techniques used for the inner control loop design. Traditional control strategies are used for the control of linear time varying plants. The control is design for the midpoint and then the controller gains are tuned according to the observed parameters like dynamic pressure [57]. In [58], an H_∞ control technique is presented for full order or approximated reduced order control laws [59], [60]. The linear matrix inequalities (LMIs) are then used to obtain the gain scheduled controller [61]. A comprehensive study on robust multivariable techniques like H_∞ control, linear quadratic optimal control (LQR/LQG) and structured singular value μ-synthesis is presented in [62]. The above discussions on all the strategies are based on linear systems and highly depend on the accuracy of the model. For nonlinear systems, dynamic inversion is used as a design technique [63, 64], while in [65] a model inversion control is combined with adaptive neural networks. This technique has the drawback that neural networks are computationally expensive and requires a large amount of data set which is usually not available in the case of UAVs. A novel strategy is presented in [66] which considers the application of an observer sliding mode controller for a highly unstable system. A SMC based design is used for the linearized aircraft model in [67]. A multi gain sliding mode controller is presented in [68] for the control of pitch angle of civil aircraft. A HOSM controller for unmanned combat aerial vehicle is presented in [69]. The flight path is divided into different maneuvers and an inner outer loop strategy with HOSM controller is developed. Global asymptotic tracking for autopilot can be achieved by designing a dynamics inversion control scheme for an unmanned aerial vehicle in [70]. The UAV dynamics are modeled as an uncertain linear time-invariant

(LTI) system with an additive bounded disturbance. The inversion error and disturbance is minimized with the designed continuous tracking controller. Lyapunov stability criteria is used to prove the global asymptotic tracking and high-fidelity simulation results are provided. For model-scale fixed wing aircraft a hybrid control strategy is proposed in [71]. The vehicles dynamics are described by means of a hybrid model for hover, level and transition with each one corresponding to a different region of the flight envelope. Robust local stabilization is achieved by linear parameter varying control technique for hover and level modes, while for the transition operating mode nonlinear input-to-state controller is designed. The combined controller's performance/robustness is tested within a simulation environment in the presence of disturbances.

1.2.2 Gap analysis

Based on the literature review the aforementioned methods have some shortcomings:

- In the previous studies of motion planning and control for UAVs, most work is focused on the derivation of the guidance laws, while few presented work regarding implementation on real hardware.

- Fixed interface structure of the autopilot may constrain the applicability of the guidance law.

- Guidance law limitation due to autopilot.

- Vehicle dynamics and environments must be taken into consideration while deriving the guidance loop.

The research work in [53] states "As far as we know, a trajectory tracking control law that incorporates an existing autopilot has not been presented in the literature". Therefore, for incorporating auto pilot dynamics into guidance design phase has potential and worth for exploring and devising new algorithms.

Time-varying feedback guidance law needs to be developed using generalized kinematic model and autopilot UAV dynamics in the outer loop to derive the augmented guidance controller. In this work, a preliminary study in path following for UAVs with autopilot constraints in the closed-loop system is presented. To incorporate the constraints due to a fixed autopilot, an additional state is introduced into the kinematic guidance model. The guidance law developed in this research takes into account constraints on the vehicle dynamics and is derived using the kinematics of vehicle motion. The objective is to drive the cross-track and course angle errors to zero with bounded control input (ϕ_{ref}). Here we extend the previous works of [55, 56] by taking into account the dynamics of the inner control loop, while designing the outer guidance loop. Due to the inclusion of extra dynamics, now the problem is of higher relative degree, which is solved using higher order sliding mode control. The overall system therefore performs better, especially when the inner loop is slower and comparable in response time to the outer loop. Proposed framework is particularly useful for systems where the autopilot is un-modifiable or slow and possibly unknown, as would occur with commercial UAVs. Hence, the developed law is well suited for practical UAV applications.

1.3 Dissertation Structure and Research Contributions

This dissertation is organized as follows. In chapter 2 some of the basic notions of the sliding mode control theory are given. The aim of this chapter is to provide a brief introduction to the HOSM control theory and to describe the main features and advantages of HOSMs. The foundation necessary to understand the basics of way-point path following guidance are explained, respective notations are discussed and kinematic state model for guidance problem is derived. In addition guidance objectives are outlined with an explicit problem formulation. The contributions of this dissertation into chapters are summarized as follows

- Chapter 3: High performance nonlinear sliding surfaces are proposed for lateral guidance of UAVs. The limitations of an existing nonlinear sliding surface for lateral guidance are indicated and two stable similar nonlinear sliding manifolds are proposed. In the outer guidance loop, the proposed guidance scheme relies on a nonlinear switching surface with 1st order SMC algorithm derived at the kinematic level generating reference bank commands. The autopilot based on super twisting algorithm, using linear sliding surface forms the inner control loop. Proof of existence of $2-$sliding mode and actuation boundedness of the closed-loop i.e., guidance and control path-following system with the UAV kinematics along the dynamics of autopilot are given. The proposed guidance and control system performance is verified via extensive flight tests of scaled YAK-54 UAV. The flight results validate the proposed guidance and control framework. This work is submitted to journal for publication.

- Chapter 4: To incorporate the constraints due to the un-modifiable autopilot, an additional state is introduced into the kinematic guidance model to develop an augmented guidance controller. The guidance law developed in this research takes into account constraints on the vehicle dynamics and is derived using geometrical considerations of the kinematics of vehicle motion. The objective is to drive the cross-track and course angle errors to zero. Here we extended our previous work [55, 56] by taking into account the dynamics of the inner control loop while designing the outer guidance loop. The structural and dynamic limitations are translated into an approximation; therefore, the generated references satisfy a constraint on the maximum admissible bank command. The overall system therefore performs better, especially when the inner loop is slower and comparable in response time to the outer loop. Because of the increase of the relative degree of the problem, we propose a novel finite-time convergence law using higher order sliding mode (HOSM) theory. Local asymptotic stability of the proposed

nonlinear law and existence of the sliding mode is demonstrated. This control design framework is particularly useful for systems where the autopilot is un-modifiable and possibly unknown. Hence, the developed law is well suited for practical UAV applications. This work is published in the 'Transaction of Institute of Measurement and Control' (TIMC).

- Chapter 5: An innovative sliding mode based partially integrated lateral guidance and control scheme for UAVs is proposed. Guidance and control framework based on SOSMs is presented to solve the problem of two dimensional path-following. The main contribution of the technique presented here is the partial integration of the two loops i.e., a guidance and control system via series interconnection of two stable sliding manifolds. In the outer guidance loop, the proposed guidance scheme relies on a nonlinear switching surface with the real twisting algorithm derived at the kinematic level, generating roll error commands. The autopilot based on the super-twisting algorithm using a linear sliding surface forms the inner loop. Proof of existence of the 2-sliding mode, control boundedness and stability of the closed-loop, i.e., the overall guidance and control path-following system with the UAV kinematics and autopilot dynamics are given. Flight results validate the proposed framework for guidance and control design. A paper on this work is published in the 'Journal of Aerospace Science and Technology'

- Chapter 6: In this chapter, guidance law for accurate following of flight path to observe tight ground track control is presented. The unique feature is to explicitly account for autopilot constraints by defining a 3-D sliding manifold. The guidance solution described is based on state stabilization of kinematics-dynamics trajectories i.e., the guidance law is evolved based on the knowledge of dynamical characteristics of UAV. The 2-D sliding surface for lateral guidance is evolved by adding an extra dimension of vehicle dynamics; thus a 3-D nonlinear sliding surface is proposed which provides improved performance. A robust First Order Sliding Mode Control (FOSMC) guidance algorithm is derived using a nonlinear 3-D sliding manifold to develop the

guidance law, its stability is assessed with the integrated aircraft dynamics. The performance and effectiveness of the proposed guidance scheme is demonstrated by presenting flight test results. This work is submitted to journal for publication.

In chapter 7, conclusions are drawn based on the overall results and future work which requires investigation is outlined in order to further improve the guidance and control strategies.

Chapter 2

PRELIMINARIES

As the basic theme of this dissertation is the application of sliding mode theory to guidance and control logic design of UAVs, fundamental knowledge and basics of SMC theory and guidance is mandatory before we can formulate the path following problem. In this chapter all the necessary mathematical terms, notations and tools that are needed for the development of the path following guidance algorithm are introduced. This chapter presents the sliding mode theory to exploit its generality and flexibility by discussing its features of interest in section 2.1 and background material related to the guidance and control of UAVs. The basics pave the way to incorporate the features of SMC by formulating the guidance problem.

2.1 Sliding Mode Control

In order to formulate any practical control problem, one has to consider the fact that there will always be discrepancy (or mismatch) between actual plant and the mathematical model for the control law design. The difference arises due to uncertainties, parasitic/un-modelled dynamics and unknown external disturbances. It is a challenging task to design such a control law which can give robust performance even in the presence of these uncertainties and disturbances. To solve this problem, intense research is carried in the development of robust control methods. In the last decade, sliding mode control emerges as a competent robust control strategy.

In the late fifties, the studies leading to the introduction of discontinuous control action into the dynamical systems resulted in the concept of sliding mode. The system states are forced to reach and subsequently remain on a predefined surface in the dynamical system's state space with the use of switched control law. The sliding mode techniques provide a robust solution for control, parameter estimation

and fault diagnosis of dynamic systems and are known to be robust with straight forward design procedures. The resulting reduced order sliding motion with judicious use of switched control laws was shown to be insensitive to a certain class of uncertainties or external disturbances, see for example [72, 73]. This section briefly introduces the sliding mode control, associated literature survey followed by higher order sliding mode control theory. This leads to the introduction of the 1st- order sliding mode control (SMC) and second order sliding modes (SOSM) algorithms, their applications to uncertain nonlinear systems is discussed.

2.1.1 Introduction

The features of SMC and its robustness properties towards the uncertain systems were first explained in a book by Itkis [74] and in survey paper by Utkin [73]. The field of the study had its real boast after the work of Utkin [73] and since then the scheme is continuously modified/improved into a generic control design method to control broad range of mechanical systems. *Essentially, sliding mode control makes use of the discontinuous control in order to compel the system trajectories to reach and then to remain on a specific surface known as the sliding manifold* [6]. The most distinguished feature of sliding mode control is the invariance property towards matched uncertainties, which makes this technique particularly suitable to be used to control uncertain nonlinear systems [6]. An ideal sliding motion represents the controlled system behavior when the system dynamics are confined to the sliding manifold. The control laws with state feedback are not functions of time, neither they are continuous, but they continuously change from one structure to the other. It can be inferred that the formation of the control law is changed on the basis of location of the system trajectories, due to this very reason SMC is referred to as variable structure control because it continuously toggles its control structure. Sliding mode control is a nonlinear method used for controlling both the linear as well as nonlinear systems. It transforms the system dynamics in such a way that it becomes robust to disturbances and uncertainties by the use of high frequency control switching. However, actuators are physical devices and the

high frequency control actions of sliding mode control can cause chattering, over heating of actuators, plant damage and can even excite un-modeled fast dynamics which can deteriorate the performance of the system.

The sliding surface designed to establish the desired sliding motion controls the behavior of the system. In SMC, some constraints are enforced on the designed sliding manifold to establish sliding motion. The system states are forced to cross and re-cross the sliding manifold repeatedly until the deviation from the sliding manifold becomes zero and it finally slides along the manifold. To do so, SMC produces a discontinuous control signal. The associated motion is referred as 'sliding motion' and corresponding state of the system is called 'sliding mode'. There are two stages in sliding mode control, reaching phase and sliding phase. With the help of appropriate control law, system trajectories are driven to a stable manifold and this is called reaching phase. The second phase is termed as sliding phase, when the system trajectories slide to an equilibrium point following the prescribed sliding surface constraint. The system is confined to a manifold using the control law and behaves like a reduced order system. Hence the sliding mode control system attributes high accuracy, robustness against external disturbances and parametric variations.

2.1.2 First order SMC design

For the stabilization of nonlinear uncertain systems, sliding mode control uses high frequency [68] control input. The sliding mode control due to its inherent properties, provides the benefit of dividing complex higher order problem into smaller tasks of relatively simpler scope [6]. The design of SMC includes a two step design procedure:

- In the state/error space, selection of stable hyperplane (switching function) on which motion should be restricted, and

- To make the sliding surface attractive, a robust control law is developed.

2.1.3   Switching function and control laws

Properties of the switching function includes the following

- Order of switching function is less than order of plant.

- The parameters of the switching function determines the sliding mode, independent of plant dynamics.

- Switching (sliding surface) is independent of the control law.

Switching function can in general have two forms based on their design i.e., non-linear manifolds with its merits and problems as

- For nonlinear systems it gives global dynamic properties

- Design options are numerous

- The surface parameters selection is difficult

or linear manifolds with its incentive and problems as

- The surface parameters are easy to obtain

- Generally, may not be appropriate for system dynamics.

- The control signal magnitude increases with the increase in tracking error.

The objective of the sliding mode is to ensure sliding motion in finite time, starting from any point in the phase portrait. The second step is the design of switching control that will drive the system's state trajectories towards the sliding surface, and upon reaching maintain sliding motion on it for all subsequent times. The idea of sliding mode can be described as in Figure 2.1. The following reaching laws have been proposed in the literature.
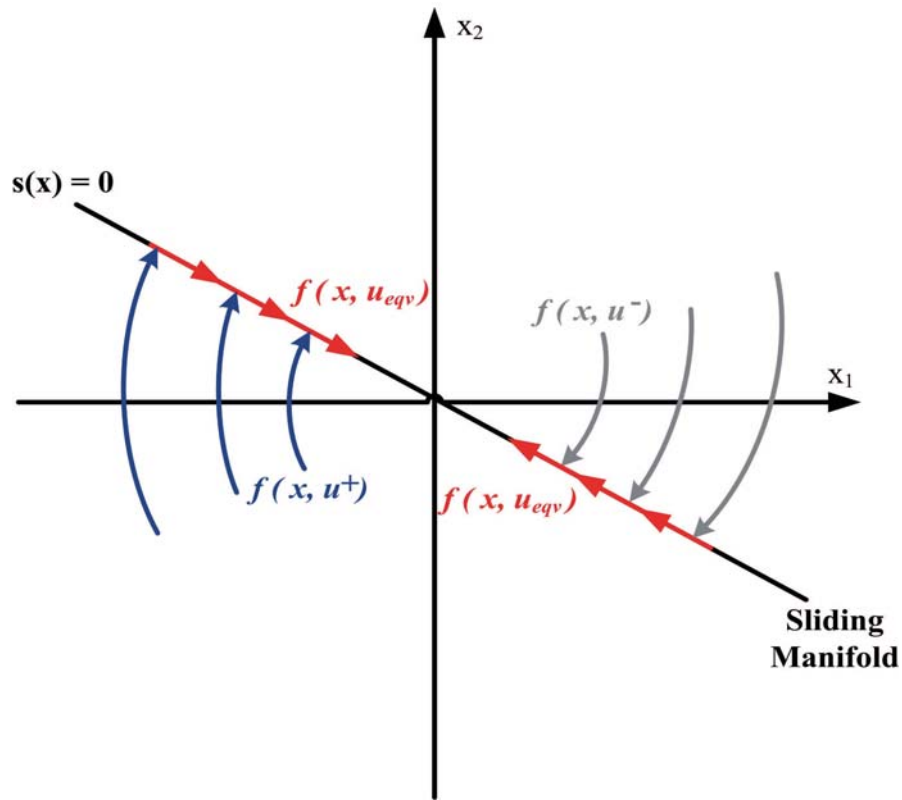
FIGURE 2.1: Sliding mode idea [6]

- Constant Rate Reaching Law:

$$\dot{s} = -k\,\mathrm{sgn}(s), \quad k > 0 \qquad (2.1)$$

where k represents the constant rate. The switching variable is forced at a constant rate k to reach the switching manifold s. Simplicity is the main merit of this reaching law. The reaching time will be long if k is selected small. On the other hand, severe chattering will be caused by large values of k.

- Exponential Reaching Law:

$$\dot{s} = -k\,\mathrm{sgn}(s) - k_1 s, \quad k > 0, k_1 > 0 \qquad (2.2)$$

23

where $-k_1 s$ represents an exponential term. When s is large, the states are forced to reach the switching manifold faster by the addition of proportional rate term.

- Power Rate Reaching Law

$$\dot{s} = -k \, |s|^{\rho} \, \text{sgn}(s), \quad k > 0, 1 > \rho > 0 \qquad (2.3)$$

This reaching law increases the reaching speed when the state is far away from the switching manifold and reduces the rate when the state is near the manifold.

2.1.4 Relative degree, reachability condition and reaching time

Relative degree: General concept of relative degree is of great importance to the practical understanding of SMC. The relative degree [6] is defined as the number of times the output of a system must be differentiated for the control input to appear. For example, in the double integrator problem the input is $u(t)$ and the output is $y(t)$. Thus the output needs to be differentiated twice to see u(t) in the equation and the relative degree of the problem is two.

Reachability condition: In sliding mode literature, the control input is designed by ensure the reachability condition. The reachability condition specifies whether the system state trajectories are always confined towards the sliding manifold or not. The sliding surface *attractivity* can be expressed by the condition:

$$\lim_{s \to 0^+} \dot{s} < 0, \qquad \lim_{s \to 0^-} \dot{s} > 0. \qquad (2.4)$$

The above condition guarantees that s and $\dot{s}$ have opposite signs, i.e.,

$$s\dot{s} < 0. \qquad (2.5)$$

The above condition is referred as the *reachability condition* [6].

Despite the presence of uncertainties, the control law $u(t)$ is designed to ensure finite time convergence to the sliding surface. Therefore, more restrictive reachability condition is given by:

$$s\dot{s} \leq -\eta |s| \qquad (2.6)$$

In literature the above condition is referred as the η-reachability condition [6] which ensures a finite time convergence to $s = 0$.

Reaching time:

The two modes of system operation can be divided in two parts representing the state space trajectory of the SMC law. Starting from any initial condition, the trajectories tends towards the sliding surface. This phase of sliding mode control is known as reaching phase or reaching mode. The time needed to reach the sliding surface is known as reaching time [6]. After reaching the sliding surface, the trajectories move towards the equilibrium point. The later phase is referred as the sliding mode. During the reaching mode, the trajectories are sensitive to disturbances, uncertainties and parametric variations. However, the trajectories are insensitive in sliding mode [75]. Thus a considerable effort is made in research to lower or eliminate reaching time.

From (2.6), for $s > 0$ we can have $\dot{s} \leq -\eta$ and for $s < 0$ we can derive $\dot{s} \geq \eta$. Therefore we can write

$$\eta \leq \dot{s} \leq -\eta \qquad (2.7)$$

By integration of (2.7)

$$\eta t \leq s(t) - s(0) \leq -\eta t \qquad (2.8)$$

when $t = t_{rch}$, $s(t_{rch}) = 0$ therefore

$$-\eta t_{rch} \leq s(0) \leq \eta t \qquad (2.9)$$

we can have

$$|s(0)| \leq \eta t_{rch} \qquad (2.10)$$

showing that starting from an initial condition $s(0)$, the time required to reach the surface [6] is given by

$$t_{rch} = \frac{|s(0)|}{\eta} \qquad (2.11)$$

Conventionally, the parameters of SMC are selected to reduce the time spent during the reaching phase. The system evolution in the reaching phase is dependent on the selected reaching laws and the systems uncertainties. A smaller reaching time would imply that sliding begins earlier. The reaching time strictly depends upon the selection of η. To achieve shorter reaching time, η might be taken high and as small as enough to limit the chattering according to (2.6).

2.1.5 Problem statement

Consider a dynamical system with the following mathematical form.

$$\ddot{x} = f(x,t) + b(x,t)u(t) + \vartheta(x,t) \qquad (2.12)$$

Where $x(t) \in R^n$ is the state vector and $u(t) \in R$ is the control input. $f(x,t) \in R^n$ and $b(x,t) \in R^n$ are measurable nonlinear functions of time and states. The term $\vartheta(x,t)$ is norm bounded uncertainty i.e., $|\vartheta(x,t)| \leq M > 0$. Despite the presence of uncertainties, model imprecision, and parametric variations in $f(x,t)$ and $b(x,t)$, the control objective is to precisely track the desired input or the reference command. For control design a time varying linear surface $s(x)$ is defined

as follows

$$s(x) = C_1 e + \dot{e} \qquad (2.13)$$

where C_1 is a positive constant tuned for the performance parameter of the system and $e = x - x_d$ is the error between the desired and actual state x. The error switching manifold takes the form

$$s(x) = C_1(x - x_d) + (\dot{x} - \dot{x}_d) \qquad (2.14)$$

Along the nonlinear system (2.12), the time derivative of (2.14) takes the following form

$$
\begin{aligned}
\dot{s}(x) &= C_1(\dot{x} - \dot{x}_d) + (\ddot{x} - \ddot{x}_d) \\
&= C_1(\dot{x} - \dot{x}_d) + (f(x,t) + b(x,t)u(t) + \vartheta(x,t) - \ddot{x}_d) \qquad (2.15)
\end{aligned}
$$

The term $b(x,t)$ is assumed to be invertible. The corresponding equivalent control is written as

$$u_{eq} = \frac{1}{b(x,t)} \{-C_1(\dot{x} - \dot{x}_d) - (f(x,t) - \ddot{x}_d)\} \qquad (2.16)$$

To make the control law robust against uncertainties and ensure reachability a reaching law (2.1), (2.2) or (2.3) can be selected. A discontinuous term is added [76]

$$u_c(t) = \left\{ \begin{array}{ll} u^+(s) & \mathrm{sgn}(s(x)) > 0 \\ u^-(s) & \mathrm{sgn}(s(x)) < 0 \end{array} \quad u^+ \neq u^- \right\} \qquad (2.17)$$

27

where u^+ is the control effort applied to the system when s is $+ve$ and u^- is the effort when s is $-ve$. Control law comprises of two terms

$$u(t) = u_{eq}(t) + u_c(t) \qquad (2.18)$$

where u_c is the corrective control used to to reach the sliding surface and compensate for the deviations from the sliding manifold and u_{eq} is the equivalent control used to stay on the sliding surface to make the derivative of the sliding surface equal to zero. High speed switching is used by the corrective control to enforce the state trajectory towards a switching function. Total control law with $u_{eq}(t)$ in (2.16) and $u_c(t)$ in (2.17) becomes

$$u(t) = \frac{1}{b(x,t)} \left\{ -C_1(\dot{x} - \dot{x}_d) - (f(x,t) - \ddot{x}_d) \right\} - k \operatorname{sgn}(s(x)) \qquad (2.19)$$

where k is the switching gain which can be selected according to the reachability condition. The reachability can be verified using Lyapunov function approach, a suitable candidate can be $L(x)$, which is given as:

$$L(x) = \frac{1}{2} s^2(x) \qquad (2.20)$$

Its time derivative can be written as

$$\dot{L}(x) = \frac{\partial(L(x))}{\partial s} \dot{s}(x) = s(x)\dot{s}(x) < 0 \qquad (2.21)$$

Condition (2.21) is often referred as reachability condition. Meeting the reachability or existence condition means that the trajectory of the system in (2.12) is driven or attracted towards the sliding surface. From the expression (2.15) of $\dot{s}$ we can write

$$\dot{L}(x) = s(x) \left\{ C_1(\dot{x} - \dot{x}_d) + (f(x,t) + b(x,t) \left\{ 1/b(x,t) \left\{ -C_1(\dot{x} - \dot{x}_d) \right. \right. \right.$$
$$\left. \left. \left. - (f(x,t) - \ddot{x}_d) \right\} - k \operatorname{sgn}(s(x)) \right\} + \vartheta - \ddot{x}_d \right\} \qquad (2.22)$$

28

After simplification the expression of $\dot{L}(x)$ can be written as

$$\dot{L}(x) = -s(x) \left\{ -\vartheta + \frac{k \operatorname{sgn}(s(x))}{b(x,t)} \right\} \tag{2.23}$$

$\dot{L}(x)$ will be negative definite if

$$k > |b(x,t)M| \tag{2.24}$$

The gain k must be chosen according to condition derived in (2.24) to ensure reachability i.e., $s\dot{s} < 0$. Sliding mode will exist and trajectories will converge towards the sliding surface. The control u in (2.18) drives the state variables to the designed sliding surface in finite time, and keeps them on the surface thereafter in the presence of $\vartheta(x,t)$ the norm bounded uncertainty. Ideal sliding mode is said to be taking place in the system (2.12) for all t. The system is stabilized by the control law in (2.19), due to switching imperfections chattering phenomenon appears in the control input.

Inherent Flaws of SMC

- The high frequency switching can result in a highly undesirable phenomenon for any physical plant or actuators called 'chattering'. The chattering can excite un-modelled high frequency dynamics of the plant.

- The SMC is applicable only if the system has relative degree one or below with respect to the constraint function i.e., the sliding manifold.

2.1.6 Problem of chattering

The chattering induced by the standard sliding mode controller causes reduced reliability and life cycle of real systems by causing early wear out of actuators and system components. Due to high frequency switching of the control law, system suffers from chattering phenomena which may lead to certain problems. In literature, a number of methods have been developed to avoid this chattering

effect e.g., dynamic sliding mode control [77], higher order sliding mode control [78], saturation approximation [79, 80], terminal sliding mode control [81] and equivalent control [82].

2.1.6.1 Chattering elimination: Quasi sliding mode

In saturation approximation [79, 80], the surface dynamics are changed within a small vicinity of discontinuous surface by replacing the sign function with a saturation approximation function thus proposing a smooth transition. To make the control function (2.18) smooth, the discontinuous function $u_c(t) = -K \operatorname{sgn}(s)$ is approximated by continuous/smooth "sigmoid function" as $\frac{s}{|s|+\epsilon}$, where ϵ is a small positive scalar. It can be observed that

$$\lim_{\epsilon \to 0} \frac{s}{|s| + \epsilon} = \operatorname{sgn}(s) \tag{2.25}$$

Higher the value of ϵ, the lesser will be the chattering and also the robustness. The selection of ϵ represents a tradeoff between the requirement to ensure a smooth control action or maintaining the ideal performance. Figure 2.2 illustrates the graphical representation of saturation approximation of switching function $\operatorname{sgn}(s)$ [79].
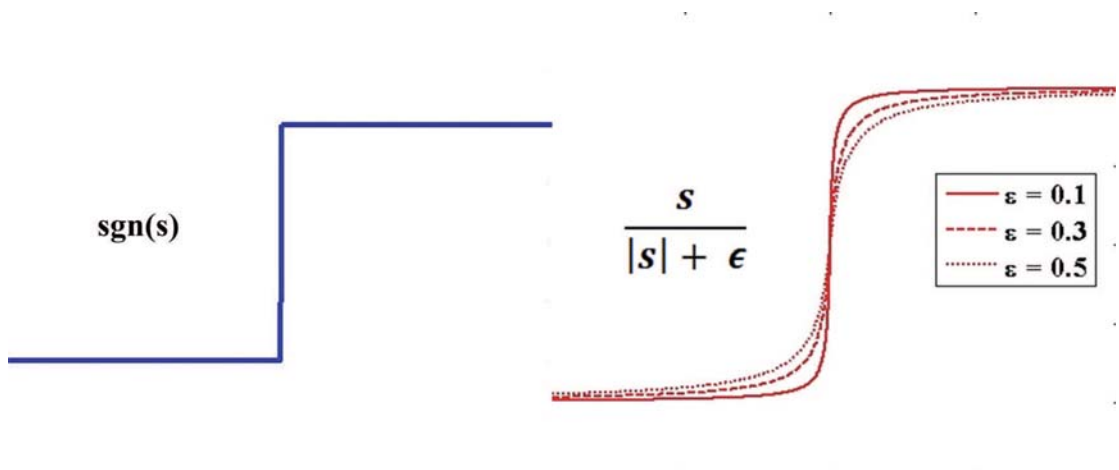
FIGURE 2.2: Approximation of Signum function, quasi sliding mode

In the presence of external disturbance, it is difficult to achieve the finite time convergence of the sliding variable with a smooth control function. Instead, these sliding variables converge towards the vicinity of the sliding manifold. Hence, in order to achieve a smooth control, the robustness has to be compromised with degradation in accuracy. The designed smooth control is not an ideal sliding mode control, as the sliding variables are not driven to zero in finite time. However, the smooth control law gives similar system performance in comparison with discontinuous sliding mode control (2.18). The above discussion converges to a point that we can call a smooth control law as a quasi-sliding mode control and the motion of the system in the vicinity of the sliding surface is known as quasi-sliding mode. This is the most commonly used technique to avoid chattering. The saturation approximation technique is extensively applied to many practical problems [82].

2.2 Higher Order Sliding Modes

Higher order sliding mode control [83, 84, 85] is a recently developed new technique that removes all the standard restrictions of sliding mode control, while the fundamental features of the sliding mode are preserved. The aim of this subsection is to provide a brief introduction to the higher order sliding mode control theory and to describe the main features and advantages of higher order sliding modes. In particular, the second order sliding mode (SOSM) control problem is described for second order real twisting and super twisting controllers. After the introduction of SMC by [86], an editorial to special edition of International Journal of Robust and Nonlinear Control on higher order sliding modes [87] has highlighted the exponential growth of publications on second order sliding mode theory and applications. This special issue highlights the salient features of the papers presented and covers current state of the art on modern higher order sliding mode control. Let r represents the relative degree of the dynamical system. The sliding mode control is said to be of rth order if the designed control law forces the sliding

variable and their $r - 1$ successive derivatives to zero in finite time. And compels them to subsequently stay there in the presence of bounded disturbance[7] i.e.,

$$s = \dot{s} = \ddot{s} \cdots = s^{r-1} = 0 \qquad (2.26)$$

Generally speaking, any r^{th} order sliding controller requires the knowledge of the time derivatives of the sliding variable up to the $(r - 1)^{th}$ order.

2.2.1 Second order sliding modes

In the second order sliding mode approach, as the name depicts, the sign and amplitude of the second time derivative i.e., $\ddot{s}$ are directly influenced by the control action. A suitable switching logic is required which ensures finite time convergence of the state trajectories to the sliding surface $s = \dot{s} = 0$ [88]. Second order sliding mode controllers are widely used in practice because of their simplicity and lower information demand. The most frequently used second order sliding mode algorithms in literature are described briefly.

2.2.1.1 Real twisting algorithm

Historically the twisting algorithm is the first known second order sliding mode algorithm [85]. Using the twisting control, system trajectories twist around origin of the 2nd order sliding manifold and converge to origin within finite time as shown in Figure 2.3. Real twisting algorithm is used for relative degree two problems. It provides good robustness properties. The algorithm requires measurement of the first derivative of the sliding manifold for implementation. Let a second order dynamical system be represented as:
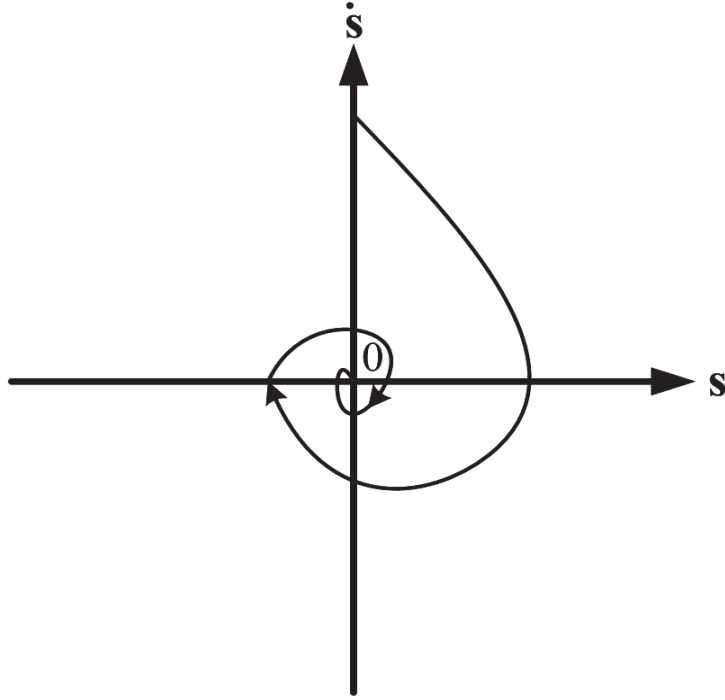
FIGURE 2.3: Real Twisting Algorithm convergence [7]

$$\ddot{s} = a(t, x) + b(t, x)u \qquad (2.27)$$

which is interpreted as dynamics of the sliding variable $s \in \Re$ calculated along the system state trajectories and $u \in \Re$ is the control input. The terms $a(t, x)$ and $b(t, x)$ are bounded as:

$$|a(t, x)| \leq C, \quad 0 \leq k_r \leq b(t, x) \leq K_R \qquad (2.28)$$

where k_r and K_R are the minimum and maximum bounds of the amplification factor on the control input [85]. The control law is given as:

$$u = -r_1 \, \text{sgn}(s) - r_2 \, \text{sgn}(\dot{s}) \qquad (2.29)$$

A system is called finite time stable if it ensures asymptotic stability and provides state convergence from any initial condition with finite settling time [89]. Let r_1 and r_2, the controller gains satisfy the following conditions:

$$r_1 > r_2 > 0 \tag{2.30}$$

$$k_r(r_1 + r_2) - C > K_R(r_1 - r_2) + C \tag{2.31}$$

$$k_r(r_1 + r_2) > C \tag{2.32}$$

Then the system (2.27) with control (2.29) is finite time stable [89] and provides the appearance of a 2-sliding mode, attracting the trajectories in finite time.

Refinement of real twisting algorithm is performed in order to minimize the magnitude to discontinuous control signal [90, 91, 92], a continuous control term was added to the (2.29) in i.e.,

$$u = u_{eq} + u_{disc} \tag{2.33}$$

where u_{eq} can be derived by solving $\ddot{s} = 0$ as

$$u_{eq} = -\frac{a(t, x)}{b(t, x)} \tag{2.34}$$

is the equivalent control used to cancel out the affine part of (2.27) i.e., the control value that nullifies $\ddot{s}$ [90]. The complete control law takes the form

$$u = -\frac{a(t, x)}{b(t, x)} - r_1 \operatorname{sgn}(s) - r_2 \operatorname{sgn}(\dot{s}) \tag{2.35}$$

with discontinuous u in (2.35), s and $\dot{s}$ are continuous functions, while $\ddot{s}$ is discontinuous [91]. With (2.35), the second order establishment is guaranteed in finite time with relative lesser values of controller gains [90, 92]. For certain class of

systems, the availability of u_{eq} is difficult due to unavailability of $\ddot{s}$, either the controller in (2.29) is used with higher magnitude of r_1 and r_2 or a robust disturbance observer [91] may be used to observe u_{eq}.

2.2.1.2 Super twisting algorithm

In super twisting algorithm [85], the trajectories are also characterized on the 2nd order sliding hyperplane by twisting around the origin as shown in Figure 2.4. The super twisting algorithm provides a 2-sliding mode by providing the control law for relative degree one problems. The structure of the control law enforces this algorithm to behave in continuous manner and reduce the chattering phenomena caused due to a signum function. The control law u in (2.37) consists of two $\text{sgn}(s)$ terms. For the first term, the control law is continuous because the chattering effects are smoothen out due to the power of the sliding variable. Chattering occurs when $s \approx 0$, and in (2.37) it is reduced by $|s|^{\gamma}$. And the second term, as can be observed in (2.37), it is concealed in the integral part of the control signal u. Consider a dynamical system
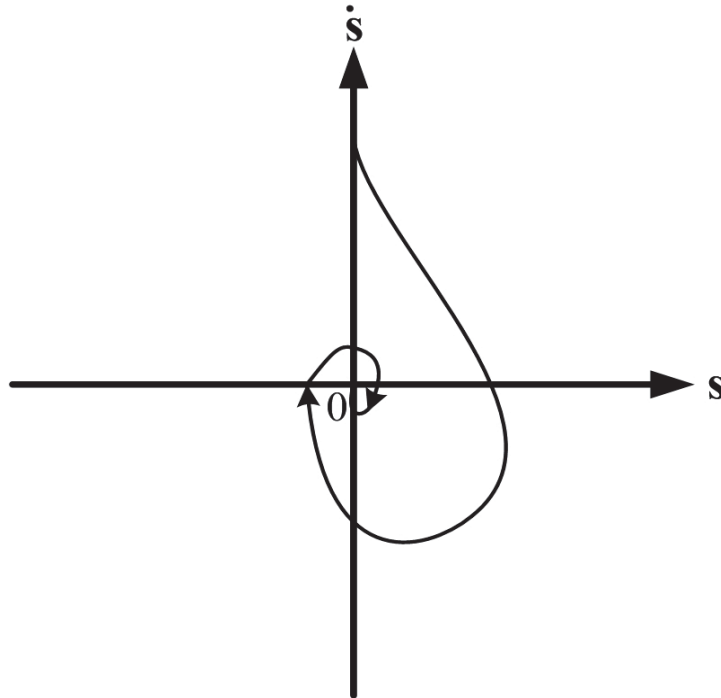
FIGURE 2.4: Super Twisting Algorithm convergence [7]

35

$$\dot{s} = a(t, x) + b(t, x)u \tag{2.36}$$

Then the super twisting control law appears in the following form and does not need measurement of $\dot{s}$.

$$u = -\lambda |s|^\gamma \operatorname{sgn}(s) + u_1, \quad \dot{u}_1 = \begin{cases} -u & |u| > U_S \\ -K \operatorname{sgn}(s) & |u| \le U_S \end{cases} \tag{2.37}$$

where γ is the smoothing parameter and U_s is the maximum allowed control input. Let the positive constants C, K_s, K_S, K, λ and $0 < \gamma < 1$ satisfy the following conditions:

$$0 \le K_s \le b(t, x) \le K_S \tag{2.38}$$

$$\gamma U_S < \left| \frac{a(t, x)}{b(t, x)} \right| \tag{2.39}$$

$$|\dot{a}(t, x)| + U_S |\dot{b}(t, x)| \le C \tag{2.40}$$

$$K_s K \ge C \tag{2.41}$$

$$\lambda > \sqrt{\frac{2}{(K_s \alpha - C)} \frac{(K_s \alpha + C) K_S (1 + \gamma)}{K_m^2 (1 - \gamma)}} \tag{2.42}$$

Then the closed-loop system (2.36) with control (2.37) is finite-time stable [85]. In the presence of bounded disturbances, the sliding dynamics s in (2.36) and $\dot{s}$ will slide towards zero, i.e., $s, \dot{s} \to 0$ in finite time using the super twisting control law [85], [89]. The control law in (2.37) can be interpreted as an SOSM control,

since it provides finite time convergence of $s, \dot{s} \to 0$.

The main objective of the classical sliding mode framework is to force the system to evolve on a "sliding surface". Practically sliding mode controllers are implemented often in micro-controllers and digital computers. For such cases information about measurements of the system are only available after specific time instances and therefore control input can only be changed at these instances. Getting around sampling time is therefore often not possible. This phenomenon introduces a discrete element in the sliding mode control law. To deal with such practical problems discrete time sliding mode control architecture [6, 93, 94] is used. Design of sliding mode control in discrete framework depends on the dynamics of the plant to be controlled. In our case of guidance problem for UAVs, the change in kinematic variables with time is relatively slow (in comparison with the 4 Hz implementation), hence the continuous time sliding mode framework is used in this work.

2.3 UAV Guidance Problem

Fundamental architecture of guidance, navigation and control of small unmanned aerial systems is shown in Figure 2.5. The first block has inputs of maps, destinations and obstacles by the operator called path planner or mission planner. Depending upon the the input, mission planner calculates the mission plan in terms of way points connected by straight lines or circular arcs, and the path manager needs to follow the sent mission plan. The key job of path manager is to toggle between way points and to generate an active straight/circular path that the vehicle should follow. According to the definition of active path, appropriate commands (e.g., reference heading/roll angle, speed, altitude) are produced for 'path following' (also known as guidance block). The control surface/engine throttle is triggered by the autopilot (control block) to track the reference commands generated by the guidance block. The 'UAV' block represents the mathematical model in simulation and an experimental UAV in flight mode. Feedback from sensors measuring/observing the current system states are used to generate the reference

commands at every time step by all the blocks. Observers may be required to estimate certain state variables if their measurement are not available directly. In aerospace systems, three terms Navigation, Guidance and Control are commonly used; these are defined and discussed below.
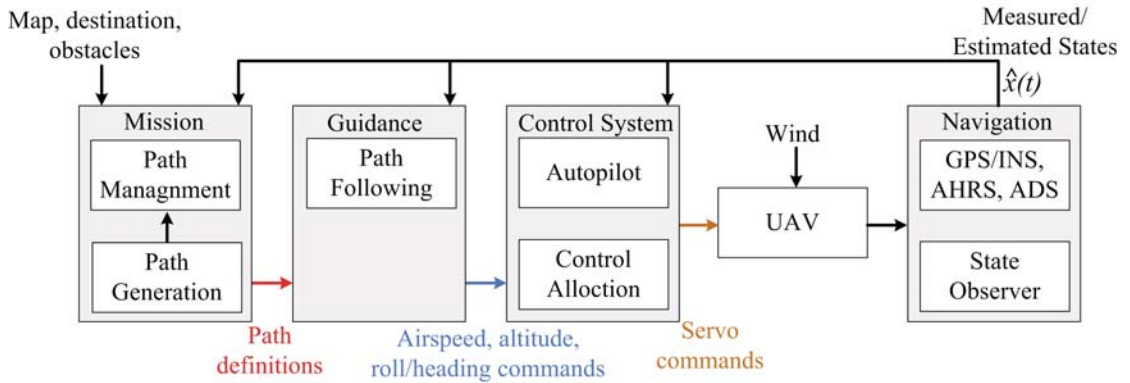
FIGURE 2.5: Guidance Navigation and Control Block Diagram.

2.3.1 Navigation

Navigation system is a measurement/sensor unit used to provide feedback about the current state variables. After measurement it outputs the vehicles full states vector or its part information which comprises the following:

- Position of UAV in space (x_e, y_e, z_e)

- Velocity of UAV (u, v, w)

- Attitude angles (ϕ, θ, ψ)

- Airspeed (V_a)

- Angle of attack (α), side-slip angle (β)

- Angular rates (p, q, r)

However, the main objective of the navigation system is to find out the UAV position, velocity and attitude at any time. The velocity and position are calculated

in the navigation frame. To make sure that the specific measured force by the accelerometers can be transformed to the navigation frame, an integral part of the navigation system is the attitude determination. The sensors (inertial measurement unit (IMU) and global positioning system (GPS) receiver) are used to estimate these variables. These sensors are called navigation sensors. The IMU measures rotation rate and force along the sensitive axis using accelerometers and orthogonally mounted gyroscopes.

Use of Micro Electro-Mechanical System (MEMS) sensors in the inertial navigation systems has been a subject of great interest in the last decade. Automotive-grade MEMS based navigation system is a six-degree of freedom IMU. It is a very small chip which confines three orthogonally aligned gyroscopes and accelerometers. Navigation systems based on MEMS are commonly used in small UAVs, since it offers low cost, light weight, low power consumption and ruggedness due to its small size. If no external measurement aids are available and if the system runs in stand-alone mode the absolute accuracy deteriorates with time. The large errors in velocity, attitude and position come about mainly due to sensor noise and bias. The MEMS inertial sensors measurements are tuned through a Kalman filter and GPS serves as an aiding device. While extra sensory feedback is employed through magnetometers to improve the system performance. Such an integrated system is known as GPS aided MEMS Inertial Navigation System. Mostly low-cost GPS receivers provide output data at 1-10 Hz update, however, there are specialized GPS receivers that can generate data up to 100 Hz.

2.3.2 Guidance

According to a definition, "A guidance system is a virtual or physical device, or a group of devices implementing a guidance process used for controlling the movement of a ship, aircraft, missile, rocket, satellite, or any other moving object". One other definition is: "Guidance is the process of calculating the changes in position, velocity, attitude, and/or rotation rates of a moving object required to follow a certain trajectory and/or attitude profile based on information about

the object's state of motion". Guidance is the driving force of a vehicle. Input is taken from the navigation system (position, speed, direction, etc.) and path information, signals are generated for flight control system through which vehicle is able to achieve its objective (within the operating constraints of the vehicle).

A guidance system for UAVs is defined as a group of components that guides the vehicle with respect to desired ground track by manipulating flight path in accordance with a law to achieve the flight mission goal. The aim of a guidance system design is to determine suitable flight path trajectories such that it can achieve and then follow the desired mission precisely. The guidance system finds the best trajectory based on the knowledge of the vehicle kinematics information and the desired mission path. Input to the guidance system is the feedback coming from navigation system. Instructions for the control system are calculated by the guidance system. A guidance system has three major parts: Inputs, Processing, and Outputs. The input section includes measurements from the sensors and mission information. To achieve accurate heading, processing section uses the data and decides the action accordingly. Output is fed to autopilot which can influence the systems course by actuating ailerons, rudders, or other devices.

Pilot is responsible for the job of the 'Guidance system' in manned aircraft (flying in manual mode). Pilot uses the information exhibited by the visual and sensors to issue the reference commands to keep the aircraft on required path. For example, the pilot may move the stick to issue pitch and roll reference to keep the aircraft on the desired altitude and ground path. Pilot may use throttle stick to generate reference commands through which required speed is achieved. Guidance system performs all these functions in unmanned systems.

2.3.2.1 Notations and variables

We first define important angles and some variables as shown in Figures 2.6 – 2.8 in order to set up the guidance problem. These figures indicate the positive sense of all these variables. Let $WP1$ and $WP2$ be two way-points on the earth's surface then

- y is the lateral displacement or cross track error of the craft when following $WP1 \rightarrow WP2$.

- χ_R is the *reference* or *desired course* angle of the line $WP1 \rightarrow WP2$ with respect to north.

- $\dot{\chi}_R$ be the rate of change of desired course angle of the line $WP1 \rightarrow WP2$ with respect to north when following curved paths.

- χ is the course angle, considered as a kinematic variable, it is the angle of the ground velocity vector V of the craft with respect to north.

- $\chi_E = \chi - \chi_R$, called the *intercept course*.

- O denotes the center of turn for the circular path.

- R is the radius of turn for the circular path.

- ϕ is the bank angle.

2.3.2.2 Assumptions

The overall objective of this work is to provide a method to endow a UAV to autonomously track a ground trajectory with minimum lateral deviations, under the following conditions:

- An altitude control design [95] is available. The longitudinal guidance scheme takes the altitude waypoints and the vehicle kinematics information as inputs, and generates reference pitch angle commands for the inner control loop to track the desired altitude.

- Speed Profile: The physical limitation of the UAV requires the speed profile along the path to be bounded, satisfying appropriate boundedness conditions. We can imply that the speed profile will be bounded and satisfies

$$0 < V_{min} \leq V(t) \leq V_{max} \quad \forall t \geq 0 \qquad (2.43)$$

41
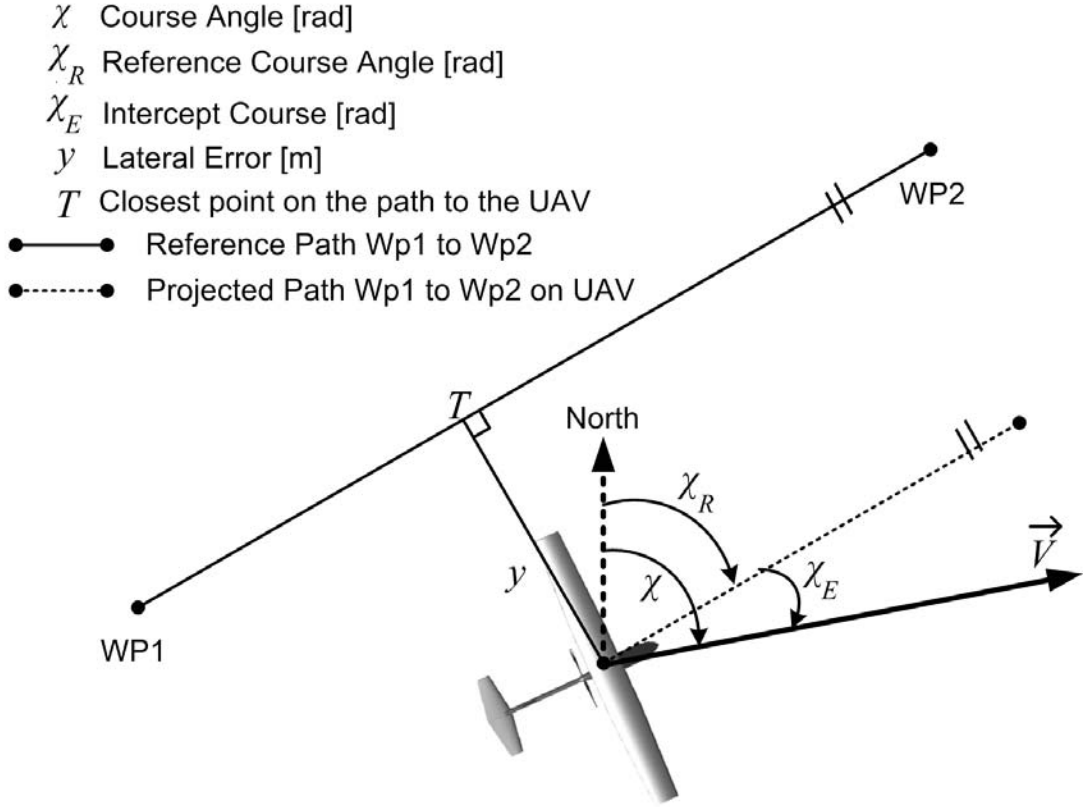
FIGURE 2.6: Definition of Cross track error y, χ, χ_R and χ_E

- Waypoint Switching: The mission plan, i.e., waypoints, the desired course angle χ_R and its rate of change $\dot{\chi}_R$ is available to the guidance algorithm.

2.3.2.3 Kinematic model

To avert or correct the cross track (lateral) error of aerial vehicles, lateral accelerations are generated using a component of aerodynamic lift. The lateral acceleration is generally produced by generating a suitable roll or bank in the vehicle: the *bank-to-turn* maneuver as depicted in Figure 2.7 by tilting the lift vector in the direction of the required turn. During turn, lift component is divided into two parts, one balances the centrifugal force and the other balances the weight of the vehicle:

$$L \cos \phi = mg, \qquad L \sin \phi = \frac{mV^2}{R} \qquad\qquad (2.44)$$
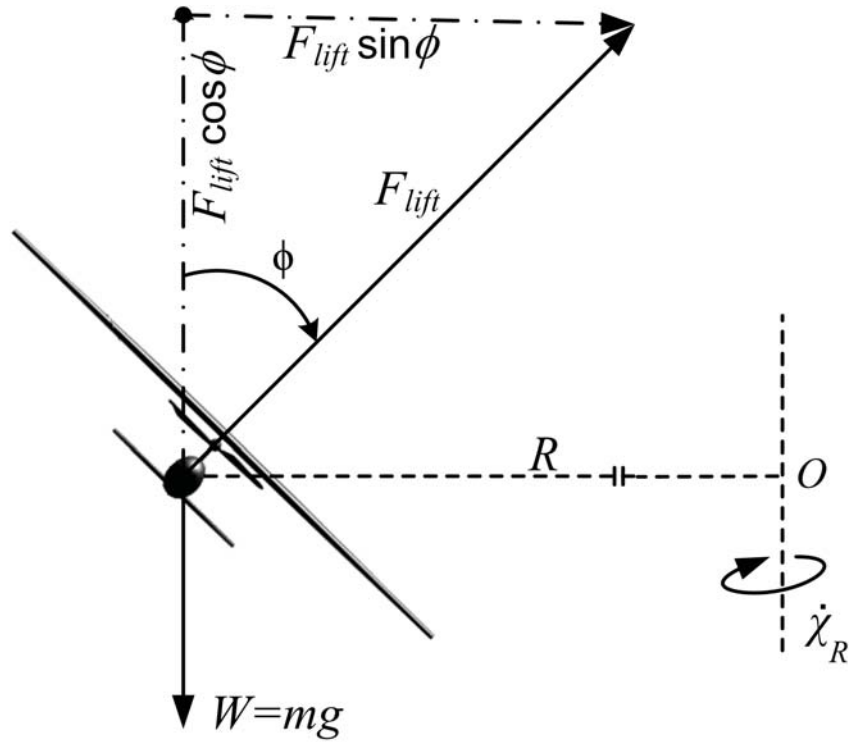
(a) Rear view during coordinated turn

FIGURE 2.7: Lift Components during turn

For a coordinated turn we have [34]:

$$\tan \phi = \frac{V^2}{Rg}.$$

(2.45)

During a steady turn $V = R\dot\chi$, so equation (2.45) takes the form:

$$\tan \phi = \frac{V\dot\chi}{g}.$$

(2.46)

Now since $\dot\chi_E = \dot\chi - \dot\chi_R$, therefore we have

$$\tan \phi = \frac{V(\dot\chi_E + \dot\chi_R)}{g},$$

(2.47)

or

$$\dot\chi_E = \frac{g}{V} \tan \phi - \dot\chi_R,$$

(2.48)

43

(b) Top view during coordinated turn

FIGURE 2.8: Lift Components during turn

where $\dot{\chi}_R$ is input from the mission plan.

Second state equation i.e., the rate of change of lateral displacement y can be derived using the component of the ground velocity vector $\overrightarrow{V}$ (Figure 2.6). We can write:

$$\dot{y} = V \sin \chi_E, \qquad\qquad (2.49)$$

2.3.2.4   State space representation

Considering the two state variables i.e., y and χ_E, we can write the state equations in the state space form as

$$
\begin{bmatrix} \dot{y} \\ \dot{\chi}_E \end{bmatrix} = \begin{bmatrix} V \sin \chi_E \\ -\dot{\chi}_R \end{bmatrix} + \begin{bmatrix} 0 \\ \frac{g}{V} \end{bmatrix} u \tag{2.50}
$$

where $u = \tan(\phi_{ref})$ or $\phi_{ref} = arctan(u)$ is the control signal generated by the guidance loop. In (2.50), $\dot{\chi}_R$ is a varying parameter and available from the mission block while following circular paths. It strictly depends upon the velocity V of the UAV and radius of turn R i.e., $\dot{\chi}_R = \frac{V}{R}$ for the circular mission.

2.3.2.5   Guidance objectives

There exist many aspects which can deviate the UAV from its desired position causing large lateral errors such as disturbing winds or loss of GPS signal. The UAV may be intended to follow a different reference path during flight and mission plan needed to be changed online, suddenly generating a large cross track error for the UAV. Or due to the loss of GPS signal, the navigation error grows quickly and within a few minutes may become significantly large. When the GPS signal is recovered and the mission block processes the available navigational data, UAV may suddenly find itself quite away from the path thus creating large lateral error. The small lateral errors can occur due to problems in the control loop, when guidance commands are not properly tracked. Therefore to achieve good performance in the presence of disturbances and uncertainties, an efficient and effective guidance system is to be designed which also caters for autopilot dynamics. The major tasks of the guidance algorithm are:

- To calculate the roll reference command for steering the vehicle back onto the desired path in the presence of disturbances, solve the guidance equations and generate a smooth and bounded ϕ_{ref}, using y, χ and ϕ as state

measurements to keep the lateral error small.

- regulate track error to zero by graceful bank-to-turn maneuvers, without excessive overshoot and maintain the general flight direction $WP1 \rightarrow WP2$,

- Keep the guidance output magnitude $|\phi_{ref}|$ below the maximum value ϕ_{max},

- In the presence of disturbances, stabilize and control the later-directional dynamics of the vehicle across the flight envelope

2.3.2.6 Way-point switching

The desired mission generated by the path planner defines the path to follow and it consists of a number of waypoints connected in series. Series interconnection of two consecutive waypoints via straight lines or arcs are included in a typical mission profile. Although the desired mission can be modified on-line anytime, it is generally planned off-line. It is assumed here that the desired waypoint information is available for the path following algorithm. The main objective of this subsection is to discuss practical aspects related to waypoint switching to follow a given mission. Two scenarios of a typical mission are described in Figure 2.9:

- A straight line segment and

- Waypoints with a turn

Three waypoints WP_1, WP_2 and WP_3 lie on a path and the UAV has to traverse through these waypoints. The following of the waypoints is distributed in three parts, first the straight path from P to P_1, then a circular path form P_1 to P_2 followed by a straight path onwards to point P_2. On the right side of the Figure 2.9 a scenario of a turn is shown. To prioritize path-following, the implementation uses a scheme of early way-point switching instead of way-point-precision. The segments can be switched by using number of ways, the following is simply the

one implemented on the scaled YAK-54 UAV. In this case a circular arc (close to $WP2$) shown in dashed red color is introduced because it is beyond the capability of the vehicle to take a sharp turn at the central waypoint ($WP2$). In Figure 2.9, O is the turn center, and P the current position of the UAV, the turn starts at a point P_1 and ends at point P_2. For this, referring to the geometry in Figure 2.9, the current position is closely monitored by the waypoint switching program and when the position P is greater than P_1, leg shift command is issued, the logic immediately switches to the next leg and a circular arc is followed by the UAV from P_1 to P_2. Upon reaching point P_2, the UAV starts to follow a straight path again towards the waypoint WP_3.

The problems in more specific terms are formulated. The task of the path manager (for the lateral guidance) is defined as to:

- From the designated track/trajectory, compute the cross-track deviation

- Compute the intercept course of the vehicle

- Monitor the distance for waypoint achievement.

- Determine the decision flags turn start and turn stop for the autopilot

All the above mentioned computations have to be done in the real time. Generation of the waypoint is beyond the scope of this study and we assume here that desired mission plan is available for the path following algorithm in terms of waypoints.

P Position of UAV
O Turn Center
F2 Flag Change Distance
P1 Position: UAV starts turning to follow WP2 ~ WP3
P2 Position: UAV stops turning and follow WP2 ~ WP3
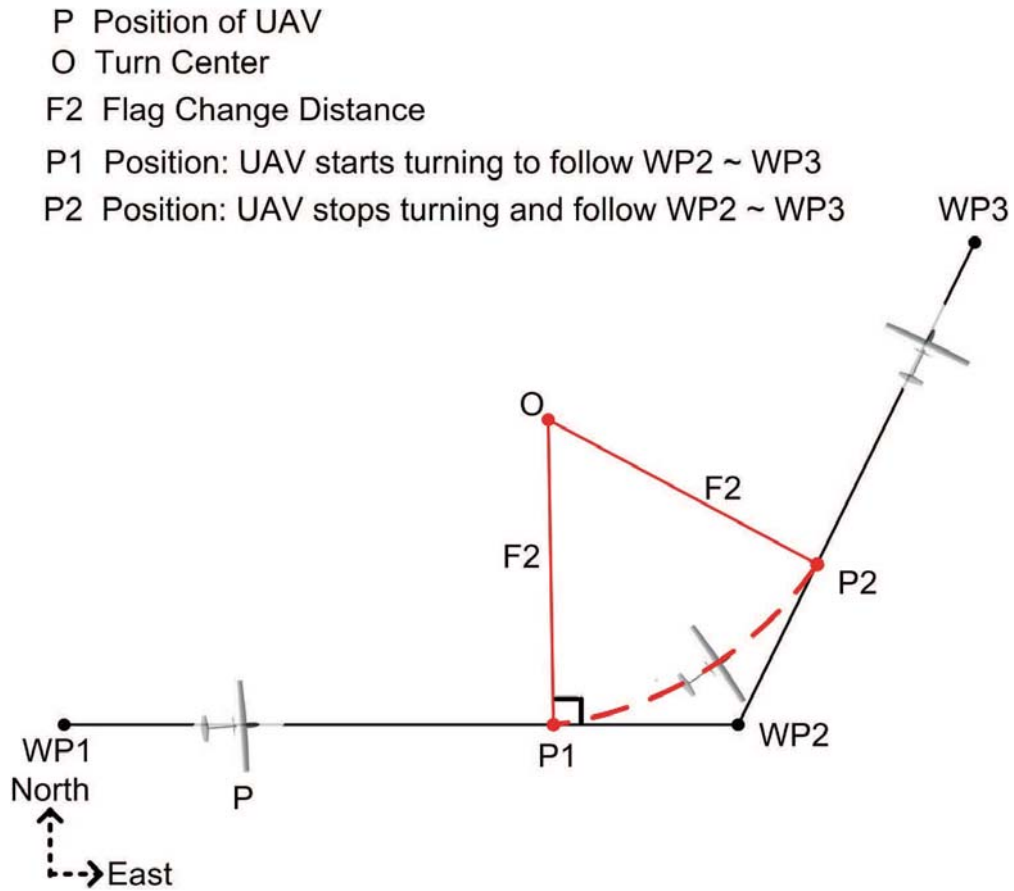
FIGURE 2.9: Waypoint Switching geometry

2.3.3 Control

Aerospace vehicle control is defined as "the methods and/or equipment used for correlating the command signals received from the guidance system with the signals received from its attitude sensors to compute and command actuation of the servos (aerodynamic surfaces, engine throttle etc)". An accurate flight control system is required to ensure that UAV exhibits stable behavior and delivers desired performance in following the desired trajectory precisely in the presence of external disturbance. The safety of the UAV is critical from flight control system perspective. Typical points mentioned below can result in poor performance or even loss of the vehicle:

- An inaccurate design

- Lack of robustness to model variations

- A component failure

Using measured vehicle states and guidance commands, the flight control system performs:

- Speed control

- Height and its rate control

- Bank angle control

- Heading control

- Turn compensation and

- Elevation control

The control system's objective is to track the guidance commands precisely despite the presence of external disturbances. The UAV states, either measured or estimated are required for control design. Several sensors are used to fuse noise by the navigation system to provide these measurements. Then, the tracking error between the desired and measured states is minimized by the control system in the presence of disturbances (like wind). The flight control system produces servomotor signals for the ailerons as δ_a, rudder as δ_r, elevator δ_e and engine throttle as δ_t. Sometimes the guidance and control loops are nested in an inner-loop outer-loop configuration. There are few challenging problems to answer. Generally, the inner control loop has fast dynamics than the outer guidance loop. Every successive outer loop has the slower dynamics as compared to the inner one. The major problem is to see if there is an interaction between the closed loops (e.g., the performance of the inner control loop might be reduced due to closing of the outer loop and hence resulting in a redesign). And what is meant by slow and fast.

The signals from the flight controller are transformed into surface deflections depending upon the servomotor dynamics. A servomotor is compact electromechanical device similar to DC motor with an additional built-in feedback circuit. Generally, the input to servomotors is pulse-width modulated (PWM) signals. An accurate model of actuators is necessary to transform control commands to proper deflection of the surfaces as explained in Appendix A.

2.4   Conclusion

With the knowledge of basics related to SMC and lateral guidance, we can formulate the guidance and control task in terms of SMC methodology i.e., to generate a smooth guidance command ϕ_{ref} to attract y and χ_E onto the specially designed manifold s and stabilize the system (2.49) and (2.48) by taking $s \to 0$ with the help of a reaching law. Control function δ_a is treated as input to the UAV inner loop dynamics for corresponding aerodynamic surface deflections accommodating the ϕ_{ref} commands. The advantages expected are increase in accuracy and robustness of way-point tracking.

Chapter 3

NONLINEAR SLIDING MANIFOLDS

As discussed in Chapter 2, sliding mode based design can be divided into two parts; the design of stable sliding surface (also known as switching manifold) followed by the design of a control law to compel the system state trajectories towards the designed sliding surface in finite time. System state trajectories starting from any point in the phase portrait are first attracted towards the sliding surface (the reaching phase) and subsequently forced to stay on the manifold (sliding phase). As it has already been discussed, the sliding surface or switching manifold completely determines the plant dynamics during the sliding phase. Therefore, design of this manifold is one of the two major tasks in the process of sliding mode based design.

One of the key requirements in path following applications is to attain high performance in uncertain environment i.e., lateral error observed by the UAV should be quickly brought to zero. Non-linear time-varying switching surfaces are proposed for lateral path following applications for different class of systems. Certain applications demand the use of sliding surfaces that provide high performance lateral control while control of certain other systems require surfaces which are computationally inexpensive. Due to limitations on available electrical power, the second set of applications require attaining adequate performance with limited power consumption by employing techniques that require lesser computational processing. For example in micro aerial vehicles payload capacity is limited in terms of battery units installed, therefore the guidance algorithm is based on relatively simpler sliding surface which requires less energy to produce its reference commands are preferable. It is ensured that for a given set of initial conditions control boundedness is guaranteed with these proposed manifolds. The proposed sliding surfaces are designed keeping in view these requirements by using the principle of variable-damping concept [96].

51

The response of a lateral path following system can be varied by the selection of intercept course χ_E versus cross range y. Initial high value of intercept course results in a quick response to drive the lateral error small and then later a lower value to avoid unnecessary overshoot and control actuation. The proposed approach delivers high performance owing to change of intercept course by means of a non-linear sliding surface. To ease the synthesis of the proposed non-linear surface first order sliding mode control (FOSMC) based guidance algorithm is also proposed which achieves high performance and robustness. Control required to ensure existence of sliding mode has two components: nonlinear equivalent control and a discontinuous part for robustness. The magnitude of the discontinuous component is chosen based on the maximum amplitude of uncertainty while the equivalent control component design depends on the sliding manifold, from which a convenient solution can be explored to guarantee reachability of sliding mode and control boundedness.

The brief outline of this chapter is as follows. Section 3.1 outlines the practical aspects for high performance lateral guidance and explains the block diagram of guidance and control system. Section 3.2 discusses two approaches to design guidance law, first is based on high performance sliding manifold and the second is based on computationally efficient manifold. Analysis of system representing the structure of nonlinear sliding surfaces and the proof of their stability with the selection of parameters is presented by solving the path-following problem at the kinematic level (outer-loop control) with a nonlinear guidance law. Control boundedness and analytical stability analysis proofs for the proposed scheme are also given in Section 3.2. Section 3.4 focuses on the flight experimental results used to validate the theoretical designed framework. Section 3.5 contains the concluding remarks and summarizes the key results.

3.1   Guidance and Control Strategy

The aim of this work is to design a SMC based guidance algorithm to guarantee high performance in the presence of uncertainties. A new algorithm based on
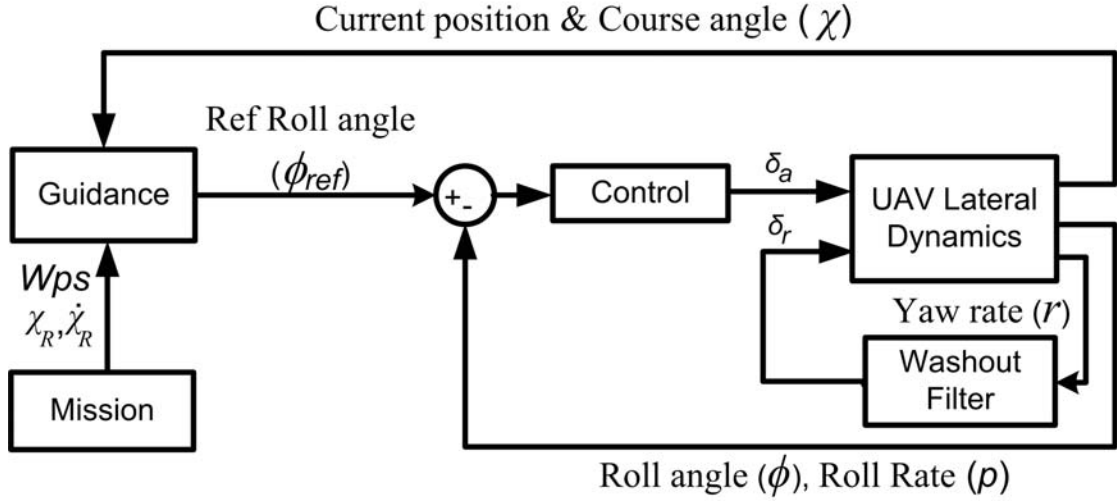
FIGURE 3.1: Block diagram of guidance and control structure

nonlinear sliding manifold was presented with FOSMC in [55] which showed that the nonlinear manifolds are better than linear surfaces applied to the lateral path following applications. The limitation explained in Section 3.3 has motivated the author to look for an improved technique which can ensure high performance in the presence of uncertainties. In this chapter two sliding manifolds are proposed, the first manifold provides benefits in terms of higher performance and second one is a simpler manifold which provides same convergence properties as in [55] with less computational load. Stability of these manifolds is analyzed with the help of a suitable Lyapunov function. Reachability and control boundedness conditions are derived which allow to cater for uncertainties present in the system while ensuring boundedness of reference commands.

The block diagram of guidance and control system is shown in Figure 3.1. Mission block is responsible for defining a pre-specified path in the form of waypoints for the guidance block. The reference course χ_R and $\dot{\chi}_R$ is also available from the mission block. The guidance block generates roll reference commands ϕ_{ref} based on two inputs: mission information by the mission block and feedback from sensors i.e., the instantaneous position and course angle χ. The roll reference command ϕ_{ref} generated by the outer guidance loop serves as input for inner control loop to follow [55]. The inner loop actuates the ailerons by generating δ_a based control

53

inputs, ϕ_{ref} the roll commands generated by the guidance loop, current roll ϕ and roll rate p of the vehicle. The autopilot loop is designed using HOSM super twisting algorithm explained in Appendix B.

3.2 Outer Guidance Loop Design

3.2.1 Proposed sliding manifold σ_p

Guidance of the vehicle towards the desired path requires a fast response time so that errors can be quickly brought to zero without any overshoot. This section presents a new nonlinear high performing sliding manifold for lateral path following applications. The performance measure in path following schemes is the ability to first minimize the error quickly and then follow the path precisely. Generally a constant $\chi_E \leq 90°$ is desired for very large lateral errors, and it is to be adjusted accordingly when the track error reduces. According to [12], a good helmsman criterion in literature is followed i.e., based on cross track error y intercept course χ_E is varied. Thus we propose a high performing nonlinear manifold in which $\chi_E \leq 90°$ is kept high to reduce y quickly and then adjusted accordingly for small lateral errors. The proposed nonlinear sliding surface results in less settling time without any overshoots. The intercept course χ_E switches between its low value to high value as per the value of the cross track error y. The proposed sliding surface exhibits better results in terms of performance. The proposed sliding manifold is

$$\sigma_p = \chi_E + \alpha_2 \text{erf}(\beta_2 y) \tag{3.1}$$

where $\text{erf}(x)$ is defined as

$$\text{erf}(x) = \frac{2}{\sqrt{\pi}} \int_0^x e^{-t^2} dt \tag{3.2}$$
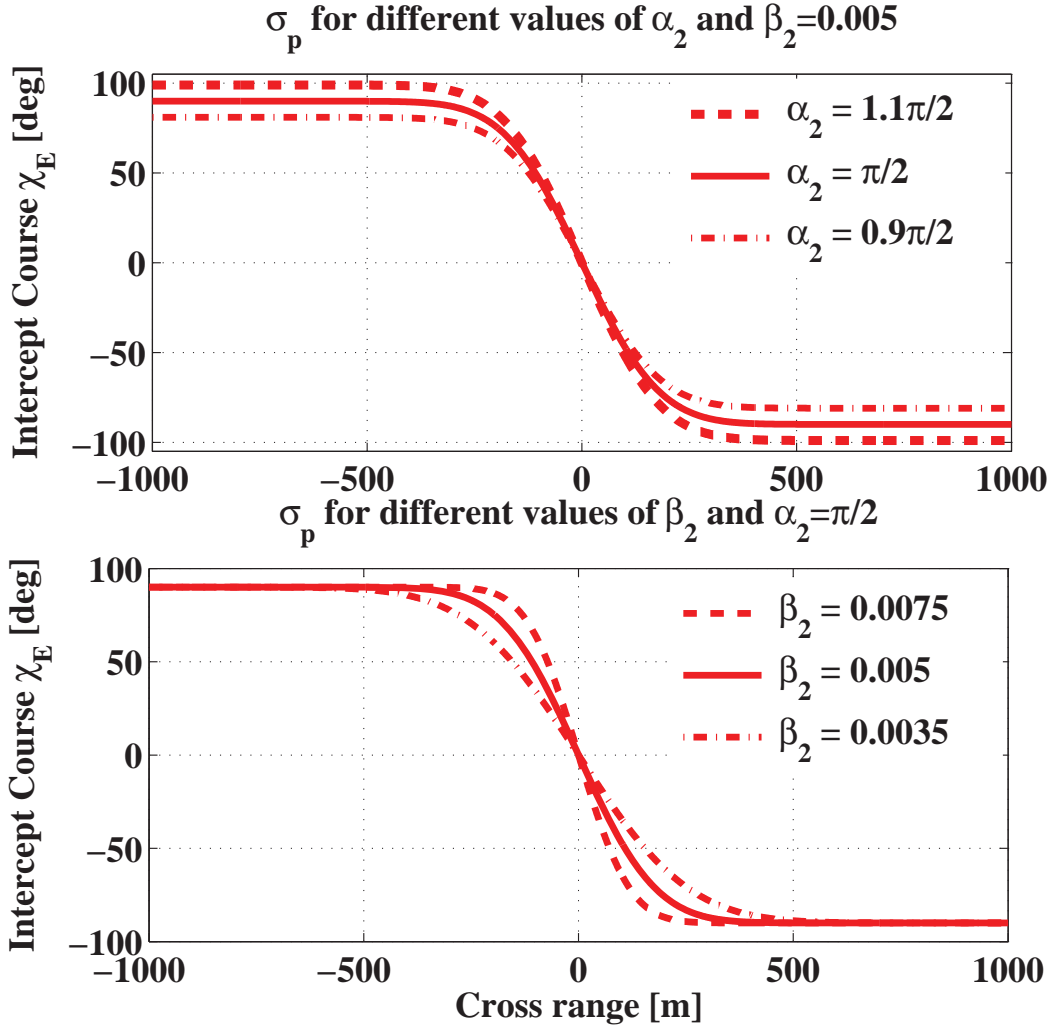
FIGURE 3.2: Proposed sliding manifold σ_p and its variation with α_2 and β_2

σ_p governs the state trajectories in sliding i.e., $\sigma_p = 0$

$$\chi_E = -\alpha_2 \mathrm{erf}(\beta_2 y) \qquad (3.3)$$

and the constants α_2, β_2 belong to the set of real numbers i.e., $\alpha_2, \beta_2 \in \Re$, and it is shown later that for the stability of the sliding surface it is necessary to have $\alpha_2 > 0$, $\beta_2 > 0$. A nonlinear sliding surface is shown in Figure 3.4 for different values of α_2 and β_2. It is evident from (3.3) that the condition $|\alpha_2| \leq \frac{\pi}{2}$ is required to ensure $|\chi_E| \leq \frac{\pi}{2}$. The motion of the system on the sliding surface is given by (3.3). In case of large cross track error $\pm \mathrm{erf}(\beta_2 y) \approx \pm 1$, and hence $\chi_E \approx \mp |\alpha_2|$

55

for $\pm y$. It is easily seen that χ_E has a direct relation with $|\alpha_2|$ in the case of large track errors. Hence a large value of χ_E indicates a high convergence rate of error to zero. So for large track errors α_2 can be used as a tuning parameter to achieve good performance. Similarly, the change in β_2 affects the curvature of the curve and indicates how fast the UAV will turn to reduce the track error. If the value of the β_2 is small, the value of χ_E will be considerably small which will result in small turning for relatively small y, hence the system dynamics will be slow. On the contrary, if the value of β_2 is selected large, an appreciable χ_E will be generated for a relatively small y, hence the systems dynamic will be fast making the error go to zero quickly. Hence in the case of small lateral error, the performance is directly related to the value of β_2; larger the value of β_2, bigger will be the control effort. Therefore arbitrarily large values of β_2 cannot be selected.

3.2.1.1 Stability analysis of σ_p

For stability analysis we select the following candidate Lyapunov function

$$ W_{p_{stab}} = \frac{1}{2}\left(y^2 + \chi_E^2\right) = \frac{1}{2}\left(y^2 + (-\alpha_2 \mathrm{erf}(\beta_2 y))^2\right) \tag{3.4} $$

Taking time derivative we have

$$ \dot{W}_{p_{stab}} = -Vy\sin\left(\alpha_2 \mathrm{erf}(\beta_2 y)\right) - \frac{2V\alpha_2^2 \beta_2}{\sqrt{\pi}} e^{-\beta_2^2 y^2}\left(\mathrm{erf}(\beta_2 y)\right)\sin\left(\alpha_2 \mathrm{erf}(\beta_2 y)\right) \tag{3.5} $$

In the above equation, sign of the term $\sin(\alpha_2 \mathrm{erf}(\beta_2 y))$ plays an important role. The function $\mathrm{erf}(x)$ is an odd function which implies that the sign of $\mathrm{erf}(\beta_2 y)$ will be the same as the sign of $\beta_2 y$. Similarly, the sign of $\alpha_2 \mathrm{erf}(\beta_2 y)$ will be same as that of y as $\alpha_2 > 0$, $\beta_2 > 0$. Also, the range of function $\alpha_2 \mathrm{erf}(\beta_2 y)$ is $\left(-\frac{\pi}{2}, \frac{\pi}{2}\right)$ as $|\alpha_2| \leq \frac{\pi}{2}$ and as $\alpha_2 > 0$, $\beta_2 > 0$, the sign of $\sin(\alpha_2 \mathrm{erf}(\beta_2 y))$ will be same as y. The right hand side first term in (3.5) is negative definite since the magnitude of velocity V and the sign of $y\sin(\alpha \arctan \beta y)$ is positive. In the same way, the second term $(\mathrm{erf}(\beta_2 y))^2 e^{-\beta_2^2 y^2}$ on the right hand side is always positive and does not change sign, which makes the overall term negative definite, hence $\dot{W}_{p_{stab}}$

56

is negative definite. With the discussion on (3.5), we conclude that the positive definite Lyapunov function $W_{p_{stab}}$ (3.4) has a negative definite $\dot{W}_{p_{stab}}$ indicating the proposed sliding surface (3.1) has stable characteristics provided $\alpha_2 > 0$, $\beta_2 > 0$ and $|\alpha_2| \leq \frac{\pi}{2}$.

3.2.1.2 Guidance law design with σ_p

From the kinematic state model in (2.50), $\dot{\sigma}_p$ can be written as

$$\dot{\sigma}_p = \frac{g}{V} \tan \phi_{ref} + \frac{2V\alpha_2\beta_2 e^{-\beta^2 y^2} \sin \chi_E}{\sqrt{\pi}} - \dot{\chi}_R \qquad (3.6)$$

In order to derive the expression for equivalent control as in (2.17), we put $\dot{\sigma}_p = 0$ and with $u = \tan(\phi_{ref})$. After solving, u_{eq} takes the following form

$$u_{eq} = \frac{-2V^2\alpha_2\beta_2 e^{-\beta^2 y^2}}{g\sqrt{\pi}} \sin(\chi_E) + \frac{V}{g}\dot{\chi}_R \qquad (3.7)$$

Complete guidance law using σ_p:

The complete lateral guidance command is the summation of continuous equivalent control in (3.7) and a discontinuous term (2.19) in order to make it robust in the presence of uncertainties. The complete guidance law is

$$u = \frac{-2V^2\alpha_2\beta_2 e^{-\beta^2 y^2}}{g\sqrt{\pi}} \sin(\chi_E) + \frac{V}{g}\dot{\chi}_R - k_p \operatorname{sgn}(\sigma_p) \qquad (3.8)$$

As $\phi_{ref} = \arctan(u)$

$$\phi_{ref} = \arctan\left(\frac{-2V^2\alpha_2\beta_2 e^{-\beta^2 y^2}}{g\sqrt{\pi}} \sin(\chi_E) + \frac{V}{g}\dot{\chi}_R - k_p \operatorname{sgn}(\sigma_p) \right) \qquad (3.9)$$

Using quasi sliding mode Section 2.1.6.1, we can write (3.9) as

$$\phi_{ref} = \arctan\left(\frac{-2V^2\alpha_2\beta_2 e^{-\beta^2 y^2}}{g\sqrt{\pi}} \sin(\chi_E) + \frac{V}{g}\dot{\chi}_R - k_p \frac{\sigma_p}{|\sigma_p| + \epsilon_p} \right) \qquad (3.10)$$

where ϵ_p is small positive scalar. The conditions on k_p are derived.

3.2.1.3 Reachability condition for σ_p

In order to check for reachability condition, consider the candidate Lyapunov function

$$W_{p_{rch}} = \frac{1}{2}\sigma_p^{\,2} \tag{3.11}$$

with its derivative as

$$\dot{W}_{p_{rch}} = \sigma_p \dot{\sigma}_p \tag{3.12}$$

From the expression of $\dot{\sigma}_p$ we have the expression for $\dot{W}_{p_{rch}}$ in which ϕ_{ref} explicitly appears

$$\dot{W}_{p_{rch}} = \sigma_p \left(\frac{g}{V} \tan\phi_{ref} + \frac{2V\alpha_2\beta_2 e^{-\beta^2 y^2} \sin\chi_E}{\sqrt{\pi}} \right) \tag{3.13}$$

In order to ensure $\sigma_p \dot{\sigma}_p < 0$ with the guidance command in (3.10)

$$\dot{W}_{p_{rch}} = \sigma_p \left(\frac{g}{V} \left\{ \frac{-2\widetilde{V}^2 \alpha_2 \beta_2 e^{-\beta^2 y^2}}{g\sqrt{\pi}} \sin(-\alpha_2 \mathrm{erf}(\beta_2 y)) \right. \right.$$
$$\left. \left. -k_p \frac{\sigma_p}{|\sigma_p| + \epsilon_p} \right\} + \frac{2V\alpha_2\beta_2 e^{-\beta^2 y^2} \sin\chi_E}{\sqrt{\pi}} \right) \tag{3.14}$$

After simplification we can write it as

$$\dot{W}_{p_{rch}} = -\frac{\sigma_p}{V} \left\{ \frac{-2\alpha_2\beta_2 e^{-\beta^2 y^2} \sin\chi_E}{\sqrt{\pi}} \left(\widetilde{V}^2 - V^2 \right) + gk_p \frac{\sigma_p}{|\sigma_p| + \epsilon_p} \right\} \tag{3.15}$$

For $\dot{W}_{p_{rch}}$ to be negative definite i.e., $\dot{W}_{p_{rch}} < 0$, the following condition must be ensured

$$|k_p| > \left| \frac{-2\alpha_2\beta_2 e^{-\beta^2 y^2} \sin\chi_E \left(\widetilde{V}^2 - V^2 \right)}{g\sqrt{\pi}} \right| \left(\frac{|\sigma_{p_{min}}| + \epsilon_p}{|\sigma_{p_{min}}|} \right) \tag{3.16}$$

where $\sigma_{p_{min}}$ is in the vicinity of zero. The maximum value of k_p occurs when $\chi_E = \pi/2$ i.e., $|\sin \chi_E| = 1$ and $y = 0$. Furthermore for illustrative purpose we assume that there exist 10% uncertainty in the measured velocity denoted as $\widetilde{V}$. We can further simplify (3.16) using

$$0.9V \leq \widetilde{V} \leq 1.1V \tag{3.17}$$

From here onwards we can derive the condition on k_p i.e., the following inequality must be satisfied to ensure finite time reachability.

$$k_p > \frac{0.42\alpha_2\beta_2 V^2}{g\sqrt{\pi}} \left(\frac{|\sigma_{p_{min}}| + \epsilon_p}{|\sigma_{p_{min}}|} \right) \tag{3.18}$$

The guidance law in (3.9) will ensure $\sigma_p \dot{\sigma}_p \leq 0$ throughout the flight envelope with the gain k_p selected according to the condition derived in (3.18). From any initial condition the state trajectories are first forced towards the sliding surface and then will be constrained to remain on it. Once the state trajectories are confined to $\sigma_p \approx \sigma_{p_{min}}$ in (3.3), the following continuous control will drive the states in (2.50) towards zero.

$$\phi_{ref_{eq}} = \arctan \left(\frac{-2V^2\alpha_2\beta_2 e^{-\beta^2 y^2}}{g\sqrt{\pi}} \sin(-\alpha_2 \mathrm{erf}(\beta_2 y)) \right) \tag{3.19}$$

3.2.1.4 Control boundedness for σ_p

The guidance and control loop are designed in a manner in which the bank reference commands generated by the outer guidance loop are to be followed by the inner autopilot loop. Therefore these roll reference commands by the guidance loop needs to checked before passing to the autopilot loop and similar checks are also required on the aileron control actuation. Our objective here to is to generate reference commands striving for best performance along with the saturation constraints before passing to the autopilot loop, thus graceful and stable maneuvers are achieved.

As previously discussed in Section 3.2.1 the selection of α_2 and β_2 plays a vital role in providing good performance. For good performance large values of α_2 and β_2 are desirable for fast performance in terms of driving the state errors to zero. The conditions on k_p derived for reachability condition (3.18) shows its direct relation with the product of $\alpha_2\beta_2$. If arbitrarily large gain k_p is selected according to the condition (3.18), it might cause signal saturation for the autopilot loop. Therefore to avoid saturation, the bank reference commands ϕ_{ref} in (3.9) needs to be bounded by the maximum allowed value ϕ_{max} which for illustration we take here as $\pi/4$,

$$|\phi_{ref}| \leq \frac{\pi}{4} \tag{3.20}$$

From (3.9)

$$\left| \arctan\left(\frac{-2V^2\alpha_2\beta_2 e^{-\beta^2 y^2}}{g\sqrt{\pi}} \sin\chi_E - k_p \operatorname{sgn}(\sigma_p)\right)\right| \leq \frac{\pi}{4} \tag{3.21}$$

Sufficient condition for control boundedness becomes

$$\left| \frac{2V^2\alpha_2\beta_2 e^{-\beta^2 y^2}}{g\sqrt{\pi}} \sin\chi_E \right| + |k_p \operatorname{sgn}(\sigma_p)| \leq \tan\frac{\pi}{4} \tag{3.22}$$

therefore

$$\left| \frac{2V^2\alpha_2\beta_2 e^{-\beta^2 y^2}}{g\sqrt{\pi}} \sin\chi_E \right| \leq \tan\frac{\pi}{4} - k_p\left(\frac{|\sigma_p|}{|\sigma_p| + \epsilon_p}\right) \tag{3.23}$$

or equivalently as

$$k_p \leq \left\{ \tan\frac{\pi}{4} - \left| \frac{2V^2\alpha_2\beta_2 \exp^{-\beta^2 y^2} \sin(\alpha_2\operatorname{erf}(\beta_2 y))}{g\sqrt{\pi}} \right| \right\} \left(\frac{|\sigma_{p_{min}}| + \epsilon_p}{|\sigma_{p_{min}}|}\right) \tag{3.24}$$

With k_p constrained as above it will ensure boundedness of guidance commands and ϕ will always be restricted to be less than ϕ_{max}.

3.2.2 Proposed sliding manifold σ_c

In previous Section 3.2.1 a nonlinear sliding surface was proposed to achieve high performance. The proposed nonlinear surface for this section is designed for low computational complexity. As power capacity is always limited, it is necessary to derive a guidance strategy which requires lesser computational power, thus solving the guidance solution in minimum time possible and with minimum resources used. A new nonlinear sliding manifold is proposed which is based on good helmsman behavior and is simpler to implement. The idea is to vary the intercept course χ_E constantly based on the cross track error y. Stability of the system is also guaranteed for this sliding manifold by deriving physical conditions that satisfy reachability of SMC and prove control boundedness. The proposed surface results in relative high settling time without any overshoot but our objective of limited computational load is achieved. The sliding manifold proposed is

$$\sigma_c = \chi_E + \frac{\alpha_3 y}{|y| + \beta_3} \tag{3.25}$$

σ_c governs the state trajectories in sliding i.e., $\sigma_c = 0$

$$\chi_E = -\frac{\alpha_3 y}{|y| + \beta_3} \tag{3.26}$$

The constants $\alpha_3, \beta_3 \in \Re$ (the set of real numbers). Nonlinear surface (3.25) for different values of α_3 and β_3 is shown in Figure 3.4. From (3.26) it is clear that in order to ensure $|\chi_E| \leq \frac{\pi}{2}$, $|\alpha_3| \leq \frac{\pi}{2}$ must be fulfilled. For a large value of cross track error y, $\pm\frac{y}{|y|+\beta_3} \approx \pm 1$, and hence $\chi_E \approx \mp|\alpha_3|1$ for $\pm y$. Hence for large cross track error, the value of α_3 is directly proportional to χ_E, large value of χ_E indicates fast convergence of the error. So we can use α_3 to adjust the performance of the system during large cross track errors. Similarly, the change in β_3 affects the curvature of the curve and indicates how fast the UAV will turn to reduce the track error. If the value of the β_3 is small, χ_E will be considerably small which will result in small

61
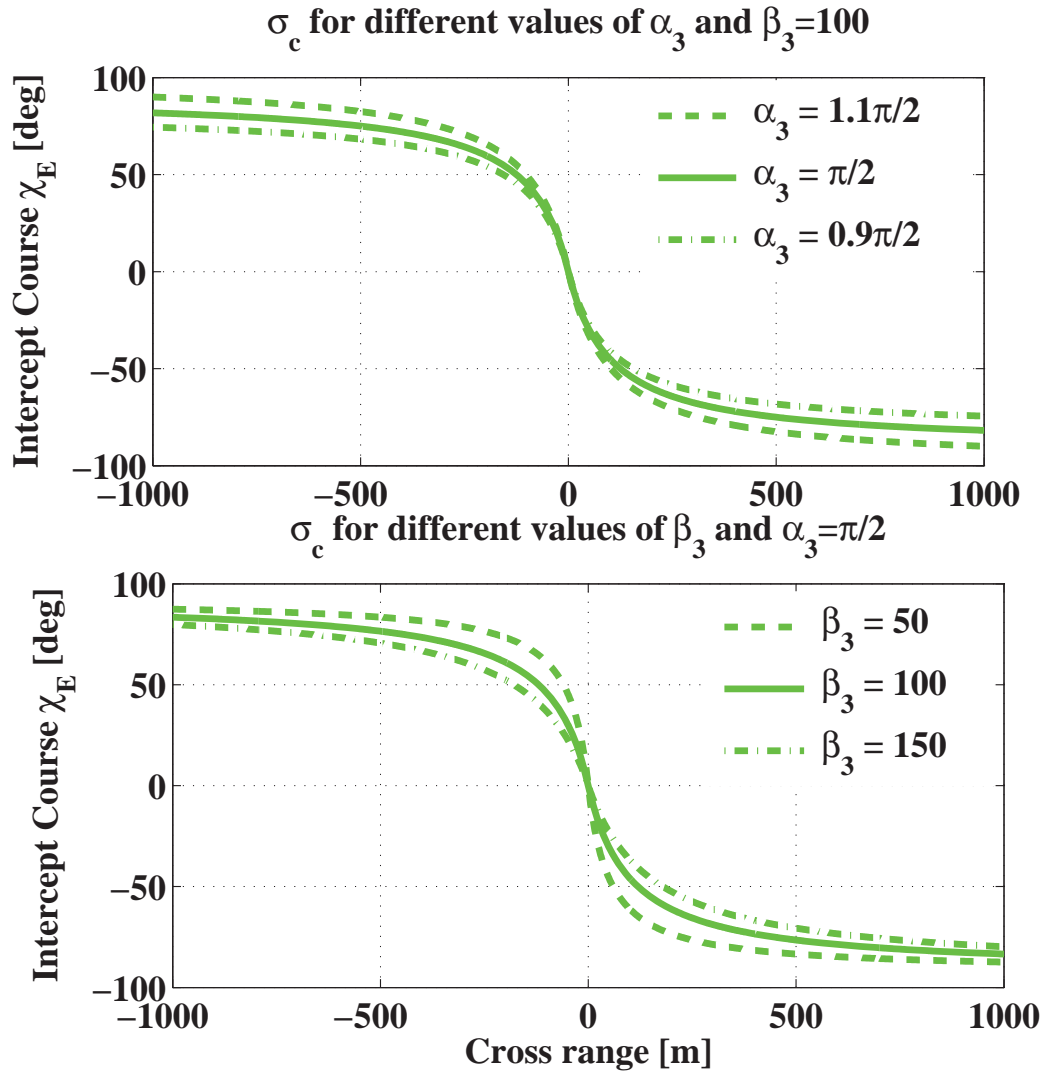
FIGURE 3.3: Proposed sliding manifold σ_c and its variation with α_3 and β_3

turning for relatively small y, hence the system dynamics will be slow. And if the value of β_3 is large, an appreciable value of χ_E will be generated for small y, hence the systems dynamic behaves fast and tries to make the error zero quickly. The performance for small lateral errors i.e., small y is directly related to the selection of β_3. However, large values of β_3 will imply a bigger control effort therefore its value cannot be selected arbitrarily large

3.2.2.1 Stability analysis of σ_c

For stability analysis we select the following Lyapunov candidate function

$$W_{c_{stab}} = \frac{1}{2}\left(y^2 + \chi_E^2\right) = \frac{1}{2}\left(y^2 + \left(-\frac{\alpha_3 y}{|y| + \beta_3}\right)^2\right) \qquad (3.27)$$

Taking time derivative we have

$$\dot{W}_{c_{stab}} = -Vy\sin\left(\frac{\alpha_3 y}{|y| + \beta_3}\right) - \frac{2V\alpha_3^2\beta_3 y}{(|y| + \beta_3)^3}\sin\left(\frac{\alpha_3 y}{|y| + \beta_3}\right) \qquad (3.28)$$

In (3.28), the sign of the term $\sin(\frac{\alpha_3 y}{|y| + \beta_3})$ plays an important role. Since $|\alpha_3| \leq \frac{\pi}{2}$, the range of the function $(\frac{\alpha_3 y}{|y| + \beta_3})$ is $(-\frac{\pi}{2}, \frac{\pi}{2})$; and $\sin(\frac{\alpha_3 y}{|y| + \beta_3})$ will have the sign of y, provided $\alpha_3 > 0$, $\beta_3 > 0$. The right hand side first term in (3.28) is negative definite as the velocity V and $y\sin(\frac{\alpha_3 y}{|y| + \beta_3})$ are positive. The second right hand side term in (3.28) is also negative definite as $V > 0$, $|y|$ is positive and $y\sin(\frac{\alpha_3 y}{|y| + \beta_3})$ is positive with $\alpha_3 > 0$. Therefore we can conclude for the positive definite Lyapunov function $W_{c_{stab}}$ in (3.27) to have a negative definite $\dot{W}_{c_{stab}}$. Thus stable sliding characteristics are observed for the proposed sliding manifold (3.25) provided $\alpha_3 > 0$, $\beta_3 > 0$ and $|\alpha_3| \leq \frac{\pi}{2}$.

3.2.2.2 Guidance law design with σ_c

Equivalent control would maintain $\dot{\sigma}_c = 0$ if the exact dynamical characteristics of the system are known. Along the system states as in (2.50),

$$\dot{\sigma}_c = \frac{g}{V}\tan\phi_{ref} + \frac{\alpha_3\beta_3}{(|y| + \beta_3)^2}V\sin(\chi_E) - \dot{\chi}_R \qquad (3.29)$$

We put $\dot{\sigma}_c = 0$ and with $u = \tan(\phi_{ref})$, we derive the expression for equivalent control u_{eq} as in (2.18)

$$u_{eq} = -\frac{V^2\alpha_3\beta_3}{g(|y| + \beta_3)^2}\sin\left(\frac{\alpha_3 y}{|y| + \beta_3}\right) + \frac{V}{g}\dot{\chi}_R \qquad (3.30)$$

Complete guidance law using σ_c:

The complete lateral guidance command comprises of two parts the continuous equivalent control in (3.7) and a discontinuous term (2.19). Using quasi sliding mode, the complete guidance law is

$$u = -\frac{V^2 \alpha_3 \beta_3}{g(|y| + \beta_3)^2} \sin(\chi_E) + \frac{V}{g}\dot{\chi}_R - k_c \operatorname{sgn}(\sigma_c) \qquad (3.31)$$

As $\phi_{ref} = \arctan(u)$

$$\phi_{ref} = \arctan\left(-\frac{V^2 \alpha_3 \beta_3}{g(|y| + \beta_3)^2} \sin(\chi_E) + \frac{V}{g}\dot{\chi}_R - k_c \operatorname{sgn}(\sigma_c)\right) \qquad (3.32)$$

Using quasi sliding mode Section 2.1.6.1, we can write (3.32) as

$$\phi_{ref} = \arctan\left(-\frac{V^2 \alpha_3 \beta_3}{g(|y| + \beta_3)^2} \sin(\chi_E) + \frac{V}{g}\dot{\chi}_R - k_c \frac{|\sigma_c|}{|\sigma_c| + \epsilon_c}\right) \qquad (3.33)$$

where ϵ_c is small positive scalar. The conditions on k_c are derived according to the conditions explained next.

3.2.2.3 Reachability condition for σ_c

It is necessary in SMC to ensure sliding motion from any arbitrary initial condition in finite time [6, 96]. The reachability of the sliding surface can be expressed by the condition

$$\sigma_c \dot{\sigma}_c \leq 0 \qquad (3.34)$$

To check the condition let us take the following Lyapunov candidate function

$$W_{c_{rch}} = \frac{1}{2}\sigma_c^2 \qquad (3.35)$$

Its derivative is

$$\dot{W}_{c_{rch}} = \sigma_c \dot{\sigma}_c \qquad (3.36)$$

64

From the expression of $\dot{\sigma}_c$ in (3.29) we have

$$\dot{W}_{c_{rch}} = \sigma_c \left(\frac{g}{V} \tan \phi_{ref} + \frac{\alpha_3 \beta_3}{(|y| + \beta_3)^2} V \sin(\chi_E) \right) \tag{3.37}$$

Substituting the guidance command ϕ_{ref} from (3.32)

$$\dot{W}_{c_{rch}} = \sigma_c \left(\frac{g}{V} \left\{ -\frac{\widetilde{V}^2 \alpha_3 \beta_3}{g(|y| + \beta_3)^2} \sin \left(\frac{\alpha_3 y}{|y| + \beta_3} \right) \right. \right.$$
$$\left. \left. -k_c \frac{|\sigma_c|}{|\sigma_c| + \epsilon_c} \right\} + \frac{\alpha_3 \beta_3}{(|y| + \beta_3)^2} V \sin(\chi_E) \right) \tag{3.38}$$

After simplification $\dot{W}_{c_{rch}}$ becomes

$$\dot{W}_{c_{rch}} = -\frac{\sigma_c}{V} \left\{ \frac{\alpha_3 \beta_3}{(|y| + \beta_3)^2} (\widetilde{V}^2 - V^2) \sin \chi_E - gk_c \left(\frac{|\sigma_c|}{|\sigma_c| + \epsilon_c} \right) \right\} \tag{3.39}$$

where $\sigma_{c_{min}}$ is close to zero. For $\dot{W}_{c_{rch}}$ to be negative definite i.e., $\dot{W}_{c_{rch}} \leq 0$ we need

$$|k_c| > \left| \frac{\alpha_3 \beta_3}{g(|y| + \beta_3)^2} \sin \chi_E (\widetilde{V}^2 - V^2) \right| \left(\frac{|\sigma_{c_{min}}| + \epsilon_c}{|\sigma_{c_{min}}|} \right) \tag{3.40}$$

or equivalently the following inequality must be satisfied.

$$k_c > \frac{0.21 \alpha_3 V^2}{g \beta_3} \left(\frac{|\sigma_{c_{min}}| + \epsilon_c}{|\sigma_{c_{min}}|} \right) \tag{3.41}$$

where the $\sigma_{c_{min}}$ is in the vicinity of zero. The guidance commands in (3.32) will ensure $\sigma_c \dot{\sigma}_c \leq 0$ throughout the flight envelope with the gain k_c selected according to the condition derived in (3.41. The state trajectories are constrained to first reach towards the sliding surface and then slide along it towards zero. Once the states reach onto the manifold i.e., $\sigma_c \approx \sigma_{c_{min}}$ in (3.26), then the following continuous control will slide the states in (2.50) to zero.

$$\phi_{ref} = \arctan \left(\frac{V^2 \alpha_3 \beta_3}{g(|y| + \beta_3)^2} \sin \left(\frac{\alpha_3 y}{|y| + \beta_3} \right) \right) \tag{3.42}$$

65

3.2.2.4 Control boundedness

For any practical system the actuator deflection is limited. Therefore it is necessary to consider the effect of control boundedness a priori. The proposed surface ensures that control limits are not exceeded. By selecting the sliding surface parameters we can improve performance of the system for matched disturbances keeping in view the invariance property.

As discussed earlier, the guidance commands ϕ_{ref} must be bounded by ϕ_{max} so that they shall not cause saturation for the inner autopilot loop. Here we derive the conditions on sliding controller parameter k_c for the both reaching and sliding phases. For σ_c, ϕ_{ref} must be bounded by $\phi_{max} = \pi/4$.

$$|\tan\phi_{ref}| \leq \frac{\pi}{4} \tag{3.43}$$

From the guidance command of ϕ_{ref} in(3.32), we have

$$\left| \frac{V^2\alpha_3\beta_3}{g(|y|+\beta_3)^2} \sin\left(\frac{\alpha_3 y}{|y|+\beta_3}\right) - k_c \operatorname{sgn}(\sigma_c) \right| \leq \tan\frac{\pi}{4} \tag{3.44}$$

We can have the sufficient condition as

$$\left| \frac{V^2\alpha_3\beta_3}{g(|y|+\beta_3)^2} \sin\left(\frac{\alpha_3 y}{|y|+\beta_3}\right) \right| + |k_c \operatorname{sgn}(\sigma_c)| \leq \tan\frac{\pi}{4} \tag{3.45}$$

The condition to bound ϕ_{ref} becomes

$$\left| \frac{V^2\alpha_3\beta_3}{g(|y|+\beta_3)^2} \sin\left(\frac{\alpha_3 y}{|y|+\beta_3}\right) \right| \leq \tan\frac{\pi}{4} - k_c\left(\frac{|\sigma_c|}{|\sigma_c|+\epsilon_c}\right) \tag{3.46}$$

or equivalently as

$$k_c \leq \tan\frac{\pi}{4} - \left| \frac{V^2\alpha_3\beta_3}{g(|y|+\beta_3)^2} \sin\left(\frac{\alpha_3 y}{|y|+\beta_3}\right) \right| \left(\frac{|\sigma_{c_{min}}|+\epsilon_c}{|\sigma_{c_{min}}|}\right) \tag{3.47}$$

With k_c constrained as in (3.47), ϕ will always be less than ϕ_{max}.

The parameters for the nonlinear surface can be found by a systematic approach in terms of desired stable limits. The performance comparison for different sliding surfaces is presented in the next section. The proposed method has combined different multi-objective sliding mode designs to achieve certain performance criteria on one hand and certain control boundedness criteria on the other hand.

3.3 Comparison of σ_p and σ_c with existing manifold

The time varying switching surface is used to enhance the performance of path following systems. For the guidance law design nonlinear sliding manifold was proposed in [55, 56].

$$\sigma_z = \chi_E + \alpha_1 \arctan(\beta_1 y) \tag{3.48}$$

Figure 3.4 shows the three switching manifolds i.e., σ_z (3.48), σ_p (3.1) and σ_c (3.25). The parameters α_1, α_2 and α_3 are selected for σ_z, σ_p and σ_c respectively in order to have a similar χ_E for large y. The parameters β_1, β_2 and β_3 of σ_z, σ_p and σ_c are adjusted for making the slope of χ_E similar for small y near the origin.
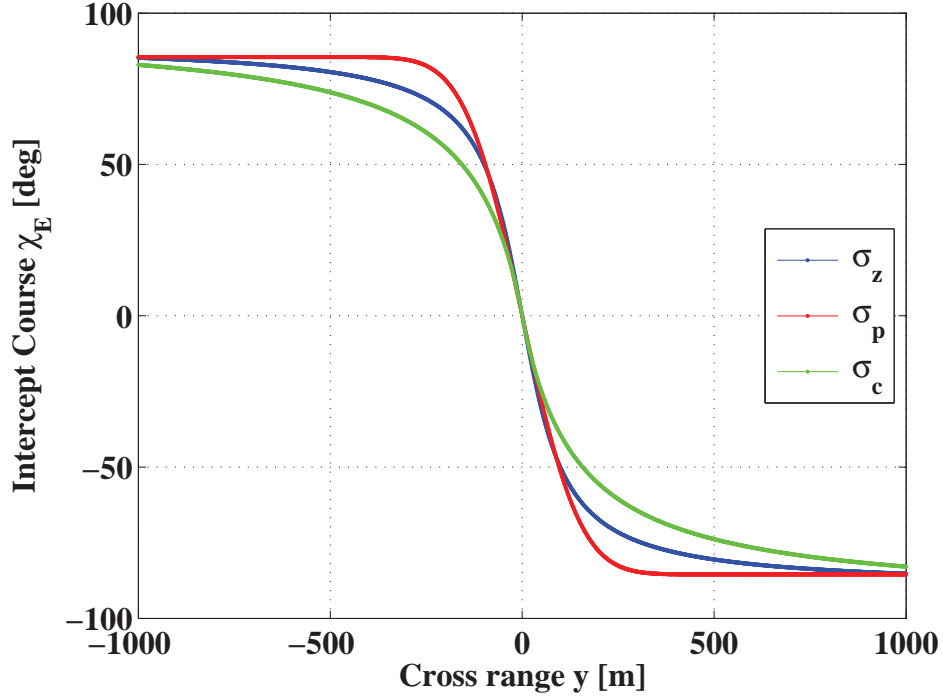
FIGURE 3.4: Intercept Course χ_E Vs Cross Track Error y for surfaces σ_z, σ_p and σ_c.

In order to compare σ_z and σ_p, we need to see the convergence properties of $-\alpha_1 \arctan(\beta_1 y)$ and $-\alpha_2 \mathrm{erf}(\beta_2 y)$. For $\sigma_z = 0$, Taylor series expansion of $-\alpha_1 \arctan(\beta_1 y)$ is given as:

$$\chi_E = -\alpha_1 \beta_1 y + \frac{\alpha_1 \beta_1^3 y^3}{3} - \frac{\alpha_1 \beta_1^5 y^5}{5} \qquad (3.49)$$

From the Taylor series expansion of $-\alpha_2 \mathrm{erf}(\beta_2 y)$ we have for $\chi_E = 0$

$$\chi_E = -\frac{2\alpha_2 \beta_2 y}{\sqrt{\pi}} + \frac{2\alpha_2 \beta_2^3 y^3}{3\sqrt{\pi}} - \frac{\alpha_2 \beta_2^5 y^5}{5\sqrt{\pi}} \qquad (3.50)$$

From the expansion we see that keeping other parameters same σ_p is $\frac{2}{\sqrt{\pi}}$ times the expansion of σ_z for the first and third order terms. It is however evident from just the degree 5 term in (3.49) and (3.50) that σ_z cannot be made to exactly coincide with σ_p.

68

We observe that slope of the sliding surfaces is a function of the state variable y. σ_p has a large magnitude of slope close to origin hence minimum convergence time. Away from the origin magnitude of its slope is smaller i.e., for larger values of y a constant χ_E can be maintained to bring the lateral error quickly to zero with $\dot{\chi}_E \approx 0$ and $\phi \approx 0$. This can also be seen from the derivative of $\alpha_2 \text{erf}(\beta_2 y)$ w.r.t y i.e.,

$$\frac{d}{dy}\sigma_p = -\frac{2\alpha_2\beta_2 \exp(-\beta_2^2 y^2)}{\sqrt{\pi}} \tag{3.51}$$

we see that for $y \to 0$, the slope is $\frac{-2\alpha_2\beta_2}{\sqrt{\pi}}$ but for large values of y slope approaches zero. Considering the other sliding surface:

$$\frac{d}{dy}\sigma_z = -\frac{\alpha_1\beta_1}{1 + \beta_1^2 y^2} \tag{3.52}$$

This is not the case with σ_z whose slope decreases for large y but not exponentially as can be inferred from (3.52). When the state reach closer to origin, the slope is smaller than the magnitude of slope for σ_p and therefore the states in this case converge slower than that for σ_p. χ_E is large for σ_p for large y, so σ_p will give faster convergence of the track error to zero for large y.

The control design problem with discontinuous laws for systems can be reduced to parameters selection of the sliding manifold that completely determines the control system performance. In Figure 3.5, the sliding manifolds i.e., σ_z and σ_p are plotted for maximum values of α_1, β_1 and α_2, β_2. The green area between the two manifolds is the one that cannot be achieved with σ_z, but can be acquired by selecting appropriate values of α_2 and β_2 for σ_p. Hence we claim that σ_p is a higher performing sliding manifold that can be used instead of σ_z. From here we can observe a limitation of σ_z that if we need high performance we may need to select higher value of α_1 and β_1, which is not possible because the reachability and control boundedness limits will overlap one practically may not have a range for gain k_z selection. On the other hand the manifold σ_p is a higher performing manifold which further allows to select larger values of α_2 and β_2 and still have

69

sufficient window for selecting k_p. It is also clear that these surfaces can be made to coincide asymptotically with each other by the choice of α_1, β_1 and α_2, β_2 upto a certain factor and acquire similar convergence properties. As the choice of α_1 and β_1 is limited by the reachability and control boundedness conditions, these cannot be selected arbitrarily large. Therefore σ_p can be used to achieve desired performance as its choice of α_2 and β_2 is more flexible in terms of reachability and control boundedness conditions.
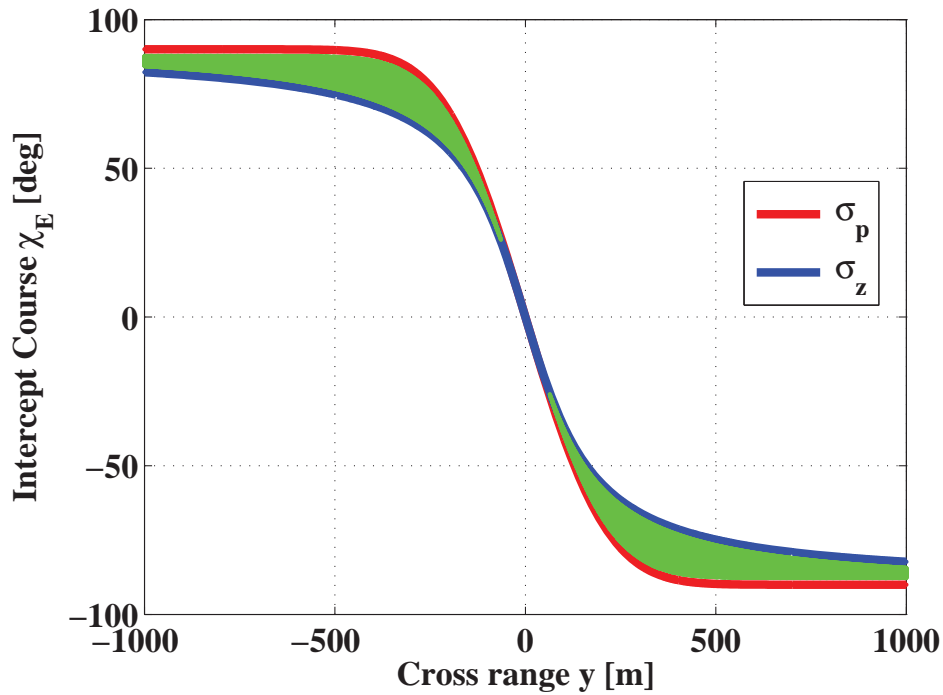
FIGURE 3.5: Comparison of sliding manifold σ_z and σ_p

For the comparison of σ_z and σ_c, the implementation aspect of the surfaces is analyzed. Usually the $arctan()$ functions are implemented using many techniques such as CORDIC (coordinate rotation digital computer) algorithm, polynomial approximation or conventional look up table methods. The architecture of these algorithms require high power consumption and long latency which are main disadvantages of $arctan()$ function. However, the implementation of $arctan()$ function is accurate using the mentioned techniques when computational cost is not an issue. But for embedded applications such implementations are computationally

70

expensive. The *arctan*() function is complicated and needs more computation time so it is difficult to realize σ_z when processing time is important. As an alternative to σ_z, σ_c is proposed. The purpose of σ_c is to provide a relatively simpler sliding manifold. Fast computation can be achieved with σ_c as replacement of σ_z to speed up the processing time and reduce power consumption. Processing time and power consumption are two important aspects when considering UAV autonomous flights. Improving processing time and lowering power consumption can increase the endurance of the UAV. Thus with these claims it is stated that the σ_p is a high performing manifold and σ_c is a simpler, computationally inexpensive sliding manifold.

3.4 Experimental Results

The proposed guidance law is programmed in the flight control computer of scaled YAK-54 UAV as discussed in Appendix A to demonstrate its effectiveness. The experimental results are presented in two sections, first the path following scheme is applied to different scenarios with σ_p as sliding manifold and then later with σ_c. The FOSMC controllers in (3.9) and (3.32) are thoroughly tested for straight path following for small and large track error cases. These controllers are verified for complex missions both in circular and rectangular loiter patterns. We now illustrate the design methodology by selecting parameters for the scaled YAK-54 UAV.

Parameter selection for σ_p

Based on the desired performance, the sliding manifold σ_p parameters α_2 and β_2 are tuned first. As discussed earlier in Section 3.2.1, to provide quick convergence α_2 is tuned to $0.95\pi/2$ for large track errors and restricting χ_E to be less than $\pi/2$. To achieve good performance for the case of small lateral errors the value of β_2 is selected as 0.005. The reachability condition (3.18) and control boundedness (3.24) will impose minimum and maximum bound on control gain respectively. With the sliding parameter values ($\alpha_2 = \frac{0.95\pi}{2}$, $\beta_2 = 0.005$, $\sigma_{p_{min}} = 0.15$ and $\epsilon_p = 0.3$)

the gain $k_p = 0.42$ is selected according to reachability condition in (3.18) and control boundedness condition in (3.24).

Parameter selection for σ_c

The sliding surface parameters α_3 and β_3 of σ_c are selected based on the required performance. For rapid convergence of large lateral errors α_3 is selected $0.97\pi/2$, while constraining $\chi_E < \pi/2$. For small lateral errors, parameter β_3 is selected as 120 for achieving good performance. The reachability condition (3.41) and control boundedness (3.47) will impose minimum and maximum control gain requirements respectively. With the sliding parameter values ($\alpha_3 = \frac{0.97\pi}{2}$, $\beta_3 = 120$, $\sigma_{c_{min}} = 0.15$ and $\epsilon_c = 0.4$) the gain $k_c = 0.35$ is selected according to reachability condition in (3.41) and control boundedness condition in (3.47).

3.4.1 Flight results of guidance law with manifold σ_p

This section describes flight results for straight and curved path following. Straight path tracking is divided into two cases: Case-1 is for small cross-track errors and Case-2 for large cross track errors. Curved path tracking is also discussed to validate the efficacy of the proposed guidance algorithm. Lastly the algorithm is tested for a complete loiter mission in which the vehicle traverses between a set of predefined waypoints. Crosswinds are a major source of disturbance for the guidance problem, it is estimated that a wind of ~ 4 m/s was generally present during the flights. Results validate robustness of the FOSMC controller in the presence of wind disturbances.

3.4.1.1 Small cross track error

Figure 3.6–Figure 3.7 presents the flight results for initial cross track error of $\sim$200 m. Figure 3.6 shows the cross range y and intercept course χ_E plotted versus time. Approximately ~ 19 sec are required by the proposed algorithm to derive the error from $\sim$200 m to $\sim$6 m. In the cross range plot (Figure 3.6), early transient part shows small steps; this is due to position update from the GPS at discrete instances (4 Hz rate); and the data logging is done in the data logger at a higher rate of 50

Hz. In Figure 3.6, the reference (commanded) roll angle is shown and when the error is 150 m at 1672 sec the maximum commanded roll angle is $\sim 40°$. The state trajectory converges to $\sigma_{p_{min}}$ and follows the manifold quite closely as is evident from Figure 3.7. The resultant inner loop control actuation i.e., (aileron) deflection δ_a is shown in Figure 3.6 which is generally less than 5°. In δ_a versus time graph in Figure 3.6, some chattering / higher frequency fluctuations in the aileron command is visible. This is mainly due to two reasons: firstly the autopilot loop is based on a super twisting HOSM controller for robustness which generates this control signal. Secondly the piston engine of the UAV also generates vibrations which produce disturbances in the roll channel, the control input is used to counter the effects of these disturbances. The appearance of a 2-sliding mode is guaranteed with SOSM super twisting controller for autopilot loop (B.30).
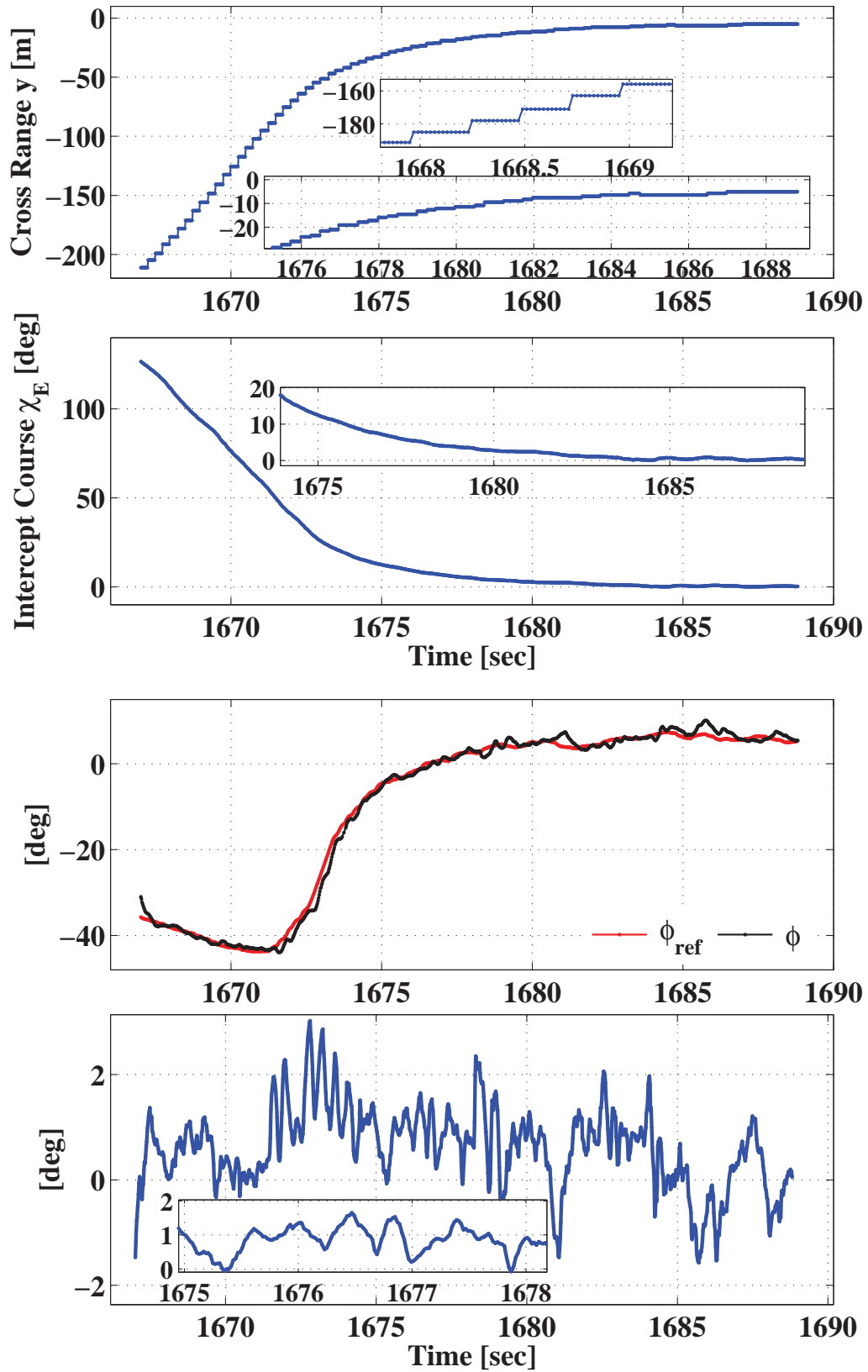
FIGURE 3.6: Cross Range y, Intercept Course χ_E, Reference bank angle ϕ_{ref}, roll angle ϕ and aileron actuation δ_a for small lateral error with σ_p
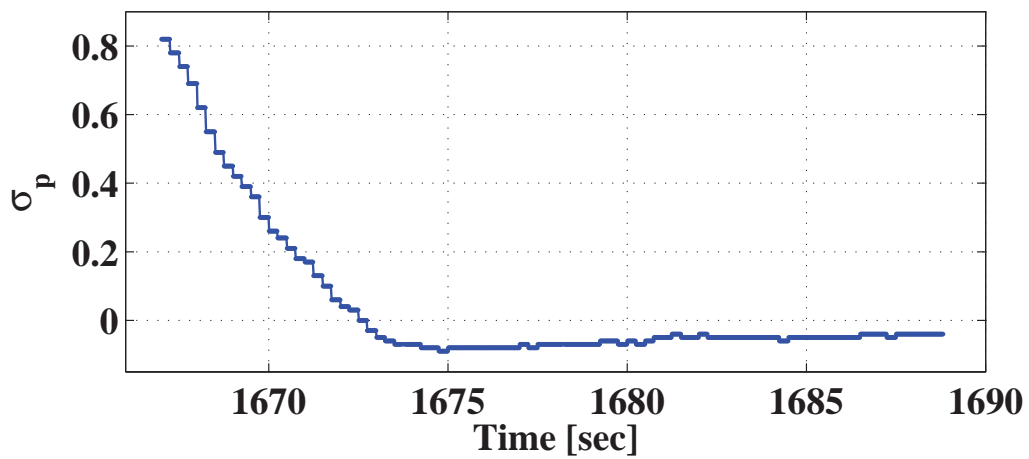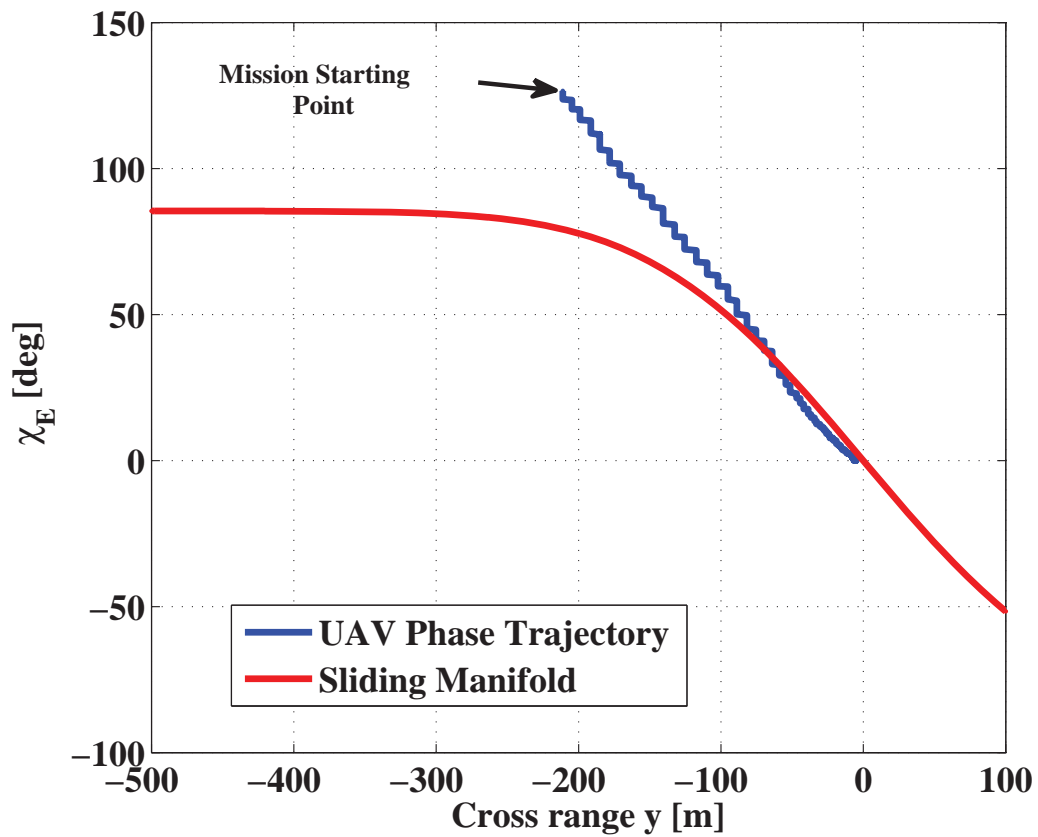
FIGURE 3.7: Phase portrait of UAV trajectory with σ_p and its evolution with time

3.4.1.2 Large cross track error

Figures 3.8–3.10 shows the following of a straight path between two way-points with an initial large cross range of 1200 m. Figure 3.8 illustrates the ground track

of the UAV, the aircraft starts east of the way point at a distance of 1200 m, with a $\sim 180°$ intercept course angle. In Figure 3.9, time evolution of the cross-track from the desired trajectory is shown along with intercept course χ_E. The cross-track error reduces to under 5 m in ~ 50 sec. Initially, the guidance algorithm with σ_p keeps χ_E large to reduce the lateral error y quickly and then it is adjusted accordingly as is evident from Figure 3.9. The commanded roll angle is shown in Figure 3.9, the maximum commanded ϕ_{ref} is less than 43° for both the turns. As is evident from Figure 3.10, the state trajectories are forced to converge to vicinity of manifold σ_p and slides along it quite closely towards origin. Performance of the controller for the large lateral error is evident from the flight results.
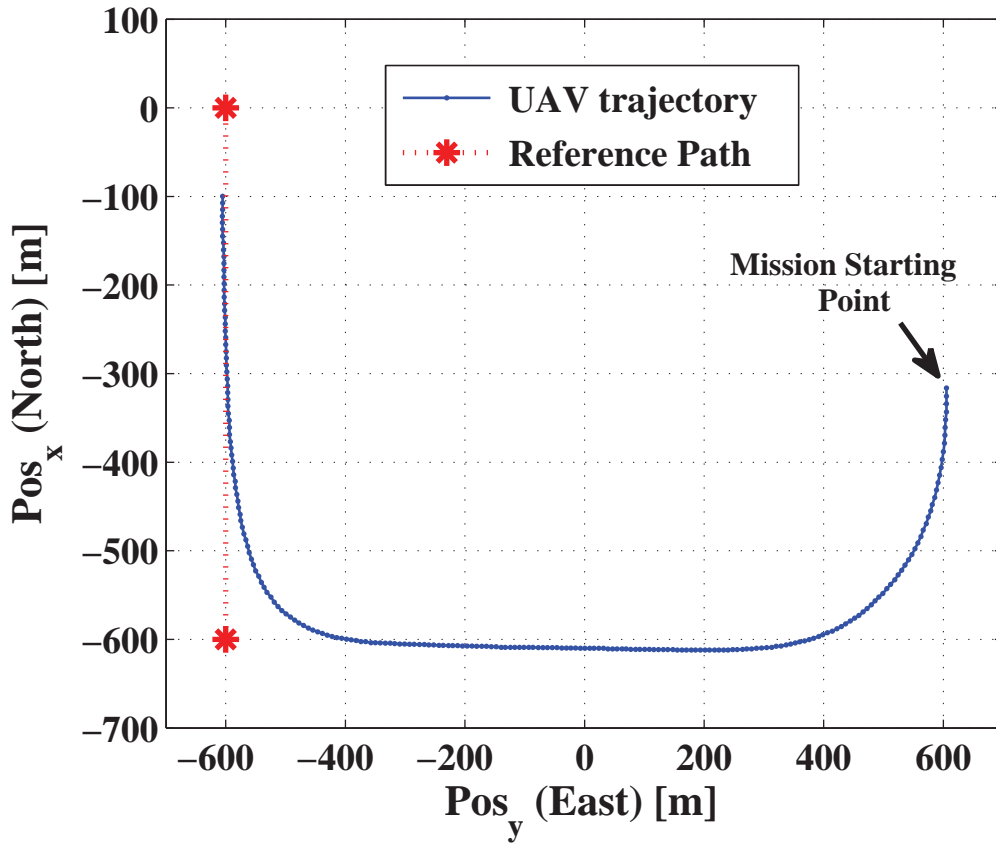
FIGURE 3.8: Reference path and UAV trajectory for large lateral error with σ_p
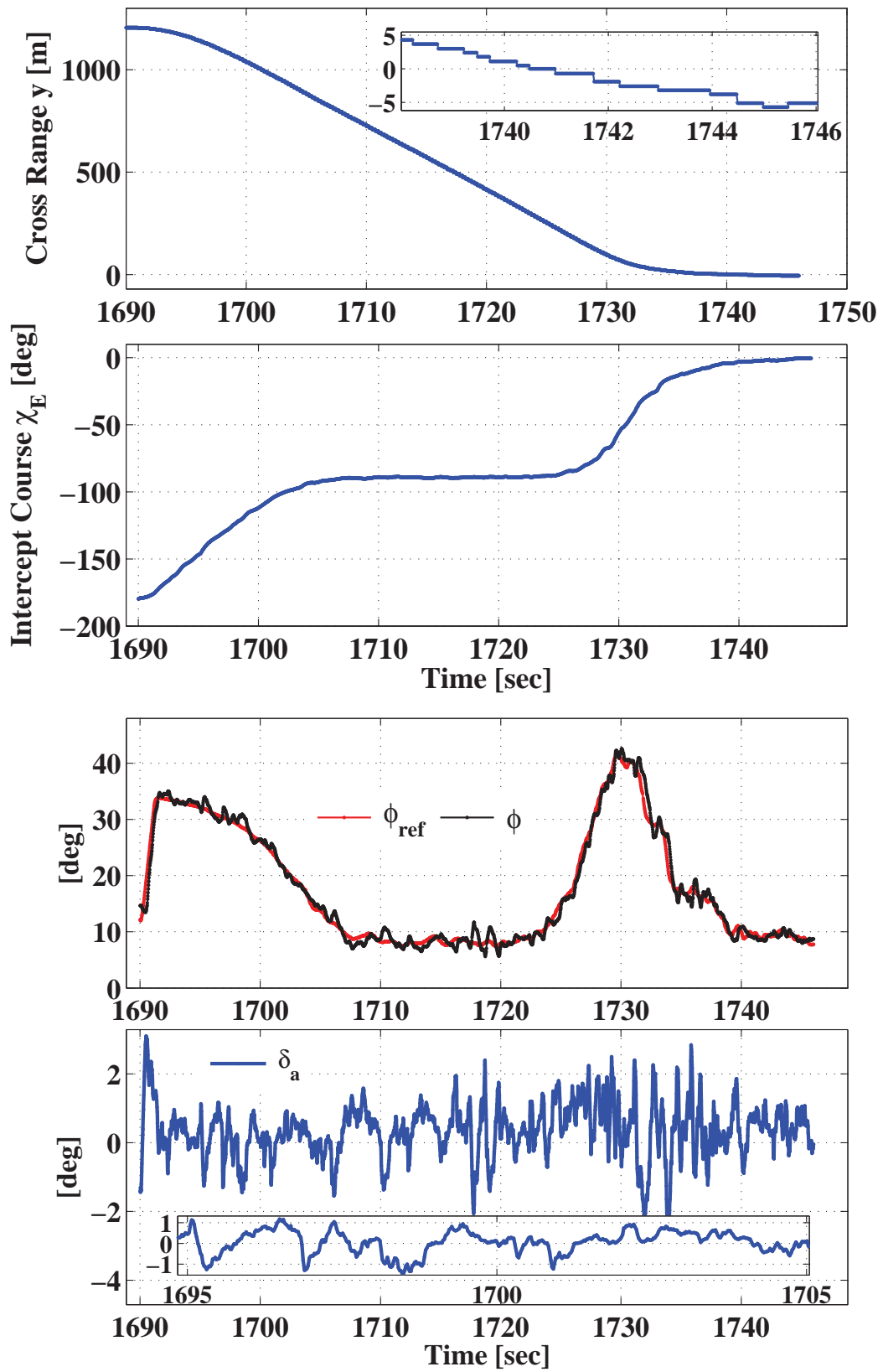
FIGURE 3.9: Cross Range y, Intercept Course χ_E, Reference bank angle ϕ_{ref}, roll angle ϕ and aileron actuation δ_a for large lateral error with σ_p
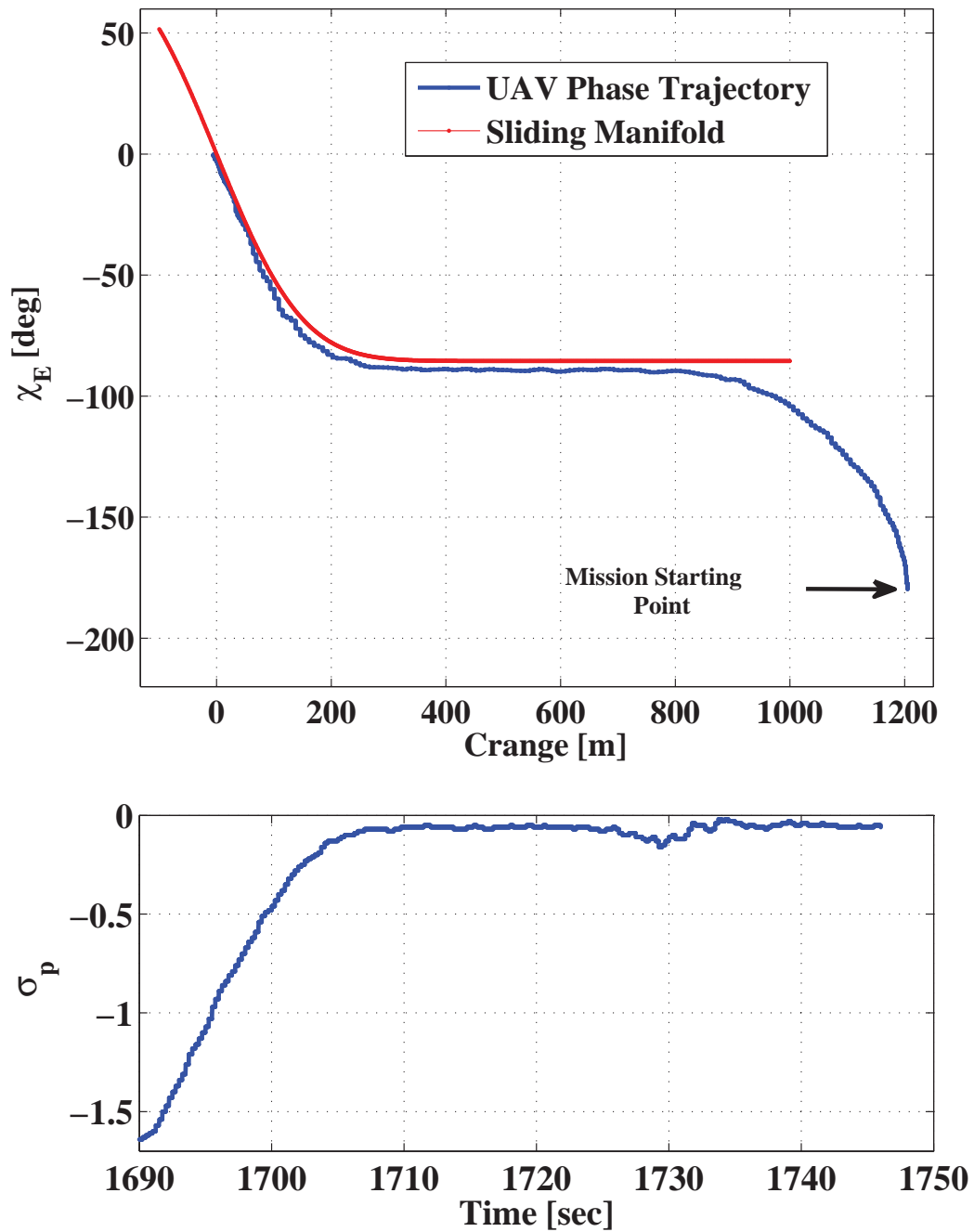
FIGURE 3.10: Phase portrait of UAV trajectory with σ_p and its evolution with time

3.4.1.3 Curved path following

In this case the UAV follows two circular missions as shown in Figure 3.11. Initially the UAV is commanded to follow a circular path of radius 400 m and then it is

commanded to follow a 250 m radius circle. The dotted red shows the desired path to follow and solid blue is the path followed by the UAV. UAV tends to follow the circular path with negative lateral error.
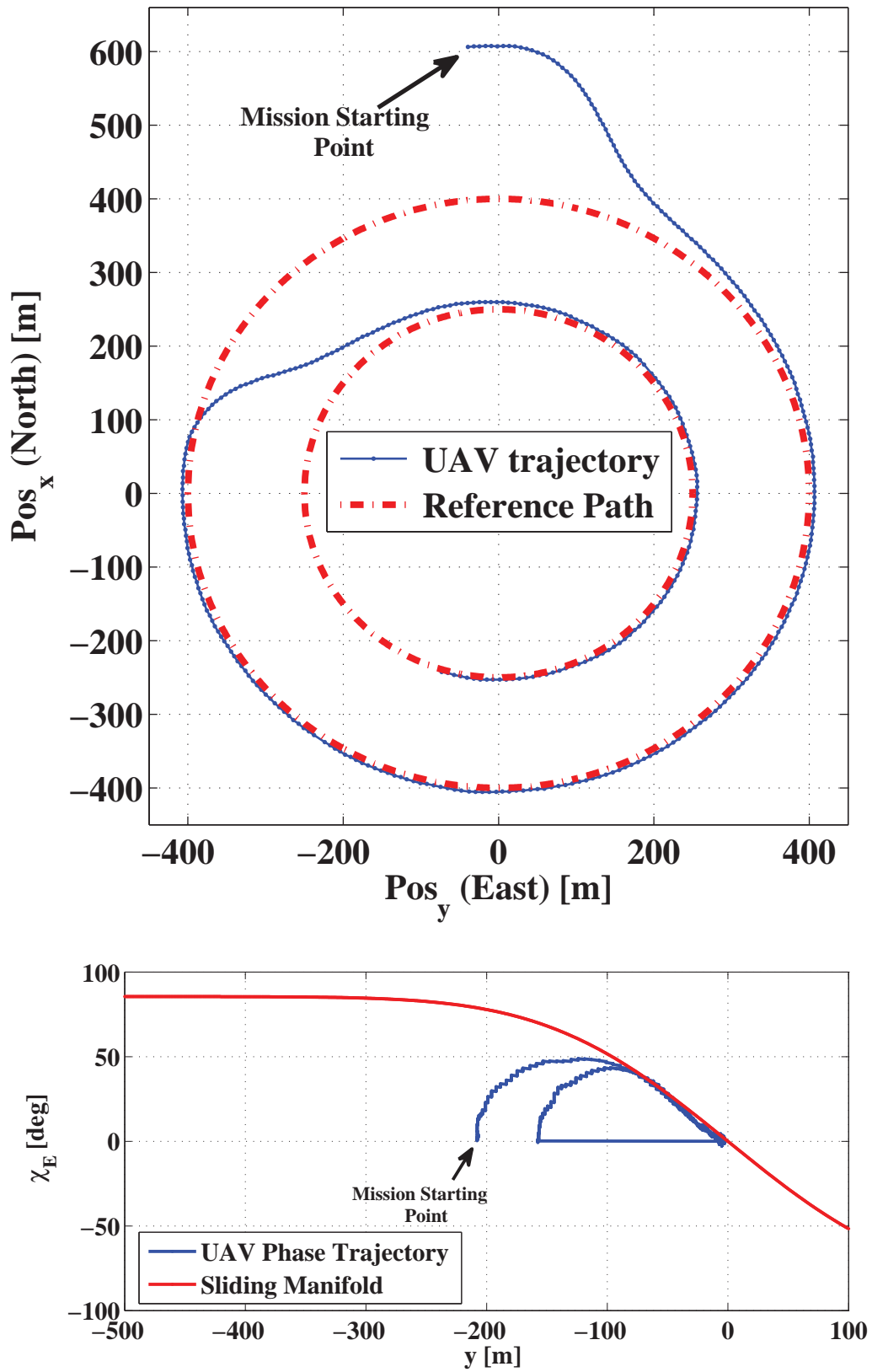
FIGURE 3.11: Reference path and UAV trajectory for circular mission along with Phase portrait of UAV trajectory with σ_p for circular case
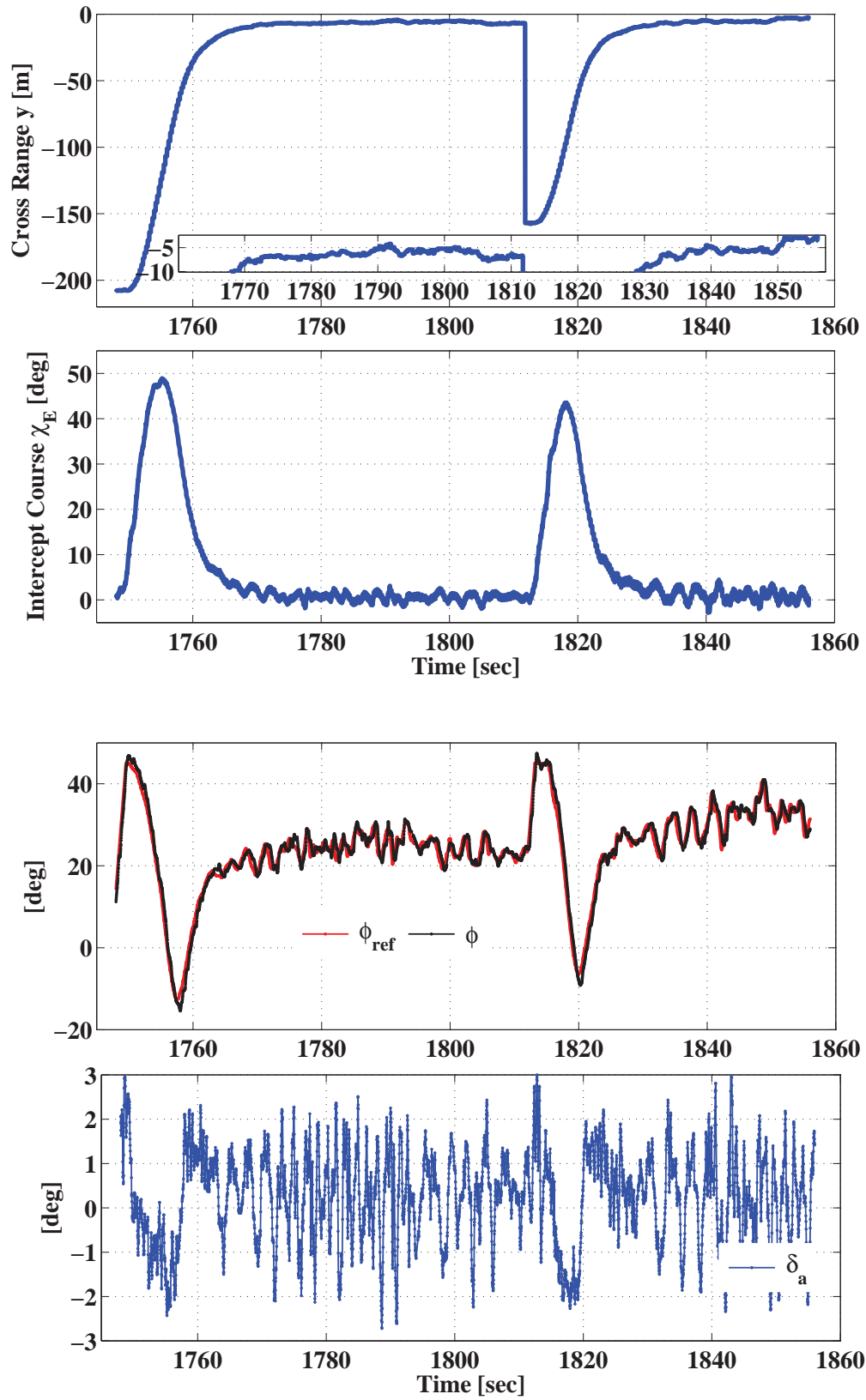
FIGURE 3.12: Cross Range y, Intercept Course χ_E, Reference bank angle ϕ_{ref}, roll angle ϕ and aileron actuation δ_a for circular case with σ_p

81

Figure 3.12 shows the cross-range error y and intercept course χ_E versus time, the error increases at the time of switching from one circle to the other, however the guidance algorithm drives y down to less than 8 m quickly and χ_E to less than 1°. Figure 3.12 also explains the feature that χ_E is initially zero and guidance algorithm first makes an intercept course and then derives the error to zero. The reference bank angle ϕ_{ref}, roll angle ϕ and control actuation δ_a are shown in Figure 3.12. The maximum commanded roll reference command is ~44°. It is clear that the proposed nonlinear guidance strategy performs well for curved path following in the presence of wind. The sliding surface along with the state trajectories is shown in Figure 3.11 for the two circles. The state trajectory gets attracted towards the sliding surface and subsequently maintains motion in the vicinity of the surface σ_p to reach the origin.

3.4.1.4 Loiter mission

Figure 3.13 shows the flight experimental results for a loiter mission. The desired path to follow by the vehicle is shown in dotted red while in solid blue is the actual trajectory flown. Way-point switch algorithm is continuously active for smooth transition and when the distance to the next waypoint reduces to a certain threshold, command is issued to follow the next leg. The maximum commanded (reference) generated by the algorithm is approximately less than 42° for this mission as shown in Figure 3.14. The proposed guidance algorithm was efficiently able to follow the complete loiter mission with lateral track steady state error of 6 m to 7 m as in Figure 3.14. Figure 3.13 shows the tracking performance of the FOSMC design since the lateral error is driven towards zero and desired course is achieved. Notice from these figures that the controller developed in (3.9) is able to provide cross track error and heading error regulation.
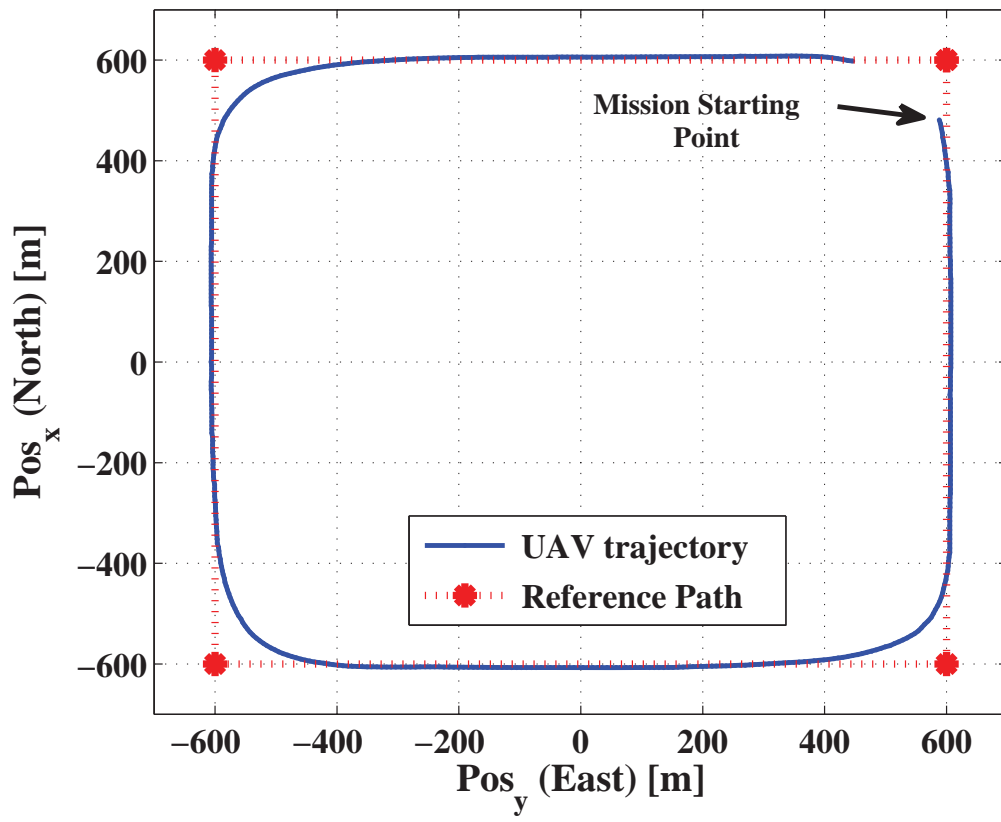
FIGURE 3.13: Reference path and UAV trajectory for loiter mission
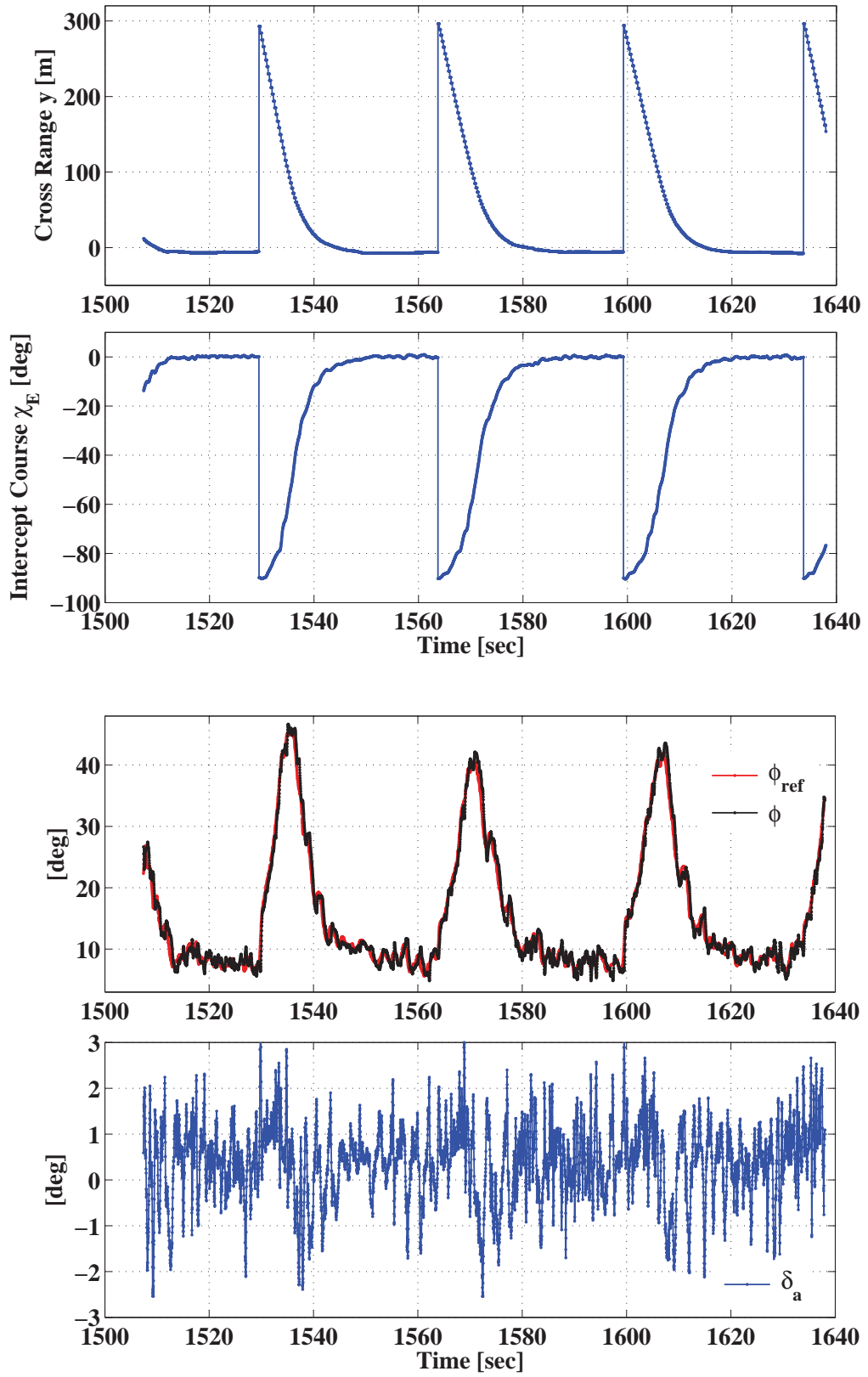
FIGURE 3.14: Cross Range y, Intercept Course χ_E, Reference bank angle ϕ_{ref}, roll angle ϕ and aileron actuation δ_a for a loiter mission

3.4.2 Flight results of guidance law with manifold σ_c

3.4.2.1 Large/small cross track error

Figure 3.16 presents the flight results of initial 250 m lateral error. The time plots of cross range y and intercept course χ_E are plotted in Figure 3.16; the algorithm reduced the error from 250 m to $\sim$4 m in $\sim$15 sec. When the lateral error of 250 m is averted to vicinity of zero, -100 m lateral disturbance is generated to further test the algorithm. The proposed algorithm is efficient in reducing the lateral error smoothly without any overshoot for this case. The sliding manifold σ_c converges to $\sigma_{c_{min}}$, and then slides alongside closely to the manifold to reach the origin as is evident from Figure 3.15. In Figure 3.16, the reference (commanded) roll angle is shown and when the cross range is $\sim$200 m, the maximum magnitude of reference roll angle generated is $\sim 40°$. The inner loop aileron control actuation δ_a corresponding to the reference commands ϕ_{ref} is shown in Figure 3.16, it is evident to be small and within limits. The SOSM super twisting inner loop controller (B.30) provides good performance in tracking the reference commands ϕ_{ref} evident from Figure 3.16.
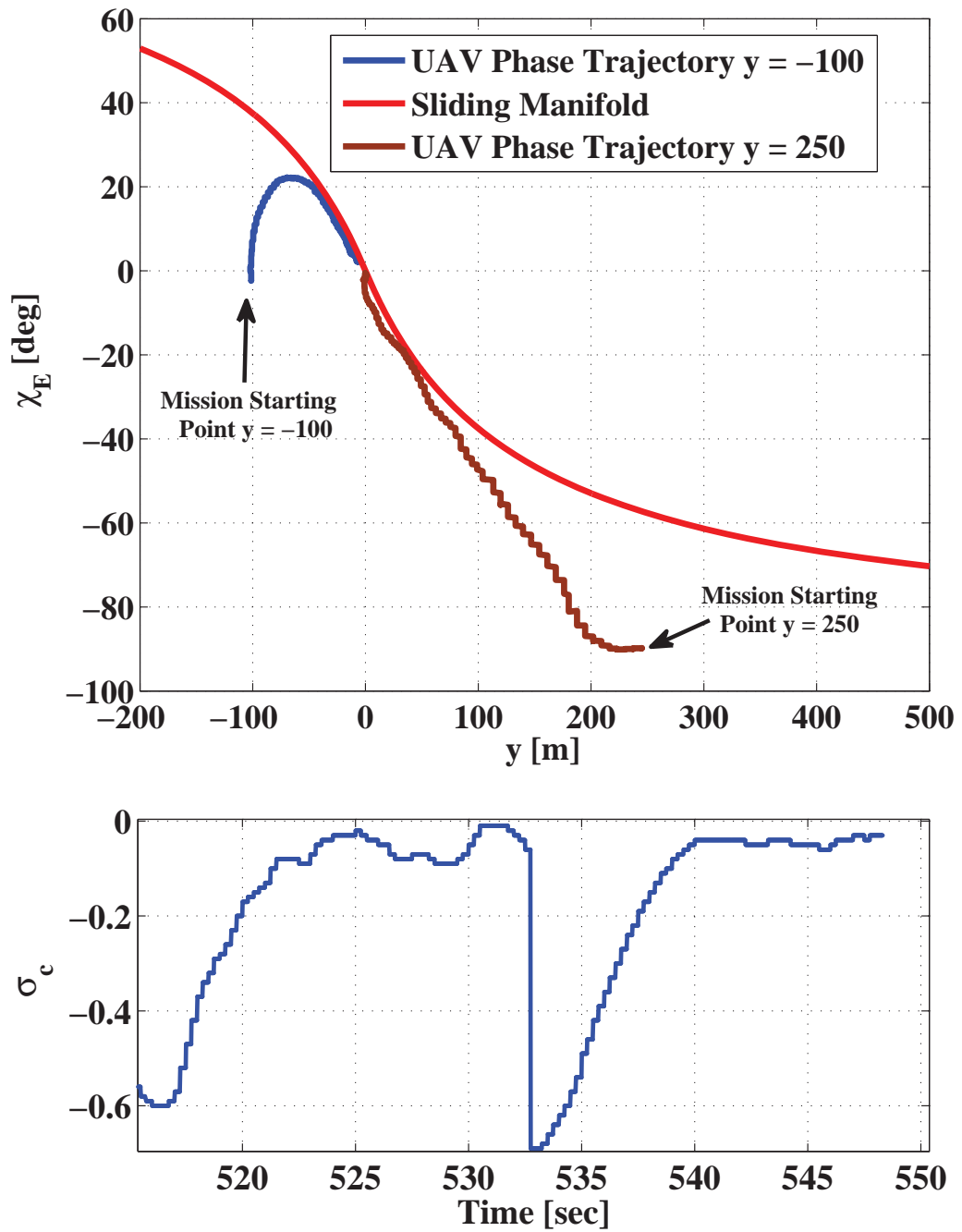
FIGURE 3.15: Phase portrait of UAV trajectory and evolution of σ_c
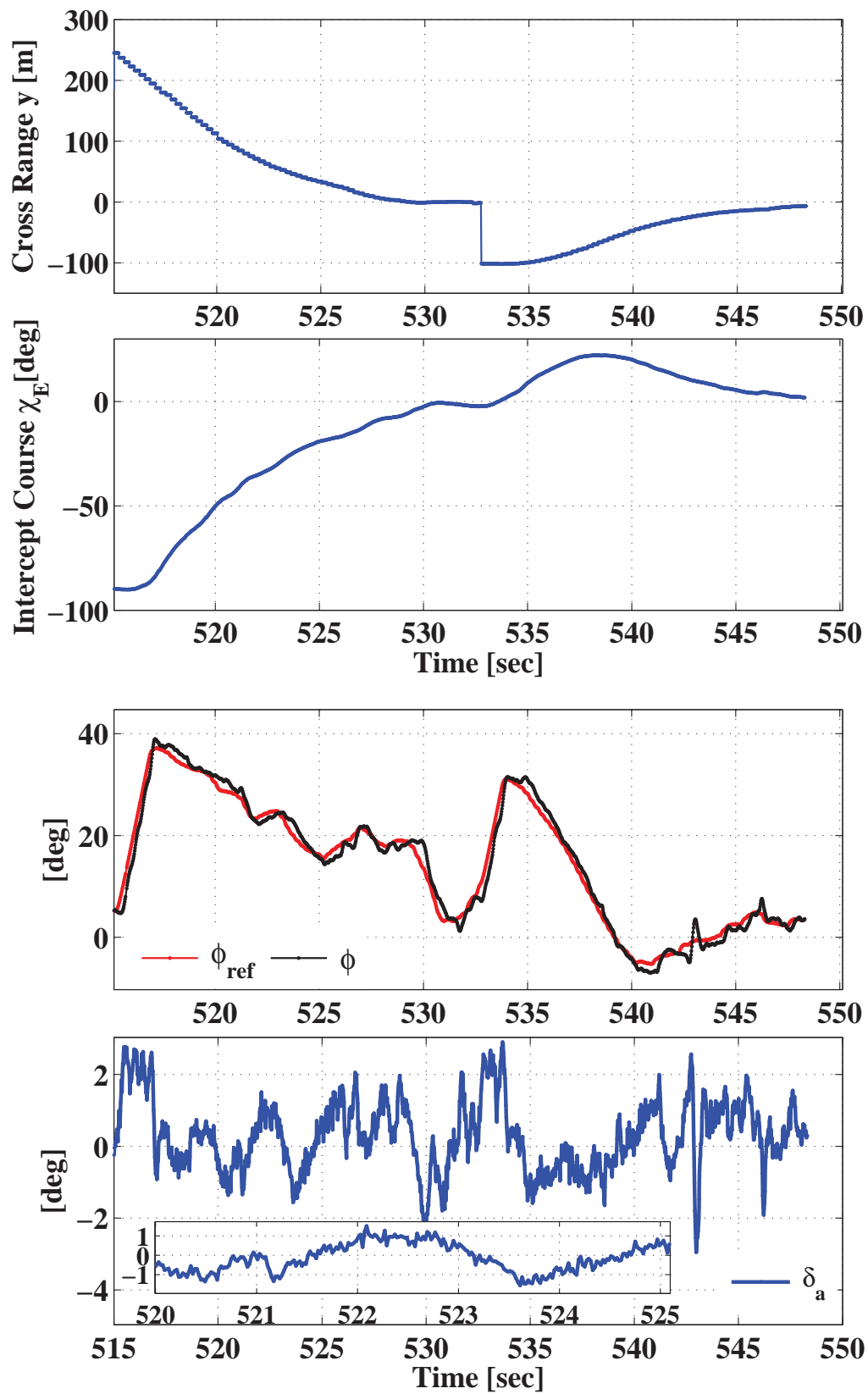
FIGURE 3.16: Cross Range y, Intercept Course χ_E, Reference bank angle ϕ_{ref}, roll angle ϕ and aileron actuation δ_a for small lateral error with σ_c

3.4.2.2 Curved path following

Next, the guidance law with σ_c is applied to curved line tracking. In Figure 3.17, the desired curved mission profile and its associated flight results are shown. Initially, the aircraft is heading due north in a level flight. The reference roll angle ϕ_{ref} generated by the guidance loop is shown in Figure 3.18 with the resulting control effort δ_a. In the case of FOSMC, a steady state error of 7 meters is obtained as evident from Figure 3.18. The sliding manifold σ_c first attract the state trajectories and then slides it towards origin as is evident from Figure 3.17. It is clear from the Figure 3.17 and Figure 3.18, the nonlinear guidance algorithm results in good curved path following with only 5 to 7 meter deviation from the curved path in the initial transient phase.
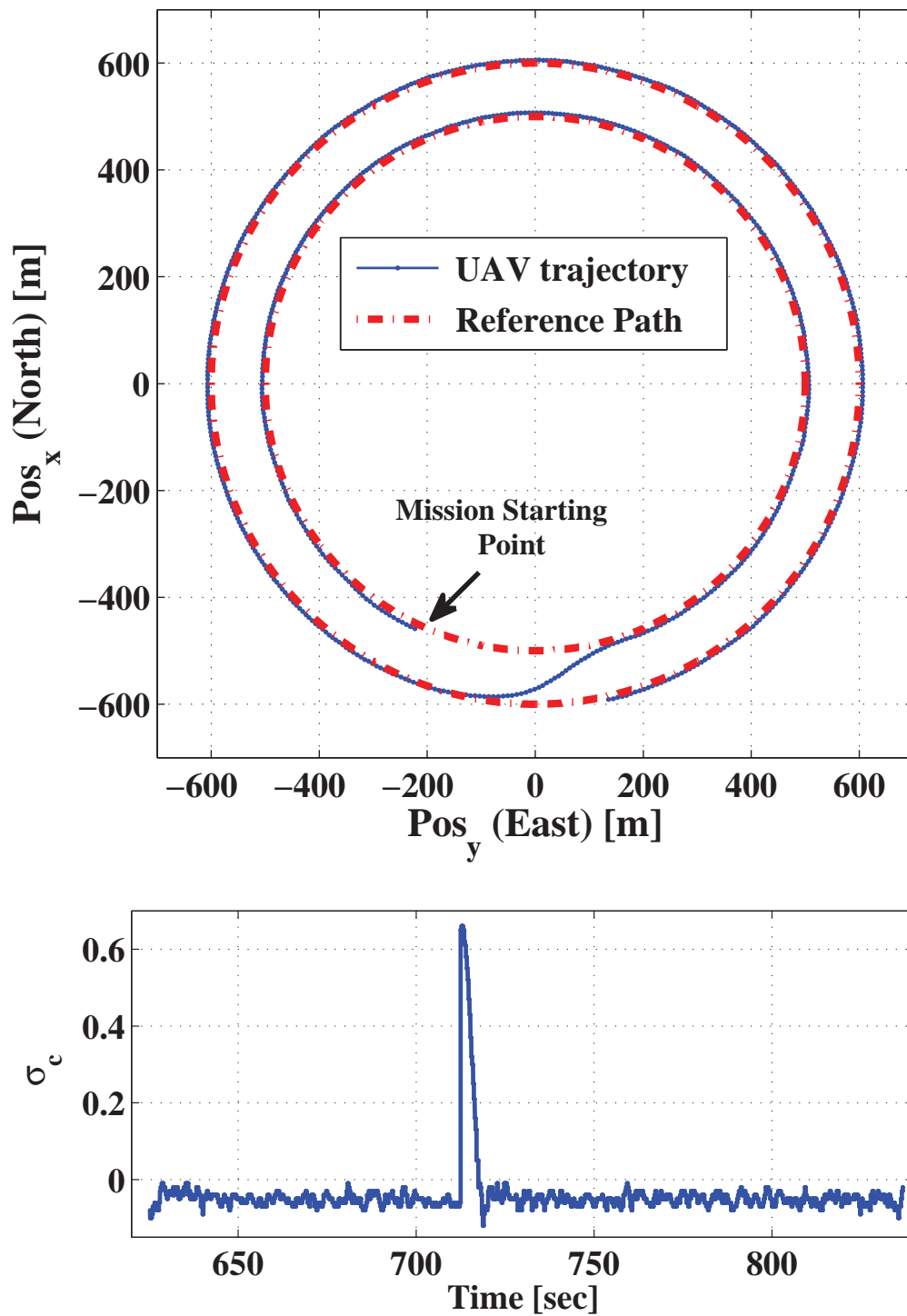
FIGURE 3.17: Reference path and UAV trajectory for circular mission along with phase portrait of UAV trajectory and evolution of σ_c
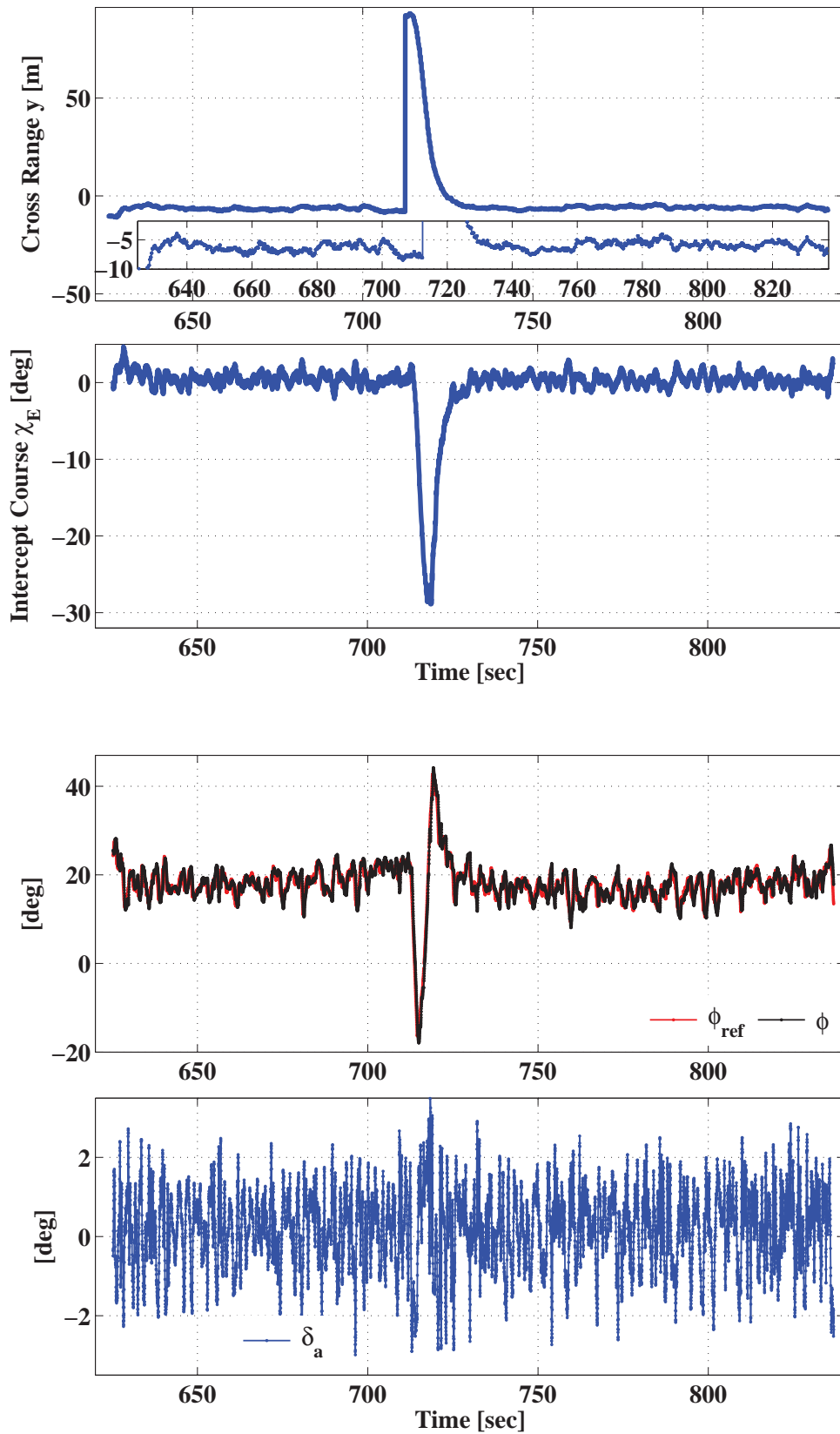
FIGURE 3.18: Cross Range y, Intercept Course χ_E, Reference bank angle ϕ_{ref}, roll angle ϕ and aileron actuation δ_a

90

3.4.2.3   Loiter mission

Figure 3.19–Figure 3.20 presents the loiter mission flight results. The actual path flown against the desired mission are shown in Figure 3.19 in solid blue and dotted red respectively. The origin is taken as the take off point with distance traveled towards north is denoted as Pos_x and distance traveled towards east as Pos_y. Throughout the mission, waypoint switch algorithm is continuously active to provide smooth transitions at the corners. The proposed algorithm is able to provide good performance as evident from Figure 3.20. The commanded roll reference angle ϕ_{ref}, along with the actual roll of the vehicle and corresponding control aileron actuation δ_a are shown in Figure 3.20. The proposed guidance algorithm generated the maximum magnitude of $\sim 35°$ reference roll angle for the whole loiter mission. In Figure 3.19 we show the time evolution of the vehicle deviation from the desired trajectory when commanded to follow the way-points. Notice from these figures that the controller developed is able to provide cross track error and heading error regulation.
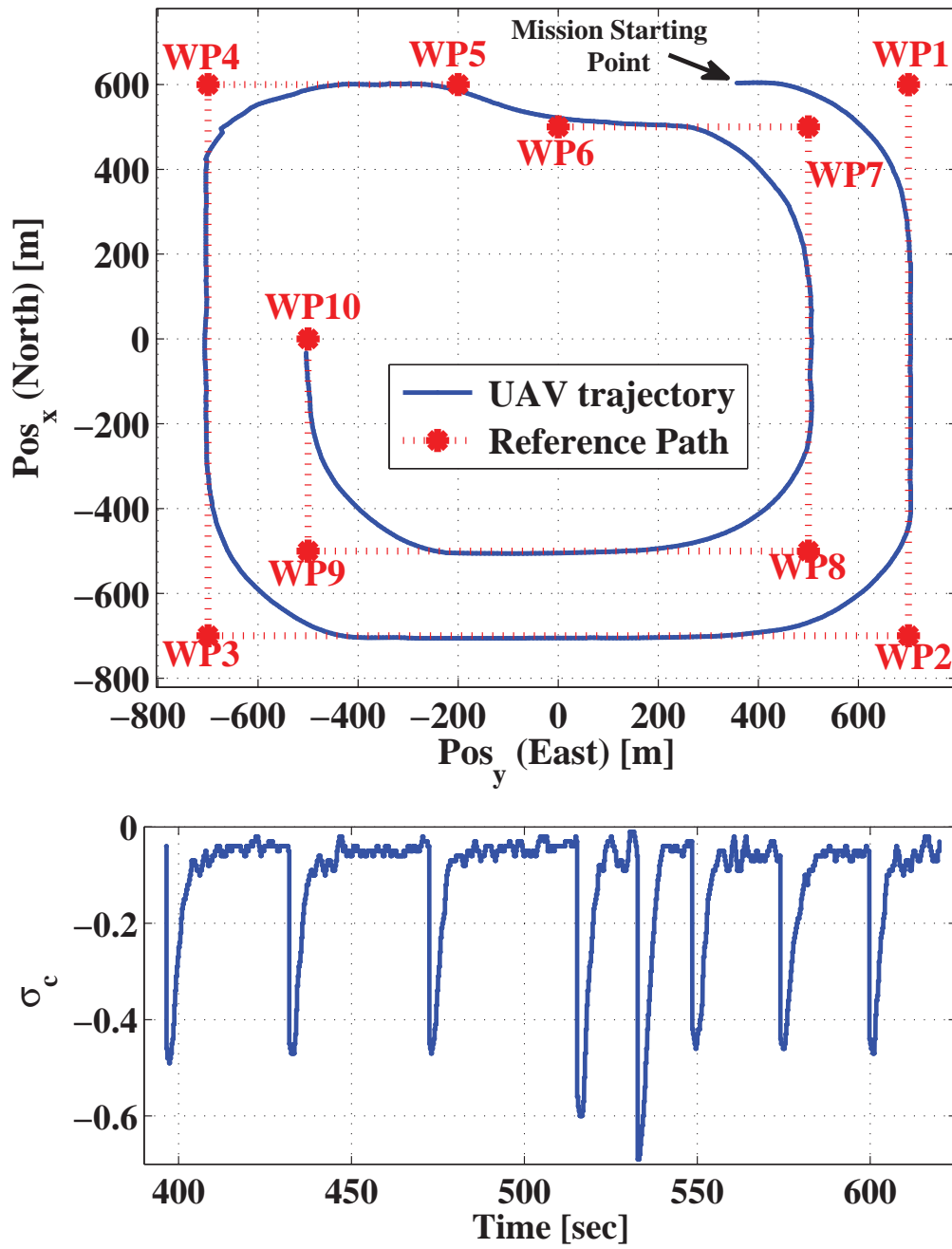
FIGURE 3.19: Reference path and UAV trajectory along-with evolution of σ_c
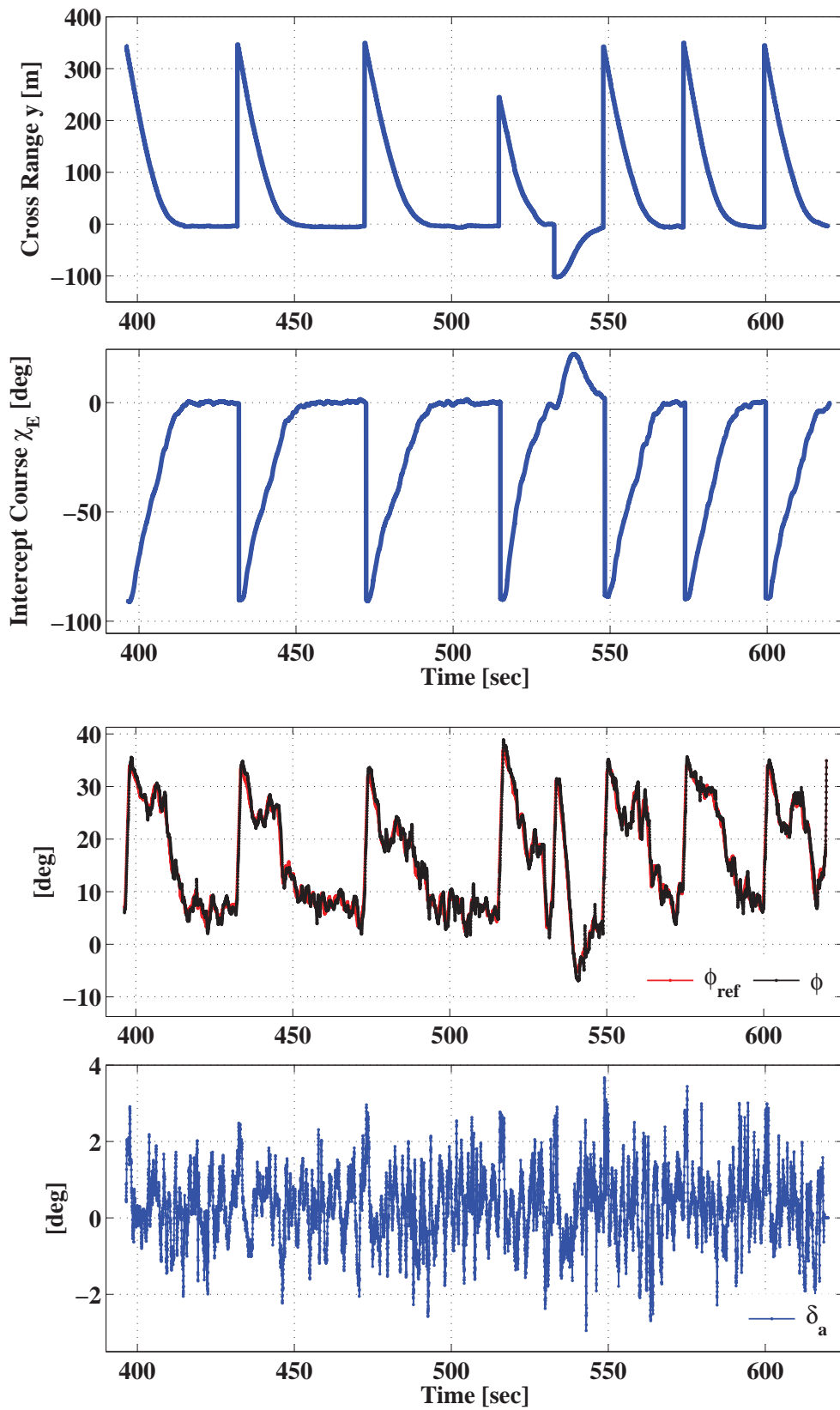
FIGURE 3.20: Cross Range y, Intercept Course χ_E, Reference bank angle ϕ_{ref}, roll angle ϕ and aileron actuation δ_a for a loiter mission

3.5 Conclusion

In this chapter, two nonlinear sliding surfaces are proposed. The manifold stability along with the existence of sliding mode and control boundedness is proved with the help of suitable Lyapunov functions. A quasi FOSMC is designed for chatter reduction and applied to lateral path following application of UAVs. The proposed high performance surface is able to achieve better performance without violating the reachability and control boundedness conditions. Sliding surface for low computational complexity is also presented. It is shown how high performance can be combined with high robustness to effectively reject disturbance while generating limited control commands. The strategy in this chapter is to extend the capabilities of previous designed nonlinear surface. For the entire state space of initial conditions, asymptotic Lyapunov stability is also demonstrated for the nonlinear guidance law, for the selected velocity range, and with limited lateral acceleration commands. The flight experiment analysis validates the proposed guidance framework and illustrates the effectiveness of the method. The guidance scheme here is designed with an assumption that $\phi_{ref} \approx \phi$.

Chapter 4

HOSM BASED LATERAL GUIDANCE WITH AUTOPILOT CONSTRAINT

As discussed earlier in Chapter 3, novel nonlinear sliding surfaces are proposed for lateral guidance of aerial vehicles showing improved performance than linear sliding manifold in [55, 56]. The guidance algorithm generates roll command ϕ_{ref} using measurements of the states y (cross-track error) and χ_{E} (intercept course). The roll command serves as a reference signal for the inner roll control loop. The guidance scheme is designed with the assumption that the inner loop dynamics from ϕ_{ref} to ϕ are fast and can be neglected (i.e., $\phi_{ref} \approx \phi$), thus the algorithm was designed using first order sliding mode theory.

The guidance law developed in this chapter takes into account constraints on the vehicle dynamics, and is derived using geometrical considerations of the kinematics of vehicle motion. The objective is to drive the cross-track and course angle errors to zero. Here we extend the work in [55, 56] and Chapter 3 by taking into account dynamics of the inner control loop while designing the outer guidance loop. The overall system therefore performs better, especially when the inner loop is slower and comparable in response time to the outer loop. Generally, commands generated by the guidance law are tracked with some lag by the inner control loop, hence the information of inner loop dynamics can enhance performance of the outer guidance loop. However this increases relative degree of the problem, hence we propose a novel finite-time convergence law using HOSM theory. Local asymptotic stability of the proposed nonlinear law and existence of the sliding mode is demonstrated. In sliding motion, it is also shown that no saturation of the guidance signal occurs for small or large lateral errors. Hence, the developed law is well suited for practical UAV applications.

This chapter is structured as follows: analytical model of the problem and its nonlinear dynamics are presented in section 4.1. Section 4.2 develops the proposed guidance law on the basis of a nonlinear sliding manifold using the HOSM real twisting algorithm. Existence of the 2-sliding mode is shown and boundedness of the guidance command is proven. The developed guidance scheme is implemented in flight control system of scaled YAK-54 UAV, different scenarios with small and large track errors and with circular and loiter missions are flown and tested. The efficiency of the proposed guidance logic is shown by flight results presented in section 4.3. Validation of the YAK-54 UAV mathematical model is presented in section 4.4. Finally conclusion is presented in section 4.5.

4.1 Guidance and Control Structure

The work presented here is about two-dimensional (2-D) guidance design, for tracking the desired ground track of the vehicle. The requirement is that the UAV must exactly follow the projection of the mission on the ground plane with minimum lateral deviation by smooth bank-to-turn maneuvers. In the two-loop approach employed here, the outer guidance loop considers kinematics with an additional information of ϕ and the UAV dynamics are considered in the inner control loop. The block diagram of the overall guidance and control system is shown in Figure 4.1. A pre-specified path is available from the mission block in the form of waypoints, and the desired course χ_R and its rate of change. Mission information and feedback from sensors measuring the instantaneous position y, course angle χ and roll angle ϕ serve as inputs to the guidance algorithm. The algorithm generates suitable roll angle commands ϕ_{ref} for the inner loop to track. The inner control loop actuates the ailerons δ_a to track the roll commands generated by the guidance loop. A HOSM real twisting controller with a nonlinear sliding manifold is designed here. The guidance law guarantees the boundedness of the roll command and finite time convergence, ensuring minimum cross-track error y for both straight and curved paths in the presence of wind disturbances.
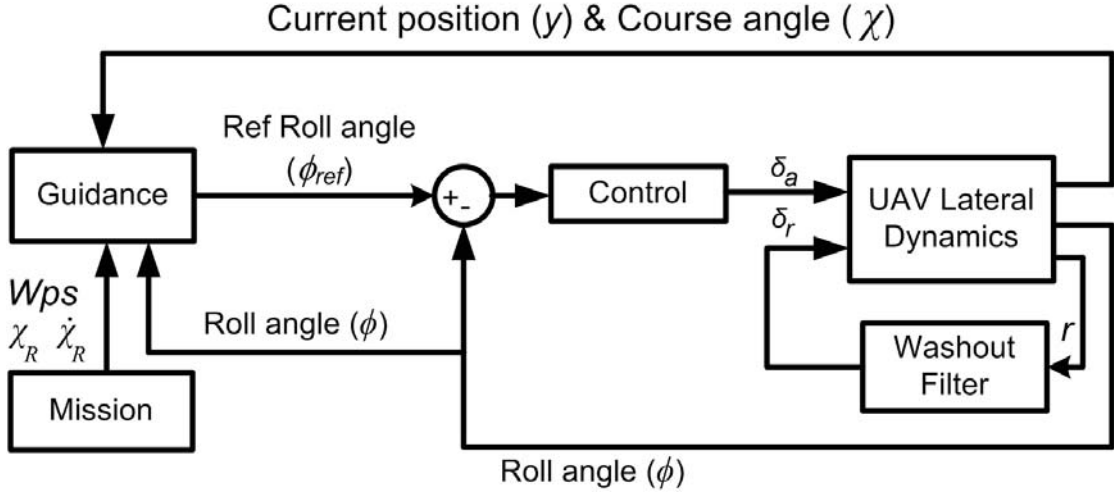
FIGURE 4.1: Block diagram of the guidance and control system.

4.1.1 Problem Formulation

UAV dynamics: The UAV motion has dynamical constraints. The UAV cannot change direction instantaneously and this raises difficulties, leading to the UAV being possibly out-maneuvered by the desired ground track. The inner roll closed-loop dynamics from ϕ_{ref} to ϕ is approximated [34] by a first order filter of the form shown in Figure 4.2:

$$\frac{\phi}{\phi_{ref}} = \frac{1}{\tau s + 1} \qquad (4.1)$$

where the constant $\tau \in \Re$ (the set of real numbers) and is incorporated into the guidance system. Therefore the third state equation represents the inner loop dynamics, i.e.,

$$\dot{\phi} = \frac{1}{\tau}(\phi_{ref} - \phi). \qquad (4.2)$$

Equations (2.48), (2.49) and (4.2) represent the dynamics to be considered during outer loop guidance design. We can write the state equations in state space form as

$$
\begin{bmatrix} \dot{y} \\ \dot{\chi}_E \\ \dot{\phi} \end{bmatrix} = \begin{bmatrix} V \sin \chi_E \\ \frac{g}{V} \tan \phi - \dot{\chi}_R \\ \frac{-\phi}{\tau} \end{bmatrix} + \begin{bmatrix} 0 \\ 0 \\ \frac{1}{\tau} \end{bmatrix} \phi_{ref} \qquad (4.3)
$$

where χ_E, y and ϕ are the state variables, and ϕ_{ref} is the control signal generated by the guidance loop.

A solution for the roll control problem is proposed using classical control theory and keeping in view the practical implementation constraints of actuators/sensors etc. For the roll autopilot, lead-lag control design technique was used, the designed controller is capable of achieving the desired roll angle profile. The controller's objective is to generate δ_a for aileron actuation as shown in Figure 4.1 to track the reference bank commands ϕ_{ref}. As actuator dynamics play a vital role in transforming the signals from the controller to aileron deflection, the actuator was modeled experimentally using a ground testing setup explained in Section A.0.1. The utilized lead-lag controller [97] appears in following form

$$
K_{lead-lag} = \frac{(2.646s + 20)(s + 1)}{(s + 52.92)(s + 0.1)} \qquad (4.4)
$$

The closed loop system response of the available controller along with the approximation of the system's response with the first order filter presented in (4.2) with different values of τ is shown in Figure 4.2.
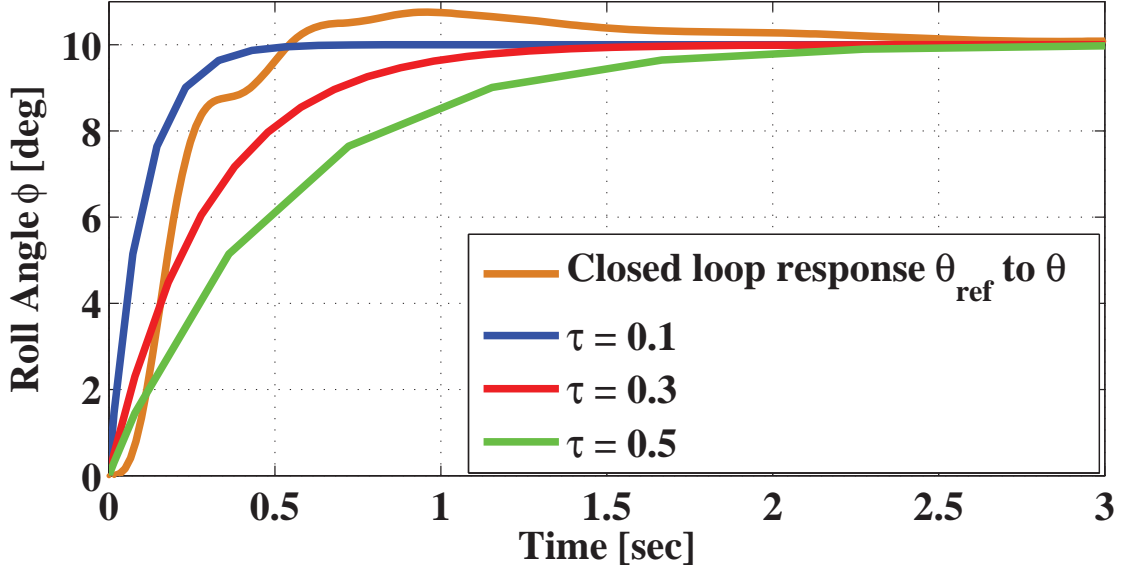
FIGURE 4.2: Closed loop response from ϕ_{ref} to ϕ and approximate fitting

With $\tau = 0.3$ gives a reasonably good response for our system, but this depends upon actuator and autopilot dynamics and can be found accordingly for other UAV systems.

4.2 Lateral Guidance Scheme Design

The guidance law is designed to attract the system states y and χ_E towards the sliding manifold from any arbitrary initial condition. The system dynamics during sliding are insensitive to disturbances and model uncertainties [88]. To restrict the magnitude of χ_E below 90°, a nonlinear sliding surface is proposed in [55] for attaining good performance for bath small and large cross track errors.

$$s = \chi_E + \alpha \arctan(\beta y), \qquad (4.5)$$

where $\alpha, \beta \in \Re$ are surface parameters, later the condition of $\alpha, \beta > 0$ is discussed for stability of sliding surface. In order to ensure $|\chi_E| \leq 90°$, we need $|\alpha| \leq 1$. As $\pm \arctan(\beta y) \approx \pm 90°$ for large lateral errors, therefore for $\pm y$ $\chi_E \approx \mp|\alpha|90°$. For large lateral errors, the selection of $|\alpha|$ is directly proportional to χ_E, hence

99
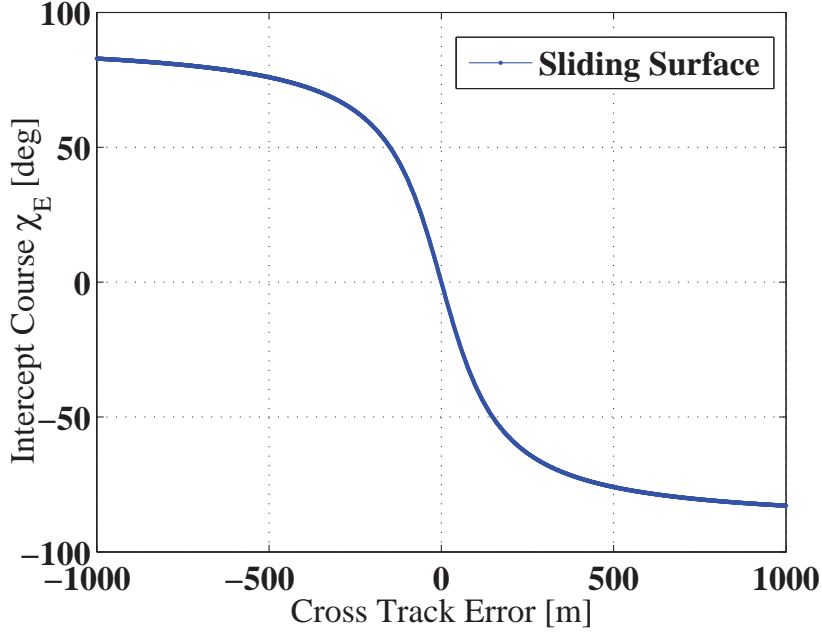
FIGURE 4.3: Motion on Sliding Surface for particular α and β

bigger value of α implies a larger χ_E and fast convergence of the error to zero. The curvature of the curve is defined by the parameter β i.e., its value determines the turning of the vehicle to reduce the lateral error. Large values of β imply fast dynamics of error convergence with considerable large χ_E for small y. The system dynamics are sluggish for small values of β indicating an appreciable χ_E for large y and hence turning of the vehicle will be slow. Selection of β is directly related to performance in case of small lateral errors. However, a larger value of β imply bigger control commands therefore its value cannot be selected arbitrarily large.

It is assumed in the previous work [55, 56] that $\phi_{ref} \approx \phi$ and the inner loop dynamics can be ignored. This results in a system with a relative degree $r = 1$, and a first order SMC guidance law was designed. Here we have approximated the inner loop dynamics with a first order lag which results in the control input ϕ_{ref} to appear in the $\ddot{s}$, transforming the system into relative degree two problem. In this particular case, we have used a real-twisting 2-sliding controller and the sliding motion is represented in (4.6), i.e.,

$$s = \chi_E + \alpha \arctan(\beta y) = 0, \qquad (4.6)$$

implying

$$\dot{s} = \dot{\chi}_E + \frac{\alpha\beta}{1 + \beta^2 y^2} \dot{y}. \qquad (4.7)$$

Along the system state derivatives in (4.3), we have

$$\dot{s} = \frac{g}{V} \tan\phi - \dot{\chi}_R + \frac{\alpha\beta}{1 + \beta^2 y^2} V \sin\chi_E. \qquad (4.8)$$

For the control input ϕ_{ref} to appear, we take the 2nd derivative of the sliding surface:

$$\ddot{s} = \frac{g \sec^2\phi}{V} \dot{\phi} - \ddot{\chi}_R + \alpha\beta V \left(\frac{\cos\chi_E}{1 + \beta^2 y^2} \dot{\chi}_E - \frac{2\beta^2 y \sin\chi_E}{(1 + \beta^2 y^2)^2} \dot{y} \right), \qquad (4.9)$$

or

$$\ddot{s} = \left(-\frac{g\phi \sec^2\phi}{V\tau} - \ddot{\chi}_R + \frac{\alpha\beta V \cos\chi_E}{1 + \beta^2 y^2} \left(\frac{g}{V} \tan\phi - \dot{\chi}_R \right) \right.$$
$$\left. - \frac{2\alpha\beta^3 V^2 y \sin^2\chi_E}{(1 + \beta^2 y^2)^2} \right) + \left(\frac{g \sec^2\phi}{V\tau} \right) \phi_{ref}. \qquad (4.10)$$

where ϕ_{ref} is the control input. Comparing (4.10) with (2.27), we have:

$$a(t,x) = -\frac{g\phi \sec^2\phi}{V\tau} - \ddot{\chi}_R + \frac{\alpha\beta V \cos\chi_E}{1 + \beta^2 y^2} \left(\frac{g}{V} \tan\phi - \dot{\chi}_R \right)$$
$$- \frac{2\alpha\beta^3 V^2 y \sin^2\chi_E}{(1 + \beta^2 y^2)^2} \qquad (4.11)$$

$$b(t,x) = \frac{g \sec^2\phi}{V\tau} \qquad (4.12)$$

Using the sliding surface (4.5) and its derivative (4.7), the expression for control law (2.29) can be written as:

$$\phi_{ref} = - r_1 \operatorname{sgn}(\chi_E + \alpha \arctan(\beta y))$$
$$- r_2 \operatorname{sgn}(\frac{g}{V} \tan \phi - \dot{\chi}_R + \frac{\alpha \beta V \sin \chi_E}{1 + \beta^2 y^2}). \tag{4.13}$$

The expression for closed loop sliding mode dynamics [91] is given by substituting the control input (4.13) in (4.3) to yield

$$\dot{y} = V \sin \chi_E$$
$$\dot{\chi}_E = \frac{g}{V} \tan \phi - \dot{\chi}_R$$
$$\dot{\phi} = -\frac{\phi}{\tau} - \frac{r_1}{\tau} \operatorname{sgn}(\chi_E + \alpha \arctan(\beta y)) - \frac{r_2}{\tau} \operatorname{sgn}(\frac{g}{V} \tan \phi - \dot{\chi}_R + \frac{\alpha \beta V \sin \chi_E}{1 + \beta^2 y^2})$$
$$\tag{4.14}$$

4.2.1 Boundedness of control effort and stability analysis

Generally, the lateral guidance and control schemes are designed in two loops with outer loop for guidance generating bank reference commands for the autopilot to follow. In practice, to avoid saturation and excessive bank maneuvers, limiters and saturation blocks are used in the inner control loop. As an example, the guidance logic generating roll reference commands could have a saturation check on, similar checks can also exist on aileron control actuation driving the actuators. In the presence of such nonlinearities, interconnected loop stability is not formally proved. Most designers and practitioners generate confidence by relying on extensive numerical simulation before going to the flight. Objective of the guidance loop is to generate suitable commands for the inner loop that do not cause saturation of signals, thus resulting in guaranteed stability margins with graceful maneuvers.

As discussed in [55], for good performance large values of α and β are desired in order to drive cross track error quickly to zero. Saturation of some signals may

occur for the control loop, if arbitrarily large gains r_1 and r_2 are selected, and thus the guidance reference commands ϕ_{ref} are not actually applied to the autopilot for tracking. Specifically, saturation of the signals may violate the reachability condition due to the result of lower *effective* gain applied to the system. Hence sliding motion will not be assured for such a case. Therefore, it is essential to bound the roll reference command (4.13) with the maximum allowed value ϕ_{max} to avoid saturation. For control boundedness ($|\phi_{ref}| \leq \phi_{max}$), the following additional constraint is imposed:

$$r_1 + r_2 \leq \phi_{max} \tag{4.15}$$

To ensure stability, criterion for existence of the 2-sliding mode and control boundedness must be evaluated together, therefore inequalities (2.30), (2.31) and (2.32) should be satisfied along with the additional constraint *(4.15)*. We have to derive the constants K_R, k_r and C to satisfy all these constraints by selecting appropriate values of the gains r_1 and r_2. The maximum bound on $b(t,x)$ in (4.12), i.e., K_R can be easily derived as:

$$K_R = \frac{g}{V_{min}\tau} \frac{1}{\cos^2(\phi_{max})} \tag{4.16}$$

and similarly the minimum bound k_r:

$$k_r = \frac{g}{V_{max}\tau} \frac{1}{\cos^2(\phi_{min})} \tag{4.17}$$

To find C we may plot $|a(t,x)|$ against the three variables: cross-track y, course intercept χ_E and roll angle ϕ, and then take the maximum value as C. After selection of the constants K_M, K_m and C, values of r_1 and r_2 that satisfy inequalities (2.30), (2.31), (2.32) and (4.15) can be chosen.

TABLE 4.1: Parameters for the scaled YAK-54 UAV.

#	Parameter	Value
1	α	0.8
2	β	0.008
4	τ	0.4
5	V	$28 - 38$ m/s
6	ϕ_{max}	$45°$
7	ϵ_1	0.20
8	ϵ_2	0.25

4.2.2 Selection of parameters for the scaled YAK-54

We now illustrate the design methodology by selecting parameters for the scaled YAK-54 UAV. Based on the desired performance the sliding surface parameters α and β are selected first. To quickly reduce the large track errors, the parameter α is selected as 0.8 and χ_E is constrained to be less than $90°$. For small lateral errors, parameter β is tuned to 0.008 for good performance. Values of K_R and k_r (upper and lower bounds on $b(t, x)$) mainly depend on variation in ground speed (V) and roll angle (ϕ), as shown in (4.16) and (4.17). For $28m/s \leq V \leq 38m/s$ and $0 \leq |\phi| \leq 45°$, values of K_R and k_r are computed as 2.1888 and 1.7658, respectively. Using the constants given in Table 4.1, Figure 4.4 shows values of $|a(t, x)|$ calculated for the scaled YAK-54 in the neighborhood of the sliding surface. From Figure 4.4 the upper bound of $|a(t, x)|$ (or C) is selected as 0.15. We can now choose the gains r_1 and r_2 satisfying the inequalities (2.30), (2.31) and (2.32) along with the constraint (4.15). We choose r_1 and r_2 as 35 and 10 respectively, satisfying all the above conditions. The above gains satisfy the existence and control boundedness conditions of the twisting guidance algorithm for the scaled YAK-54. The controller (4.13) is stable and provides for the appearance of 2-sliding mode, i.e., $s = \dot{s} = 0$ in finite time.
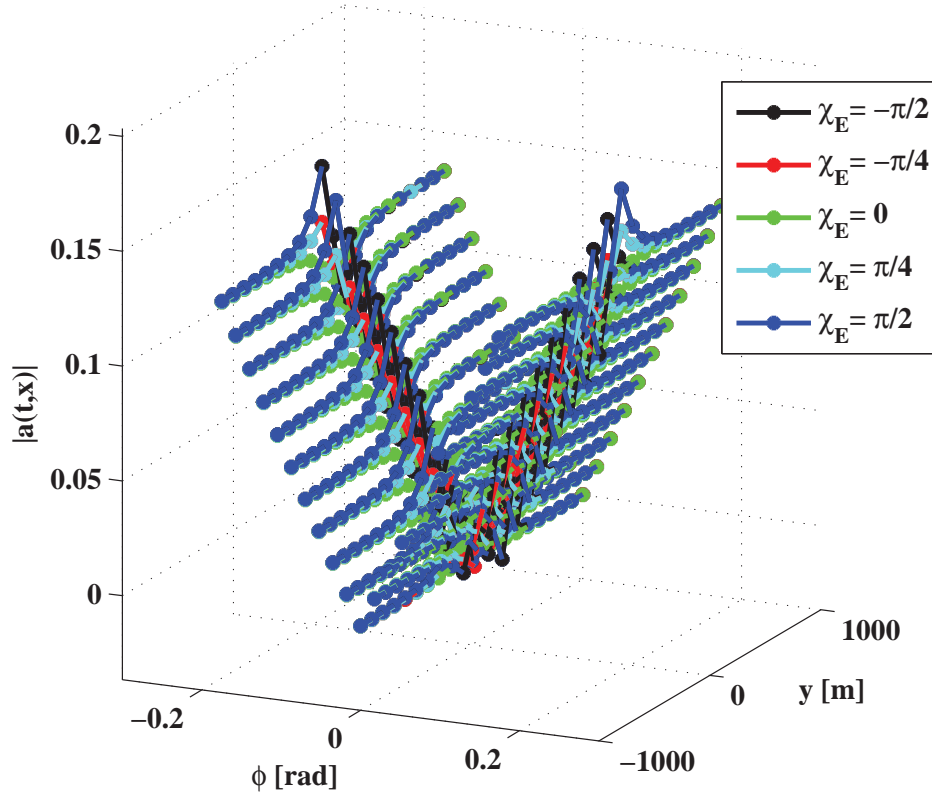
FIGURE 4.4: $|a(t,x)|$ plotted for different ϕ, y and χ_E.

4.2.3 Implementation aspects

The nonlinear guidance scheme proposed in Section 4.2 is programmed in flight control computer of Scaled YAK-54 UAV discussed in Appendix A. For the implementation of the guidance law (4.13), the *signum* function is approximated as $\text{sgn}(s) \approx \frac{s}{|s|+\epsilon}$, where ϵ is small and positive. Now ϕ_{ref} expression becomes:

$$\phi_{ref} = -r_1 \frac{\chi_E + \alpha \arctan(\beta y)}{|\chi_E + \alpha \arctan(\beta y)| + \epsilon_1} - r_2 \frac{\frac{g}{V}\tan\phi - \dot{\chi}_R + \frac{\alpha\beta V \sin\chi_E}{1+\beta^2 y^2}}{\left|\frac{g}{V}\tan\phi - \dot{\chi}_R + \frac{\alpha\beta V \sin\chi_E}{1+\beta^2 y^2}\right| + \epsilon_2}. \quad (4.18)$$

Since we are approximating the *signum* function, the surface s will never be exactly zero, but close to zero since the effective gain to the system reduces as $|s|$ decreases. Close to the origin the value of $|a(t,x)|$ reduces (Figure 4.4) and hence a high control gain is not required here, this is clear from the discussion on the real twisting algorithm in the preceding sections. For flight performance we target

$|y| \leq 10$ m and $|\chi_E| \leq 1°$, this implies $|\sigma| \leq 0.0893$ for the chosen values of α and β. Therefore we selected $|s| < 0.1$ (the boundary layer width will be 0.2 in this case). Choosing $\epsilon_1 = 0.2$ yields $\frac{s}{|s|+\epsilon} = \pm 0.3333$ for $s = \pm 0.1$, which implies that the actual gain delivered to the system at the edges of the boundary layer will be 33.33% of the chosen value of r_1. Thus for this case we can have $|s| < 0.1$ for $\epsilon_1 = 0.2$. Similarly choosing $\epsilon_2 = 0.25$ yields $\frac{\dot{s}}{|\dot{s}|+\epsilon} = \pm 0.25$ for $\dot{s} = \pm 0.1$, which implies that the actual gain delivered to the system at the edges of the boundary layer for $\dot{s}$ will be 25% the chosen value of r_2. Thus we can have $|\dot{s}| < 0.1$ for $\epsilon_2 = 0.25$.

For improved performance during circular path following, a feed-forward term is added to the guidance law (4.18). Since the controller in (4.18) provides good performance for straight paths, but following curved paths steady state error is more. Therefore an additional term is required which only assist the existing controller for circular cases. For following the paths with constant curvature, an extra bank is required by the vehicle to balance its centripetal force. So $\arctan\left(\frac{V\dot{\chi}_R}{g}\right)$ which acts as the minimum reference bank to keep the vehicle on desired curvature is added. During a straight leg $\dot{\chi}_R$ is zero and hence this term has no effect. Now the final guidance law becomes:

$$\phi_{ref} = -r_1 \frac{\chi_E + \alpha \arctan(\beta y)}{|\chi_E + \alpha \arctan(\beta y)| + \epsilon_1} - r_2 \frac{\frac{g}{V}\tan\phi - \dot{\chi}_R + \frac{\alpha\beta V \sin\chi_E}{1+\beta^2 y^2}}{\left|\frac{g}{V}\tan\phi - \dot{\chi}_R + \frac{\alpha\beta V \sin\chi_E}{1+\beta^2 y^2}\right| + \epsilon_2} + \arctan\left(\frac{V\dot{\chi}_R}{g}\right) \quad (4.19)$$

The feed forward term $\arctan\left(\frac{V\dot{\chi}_R}{g}\right)$ is independent of the feedback path (not dependent on state variables) and provides an extra benefit by assisting the feedback controller. Therefore, the stability of the system will not be affected by the feed forward term. Thus, the control law in (4.19) will still attract the trajectories towards the sliding surface and sliding mode will exist.

The benefit of sliding mode control design: Its controller does not contain any dynamical characteristics and does not require any discretization to implement it.

The expression in (4.19) can be implemented directly in the microprocessor board of flight control system of YAK-54 UAV explained in Appendix A. The states y, χ and ϕ are measurable and χ_E can be formed using $\chi_E = \chi - \chi_R$, where χ_R and $\dot{\chi}_R$ is available from mission block to the guidance scheme. This expression is instantly applied based on the current position and attitude and generates the commanded bank angle.

4.3 Experimental Results

This section describes flight results for straight and curved path following. Straight path tracking is divided into two cases: Case-1 is for small cross-track errors and Case-2 for large errors. Curved path tracking is also considered to validate the efficacy of the proposed guidance algorithm. Lastly the algorithm is tested for a complete loiter mission in which the vehicle traverses between a set of predefined way-points. Crosswinds is a major source of disturbance for the guidance problem, it is estimated that a wind of ~ 4 m/s was generally present during the flights.

4.3.1 Straight path following

4.3.1.1 Small cross track error

Figure 4.5 presents the flight results to follow a straight path A→B between the two way-points with an initial small lateral deviation of 100 m. Figure 4.5 illustrates the ground track of the UAV, the aircraft starts east of the way point A at a distance of 100 m, with a 45° course angle. In the figure, time evolution of the cross-track from the desired trajectory line segment AB is shown along with intercept course χ_E . The cross-track error is reduced to under 7 m in ~ 14 sec by the proposed algorithm. The maximum commanded roll angle is shown in Figure 4.5 and it is approximately less than 25° at ~ 1590 sec when the error is about 100 m. Performance of the controller is evident from the flight results.
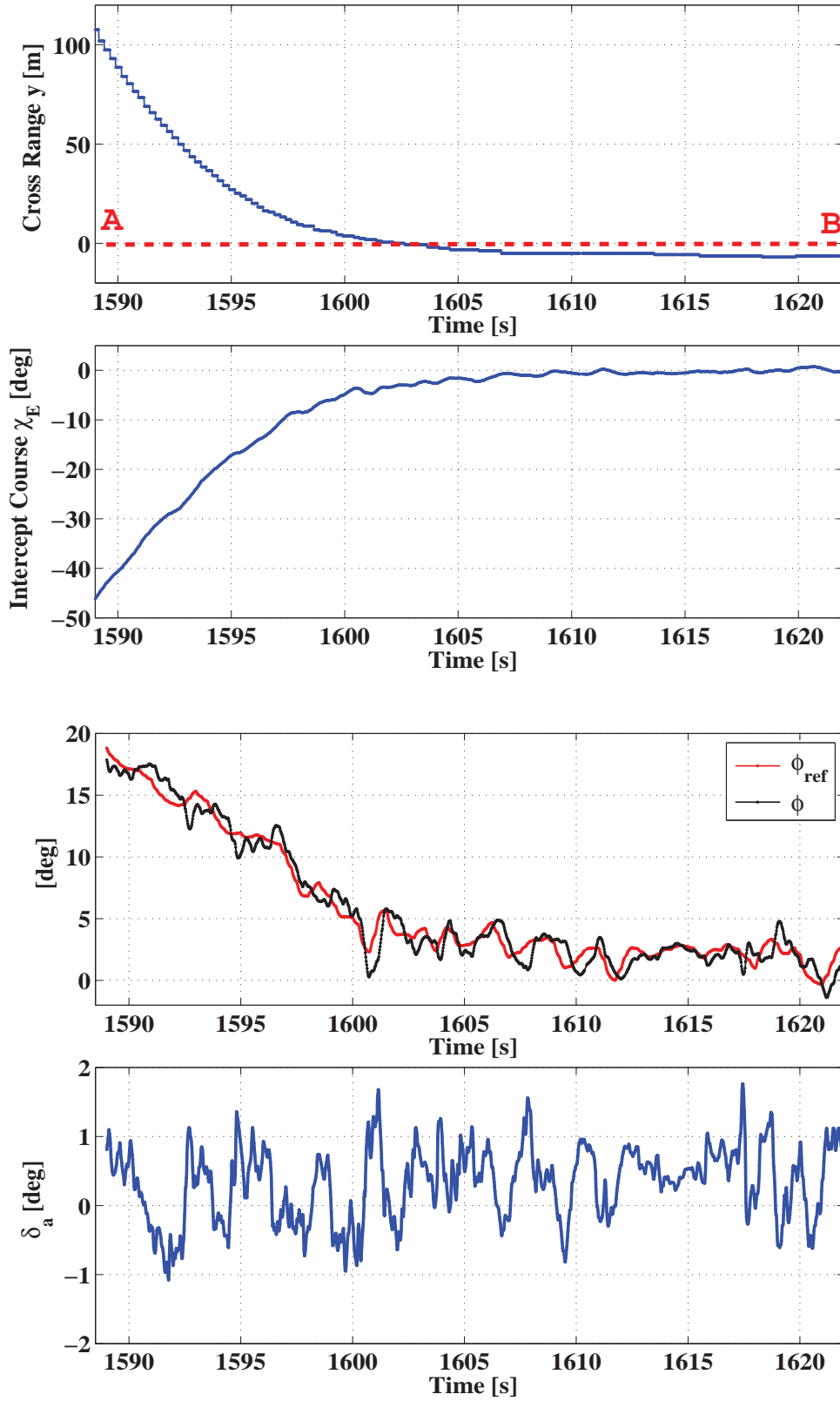
FIGURE 4.5: Cross-track error y, intercept course χ_E, roll angle ϕ, commanded roll reference ϕ_{ref} and δ_a for an initial small cross-track error for Case-1

4.3.1.2 Large cross track error

Figures 4.6−4.8 presents the flight results for case 2, the UAV is intended to follow the path A→B with an initial lateral deviation of 450 m. The time evolution of the states i.e., lateral error y and intercept course χ_E are shown in Figure 4.6, approximately 18 sec are required for the error to reduce from 450 m to under 8 m. The sliding mode real twisting controller provides appearance of a 2-sliding mode, attracting the state trajectories i.e., $s = \dot{s} = 0$ in finite time as evident from Figure 4.7. The cross-track error is reduced quickly as for the initial few seconds χ_E is large. The actual roll ϕ of the vehicle against the commanded reference roll angle ϕ_{ref} to follow the path A→B is shown in Figure 4.8. The maximum commanded roll angle is $\sim 28°$ for the first few seconds. It is evident from Figure 4.8 that the corresponding aileron actuation δ_a by the autopilot loop is well behaved and is usually less than 3°.
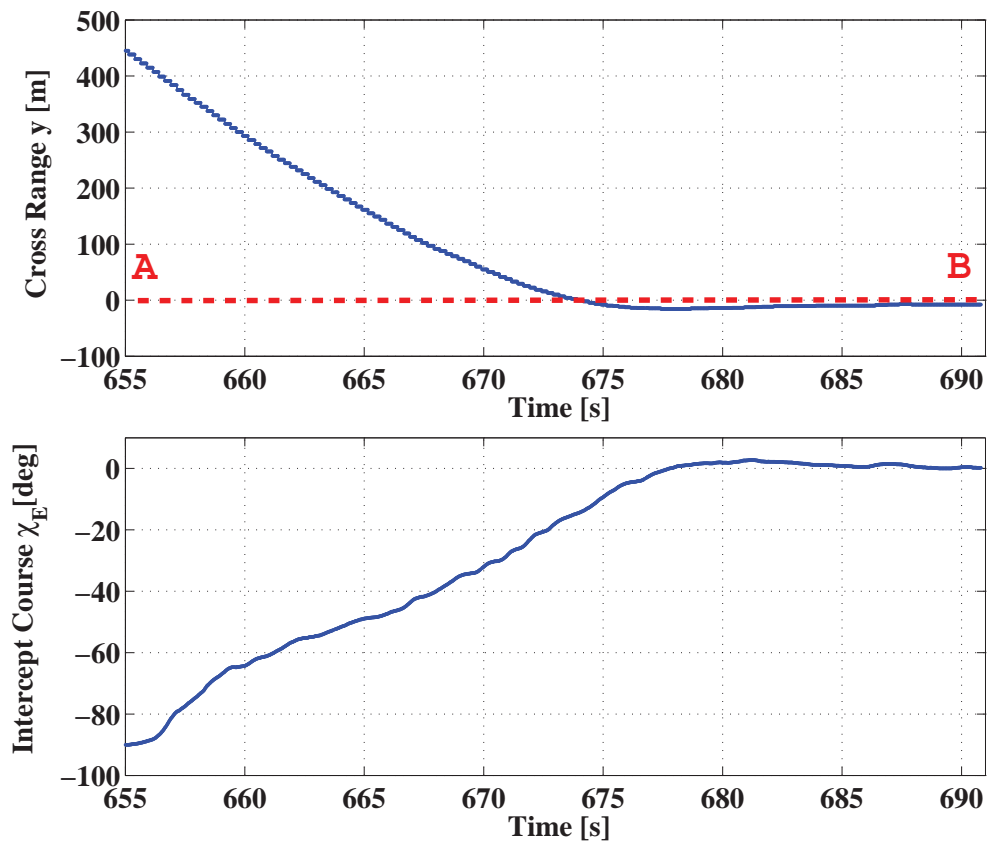
FIGURE 4.6: Large cross-track error (y and χ_E) flight results for Case-2
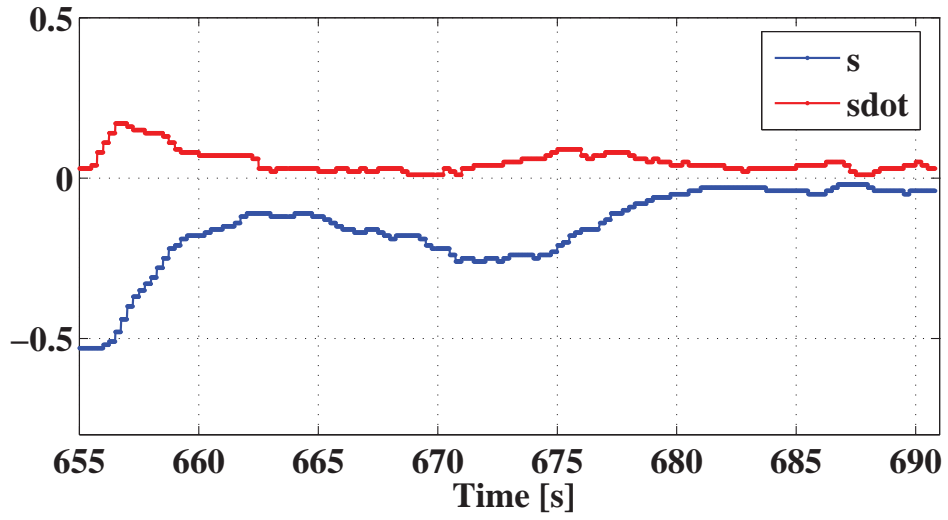
FIGURE 4.7: Flight results s and $\dot{s}$ for a large cross-track error for Case-2
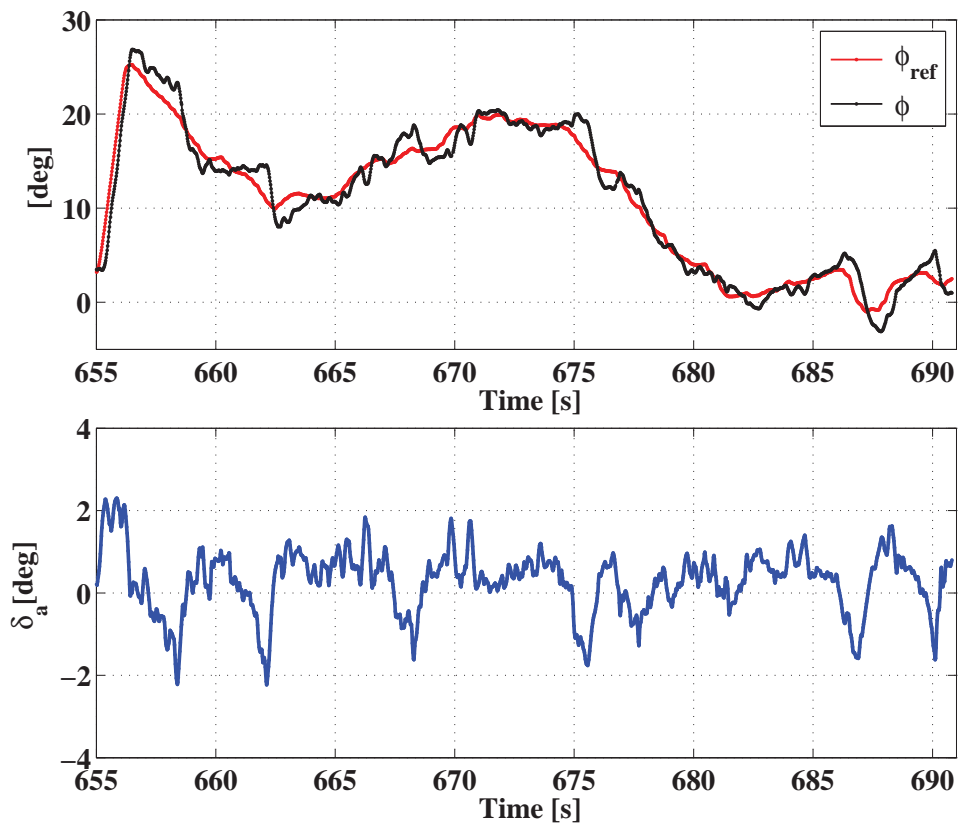
FIGURE 4.8: Roll angle ϕ, commanded ϕ_{ref} and aileron deflection δ_a for the large cross-track error for Case-2

4.3.2 Curved path following

Next the guidance scheme is tested for curved path tracking. In this case the UAV takes different circular trajectories as shown in Figure 4.9. Initially the UAV is commanded to follow a circular path of radius 700 m, then it is commanded to follow a 500 m radius circle, and lastly a 600 m circle. The reference trajectory is shown in dotted red, whereas the actual trajectory flown is shown in solid blue line (Figure 4.9).
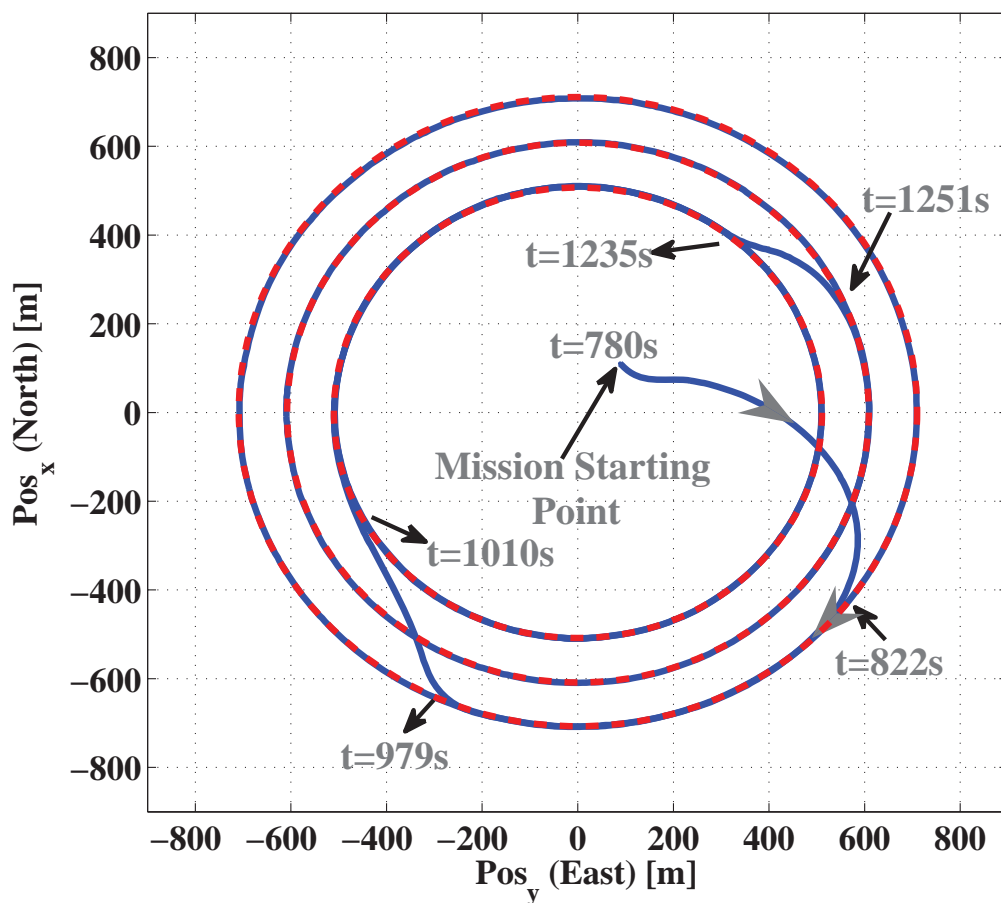
FIGURE 4.9: Flight results for Circular case (desired and actual flight paths).
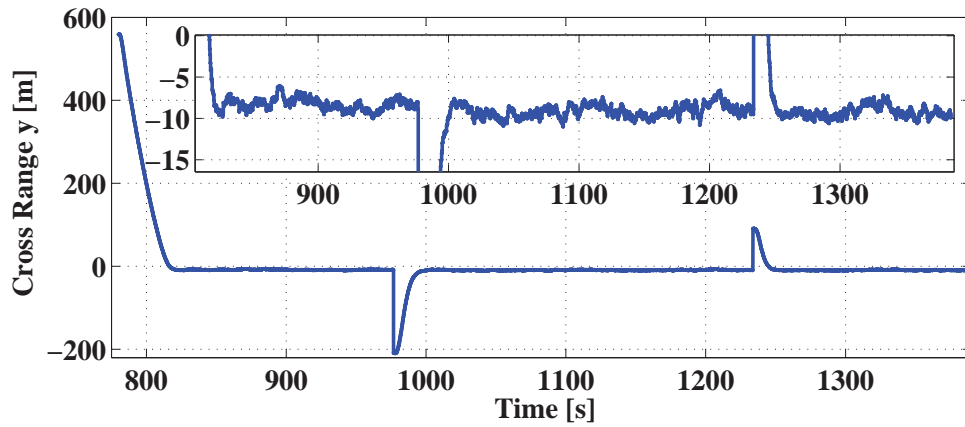
FIGURE 4.10: Flight results of Cross Range y for Circular path following.
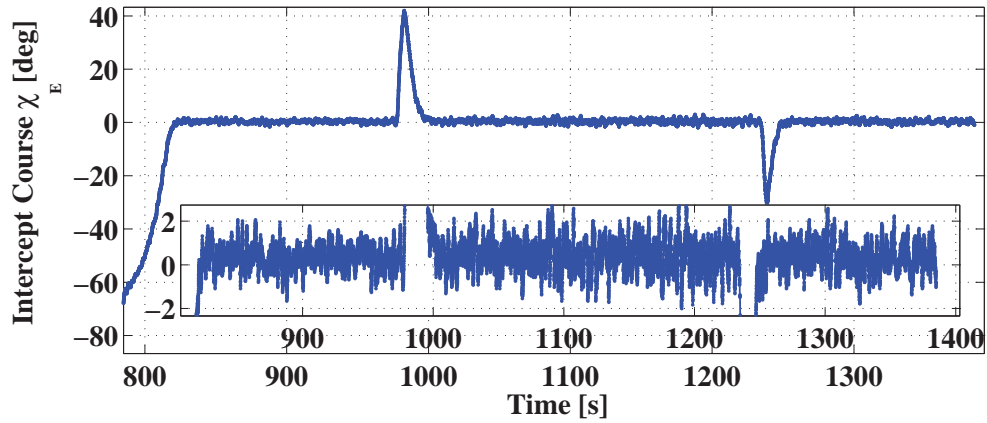
FIGURE 4.11: Flight results of Intercept Course χ_E for Circular path following.
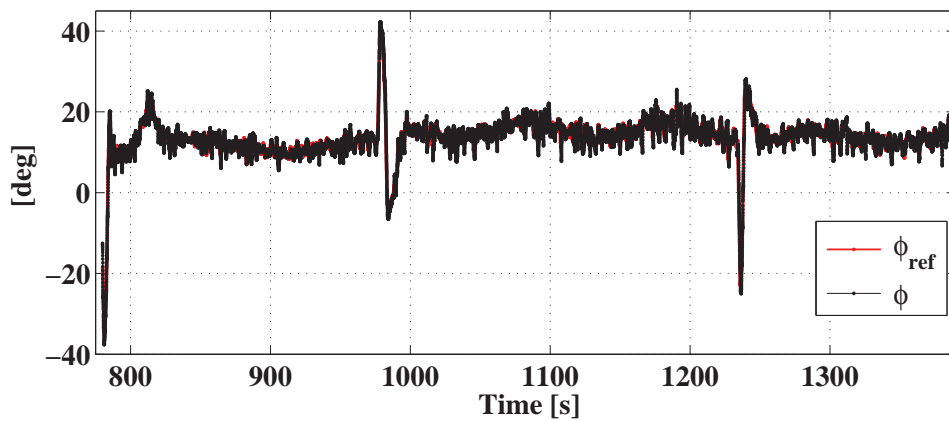
FIGURE 4.12: Flight result of ϕ, Roll Reference Command ϕ_{ref} for Circular path following.
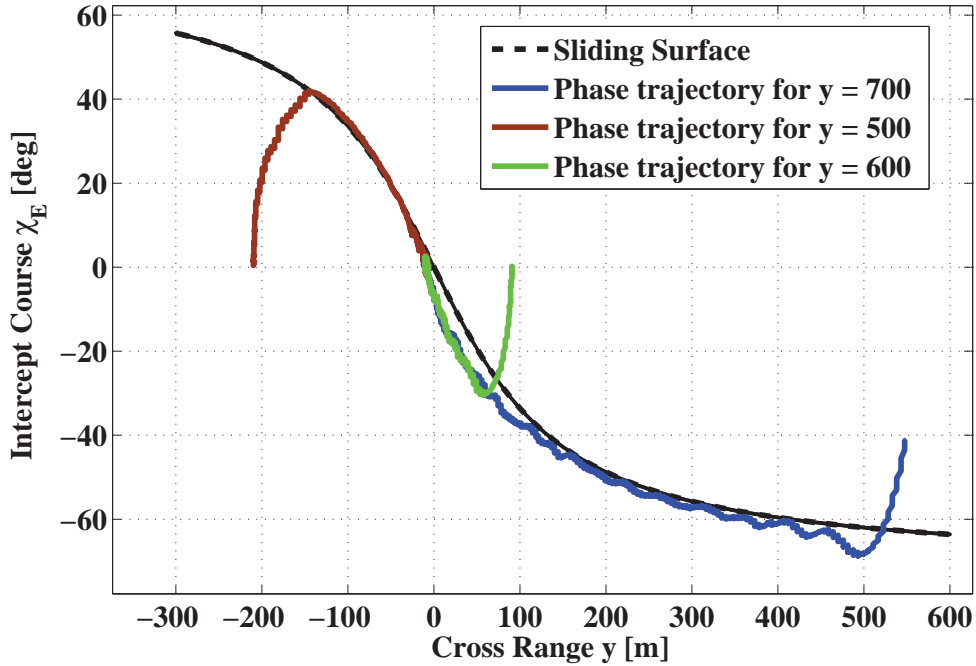
FIGURE 4.13: Phase portrait for the circular case(χ_E versus y).

Figure 4.10 shows the cross-range error versus time, the error increases at the time of switching from one circle to the other, however the guidance algorithm drives it down to less than 8 m quickly. The intercept course and the roll angles are shown in Figures 4.11 and 4.12, respectively. It is clear that the proposed nonlinear guidance strategy performs well for circular/curved path following in the presence of wind. The sliding surface along with the state trajectories is shown in Figure 4.13 for the three circles. The state trajectory gets attracted towards the sliding surface and subsequently maintains motion in the vicinity of the surface to reach the origin.

4.3.3 Loiter mission

For a loiter pattern, the flight results are shown in Figures 4.14 and 4.15. The vehicle's reference mission profile and the actual trajectory flown is shown in the Figure 4.14 The distance traveled along North is represented by Pos_x (North) while the distance traveled along north is represented by Pos_y (East). For smooth transition between the waypoints, the Waypoint switching scheme is active throughout

113
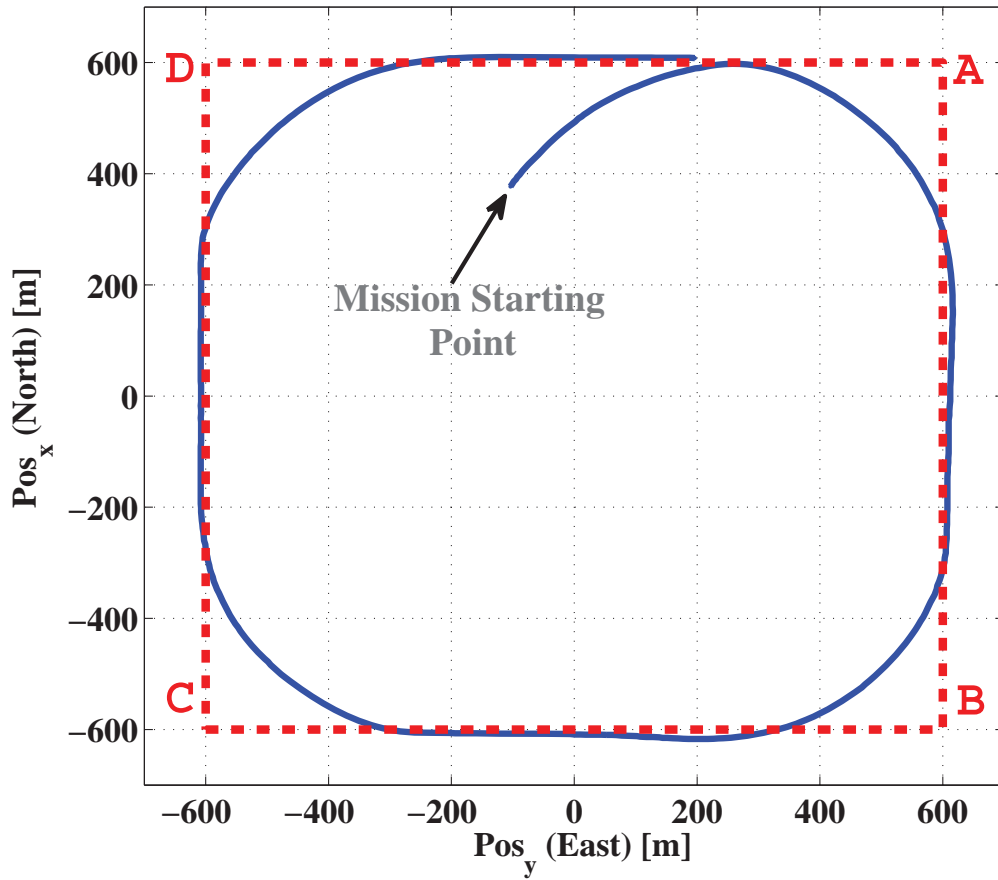
FIGURE 4.14: Loiter pattern flight results (reference profile and actual flight).

the mission. The switching algorithm issues a 'leg shift' command (explained in
2.3.2.6) and the UAV is intended to follow the next leg of the mission. In the Figure 4.15, the actual roll angle ϕ and the commanded roll angle ϕ_{ref} are shown. The algorithm generated the maximum commanded roll angle less than 30°. The proposed guidance algorithm is efficient and provides good performance for following the loiter mission
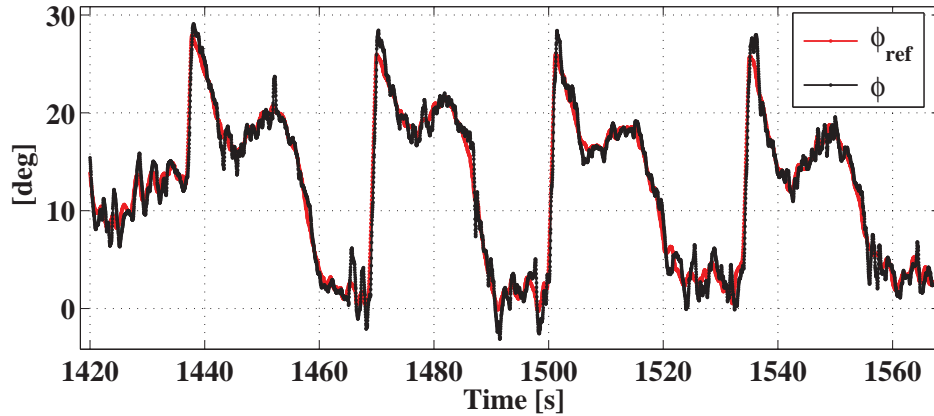
FIGURE 4.15: Flight results of Roll ϕ and Roll Reference Command ϕ_{ref} for complete Mission

4.4 Flight Results Comparison with Simulation

Computer simulations are necessary in control design process for development of any new algorithm. A number of iterative simulations are carried out before testing the controller in flight to see its performance and robustness in the presence of disturbance (like wind, gusts etc), delays and noise in sensor data, and parametric uncertainties in aerodynamic and structural coefficients of the UAV.

In this section, flight and simulation results are compared to show the efficacy of the accurate mathematical model and simulation of scaled YAK-54 UAV. Flight test data is compared with mathematical model simulated for the same initial conditions and disturbances (as in flight). The side-by-side comparison technique is used throughout this validation process. The validation procedure is conducted for lateral dynamics of two different missions. This process is helpful for examining the differences between the actual flight and simulated dynamics. The 'pilot' command when the automatic flight mode is active, stores the information of all the initial conditions. To simulate the similar response, these initial conditions are then placed into a 6-dof nonlinear mathematical model developed in MATLAB/Simulink. Based on identical inputs, side-by-side comparison can be done for simulated data and flight test data.
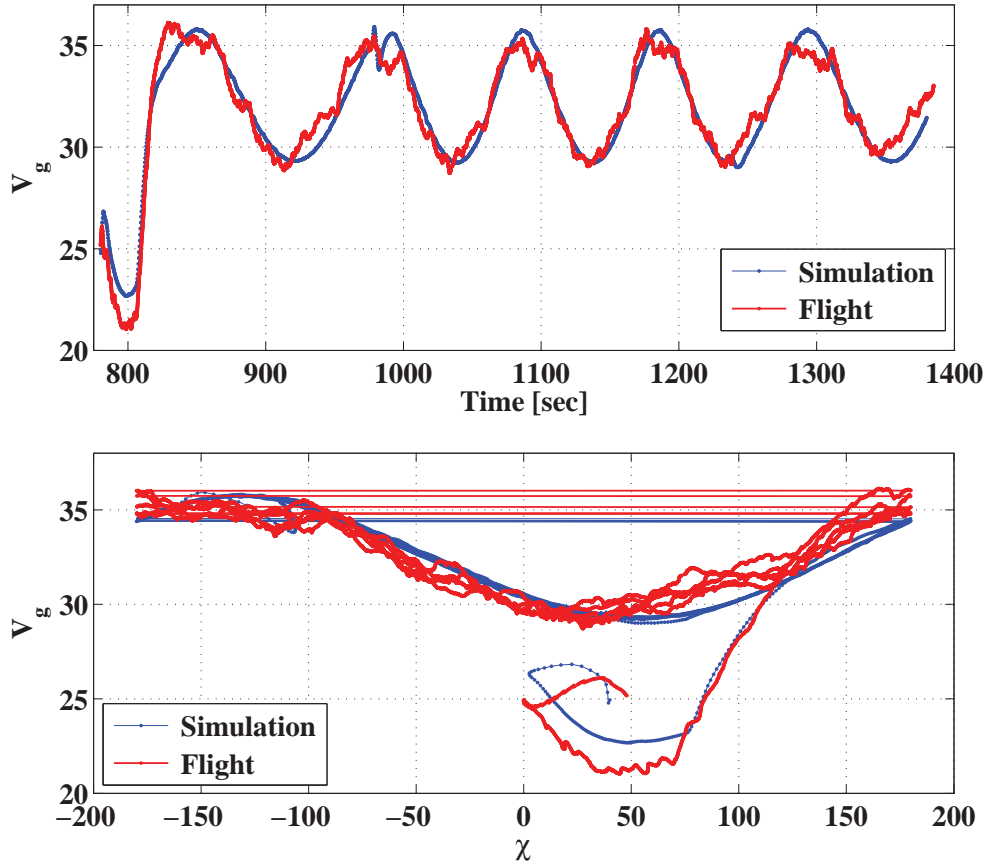
FIGURE 4.16: Flight and Simulation Result of Ground Speed V_g vs χ

As the simulation model does not have any knowledge of the wind speed on flight day and the lateral directional responses of flight are most likely to be affected by wind forces therefore a justified comparison between flight data and simulated data is only possible if wind effects are also incorporated in the model. In the simulation, first the approximates of wind speed and direction are estimated.

Speed controller maintains constant V_a either through feedback or preset open loop throttle setting. As a result, V_a is constant but ground speed V_g varies due to wind. Guidance law mainly depends upon ground speed. It is important to match the V_g of flight with simulation as it plays a significant role in implementation of ϕ_{ref} in (4.19). Comparison between the guidance commands of flight and simulation can only be made if V_g of flight matches with simulation. It is only possible if the correct magnitude and direction of wind is determined. When we plot V_g

116

vs χ plot we can have two information, firstly we can have a clear idea about the magnitude of wind i.e., for $\chi = \pm 180°$ the difference between V_g is of $8m/s$ therefore average V_g is $34m/s$ and wind of $4m/s$ is present. Secondly, we can have the idea of direction of wind i.e., *chi* corresponding to minimum V_g Figure 4.16 means the UAV was facing head wind therefore wind of $\approx 30°$ north wind was present. Figure 4.16 shows the ground velocity of UAV measured by an on-board GPS in solid red and that provided by the sensor model in simulation in solid blue. Figure 4.16 shows the comparison of flight response and simulated response for matched V_g vs χ which clearly shows that UAV in flight and UAV model in simulation are influenced by approximately the same magnitude and direction of wind.

In flight due to engine vibration, noise is present in the sensors as evident in Figure 4.19, Figure 4.20 and Figure 4.23. To incorporate the same effect in simulation the sensors are modeled. Sensor modeling addresses the problem of accurate and reliable sensing and makes a detailed analysis of the design. Noise is fused into sensor data. Gaussian (or normally-distributed) white noise is the most common noise model for analysis and simulation. It requires an iterative tuning to adjust the noise levels present in the sensors, the power spectral density of noise power induced was 1.2 Watt/Hz . Now the guidance and control schemes are excited by the similar sensor data in flight as well as in simulation.

Generally, propeller driven tractor configurations have a down wash effect on the vertical tail due to flow from the propeller that generated a side force in flight. In our case, we have not modeled this down wash effect in our simulation and as a result some side force is observed in our flights. As an approximation of this down wash effect, the flight results match with the simulation when $C_{y_0} = -0.013$ is used in simulation.

4.4.1 Curved path following

Flight result for the circular path following case are compared with the simulation results in Figure 4.17–Figure 4.21.
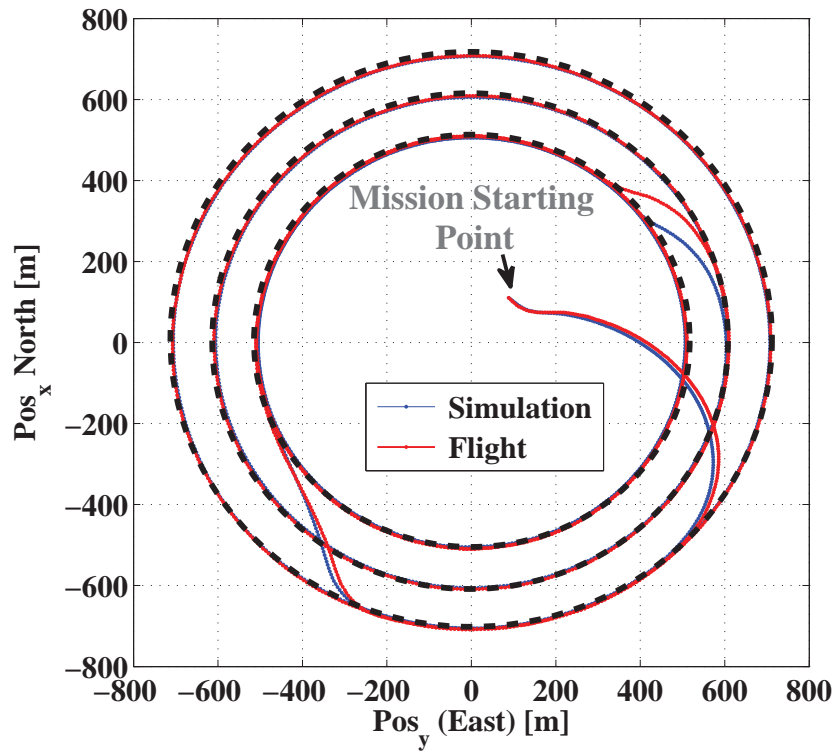
FIGURE 4.17: Flight and Simulation Result For different Cross Ranges y
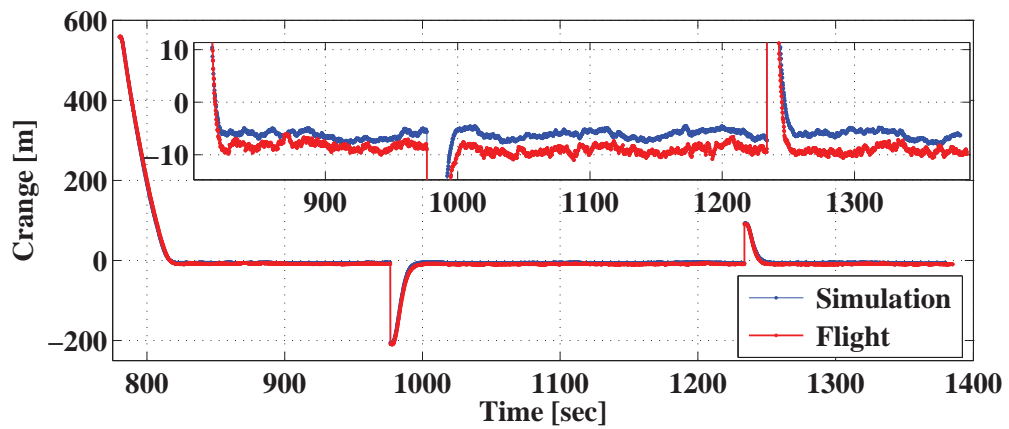
FIGURE 4.18: Flight and Simulation Result For different Cross Ranges y

Figure 4.17 shows the complete mission followed by the UAV in solid red and that simulated by the model in solid blue when commanded to follow the three circles with different radii and different initial cross errors. Figure 4.18 shows the simulation results comparison with the flight test data for reducing the cross range error.
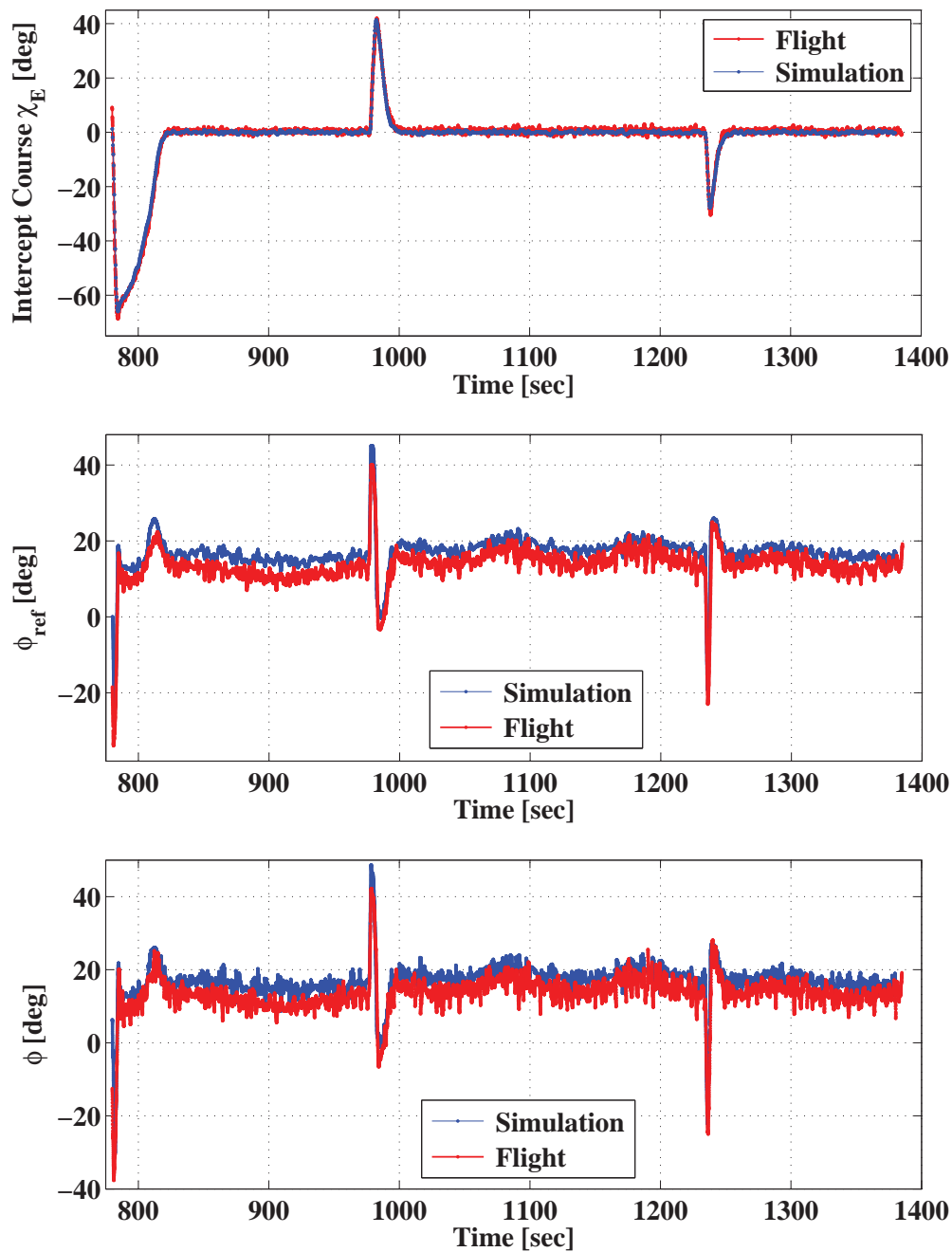
FIGURE 4.19: Flight and Simulation Result of Intercept Course χ_E, reference command ϕ_{ref} and ϕ
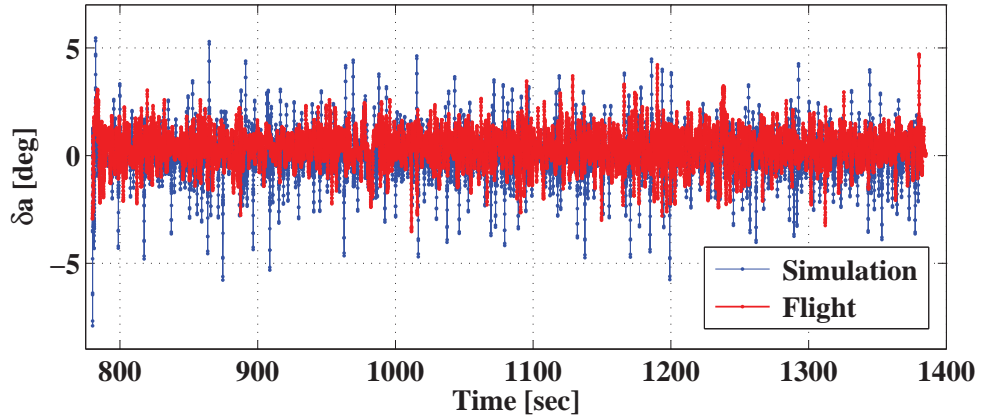
FIGURE 4.20: Flight and Simulation Result of Control actuation δ_a

Figure 4.19 shows the intercept course of the UAV in solid red and that simulated by the model in solid blue when intended to follow the three circles with different initial cross errors. The simulation results are in good agreement with the flight results. The maximum difference in y and χ_E is 4m and 3° respectively. Figure 4.19 also shows the reference command generated by the outer loop in simulation and the one generated in flight along with the corresponding control actuation commands shown in Figure 4.20. The actual bank angle observed by the UAV in flight is given in solid red and the bank observed by the UAV model is shown in solid blue in Figure 4.19. Figure 4.19 and Figure 4.20 show that χ_E, ϕ_{ref}, ϕ and δ_a dynamics simulation results closely match with the flight test data.
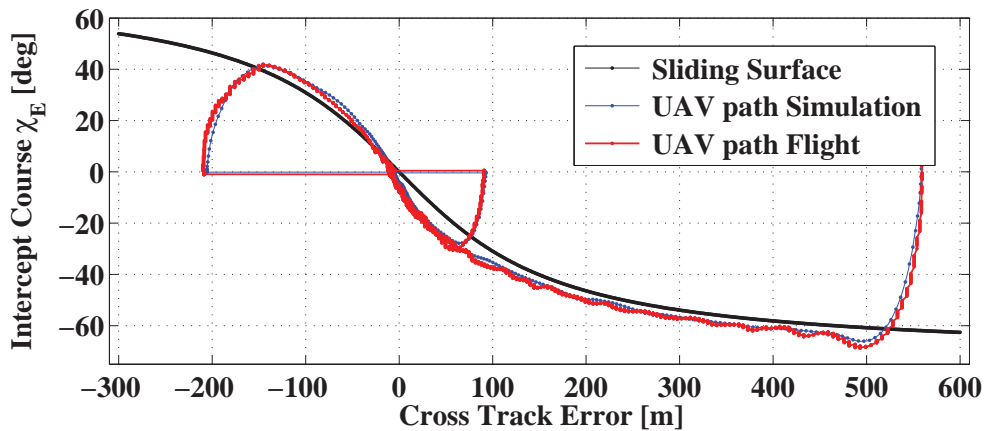
FIGURE 4.21: Flight and Simulation Result of phase portrait of manifold s

Figure 4.21 shows the phase portrait comparison of flight and simulated trajectories plotted along side with the manifold. The state trajectories reach to and then slide along the sliding manifold quite closely.

4.4.2 Large cross track error

In Figure 4.22–Figure 4.23, comparison is shown for straight path following case with large initial cross error. The comparison is elaborated in Figure 4.22, the state variables i.e., y and χ_E for both flight and simulation are plotted versus time. The difference of flight and simulation is negligible. The simulation results are in good agreement with the flight results in this case also, the maximum difference in y and χ_E is 3m and 4° respectively.
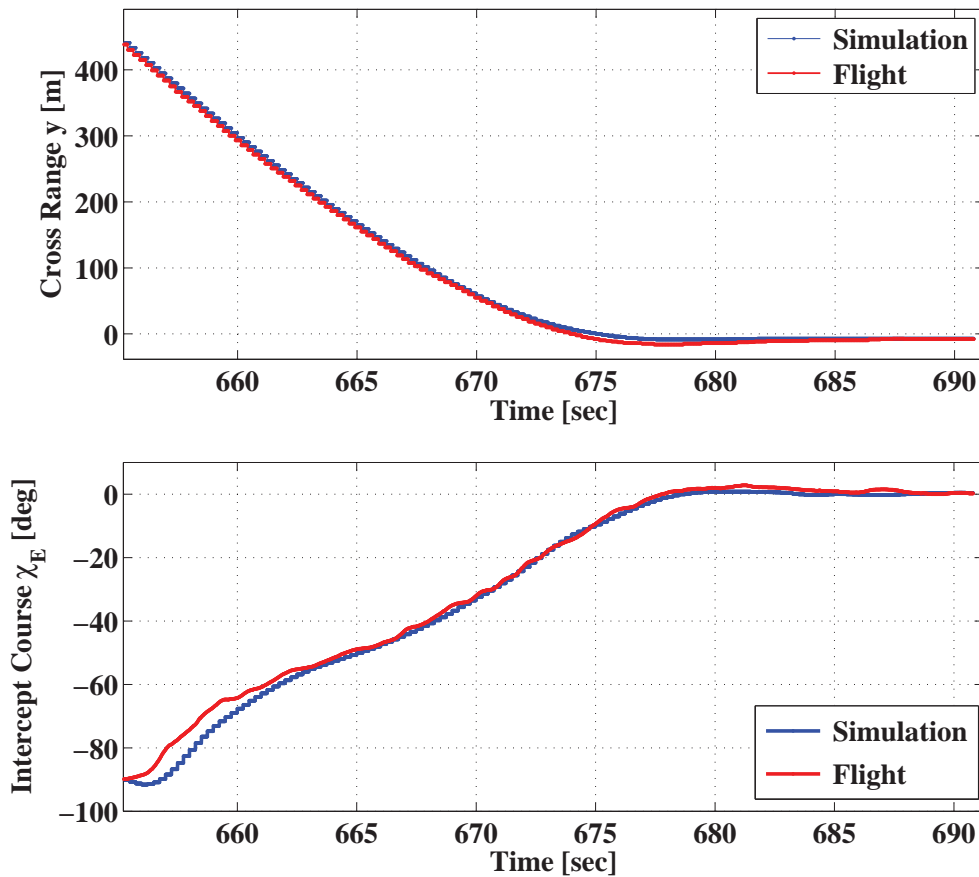
FIGURE 4.22: Flight And Simulated data for Large Cross Range y, Intercept Course χ_E

The comparison between the guidance logic generated signal ϕ_{ref}, the actual roll angle ϕ in flight and simulation is shown in Figure 4.23 with respective control actuation δ_a. The matching in these variables is good, however minor differences can be observed.
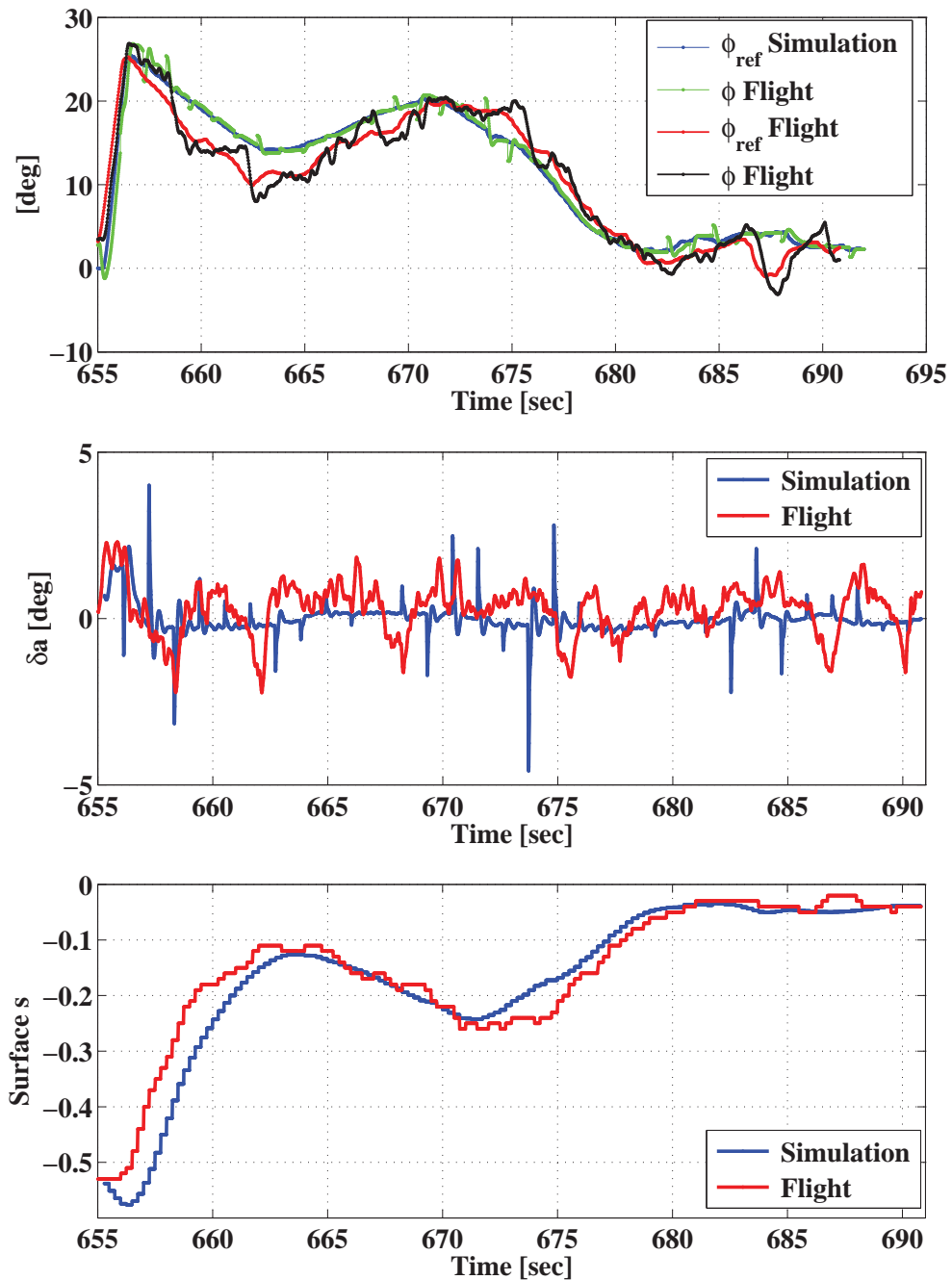
FIGURE 4.23: Flight And Simulated data for ϕ_{ref}, ϕ, control actuation δ_a surface s

Another important parameter is the sliding manifold in SMC based guidance schemes, its comparison versus time is shown in Figure 4.23. Good matching of this variable can be observed and no significant difference in magnitude and trend is observed. Conclusively, simulation results are in good agreement with the flight results.

4.5 Conclusion

A robust nonlinear guidance system for UAVs is proposed. HOSM control theory based on a nonlinear sliding surface is used to address the guidance problem. The nonlinear surface ensures good performance for small as well as large track errors. Inner loop dynamics from ϕ_{ref} to ϕ is considered during derivation of the guidance law, resulting in a relative degree two problem. Selection of gains r_1 and r_2 is discussed which guarantees stability and existence of a 2-sliding mode, and ensures boundedness of the control signal. Flight performance of the algorithm is investigated for different cases of straight and curved path tracking. It is seen that the algorithm provides very good performance in the presence of wind, generating smooth and graceful maneuvers, driving the cross-track error to within a few meters. These results are further compared with the 6-DOF nonlinear simulation model to verify and validate the complete cycle of a control system design. The strategy explained in this chapter is about the indirect control where the angular commands are used to generate lateral acceleration. However, using the direct control i.e., rate command control the speed of response can be improved (e.g., using Partially Integrated guidance and control structure).

Chapter 5

PARTIALLY INTEGRATED GUIDANCE AND CONTROL (PIGC) SCHEME

As discussed in Chapter 4, the control loop dynamics are incorporated into the guidance scheme design requiring the knowledge of dynamical characteristics in both the loops. A guidance algorithm is designed here exploiting the PIGC framework. The novelty is the interconnection of two sliding surfaces augmented in series to achieve a quick response with an optimized guidance and control structure. The guidance algorithm detects the lateral track error based on navigational data and the correction maneuver is performed. In the outer loop, as the relative degree of the problem is 2, the guidance command tracking is executed through a nonlinear sliding manifold using second order sliding mode (SOSM) real twisting algorithm. The velocity vector is forced to align with the direction of the desired track, while ensuring turn coordination and correcting cross-track error. The guidance commands are then tracked by the UAV auto pilot, i.e., the inner control loop. Enforcement of the desired angle correction generates the necessary control surface deflections required to turn the UAV to the desired course. The inner loop employs a linear sliding manifold and the relative degree is 1 therefore SOSM super twisting algorithm (STA) is used.

The organization of the chapter is as follows: Section 5.1 explains the PIGC guidance and control scheme and formulates the guidance and control problem for waypoint tracking. In section 5.2, kinematic state space model along with bank error dynamics is discussed. Section 5.2 also explains the PIGC structure and presents guidance law design based on the SOSM algorithm along with autopilot for the control loop. Section 5.3 addresses the existence of 2-sliding mode for guidance as well as control framework, boundedness of control signals to validate the design methodology. Implementation aspects are also discussed along with

flight results of the designed guidance and control scheme in section 5.3. Section 5.4 summarizes the conclusion.

5.1 Guidance and Control Strategy

In principle, the integrated guidance and control (IGC) design framework strive to design guidance and control in a single loop and hence minimizing the overall time lag. It also gives the advantage of a unified scheme rather than optimizing a set of subsystems independently and then combining them in limited sense. The major disadvantage of IGC scheme is that it does not address explicitly the inherent time scale separation that exists in aerial vehicles [98]. This technique is more complicated due to the coupling between slower guidance and faster control variable and clear/detailed insight of the variables is not available. These schemes are over ambitious to directly generate the control surface deflections and ignore the fundamental feature of divide and conquer. Due to the unified framework tuning of the control law turns out to be extremely complicated and scenario specific, which is undesirable [98]. It is required that a good algorithm should clearly predict the body angular commands to generate control surface deflections in order to achieve good tracking performance. This is the essence of conventional two loop guidance and control philosophy. On the contrary, in the conventional two loop design the settling time of the response of different loops will not be able to match the stringent window of tight path following [17]. This affects the system performance adversely and hence UAV will fail to provide the desired performance. In fact, the proposed partial IGC (PIGC) approach [19, 20, 98] can be interpreted as an attempt to combine the best of both philosophies. Also, note that the classical guidance and control formulation is eliminated here i.e., generation of desired angular commands but the idea of two loops is retained, and a very important advantage of IGC, namely, the minimization of the overall settling time is secured by the generation of body rates.

5.1.1 Problem formulation

In this work, the problem is addressed in the SOSM framework [6, 85] with the PIGC technique [20]. The new two-loop PIGC structure proposed in this chapter is implemented using the timescale-separated nonlinear manifolds. An asymptotic SOSM algorithm [85] is used for the PIGC system, and two dynamical sliding surfaces are selected. For the guidance problem, the nonlinear sliding surface attracts the kinematic variables in finite time using the SOSM real twisting algorithm. For the control problem the super twisting autopilot based on a linear sliding surface is designed. The PIGC idea developed in this work achieves suitable closed-loop waypoint tracking using the input signal to the actuator as the control variable. The control problem of employing the actuators to achieve good performance and stability thus becomes a non-linear control problem. Here the problem is transformed into an output regulation problem in which the UAV dynamics and lateral kinematics are integrated into one combined state space. In addition, the boundedness of coordinated turn is ensured in the outer loop by forcing ϕ_E to zero.

The SOSM based guidance and control system is divided into two sequential sub systems working together to achieve the task. Guidance is responsible for keeping the lateral track error y small despite disturbances, and also to keep $\chi_E \approx 0$ when $y \approx 0$, by generating smooth and bounded ϕ_E. The control task is to enforce tracking of the commanded signal ϕ_E in real time by generating smooth aileron deflections δ_a to turn the UAV towards the desired course despite model uncertainties. If a lateral displacement is observed, i.e., y is not in the vicinity of zero, the guidance and control system will force the vehicle back on track by manipulating χ_E through banking. For very large lateral errors, the good helmsman criterion in literature [12, 99] is observed, i.e., a constant χ_E $(\leq \frac{\pi}{2})$ is desired and χ_E is later adjusted accordingly when the track error becomes small. This criterion is enforced in the guidance loop through a nonlinear sliding surface. SOSM based guidance must guarantee boundedness of ϕ_E, and SOSM based control must ensure boundedness of δ_a for the entire flight envelope while maintaining stability

126

and performance during flight.

Block diagram representation of the overall guidance and control system is shown in Figure 5.1. The PIGC framework essentially considered the two loop strategy while keeping in account the inherent separation of slower and faster dynamics of these inner-outer loops as well. The outer loop forms the slower dynamical loop, generating the reference commands for tracking in the inner control (fast dynamics) loop. In PIGC, the outer loop generally generates body angular rate commands for the control loop. This is different from the *traditional* or *conventional* schemes where roll angle is commanded instead of roll rate. Basically, the change in roll angle divided by time is the roll rate. But as the time is constant therefore the change in roll angle multiplied by some constant can be considered as roll rate. In PIGC scheme Figure 5.1, cross track error y, intercept course χ_E and roll angle ϕ forms the slow dynamical outer loop and current role rate p and commanded roll rate p_d forms the fast dynamical inner loop. Here in this chapter we design the outer guidance loop to generate command signals in terms of the roll error ϕ_E which gives the change required in roll angle at every time step. The feedback measurement is the body roll rate p. The objective of the inner control loop is to keep the sliding surface $s_a = C_s \phi_E + p$ equal to zero (section 5.2.2). In other words the inner loop maintains $p = -C_s \phi_E$, hence $-C_s \phi_E$ serves as the reference generated by the outer loop. Commanded body rate $\approx \phi_E$ is tracked by the inner control loop generating the corresponding control surface deflections δ_a for the vehicle.

5.2   Guidance and Control Law Design

To compensate for autopilot constraints, closed-loop dynamics from ϕ_{ref} to ϕ is approximated by a first order filter of the form (4.2) explained in chapter 4 section 4.1 and is incorporated into the guidance system. The third state equation takes the form

$$\dot{\phi} = \frac{1}{\tau} \phi_E \tag{5.1}$$

Current position (y), Course angle (χ) and Roll angle (ϕ)
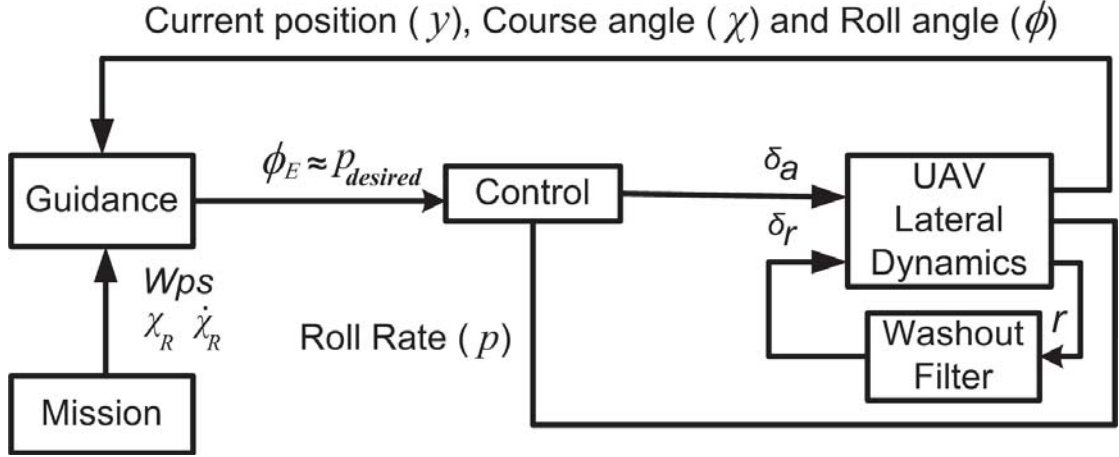
FIGURE 5.1: Block Diagram of PIGC Guidance and Control Methodology

where $\phi_E = \phi_{ref} - \phi$. In state space form we can write the state equations as

$$
\begin{bmatrix} \dot{y} \\ \dot{\chi}_E \\ \dot{\phi} \end{bmatrix} = \begin{bmatrix} V \sin \chi_E \\ \frac{g}{V} \tan \phi - \dot{\chi}_R \\ 0 \end{bmatrix} + \begin{bmatrix} 0 \\ 0 \\ \frac{1}{\tau} \end{bmatrix} \phi_E \qquad (5.2)
$$

χ_E, y and ϕ are the state variables, and ϕ_E is the control signal.

Mission information and feedback from sensors measuring instantaneous position y, course angle χ and roll angle ϕ serve as inputs to the guidance algorithm. Guidance commands are tracked by the inner loop super twisting controller which generates necessary control surface deflections. Application of SOSM methodology is suitable due to its inherent robustness to disturbances and uncertainties [89].

5.2.1 Outer guidance loop RTA design

Nonlinear SMC used in PIGC framework has several advantages, like asymptotic stability of the tracking error, ease of implementation and simplicity of the control structure. One advantage of the real twisting technique used for the outer guidance loop is that it is computationally inexpensive and does not need iterative solutions. For good performance in case of both small and large track errors, and to keep

the magnitude of χ_E less than $\frac{\pi}{2}$, a nonlinear sliding surface was proposed in [11]:

$$s = \chi_E + \alpha \arctan(\beta y) = 0, \tag{5.3}$$

where $\alpha, \beta \in \Re$, and the sliding surface stability requires $\alpha, \beta > 0$. Here we have used the same sliding surface.

$$\dot{s} = \dot{\chi}_E + \frac{\alpha\beta}{1 + \beta^2 y^2}\dot{y} \tag{5.4}$$

Along the system state derivatives in (5.2):

$$\dot{s} = \frac{g}{V}\tan\phi - \dot{\chi}_R + \frac{\alpha\beta}{1 + \beta^2 y^2}(V\sin\chi_E) \tag{5.5}$$

For the control input i.e., ϕ_E to appear and to render in the form of (2.27), differentiating $\dot{s}$ we have

$$
\begin{aligned}
\ddot{s} =& \frac{g\sec^2\phi}{V}\dot{\phi} - \ddot{\chi}_R + \frac{V\alpha\beta\cos\chi_E}{(1 + \beta^2 y^2)^2}\dot{\chi}_E \\
&+ \frac{V\alpha\beta^3 y^2\cos\chi_E}{(1 + \beta^2 y^2)^2}\dot{\chi}_E - \frac{2V\alpha\beta^3 y\sin\chi_E}{(1 + \beta^2 y^2)^2}\dot{y}
\end{aligned}
\tag{5.6}
$$

Normally, the straight or circular arcs of fix radius are followed therefore $\ddot{\chi}_R = 0$, we have

$$
\begin{aligned}
\ddot{s} =& \left(\frac{g\alpha\beta\tan\phi\cos\chi_E}{(1 + \beta^2 y^2)} - \frac{2V^2\alpha\beta^3 y\sin^2\chi_E}{(1 + \beta^2 y^2)^2} \right. \\
&\left. - \frac{V^2\alpha\beta\cos\chi_E}{R(1 + \beta^2 y^2)} \right) + \left(\frac{g\sec^2\phi}{V\tau} \right)\phi_E
\end{aligned}
\tag{5.7}
$$

Since ϕ_E is the control input for the outer guidance loop, therefore from comparison of $\ddot{s}$ in (5.7) with (2.27), we can write:

$$a(t,x) = \frac{g\alpha\beta\tan\phi\cos\chi_E}{(1 + \beta^2 y^2)} - \frac{V^2\alpha\beta\cos\chi_E}{R(1 + \beta^2 y^2)} - \frac{2V^2\alpha\beta^3 y\sin^2\chi_E}{(1 + \beta^2 y^2)^2} \tag{5.8}$$

$$b(t,x) = \frac{g\sec^2\phi}{V\tau} \tag{5.9}$$

129

The guidance signal ϕ_E will comprise of two terms, first is the equivalent contin-uous control $\phi_{E_{eq}}$ and second is the discontinuous control $\phi_{E_{TA}}$. For $\phi_{E_{eq}}$ we put $\ddot{s} = 0$ and derive the equivalent control:

$$\phi_{E_{eq}} = -\frac{V\tau\alpha\beta \tan\phi \cos\chi_E}{(1+\beta^2 y^2)\sec^2\phi} + \frac{V^3\tau\alpha\beta \cos\chi_E}{R(1+\beta^2 y^2)g\sec^2\phi} + \frac{2V^3\tau\alpha\beta^3 y \sin^2\chi_E}{(1+\beta^2 y^2)^2 g\sec^2\phi} \quad (5.10)$$

For the discontinuous term the expression for $\phi_{E_{TA}}$ using the control law in (2.29) with s as in (5.3) and $\dot{s}$ as in (5.4) becomes:

$$\phi_{E_{TA}} = -r_1 \operatorname{sgn}(\chi_E + \alpha \arctan(\beta y)) - r_2 \operatorname{sgn}\left(\frac{g}{V}\tan\phi + \frac{\alpha\beta V \sin\chi_E}{1+\beta^2 y^2}\right) \quad (5.11)$$

Now since $\phi_E = \phi_{E_{eq}} + \phi_{E_{TA}}$, we have:

$$\begin{aligned}
\phi_E = &-\frac{V\tau\alpha\beta \tan\phi \cos\chi_E}{(1+\beta^2 y^2)\sec^2\phi} + \frac{V^3\tau\alpha\beta \cos\chi_E}{R(1+\beta^2 y^2)g\sec^2\phi} \\
&+ \frac{2V^3\tau\alpha\beta^3 y \sin^2\chi_E}{(1+\beta^2 y^2)^2 g\sec^2\phi} - r_1 \operatorname{sgn}(\chi_E + \alpha \arctan(\beta y)) \\
&- r_2 \operatorname{sgn}\left(\frac{g}{V}\tan\phi + \frac{\alpha\beta V \sin\chi_E}{1+\beta^2 y^2}\right)
\end{aligned} \quad (5.12)$$

Circular Case: The convergence acceleration of the twisting algorithm is improved by adding a proportional term [100]. For good performance during circular path following, a term $K_{circ}\dot{\chi}_R s$ is added to the guidance law (5.12). This term $K_{circ}\dot{\chi}_R s$ caters for the lateral acceleration required during a steady turn and provides strong reachability for circular cases. Using the proportional term $K_{circ}\dot{\chi}_R s$, the states in (5.2) are forced to approach the switching manifold s faster when s is large. During straight legs $\dot{\chi}_R$ is zero and hence this term has no effect. Now the final

guidance law becomes:

$$
\begin{aligned}
\phi_E = & -\frac{V\tau\alpha\beta\tan\phi\cos\chi_E}{(1+\beta^2 y^2)\sec^2\phi} + \frac{V^3\tau\alpha\beta\cos\chi_E}{R(1+\beta^2 y^2)g\sec^2\phi} \\
& + \frac{2V^3\tau\alpha\beta^3 y\sin^2\chi_E}{(1+\beta^2 y^2)^2 g\sec^2\phi} - r_1\operatorname{sgn}(\chi_E + \alpha\arctan(\beta y)) \\
& - r_2\operatorname{sgn}\left(\frac{g}{V}\tan\phi + \frac{\alpha\beta V\sin\chi_E}{1+\beta^2 y^2}\right) \\
& - K_{circ}\dot{\chi}_R(\chi_E + \alpha\arctan(\beta y))
\end{aligned}
\qquad (5.13)
$$

In Section 5.2.1.1 we discuss the details about the selection criteria for sliding surface parameters α and β along-with the existence of 2-sliding mode with the selection of r_1 and r_2, satisfying conditions (2.30), (2.31) and (2.32), along with boundedness of ϕ.

5.2.1.1 Existence of 2-sliding mode and parameter selection

For the case study of the YAK-54 the expressions in (2.30), (2.31) and (2.32) prove the existence of a 2-sliding mode system and stability of the Real Twisting Algorithm [85]. For K_R i.e., the maximum bound on (5.9), we have:

$$
K_R = \frac{g}{V_{min}\tau}\frac{1}{\cos^2(\phi_{max})}
\qquad (5.14)
$$

For k_r i.e., the minimum bound on (5.9):

$$
k_r = \frac{g}{V_{max}\tau}\frac{1}{\cos^2(\phi_{min})}
\qquad (5.15)
$$

Based on the required performance, the parameters α and β of the sliding manifold are selected first. For the rapid convergence of large cross-track errors, parameter α is tuned to 0.95, while constraining χ_E to be less than 90°. To achieve good performance, the value of β is selected as 0.014 for small track errors. Figure 5.2 shows values of $|a(t,x)|$ calculated for the scaled YAK-54. From Figure 5.2 the upper bound of $|a(t,x)|$ (or C) is selected as 0.16. We choose ϕ_{max}=45° for our application. Computed values of K_R and k_r (upper and lower bounds on $b(t,x)$) are

0.9335 and 0.7568, respectively. We can now choose the gains r_1 and r_2 satisfying the inequalities (2.30), (2.31) and (2.32). Using iterative simulation tuning we choose r_1 and r_2 as 26 and 16 respectively, these satisfy all the above conditions and hence a 2-sliding mode will exist attracting the trajectories in finite time towards the equilibrium point.

Stability of ϕ_E doesn't guarantee the boundedness of ϕ which also needs to be ensured. Using the relation $\phi_E = \phi_r - \phi$, we can devise a logic to bound ϕ: if $|\phi| \geq \phi_{max}$ then ϕ_E is forced to zero. In this case the UAV will keep turning towards the desired path with $\phi \approx \phi_{max}$, and try to minimize the cross track y and intercept course χ_E as quickly as possible. The dynamics of the system will be driven towards the sliding manifold s in (5.3). Whenever a new ϕ_E is generated with a sense to reduce the magnitude of ϕ away from ϕ_{max}, the same will be passed on to the inner control loop and the guidance loop will become active again.

5.2.2   Inner control loop STA design

The inner loop generates the necessary control surface deflections to track the outer loop guidance commands. Design of SOSM is performed to track the desired angle via a linear switching manifold with the following expression:

$$s_a = C_s \phi_E + p \tag{5.16}$$

where the constants $C_s \in \Re$, $C_s > 0$ is required for a stable manifold [6] and p is the roll rate. The inner loop takes the roll angle error as an input and generates the necessary aileron deflections required to reduce the error to zero; this results in guidance of the vehicle to the desired ground track. In [44] the roll channel is controlled by defining a similar manifold employing SOSM control combined with HOSM differentiator. On the contrary instead of estimating, we calculate the sliding data based on sensor information. Taking the time derivative of (5.16)

$$\dot{s}_a = C_s \dot{\phi}_E + \dot{p} \tag{5.17}$$
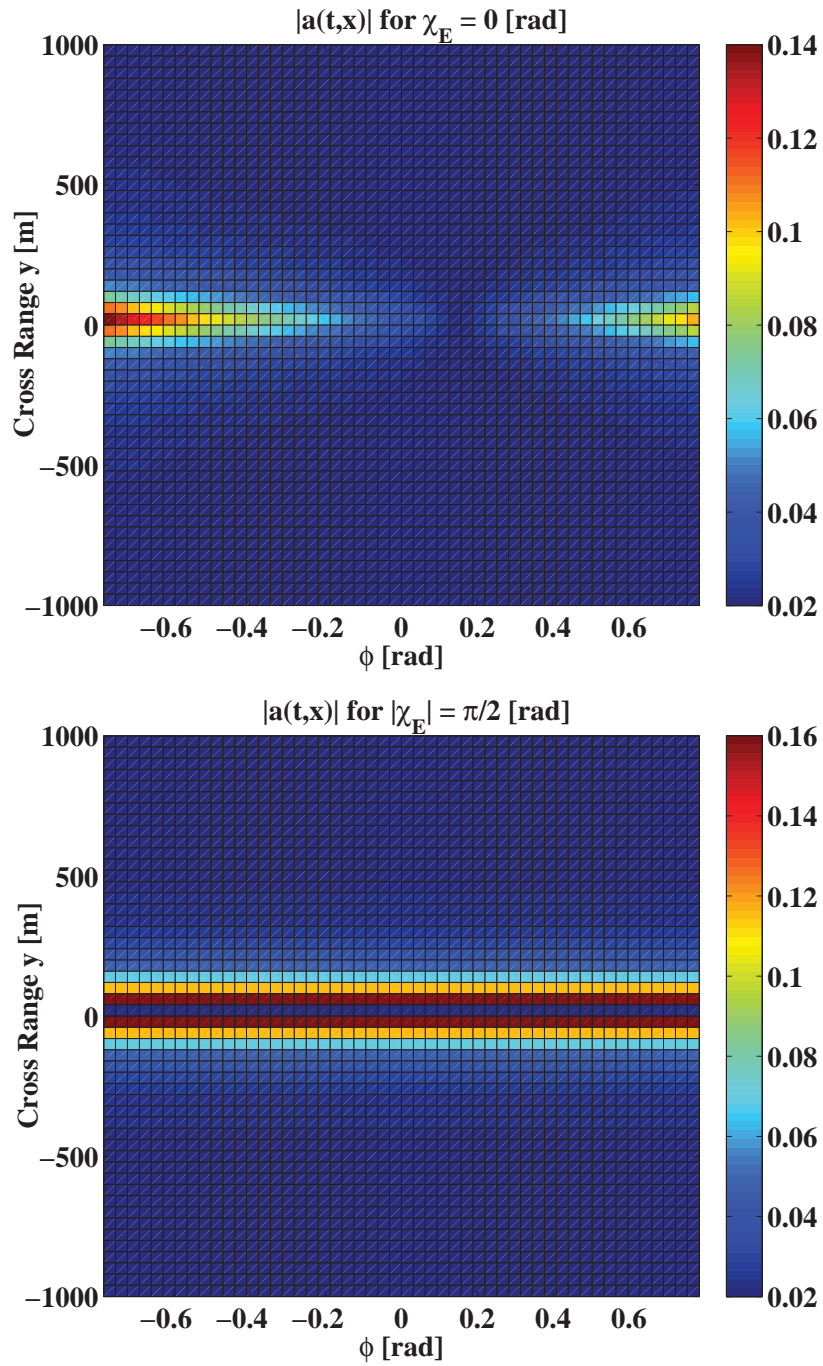
FIGURE 5.2: Upper bound on $|a(t, x)|$, the corresponding value of C

Along the system state $\dot{p}$ in (B.13), we have

$$\dot{s}_a = C_s \dot{\phi}_E + a_{1_\delta} \delta_a + \eta_p \qquad (5.18)$$

where a_{1_δ} and η_p are given in Appendix B. Since δ_a is the control input therefore comparison with (2.36) gives:

$$a(t,x) = C_s \dot{\phi}_E + C_3 \bar{q} Sb \left(C_{l_\beta} \beta + \left(C_{l_p} p + C_{l_r} r \right) \frac{b}{2V} \right) \qquad (5.19)$$

$$b(t,x) = a_{1_\delta} = C_3 \bar{q} Sb C_{l_{\delta_a}} \qquad (5.20)$$

SMC based super twisting controller is designed for generating the control input δ_a based on ϕ_E (bank error) and p (roll rate). Using (2.37), the control effort can be written as:

$$
\begin{aligned}
\delta_a &= -\lambda |C_s(\phi_E) + p|^\gamma \, \mathrm{sgn}(C_s \phi_E + p) + u_1 \\
\dot{u}_1 &= \left\{ \begin{array}{ll} -\delta_a & |\delta_a| > U_S \\ -K \, \mathrm{sgn}(C_s \phi_E + p) & |\delta_a| \leq U_S \end{array} \right\}
\end{aligned}
\qquad (5.21)
$$

In Section 5.2.2.1 we describe the selection of sliding surface parameter C_s and controller parameters K, ρ and λ satisfying the conditions (2.38), (2.39), (2.40) and (2.42), along with boundedness of δ_a.

5.2.2.1 Existence of 2-sliding mode and parameter selection

The expressions in *(2.38)*, *(2.39)*, *(2.40)* and *(2.42)* prove the existence of a $2-$sliding mode system. For k_s, i.e., the minimum bound on (5.20):

$$k_s = \frac{C_3}{2} \rho V_{min}^2 Sb C_{l_{\delta_a}} \qquad (5.22)$$

For K_S, i.e., the maximum bound on (5.20):

$$K_S = \frac{C_3}{2}\rho V_{max}^2 SbC_{l_{\delta_a}} \tag{5.23}$$

For the parameters S, b, ρ and $C_{l_{\delta_a}}$ given in Appendix B, the condition (2.38) takes the form

$$0 \le 320.76 \le b(t,x) \le 487.9116 \tag{5.24}$$

For condition 2.39, we need to evaluate the $|a(t,x)|_{max}$.

$$\gamma U_S < \left| \frac{C_s\dot{\phi}_E + C_3\bar{q}Sb\left(C_{l_\beta}\beta + \left(C_{l_p}p + C_{l_r}r\right)\frac{b}{2V}\right)}{C_3\bar{q}SbC_{l_{\delta_a}}} \right| \tag{5.25}$$

First the sliding surface parameter C_s is selected based on required performance. Here C_s is chosen as 10 to provide rapid convergence of the error to zero to achieve good performance and relatively smooth δ_a. For $V_{max} = 37$m/sec and $\dot{\phi}_E = 0.7854$rad/sec, $|a(t,x)|_{max} = 9.4128$. The control u enters the segment $[-U_S, U_S]$ in finite time and stays there, i.e., $\delta_a = [-5°, 5°]$ as can be observed in Figure 5.4, Figure 5.7 and Figure 5.10. We can now choose the γ as 0.3 satisfying the following expression

$$\gamma < \left| \frac{|a(t,x)|_{max}}{k_s U_S} \right| \tag{5.26}$$

For condition (2.40), we need to derive the value of C i.e., the maximum upper bound on $|\dot{a}(t,x)| + U_S|\dot{b}(t,x)|$. These can be calculated as

$$\dot{a}(t,x) = \dot{\eta}_p \tag{5.27}$$

$$\dot{b}(t,x) = \dot{a}_{1_\delta} \tag{5.28}$$

where $\dot{a}_{1_\delta}$ and $\dot{\eta}_p$ are given in Appendix B. From these values we can now select C as 633.6121. We can now choose the gains K and λ satisfying inequalities (2.38), (2.39), (2.40) and (2.42). We choose K and λ as 2.5 and 1.5 respectively, these satisfy all the above conditions and hence a 2-sliding mode will exist for the inner loop with $s_a = \dot{s}_a = 0$.

5.3 Experimental Results

5.3.1 Implementation aspects

For implementation of the guidance and control law, the *signum* function is approximated as $\mathrm{sgn}(s) \approx \frac{s}{|s|+\epsilon}$, where ϵ is small and positive. Therefore expressions for ϕ_E in (5.12) and δ_a in (5.21) take the form:

$$
\begin{aligned}
\phi_E = & + \frac{V\tau\alpha\beta\tan\phi\cos\chi_E}{(1+\beta^2 y^2)\sec^2\phi} - \frac{V^3\tau\alpha\beta\cos\chi_E}{R(1+\beta^2 y^2)g\sec^2\phi} \\
& - \frac{2V^3\tau\alpha\beta^3 y\sin^2\chi_E}{(1+\beta^2 y^2)^2 g\sec^2\phi} - r_1\frac{(\chi_E + \alpha\arctan(\beta y))}{|(\chi_E + \alpha\arctan(\beta y))| + \epsilon_1} \\
& - r_2\frac{\left(\frac{g}{V}\tan\phi + \frac{\alpha\beta V\sin\chi_E}{1+\beta^2 y^2}\right)}{\left|\left(\frac{g}{V}\tan\phi + \frac{\alpha\beta V\sin\chi_E}{1+\beta^2 y^2}\right)\right| + \epsilon_2} \\
& - K_{circ}\dot{\chi}_R(\chi_E + \alpha\arctan(\beta y))
\end{aligned}
\tag{5.29}
$$

$$
\begin{aligned}
\delta_a &= -\lambda|C_s\phi E + p|^\gamma \frac{C_s\phi_E + p}{|C_s\phi_E + p| + \epsilon_3} + u_1 \\
\dot{u}_1 &= \left\{ \begin{array}{ll} -\delta_a & |\delta_a| > U_S \\ -K\frac{C_s\phi_E + p}{|C_s\phi_E + p| + \epsilon_3} & |\delta_a| \leq U_S \end{array} \right\}
\end{aligned}
\tag{5.30}
$$

Expressions (5.29) and (5.30) are generalized control laws, for our case study the following parameters are selected for experimental flights. Selection of these parameters is explained in Sections 5.2.1.1 and 5.2.2.1.

TABLE 5.1: Outer Loop Controller Parameters

#	Parameter	Value
1	α	0.95
2	β	0.014
3	r_1	26
4	r_2	16
5	τ	0.35
6	ϵ_1	0.7
7	ϵ_2	0.1
8	K_{circ}	6

TABLE 5.2: Inner Loop Controller Parameters

#	Parameter	Value
1	C_s	10
2	λ	3
3	γ	0.65
4	K	0.5
5	ϵ_3	0.5

Now we address the results obtained from test flights for three different scenarios, the objective is to validate the designed guidance and control system. Testing is performed for three cases: Mission-1 tests the capabilities of the strategy to navigate between a series of predefined way points with large as well as small lateral track errors. Mission-2 validates the efficacy of the technique for curved path tracking. In the last Mission, the guidance problem is tested for a complete loiter mission for which the vehicle must traverse between a set of predefined waypoints. For the guidance problem a major source of disturbance are crosswinds, it is estimated that a wind of ~ 6 m/s was generally present during these flights. Results also validate the robustness of the SOSM controller in the presence of wind disturbances.

5.3.2 Mission-1: Large/small cross track error

For a mission of 1000 m initial cross-track error followed by two turnings, flight results are shown in Figure 5.3 – Figure 5.5. The dotted line shows the desired path and the solid blue line shows the actual trajectory flown. Figure 5.4 shows the time plots of track error y and intercept course χ_E; ~ 33 sec are required for the error to reduce from 1000 m to 2 m for tracking $WP1 \rightarrow WP2$. The cross track error is reduced smoothly to vicinity of zero without any overshoot. The state trajectories are forced towards the sliding manifold and converged to the origin as is evident from Figure 5.5. To achieve good performance i.e., to avert the cross-track error rapidly χ_E is large and almost constant for the initial few seconds evident from Figure 5.4. The (commanded) reference roll error ϕ_E and the corresponding roll of the vehicle i.e., ϕ is shown in Figure 5.4. Due to the logic explained in Section 5.2.1.1, ϕ is bounded, i.e., $\phi \leq 45°$. The resultant inner loop control effort δ_a is shown in Figure 5.4. It is evident that the control actuation is within the desired limits.
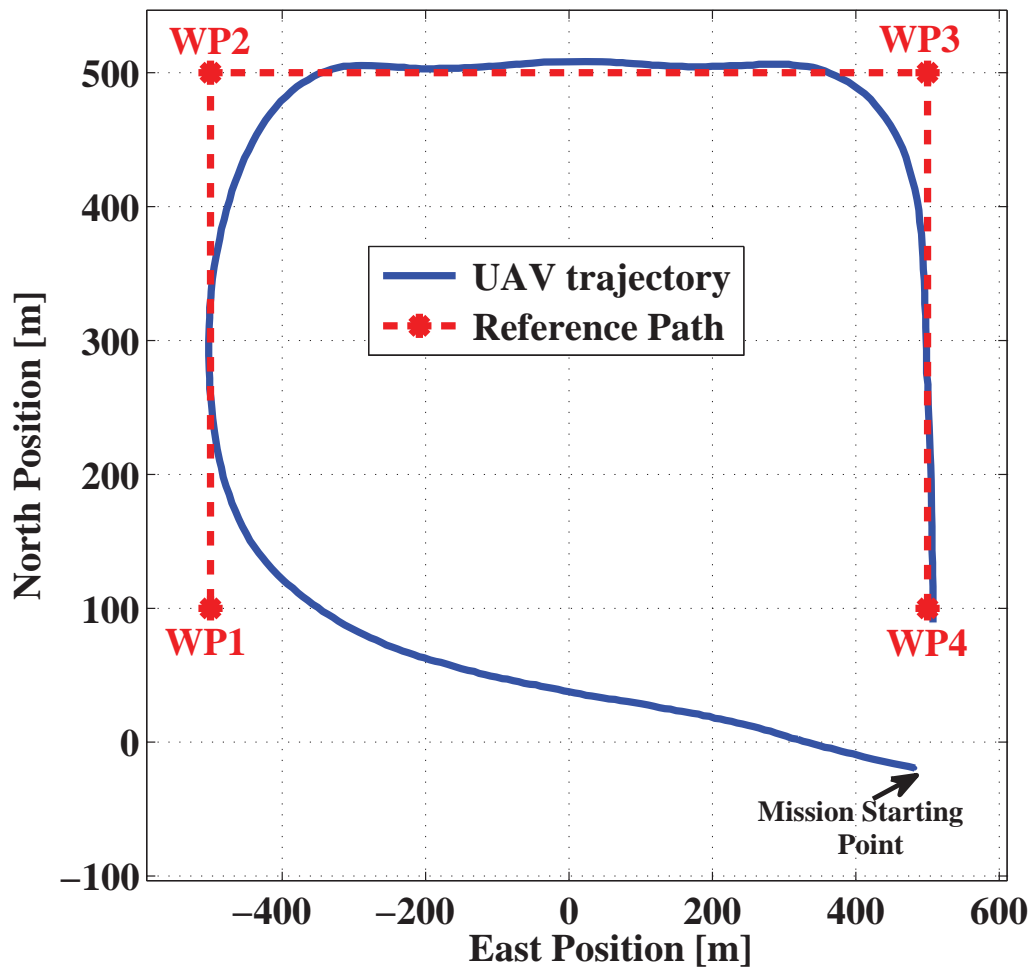
FIGURE 5.3: Mission-1 reference path and UAV trajectory
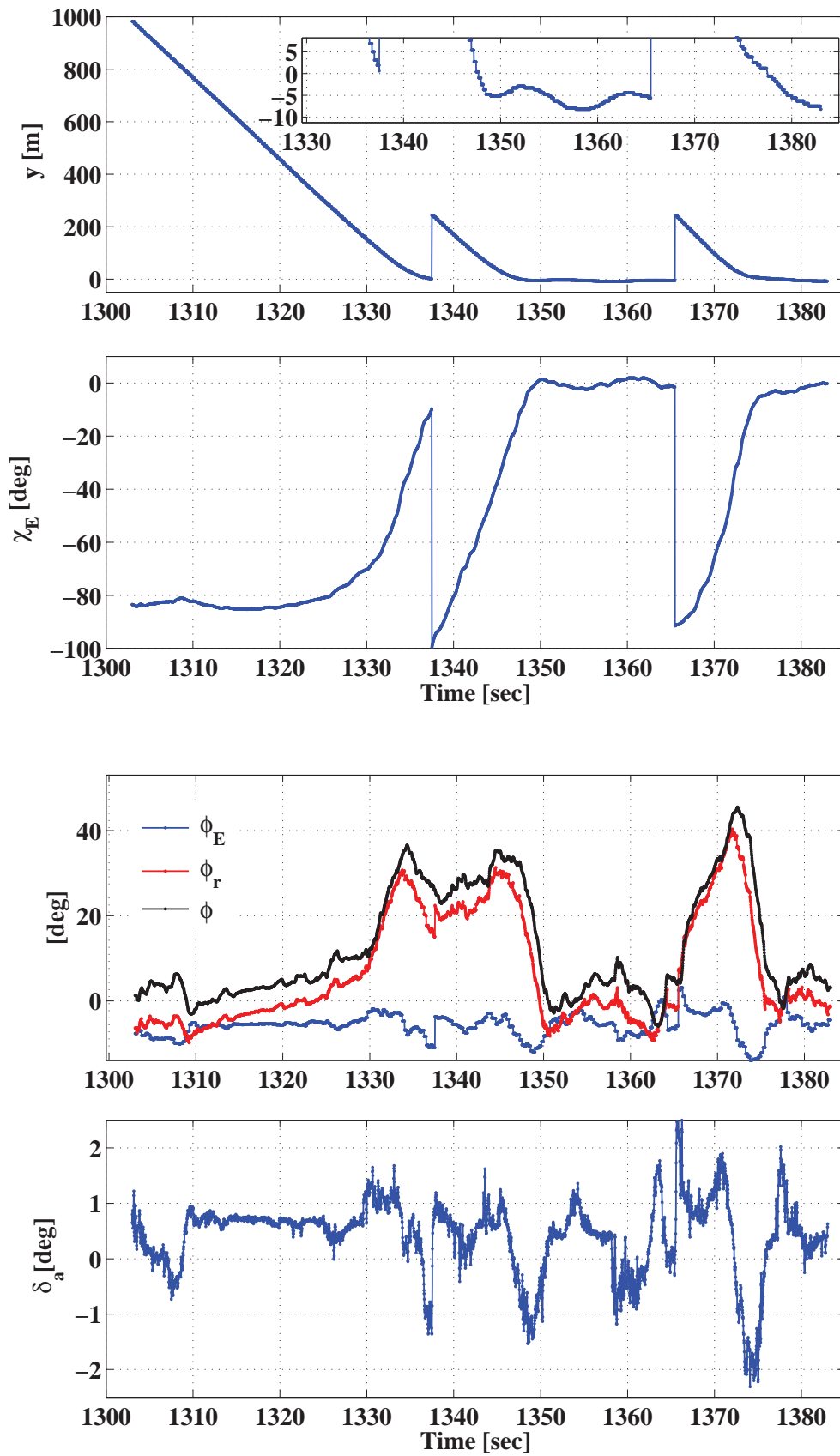
FIGURE 5.4: Cross Range y, Intercept Course χ_E, Commanded error ϕ_E, roll angle ϕ and aileron actuation δ_a for Mission-1
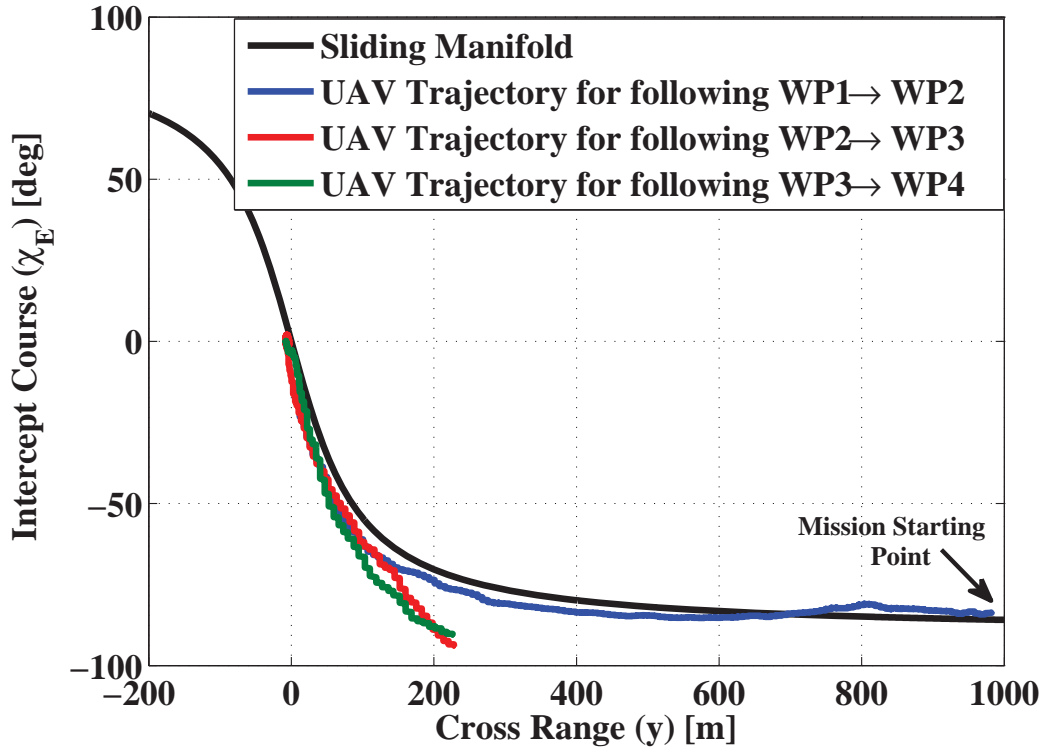
FIGURE 5.5: Phase portrait of UAV trajectories for Mission-1

5.3.3   Mission-2: Curved path

Next we conduct an experimental flight for curved path tracking. The reference trajectory is shown in dotted line, whereas the actual trajectory flown is shown in solid blue line in Figure 5.6. Figure 5.7 shows the lateral error y and intercept course χ_E versus time, the error is maximum at start of the mission, however the guidance algorithm drives it to less than 9 m quickly. Figure 5.7 shows the reference error command ϕ_E generated by the outer guidance loop and the corresponding control effort δ_a for actuation. The real twisting controller results in a steady state error of about 7 meters to 8 meters as shown in Figure 5.7. This error occurs because the desired (reference) direction for circular paths is continuously changing. It is clear that the proposed nonlinear guidance strategy performs well for curved path following in the presence of wind. The sliding manifold along with its phase trajectory is shown in Figure 5.8 for the circular path. The state

141

trajectory gets attracted towards the sliding surface and subsequently maintains motion in close vicinity of the surface to reach the origin.
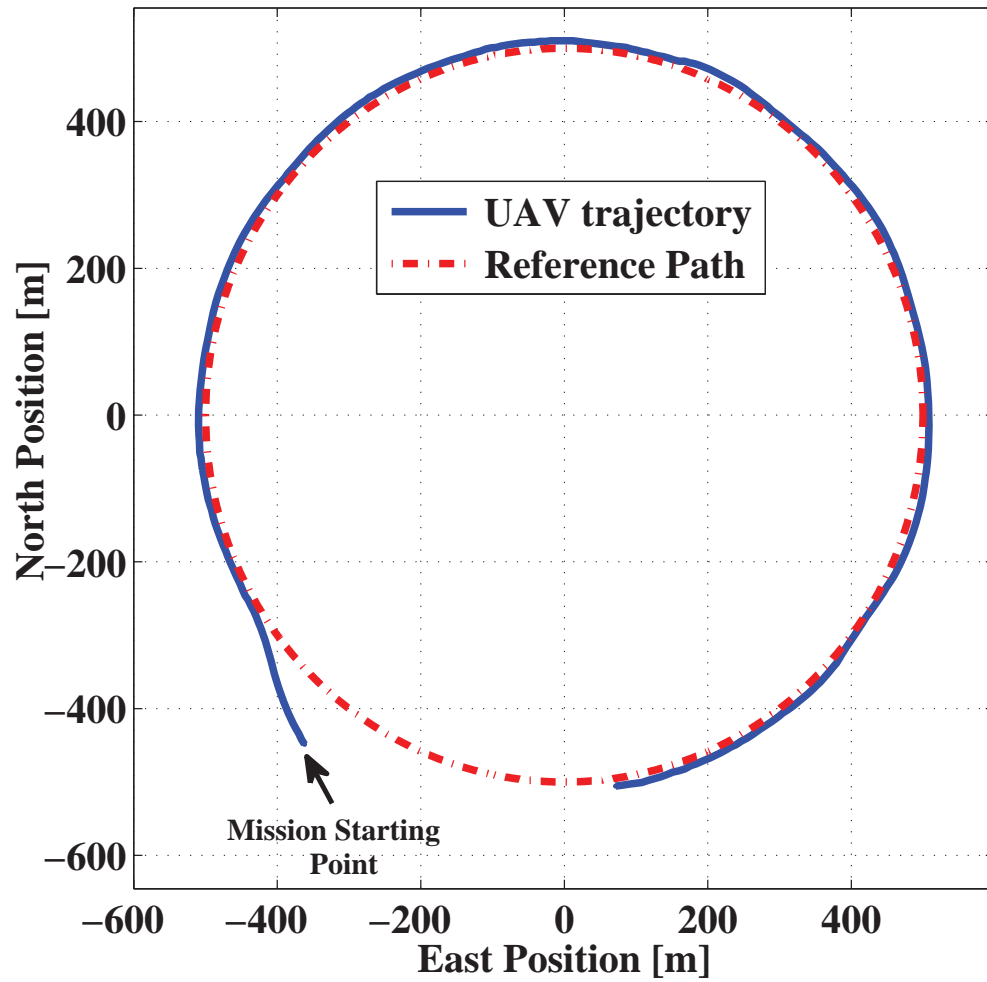
FIGURE 5.6: Mission-2 circular reference path and the UAV trajectory
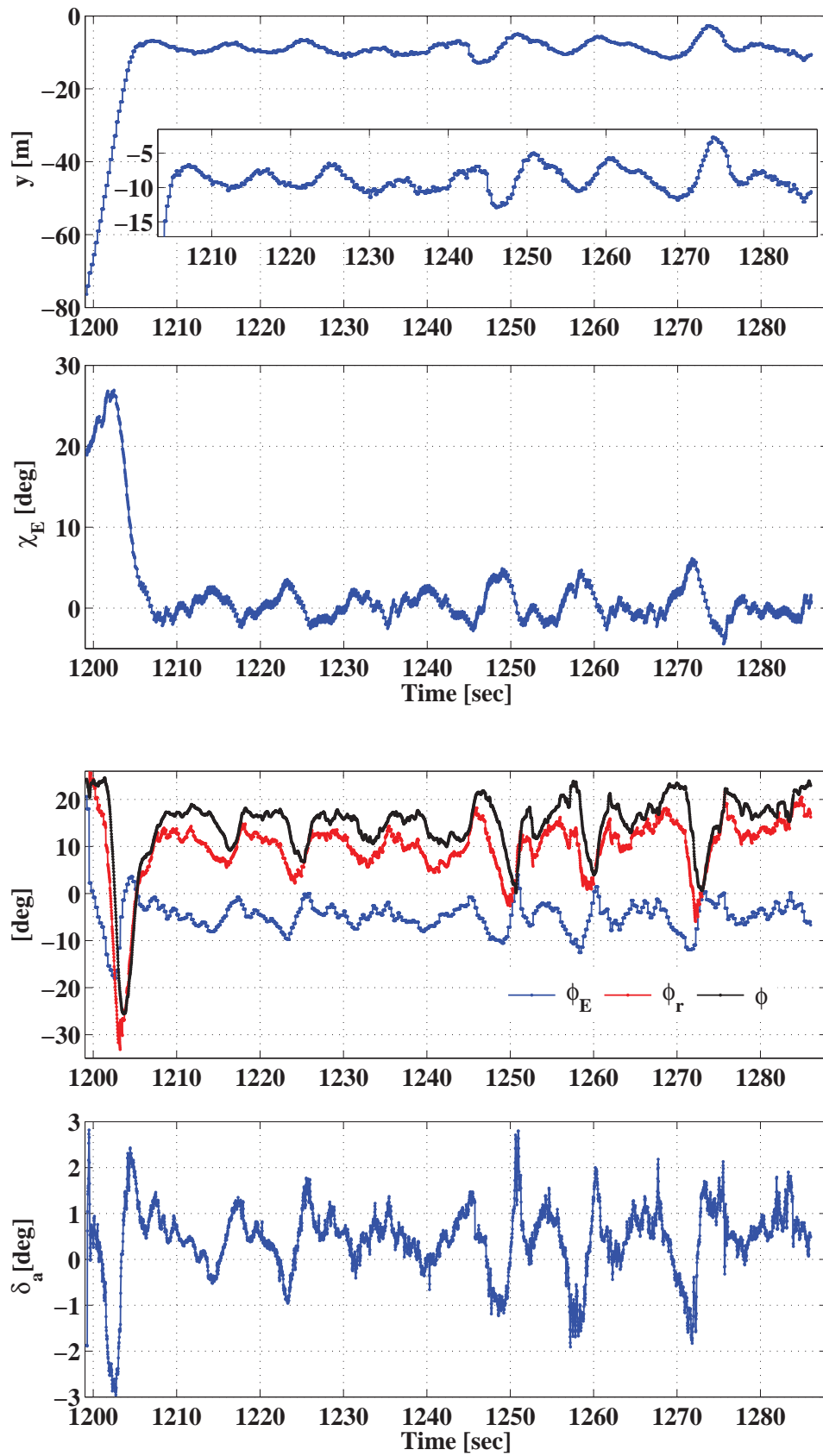
FIGURE 5.7: Cross Range y, Intercept Course χ_E, Commanded error ϕ_E, roll 143 angle ϕ and aileron actuation δ_a for Mission-2
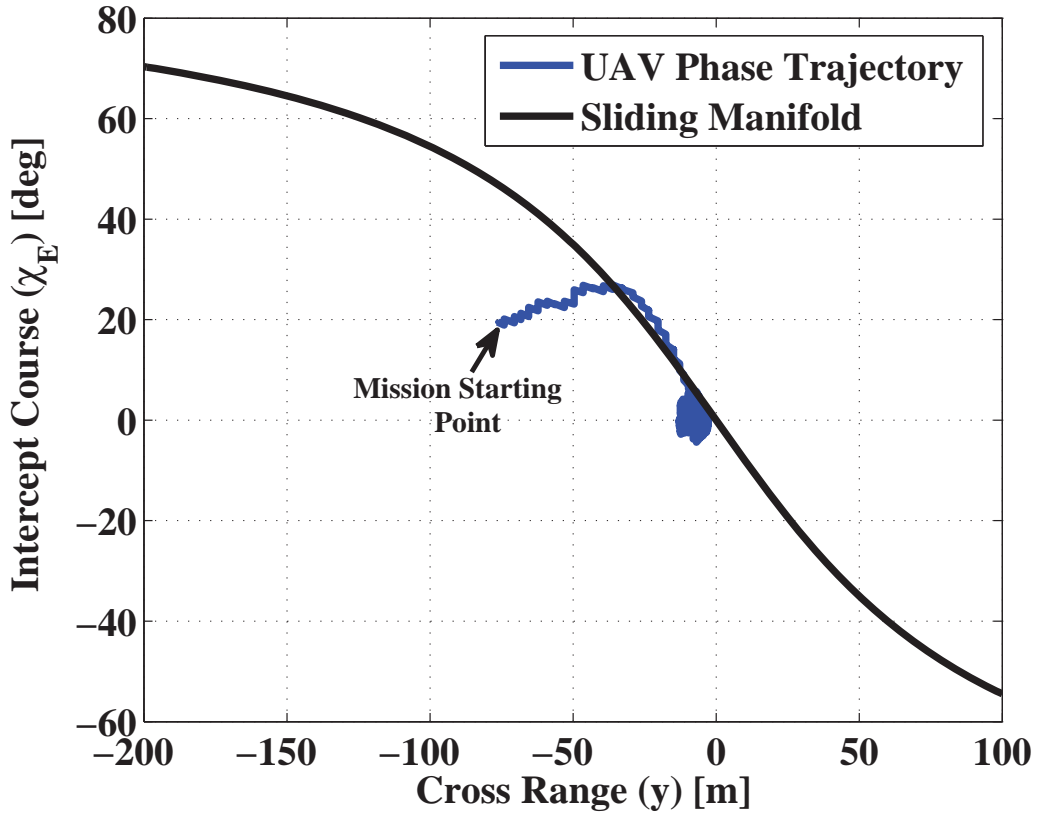
FIGURE 5.8: Phase portrait of UAV trajectories for Mission-2

5.3.4 Mission-3: Loiter pattern

In mission-1 it was shown (Figure 5.3 and Figure 5.4) that the designed framework is capable of recovering quickly from large track errors with constant χ_E, and then follow the mission. In mission-3 the vehicle is required to follow a loiter pattern with an initial lateral error; here the surface (5.3) ensures that χ_E is always regulated towards zero. Figure 5.9 shows a simple hold or loiter pattern that can be flown while the aircraft awaits further instructions. Flight results for a loiter pattern are shown in Figure 5.9 – Figure 5.10. The desired path to follow (dotted red) and the actual flight path (solid blue) of the vehicle is shown in Figure 5.9. The origin is taken as the take off point, distance traveled by the vehicle towards east is denoted as East position while traveled towards north is North position. Waypoint switching is continuously active for smooth transition at the corners. In

this case also the proposed algorithm provides good performance. The commanded error ϕ_E and aileron deflection δ_a are shown in Figure 5.10. The corresponding ϕ is approximately less than 42° as observed in Figure 5.10. The proposed guidance algorithm efficiently follows the complete loiter mission with a lateral steady state error of $8 \sim 11$ m. It is therefore noted that the controllers developed in (5.29) and (5.30) provide good cross track and heading error regulation.
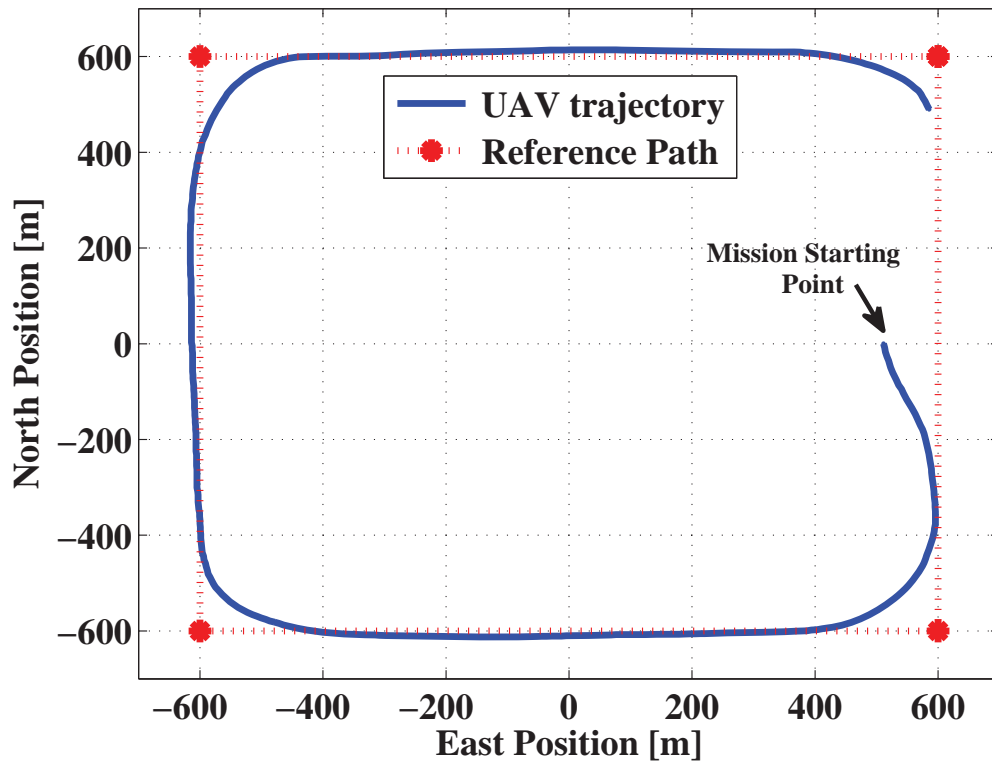
FIGURE 5.9: Mission-3 loiter reference path and the UAV trajectory
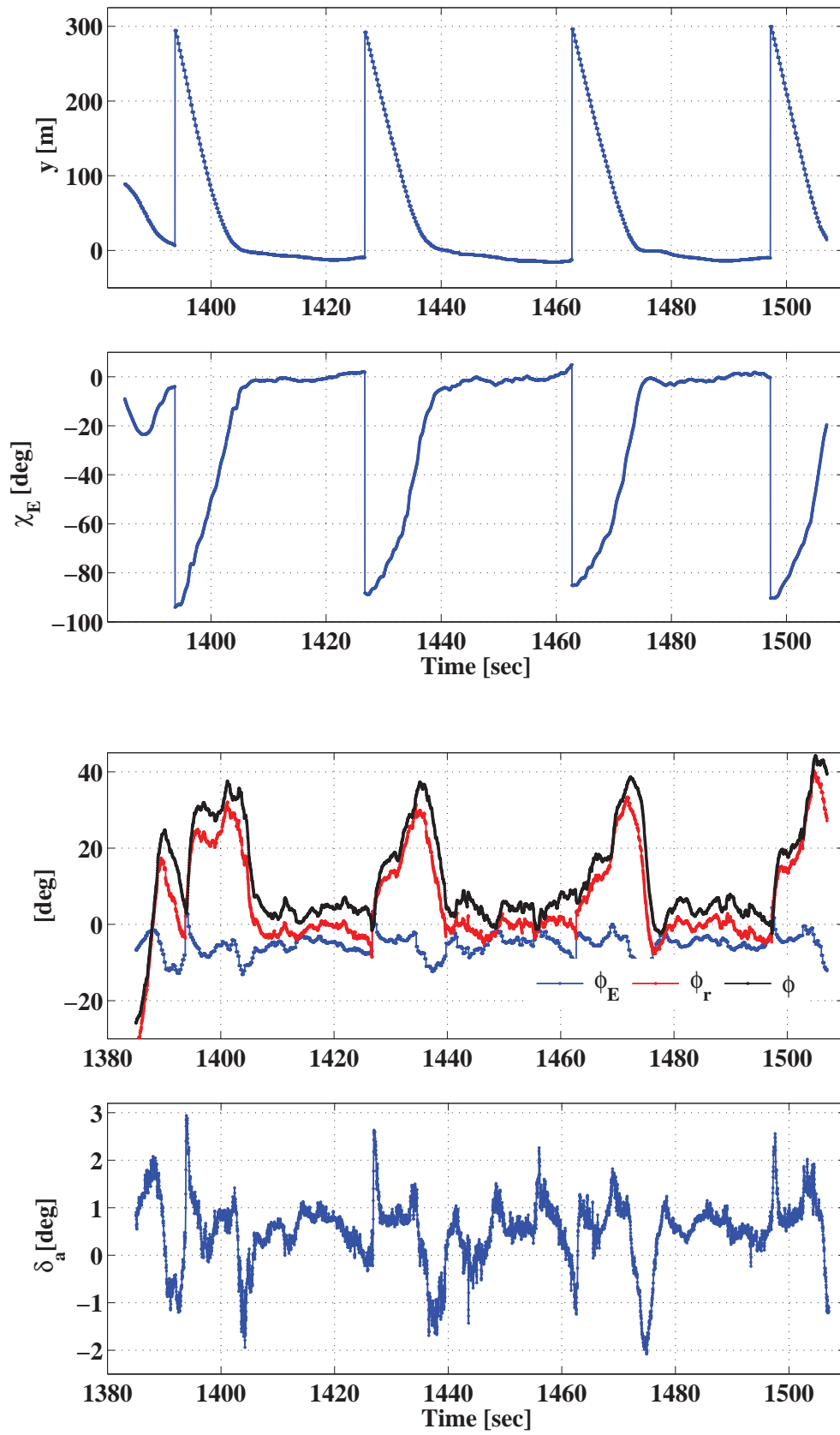
FIGURE 5.10: Cross Range y, Intercept Course χ_E, Commanded reference ϕ_E, 146 corresponding ϕ and aileron actuation δ_a for Mission-3

5.3.5 Flight results comparison with the conventional approach

A comparison is given here between the conventional angle control approach [101], and the proposed PIGC technique. Flight results for similar initial conditions are shown. In case of PIGC, the guidance output is in terms of changes in roll angle, which is used to generate a reference roll rate to drive the cross track error to zero. Because of direct roll rate control, the PIGC shows faster convergence of the track error towards zero. For case-1 (small lateral error), results are shown in Figure 5.11. The PIGC scheme takes ∼5 sec to reduce the lateral error from 100 m to 2 m, the conventional scheme takes ∼8 sec for the same reduction. This faster reduction of the error to zero is at the cost of a larger bank angle, the maximum roll angle reaches 40 degrees for the PIGC technique and 25 degrees for the conventional approach.
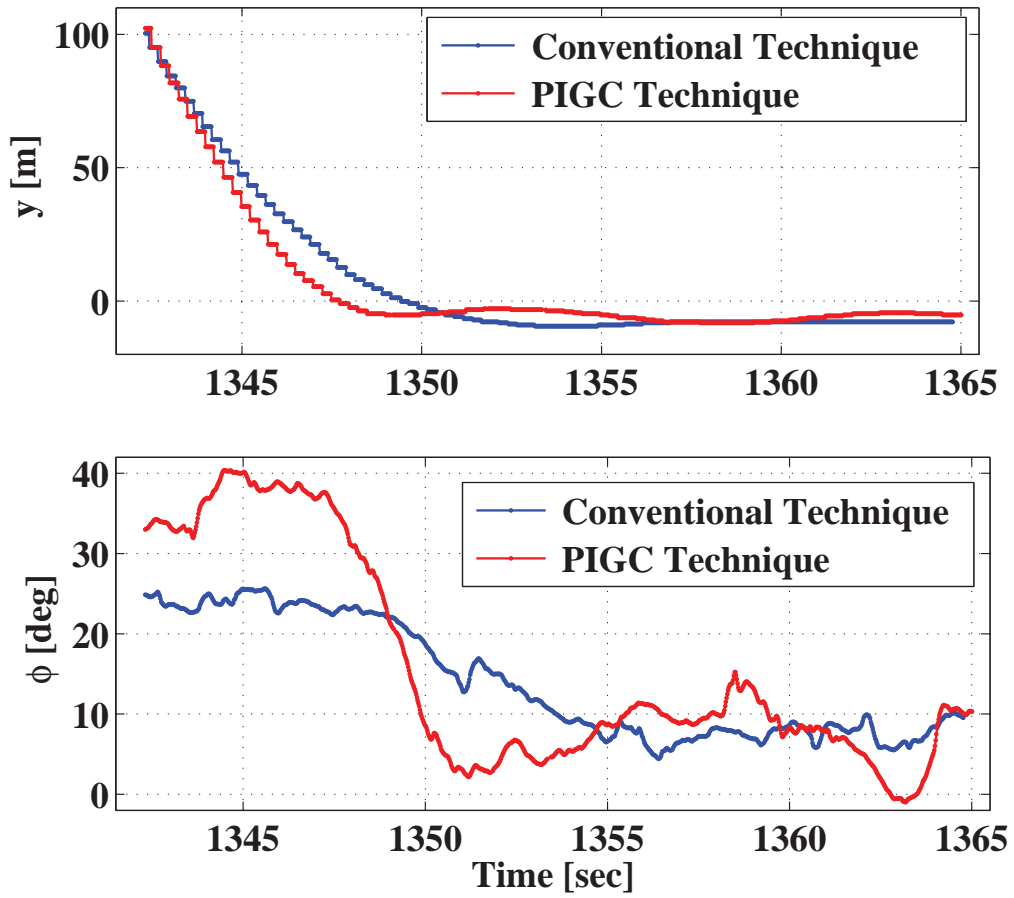
FIGURE 5.11: Case-1 comparison of cross track y and roll angle ϕ for the conventional and PIGC techniques.

For case-2 (large lateral error of 300 m), results are shown in Figure 5.12. The steady state cross track error is less than 5 m for both techniques. The time taken to reduce the error from 300 m to 3 m with the PIGC technique is ∼11.5 sec, for the conventional technique this time is ∼12 sec. The trend of χ_E versus time is slightly different for the two techniques but their average values are almost identical, and hence the lateral error converges to zero in approximately the same time. Like the previous case the roll angle is relatively large for the PIGC scheme, however its magnitude remains less than the maximum allowed.
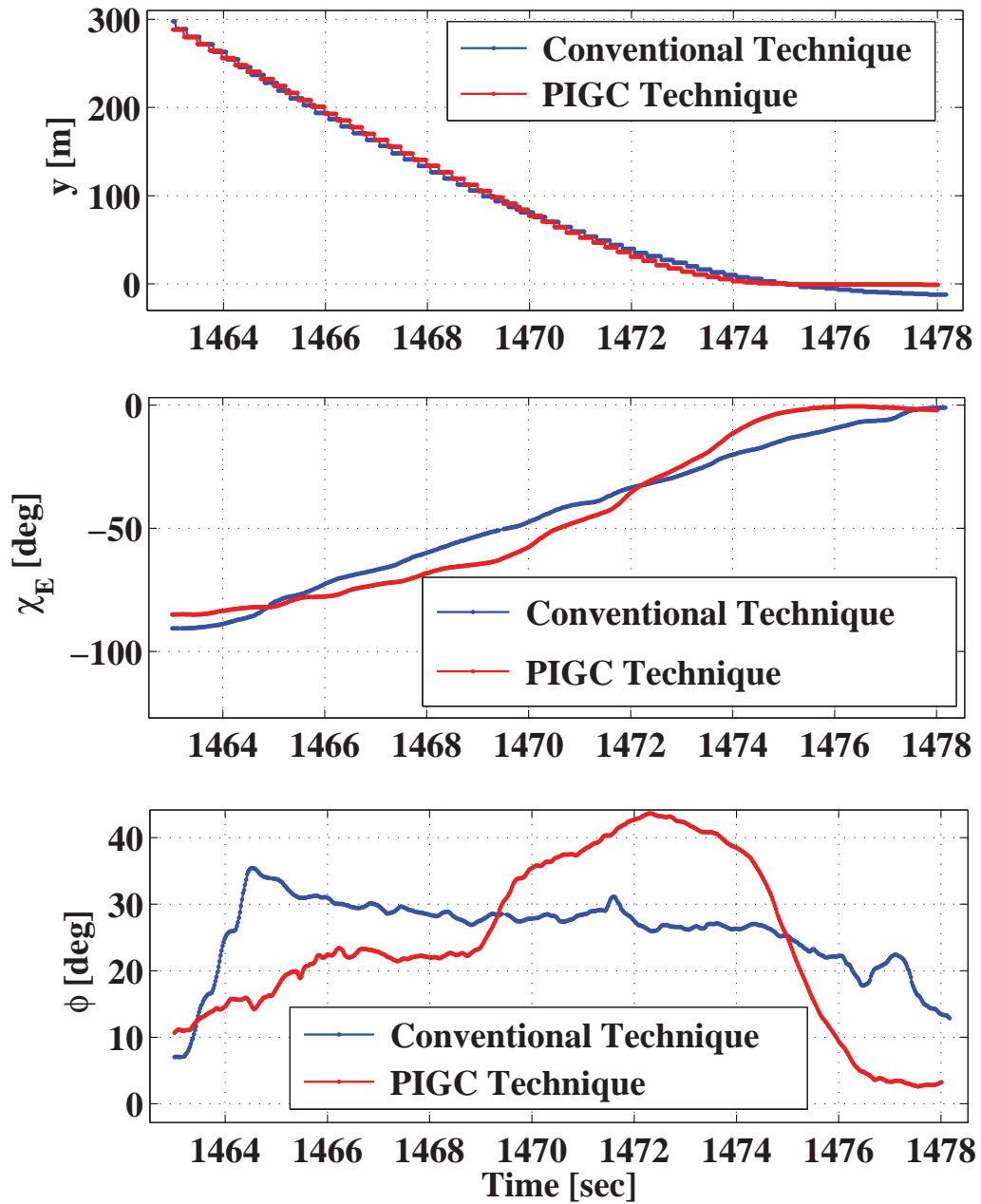
FIGURE 5.12: Case-2 comparison of cross track y, Intercept Course χ_E and roll angle ϕ for the conventional and PIGC techniques.

For case-3, i.e., a circular mission, the comparison is shown in Figure 5.13 and Figure 5.14. The steady state cross track error for the two techniques is approximately the same. The time consumed by the PIGC scheme to reduce the initial

lateral track error and follow the circular path of radius 500 m is ∼6 sec, that for the conventional scheme is ∼12 sec as seen from Figure 5.14.
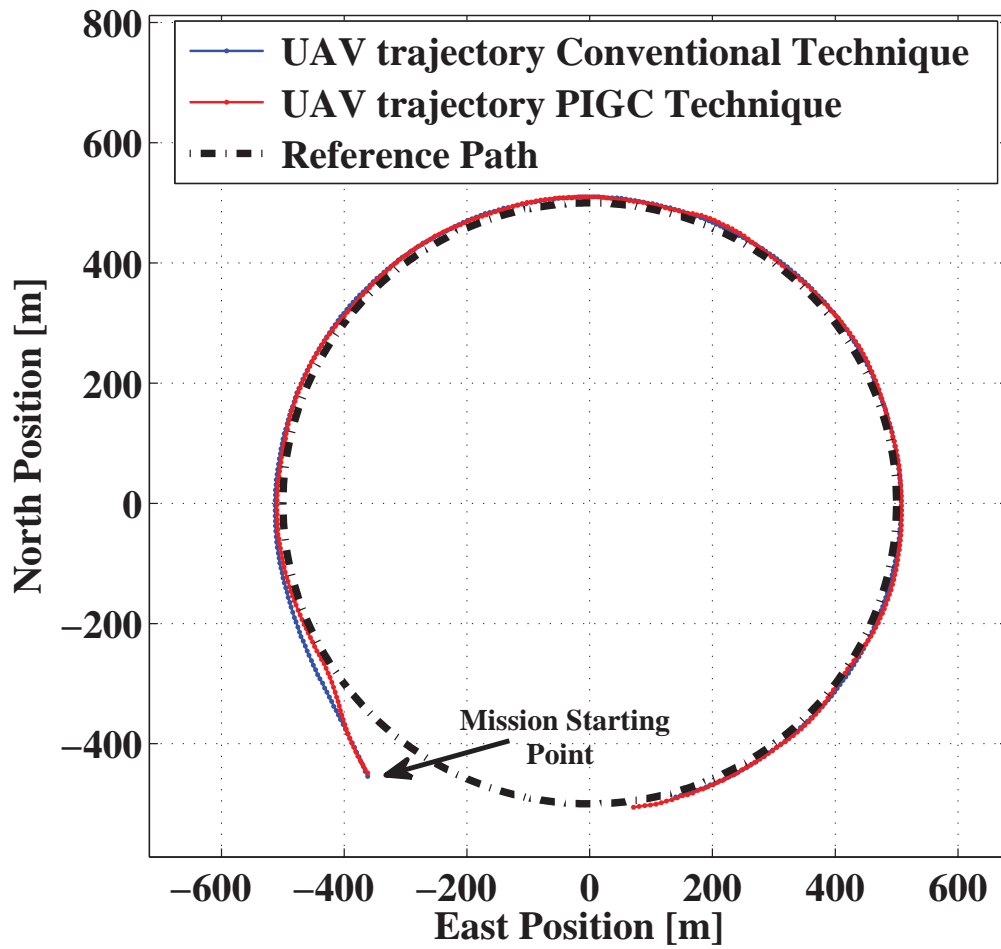
FIGURE 5.13: Case-3 comparison of UAV trajectory for the conventional and PIGC techniques.
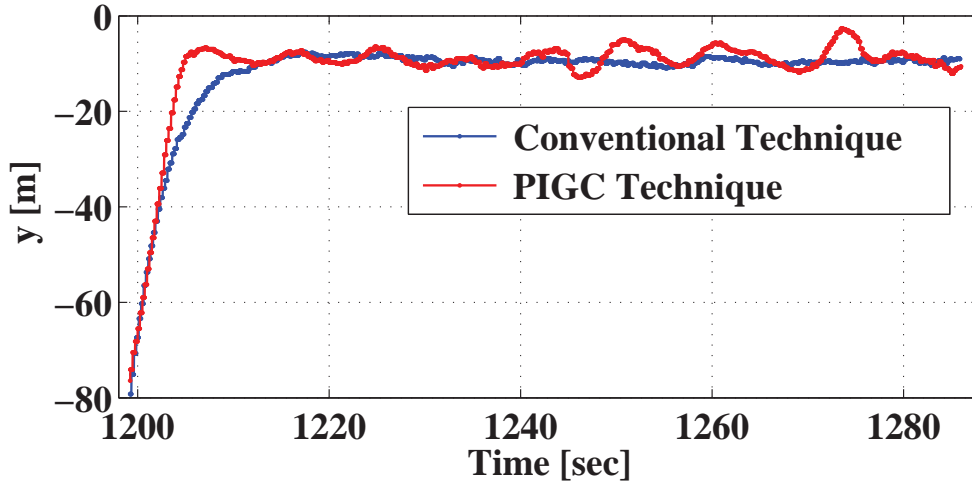
FIGURE 5.14: Case-3 comparison of cross range y for the conventional and PIGC techniques.

5.4 Conclusion

This chapter presents a PIGC strategy for the problem of path-following control of UAVs. A nonlinear sliding surface based on SOSM control theory is used. The design objective is to regulate the cross-range and intercept course angle with respect to the desired mission path. The proposed solution leads to a inner loop - outer loop control structure that exploits an SOSM autopilot for bank error command tracking. The theoretical framework is based on path following in 2-D space using the SOSM real twisting algorithm for guidance, along with a SOSM super twisting algorithm for inner loop control. The manifold augmentation strategy was introduced to achieve robustness in the presence of environmental disturbances and modeling uncertainties. The guidance and control strategy effectively copes with the autopilot dynamics, and maintains performance for both small and large lateral errors. Flight results show good transient and steady-state performance and effectiveness of the framework for UAV path following. Experimental results for conventional two loop scheme and PIGC approach are compared to show that PIGC provides faster convergence of cross track error and intercept course towards zero. However, the relative degree for the guidance scheme needs to be improved as higher the relative degree more noisy are the control channels. An

improved sliding surface needs to be evaluated which provides better realization of incorporating autopilot dynamics.

Chapter 6

3-D SLIDING MANIFOLD FOR LATERAL GUIDANCE

In this chapter, lateral path following problem of UAVs is discussed and a novel guidance law is proposed for desired flight path tracking. The unique feature is to explicitly account for the autopilot constraints by defining a 3-D sliding manifold. The guidance solution described is based on state stabilization of kinematics-dynamics trajectories i.e., the guidance law is evolved based on the knowledge of kinematics as well as dynamical characteristics of the UAV. The scheme integrates the guidance and control structure to the extent that the information of the inner control loop dynamics is known to the outer guidance algorithm and it generates reference commands in accordance with the control loop constraints/dynamics. Generally, the guidance law performance is affected by wind/gust disturbances, parametric uncertainties and lag of inner control (autopilot) loop. To cater for these disturbances, a robust First Order Sliding Mode Control (FOSMC) guidance algorithm is derived using proposed nonlinear 3-D sliding manifold to develop a good helmsman behavior. A suitable Lyapunov function is used to ensure the stability of the sliding manifold. The designed guidance law is implemented in the flight control computer of a scaled YAK-54 for thorough evaluation of its capabilities.

In our previous work [55, 56], lateral path following scheme for aerial vehicles with a novel nonlinear sliding manifold was proposed. However, the guidance scheme was designed with the assumption that the autopilot dynamics of inner loop from ϕ_{ref} to ϕ were fast enough to be neglected (i.e., $\phi_{ref} \approx \phi$). The algorithm was designed using first order sliding mode theory. Next the guidance scheme was improved in chapter 4, which took into account the constraints on the vehicle dynamics. In chapter 4 [101], we extended the previous work [55, 56] by taking into

account the dynamics of the inner control loop while designing the outer guidance loop, the relative degree of the problem was increased to 2. We proposed a novel finite-time convergence law using HOSM theory and validated by flight tests. In chapter 5, we further improved the guidance and control strategy by designing a partially integrated guidance and control scheme which provided fast convergence of the states towards zero using HOSM. Real twisting algorithm was designed for guidance loop and super twisting algorithm for control loop. However in both the schemes the sliding surface proposed in [55, 56] is used and the autopilot constraints are included into the guidance law design either in the form of equivalent control dynamics or the control gains are selected by explicitly satisfying conditions that depends upon these constraints.

Generally, when the lateral deviation is observed by the UAV, the characteristics of the vehicle dynamics are coupled with the guidance kinematics. This coupling arises due to the inner loop limitations being solely dependent on the autopilot characteristics of UAV [34]. The bandwidths of guidance and control feedback loops for accurate path following may overlap. Therefore, it is necessary to design a path following strategy that explicitly accounts for inner loop constraints. The constraining function i.e., the sliding manifold is the key variable in SMC which depicts the performance of overall system, the sliding surface in [55] is improved by adding the vehicles roll dynamics to the manifold to cater for auto-pilot lag. Due to the nature of tight path tracking, we rely on convergence to specified paths with limited control effort. This requires slowly varying efficient and effective path following and it is important to take the vehicle capabilities into consideration. The vehicle kinematics in terms of path following parameters are represented with a kinematic model, which provides convenient description of intercept course and lateral error. The integration of guidance law control dynamics will recompense for auto pilot lag. The objective of this chapter is to develop a path following strategy which has the capability to control lateral deviations by generating reference commands based on the information of current bank angle of the vehicle.

For curved path following, the guidance logic contains an element of anticipatory action for accurate convergence.

The rest of the chapter is structured as follows. In Section 6.1, the path following problem is formulated by describing the guidance and control scheme and presents the state space representation for the problem. In Section 6.2, the stabilizing function for the guidance problem is discussed with a brief review of previous work regarding 2-D nonlinear sliding manifold is analyzed and a new 3-D manifold is proposed. The benefits obtained by transformation of 2-D manifold into 3-D manifold are also described in 6.2. In Section 6.3, the path-following problem is solved at the kinematic level (outer-loop control) with a nonlinear guidance law for straight and circular path following. Control boundedness and analytical stability analysis proofs for the proposed scheme are also given in Section 6.3. Section 6.4, addresses the implementation issues and finally the flight test results of the proposed law. Section 6.5, summarizes the key results and contains the concluding remarks.

6.1 Guidance and Control Strategy
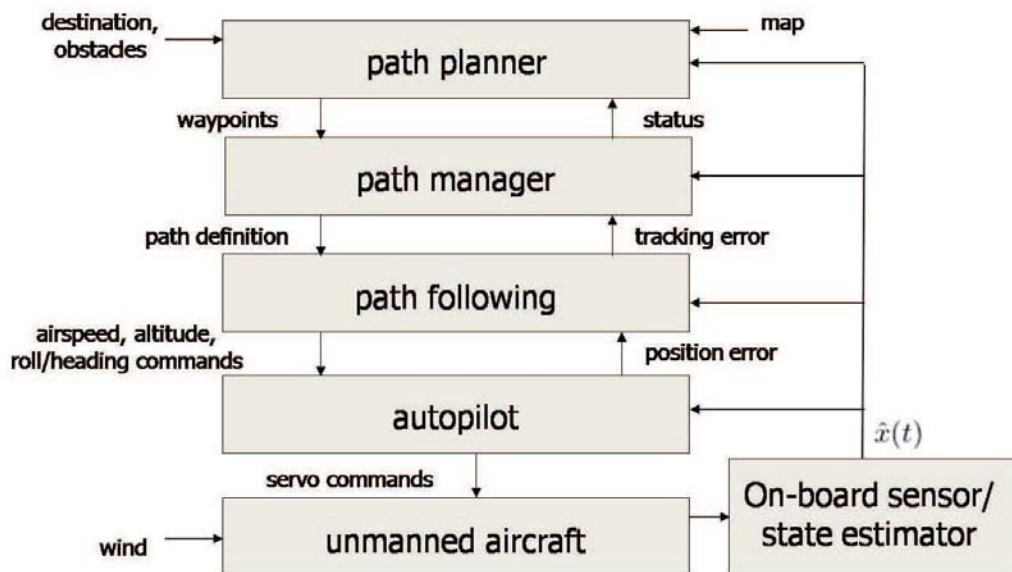
FIGURE 6.1: Guidance and Control architecture

The system architecture used for guidance and control logic design is shown in Figure 6.1. The path planner produces straight-line or arcs as a reference/desired path. The path manager switches between orbit following and straight-line path following to maneuver along the waypoints. The path-following (Guidance) block produces commands to the low-level autopilot, which controls the dynamical variables. Each of the blocks relies on estimates of the states measured by on-board sensors. In this work the state space form (5.2) is used, where χ_E, y and ϕ are the state variables and ϕ_E is the control signal. A pre-specified path is available from the mission block in the form of waypoints, the desired course χ_R and its rate of change $\dot{\chi}_R$. Mission information and feedback from sensors measuring the course angle χ, instantaneous position y and roll angle ϕ serve as inputs to the guidance (path following) algorithm.

The proposed guidance scheme generates reference bank error commands ϕ_E for the autopilot to track. The guidance commands are generated by following the concept of coordinated bank to turn maneuver with FOSMC using a novel 3-D sliding manifold. Firstly to achieve the path i.e., minimize the lateral error and then secondly to follow it accurately with minimum deviation. The autopilot (control) law actuates the ailerons δ_a to regulate the roll error commands generated by the guidance scheme.

6.2   Proposed Sliding Manifold

The guidance law objective is to converge χ_E and y simultaneously to zero. In case of a non-zero lateral error y, the guidance algorithm will bank the vehicle in order to manipulate χ_E to avert the error. Generally, a constant χ_E ($\leq 90°$) is required to avert very large track errors and χ_E is accordingly adjusted for small lateral error. Here a 3-D nonlinear sliding surface is proposed which also caters

for autopilot dynamics as shown in Figure 6.2. The proposed sliding manifold is:

$$\sigma = \chi_E + \alpha \arctan(\beta y) + \gamma \phi \qquad (6.1)$$

Motion on the sliding surface is represented by $\sigma = 0$, i.e.,

$$\chi_E = -\alpha \arctan(\beta y) - \gamma \phi \qquad (6.2)$$
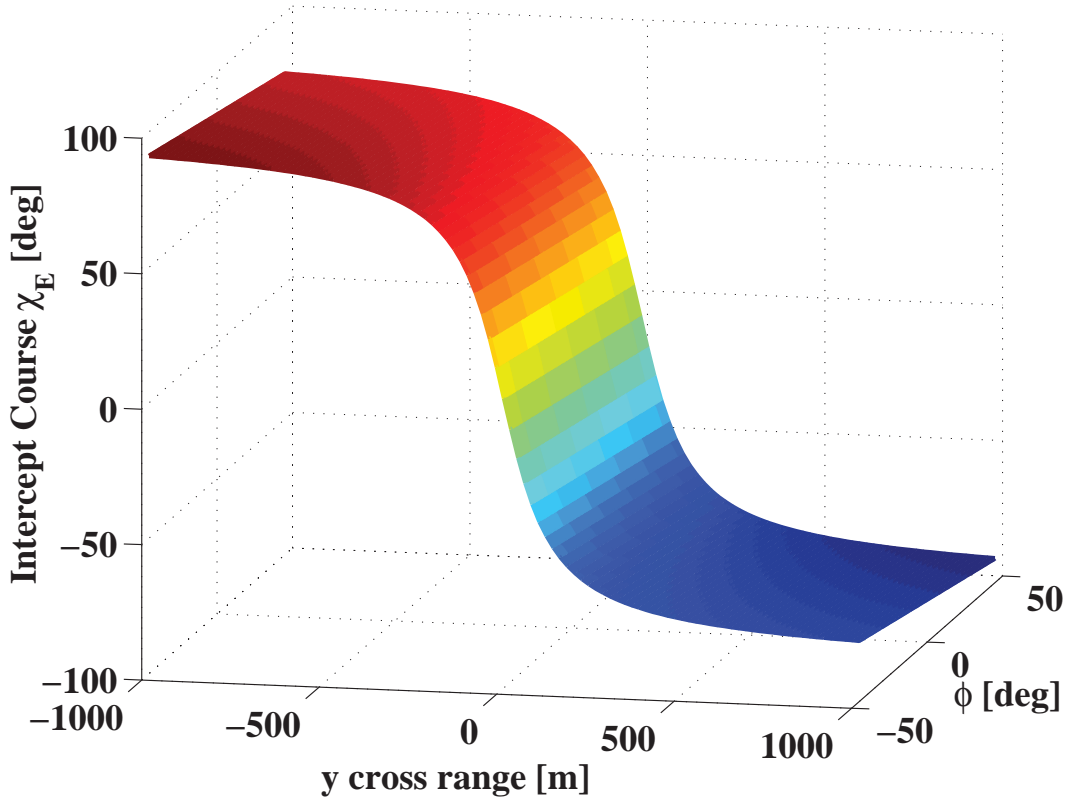
FIGURE 6.2: New Proposed Surface 3-D Sliding Manifold

where the constants α, β and $\gamma \in \Re$ are surface parameters, later the condition $\alpha, \beta, \gamma > 0$ is discussed for sliding surface stability. The nonlinear surface (6.1) is shown in Figure 6.2 for particular values of α, β and γ. The nonlinear manifold for different values of α, β and γ are plotted in Figure 6.3 and Figure 6.4. In order

157

to ensure $|\chi_E| \leq \frac{\pi}{2}$ in all situations, the following condition should be satisfied while the selection of sliding parameters:

$$\alpha \leq 1 - \left(\frac{\gamma}{2}\right) \qquad\qquad (6.3)$$

In Figure 6.3 the result of changing α is shown with β and γ held to specific values; it is clear that χ_E for large track errors depends on the value of α. The parameter γ defines the curvature between χ_E and ϕ, the required χ_E for respective y is calculated based on current roll angle of the vehicle. Larger values of α will in turn reduce the lateral error y quickly and larger γ will force guidance law to minimize ϕ quickly. For good performance, we want to minimize lateral error quickly therefore values of α should not be kept too small to force the guidance algorithm to put more emphasis on minimizing y first and then adjust ϕ accordingly.

In Figure 6.4, the effect of changing β is shown with α and γ constant. Likewise as in Section (3.2), the effects of varying β is similar i.e., it defines the curvature of the curve. The system dynamics would be slow for small value of β while large value of β indicates faster dynamics for reducing the track error to zero. The value of β is directly related to adjusting performance for the case of small track errors. However, large selected value of β would imply a bigger control command.

Lyapunov theory is used to prove the stability of the proposed sliding manifold. For proving the stability of the sliding motion, the following Lyapunov candidate function is selected as

$$W = \frac{1}{2}\left(y^2 + \chi_E^2 + (\gamma\phi)^2\right) \qquad\qquad (6.4)$$
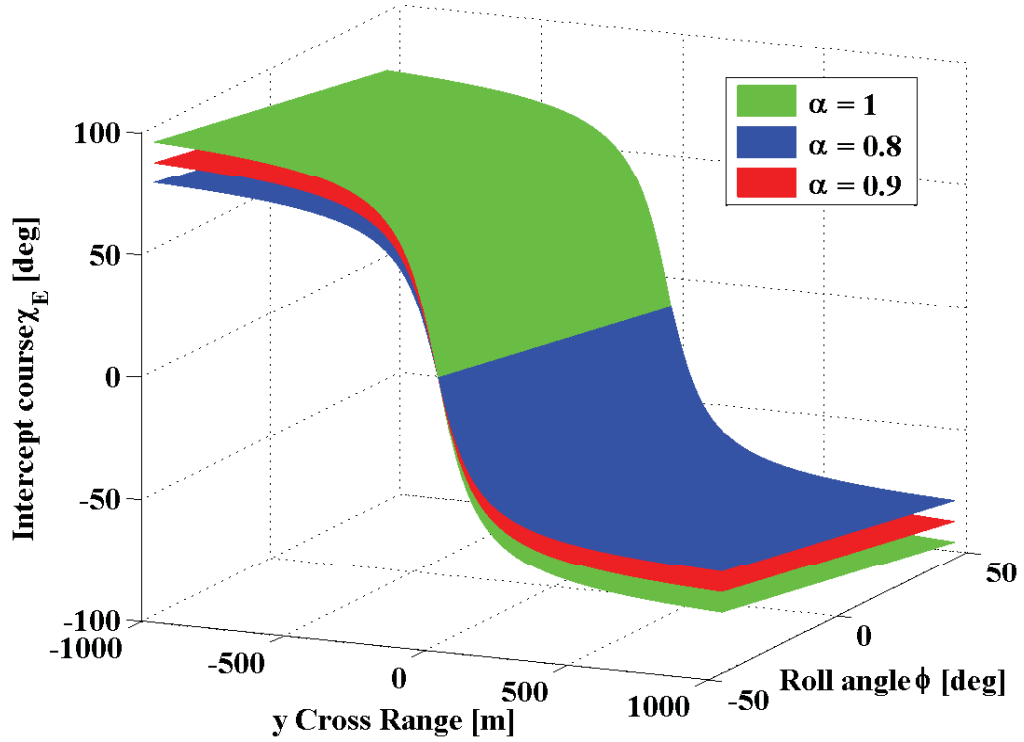
FIGURE 6.3: Surface Analysis for different values of α with β and γ fixed

Here three state variables appear, using $\sigma = 0$ we can write one state in terms of other two. As a result W depends on two state variables as

$$W = \frac{1}{2} \left(y^2 + \chi_E^2 + (\alpha \arctan(\beta y) + \chi_E)^2 \right) \tag{6.5}$$

Taking the time derivative, we have

$$\dot{W} = y\dot{y} + \chi_E\dot{\chi}_E + (\alpha \arctan(\beta y) + \chi_E) \left\{ \frac{\alpha\beta}{1 + \beta^2 y^2}\dot{y} + \dot{\chi}_E \right\} \tag{6.6}$$

And along system states (5.2), $\dot{W}$ takes the following form

$$\begin{aligned}
\dot{W} = {} & yV \sin \chi_E + 2\chi_E \frac{g}{V} \tan \phi + \frac{\alpha\beta}{1 + \beta^2 y^2} \chi_E V \sin \chi_E \\
& + \alpha \arctan(\beta y) \frac{g}{V} \tan \phi + \frac{\alpha^2 \beta V}{1 + \beta^2 y^2} \arctan(\beta y) \sin \chi_E
\end{aligned} \tag{6.7}$$
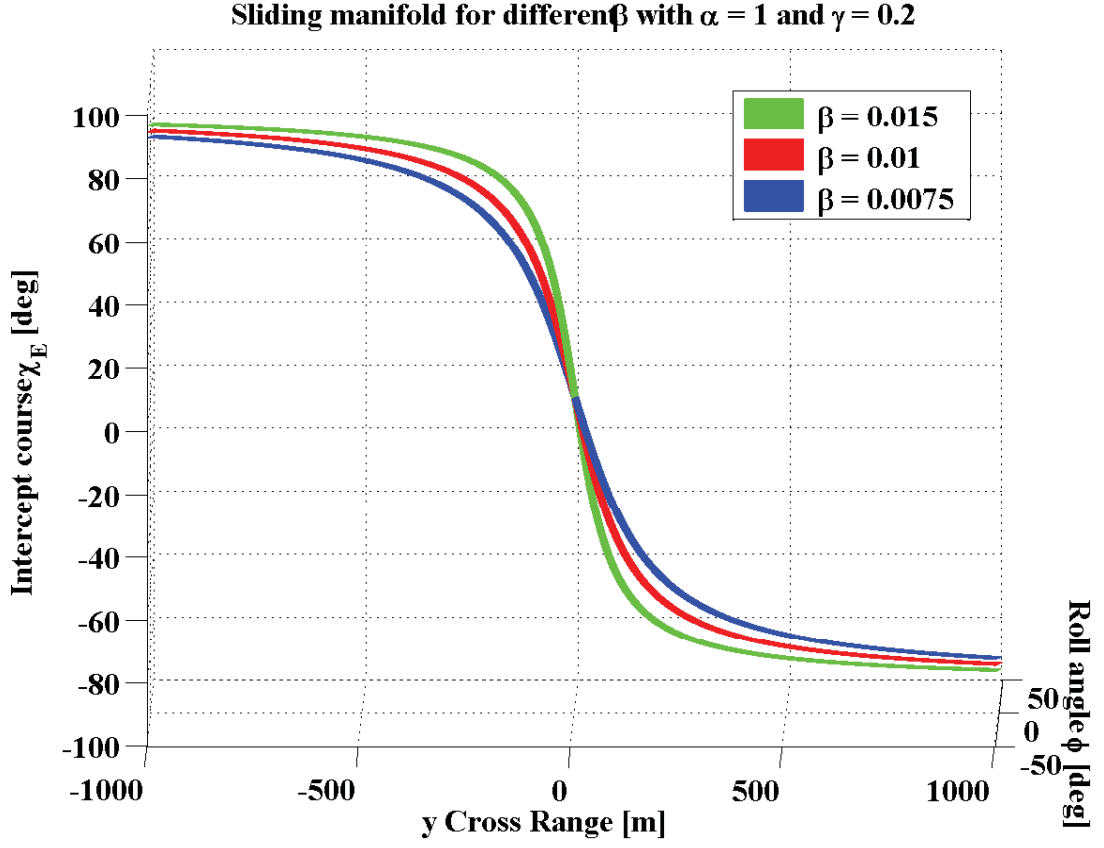
FIGURE 6.4: Surface Analysis for different values of β with α and γ fixed

After simplification and using (6.2), we have the final expression of $\dot{W}$

$$
\begin{aligned}
\dot{W} = & -yV \sin\left(\alpha \arctan(\beta y) + \gamma \phi\right) \\
& - \frac{2g\gamma\phi}{V} \tan\phi \\
& - \frac{g}{V}\alpha \arctan(\beta y) \tan\phi \\
& + \frac{\alpha\beta\gamma V}{1 + \beta^2 y^2} \sin\chi_E \phi
\end{aligned}
\tag{6.8}
$$

Since we are interested in showing that once the trajectories reach the sliding manifold in (6.1), they will consequently stay on it and will always be directed towards the origin. In sliding if we observe the kinematics of the UAV as shown in Figure 6.5, for large lateral error, the guidance law using 3-D manifold will keep χ_E large and almost constant to reduce the lateral error quickly to zero keeping $\dot{\chi}_E \approx 0$. If we observe the state equation of $\dot{\chi}_E$ in (2.48) we can see that for $\dot{\chi}_E \approx 0$

(b) Top View: Path following for positive cross range
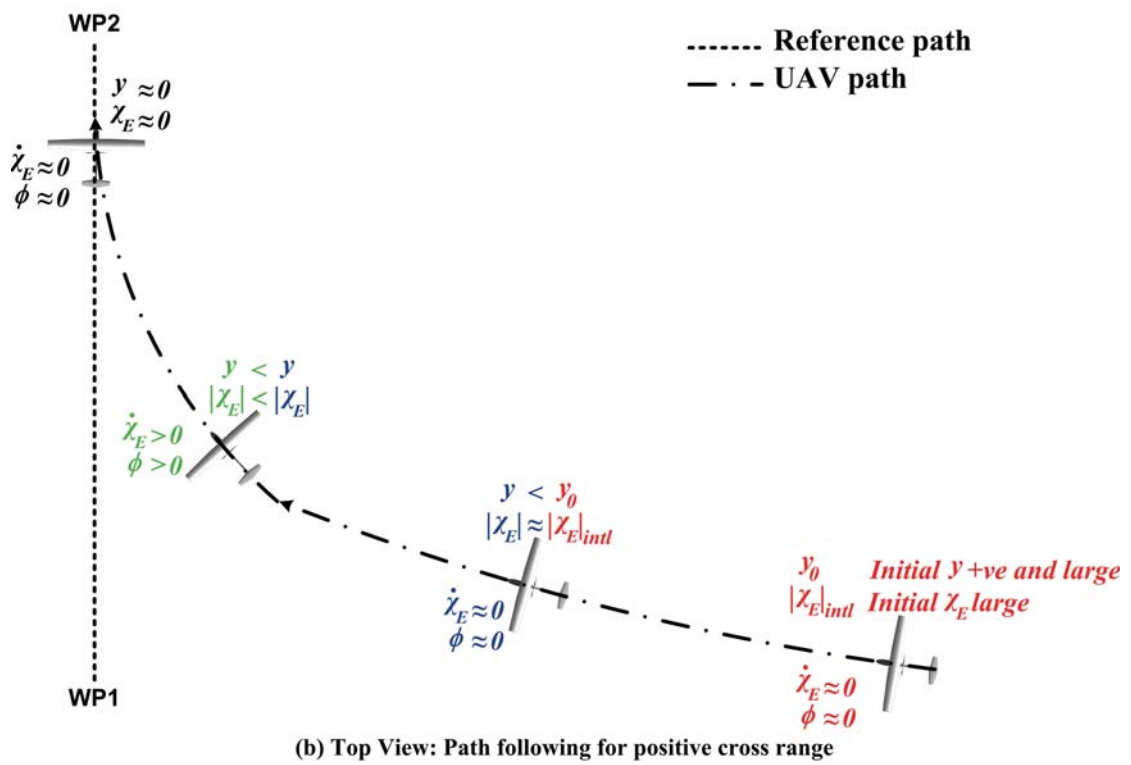
FIGURE 6.5: Path following of UAV
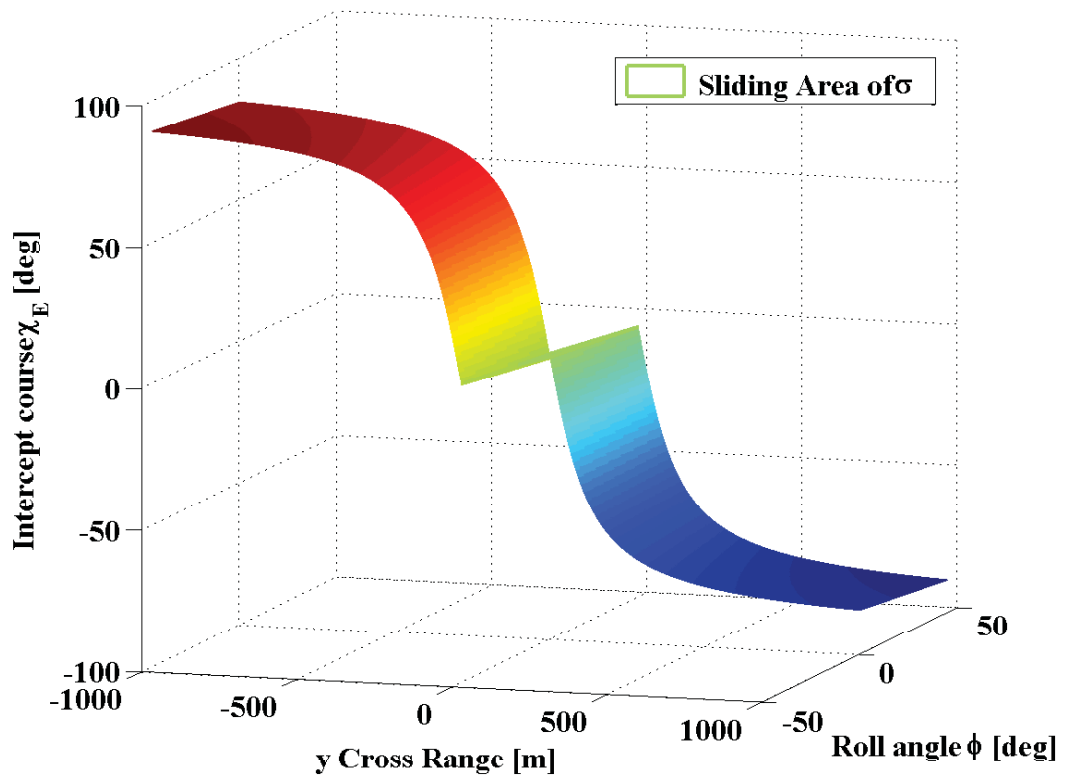
FIGURE 6.6: Surface sliding area for particular α, β and γ

the roll angle $\phi \approx 0$. Now when the cross range y is minimized within a certain band, χ_E will be adjusted causing $\dot{\chi}_E > 0$. Now from (2.48) we can see that ϕ will be greater than zero as well. The guidance scheme will manipulate ϕ_E to generate a positive roll angle ϕ to turn the UAV. We can have the idea of system dynamics while on sliding i.e., if y is positive, ϕ will also be positive and χ_E will be negative while sliding. Similarly for a negative lateral error y, ϕ will be negative and χ_E will be positive. From the scenario explained in Figure 6.5 we can have the surface convergence sliding area shown in Figure 6.6. Let us analyze the $\dot{W}$ expression in (6.8) for a positive lateral error case i.e., $y > 0$.

- For the above case, the odd function $\alpha \arctan(\beta y)$ will carry the sign of y provided $\beta > 0$. As for a positive lateral error i.e., $y > 0$ while in sliding the roll observed by the vehicle is also always positive i.e., $\phi > 0$ therefore the sign of $(\alpha \arctan(\beta y) + \gamma \phi)$ is positive provided $\alpha, \beta, \gamma > 0$. As the sign of $\sin(\alpha \arctan(\beta y) + \gamma \phi)$ and V (the magnitude of the velocity) is positive, the first term on the right hand side in (6.8) is negative definite.

- The second term already carries a negative sign, we just need to ensure that it will remain negative for whole state space since γ, V and g (the gravitational acceleration) are positive and the product $\phi \tan \phi$ will always be positive, therefore this term will always be negative definite.

- For the third term as $\alpha \arctan(\beta y)$ will have the sign y due to its odd functionality, which is positive as $\alpha, \beta > 0$. The $\tan \phi$ will be positive as ϕ is greater than zero, therefore since g and V are positive this term will be negative definite.

- From the analysis of fourth term in $\dot{W}$ (6.8), as for a positive y, χ_E is negative therefore $\sin \chi_E$ will give us a negative sign. And as $\phi > 0$, velocity V is positive along with $\alpha, \beta, \gamma > 0$, this term also will be negative definite.

From here we can conclude, the positive definite Lyapunov function W in (6.5) will ensure a negative definite $\dot{W}$ and trajectories will converge towards origin. Similar arguments also hold true for the case of the negative lateral error i.e., $y < 0$.

The design of new sliding manifold i.e., adding an extra dimension or state to the surface has its benefit. In [101, 102], the auto pilot dynamics were incorporated into the guidance algorithm using sliding manifold from existing literature [55, 56] and $\dot{\phi}$ as an extra state and the relative degree of the problem was 2. Hence a HOSM real twisting algorithm was designed. In this work, we have explicitly added an extra dimension into 2-D manifold of [55, 56] by adding $\gamma\phi$ to it, thus evolving a 3-D manifold. By doing so the relative degree of the problem is decreased to 1 for control design using SMC. The problem of HOSM controllers for relative degree greater than one is the extra information demand of sliding surface parameters. Generally, the knowledge of the time derivative of the sliding variable up to $r-1$ order is required by any r^{th} order sliding controller [6]. This requires additional sensor units to be installed for measurement or some estimation routines to estimate the true values. Therefore HOSM controllers are generally computationally expensive and on the other hand if it needs to be implemented/estimated the control channel becomes noisy. For example, if the measured value from sensor is noisy and is used in surface implementation σ and for $r > 1$ it may be also used in $\dot{\sigma}$, thus noise added into the algorithm for HOSM is twice than the SMC.

Compared to the sliding surface in [55] where we had two tunable parameters α and β. Now we have three adjustable parameters α, β and γ for performance tuning of small and large track errors. These parameters can be tuned independently to achieve suitable performance and the constraint $\chi_E \leq \frac{\pi}{2}$ can be met. The nonlinear sliding surface therefore provides an extra edge over to the sliding surface presented earlier since the guidance (outer) loop is well aware of the inner loop dynamics.

6.3   Guidance Law Design: FOSMC Controller

The instantaneous location i.e., position of the UAV in the 2D plane is available to the guidance algorithm using on-board sensors. Figure 2.6 depicts the 2D vectorial representation of the vehicle and the aiming position by the guidance scheme which needs to be formulated. Continuous control is an interpretation of equivalent control which would maintain $\dot{\sigma} = 0$ if the dynamics are known exactly. For our case (6.2):

$$\dot{\sigma} = \dot{\chi}_E + \frac{\alpha\beta}{1 + \beta^2 y^2}\dot{y} + \gamma\dot{\phi} \tag{6.9}$$

Using (5.2), $\dot{\sigma}$ can be written as:

$$\dot{\sigma} = \frac{g}{V}\tan\phi - \dot{\chi}_R + \frac{\alpha\beta V}{1 + \beta^2 y^2}\sin\chi_E + \frac{\gamma\phi_E}{\tau} \tag{6.10}$$

The equivalent control $\phi_{E_{eq}}$ becomes:

$$\phi_{E_{eq}} = -\frac{g\tau}{V\gamma}\tan\phi + \frac{\tau}{\gamma}\dot{\chi}_R - \frac{\alpha\beta V\tau}{\gamma(1 + \beta^2 y^2)}\sin\chi_E \tag{6.11}$$

In the presence of uncertainties, to ensure sliding a discontinuous control term is added to the equivalent control (6.11) to obtain lateral guidance command i.e., $\phi_E = \phi_{E_{eq}} - k\,\mathrm{sgn}(\sigma)$.

$$\phi_E = -\frac{g\tau}{V\gamma}\tan\phi + \frac{\tau}{\gamma}\dot{\chi}_R - \frac{\alpha\beta V\tau}{\gamma(1 + \beta^2 y^2)}\sin\chi_E - k\,\mathrm{sgn}(\sigma) \tag{6.12}$$

For improved performance during circular path following, a feed-forward term is added to the guidance law (6.12). This feed-forward term $\arctan\left(\frac{V\dot{\chi}_R}{g}\right)$ is equal to the lateral acceleration required during a steady turn.

164

6.3.1 Complete guidance law

Now the final guidance law becomes:

$$\phi_E = -\frac{g\tau}{V\gamma}\tan\phi + \frac{\tau}{\gamma}\dot{\chi}_R - \frac{\alpha\beta V\tau}{\gamma(1+\beta^2 y^2)}\sin\chi_E$$
$$- k\,\mathrm{sgn}(\chi_E + \alpha\tan^{-1}(\beta y) + \gamma\phi) \tag{6.13}$$
$$+ \arctan\left(\frac{V\dot{\chi}_R}{g}\right).$$

where $\alpha,\beta > 0$, $\gamma > 0$ and $\alpha \leq 1 - \left(\frac{\gamma}{2}\right)$. The expression in (6.13) formulates the guidance law which takes lateral error y, intercept course χ_E and ϕ as inputs and generates a commanded bank angular error ϕ_E as output. Conditions on k are derived in the following subsection.

6.3.2 Reachability Condition

To ensure reachability, let us take following Lyapunov candidate function.

$$W = \frac{1}{2}\sigma^2 \tag{6.14}$$

The derivative of W is:

$$\dot{W} = \sigma\dot{\sigma} \tag{6.15}$$

Using the expression of (6.9),

$$\dot{W} = \sigma\left(\frac{g}{V}\tan\phi - \dot{\chi}_R + \frac{\alpha\beta V}{1+\beta^2 y^2}\sin\chi_E + \frac{\gamma\phi_E}{\tau}\right) \tag{6.16}$$

165

The control input ϕ_E from (6.12) is substituted in (6.16)

$$
\dot{W} = \sigma(\frac{g}{V}\tan\phi - \dot{\chi}_R + \frac{\alpha\beta V}{1 + \beta^2 y^2}\sin\chi_E + \frac{\gamma}{\tau}(-\frac{g\tau}{\widetilde{V}\gamma}\tan\phi + \frac{\tau}{\gamma}\dot{\chi}_R
$$
$$
- \frac{\alpha\beta\widetilde{V}\tau}{\gamma(1 + \beta^2 y^2)}\sin\chi_E - k\,\mathrm{sgn}(\sigma)))
$$

(6.17)

where $\widetilde{V}$ is the measured values of velocity. After simplification, we have:

$$
\dot{W} = -\sigma(-\frac{g}{V}\tan\phi - \frac{\alpha\beta V}{1 + \beta^2 y^2}\sin\chi_E + \frac{\widetilde{g}}{\widetilde{V}}\tan\phi
$$
$$
+ \frac{\alpha\beta\widetilde{V}\sin\chi_E}{(1 + \beta^2 y^2)} + \frac{\gamma k\,\mathrm{sgn}(\sigma)}{\tau})
$$

(6.18)

$\dot{W}$ will be negative definite if the following condition is satisfied:

$$
\left|\frac{\gamma k}{\tau}\right| > \left|\frac{g}{\widetilde{V}}\tan\phi - \frac{g}{V}\tan\phi + \frac{\alpha\beta\widetilde{V}\sin\chi_E}{1 + \beta^2 y^2} - \frac{\alpha\beta V\sin\chi_E}{1 + \beta^2 y^2}\right|
$$

(6.19)

or

$$
|k| > \frac{\tau}{\gamma}|\tan\phi|\left|\frac{g}{\widetilde{V}} - \frac{g}{V}\right| + \frac{\alpha\beta\tau}{\gamma(1 + \beta^2 y^2)}|\sin\chi_E|\left|\widetilde{V} - V\right|
$$

(6.20)

Analyzing the above expression, we can further simplify it by incorporating the maximum values of variables on R.H.S. of equation as:

- The maximum value of $|\tan\phi|$ is equal to 1 for $\phi = \pm 45°$.

- The maximum value of $|\sin\chi_E|$ is equal to 1 for $\chi_E = \pm 90°$.

- The term y when minimum, maximizes the above expression, therefore $y \approx 0$ is the worst case.

We neglect the error in the gravity term and assume a worst case error of 10% in the measurement of velocity (i.e., $\widetilde{V} \approx 1.1V$). Now, for all the controlled flight

envelope $\dot{W}$ will be negative definite, only if:

$$k \geq \frac{\tau}{\gamma}(1)\left|\frac{g}{\widetilde{V}} - \frac{g}{V}\right| + \frac{\alpha\beta\tau}{\gamma}(1)\left|\widetilde{V} - V\right| \tag{6.21}$$

or alternatively in simplified form as:

$$k \geq \frac{\tau g}{\gamma V}(0.091) + \frac{\alpha\beta\tau V}{\gamma}(0.1) \tag{6.22}$$

Throughout the controlled region of operation, the reachability condition $\sigma\dot{\sigma} < 0$ will be satisfied if gain k is selected according to the expression in (6.22). Hence the state trajectories from any initial condition will always be forced towards the sliding manifold. And once these trajectories hit the manifold shall be forced subsequently to stay on it while sliding towards the equilibrium point.

Finite time convergence :

The designed control law performance is completely determined by the selection of sliding manifold parameters. For discontinuous control laws, the selection of these parameters can improve the response time of a system. Here for the proposed sliding manifold as in (6.1), the η-reachability condition is satisfied with k as in (6.22). We now derive the expression for reaching time showing finite time convergence according to (2.6). From (6.18), the difference between the actual and measured value is the uncertainty therefore

$$\left|\frac{g}{\widetilde{V}}\tan\phi - \frac{g}{V}\tan\phi + \frac{\alpha\beta\widetilde{V}\sin\chi_E}{1 + \beta^2 y^2} + \frac{\alpha\beta V\sin\chi_E}{1 + \beta^2 y^2}\right| \leq \xi \tag{6.23}$$

the expression in (6.18) can be further simplified into the form

$$\dot{W} \leq |\sigma|\left(\xi - \frac{\gamma k}{\tau}\right) \tag{6.24}$$

Comparing it with the (2.6) condition i.e., $\sigma\dot{\sigma} \leq -\eta\,|\sigma|$

$$|\sigma|\left(\xi - \frac{\gamma k}{\tau}\right) = -\eta\,|\sigma| \tag{6.25}$$

Finally the control gain k is computed that ensures $\dot{W} \leq -\eta\,|\sigma|$

$$k = \frac{\tau}{\gamma}\left(\xi + \eta\right) \tag{6.26}$$

Now we can derive the expression for calculating the reaching time from (2.11)

$$t_{r_n} = \frac{|\chi_E + \alpha\arctan(\beta y) - \gamma\phi|}{\eta} \tag{6.27}$$

where the value of η can be selected using the expression in (6.22). The controller gain k in (6.22) has two portions according to (6.26). First that caters for ξ i.e., the uncertainty present in the system and the second part that provides finite time convergence using η. The control law ϕ_E in (6.12) will attract y, χ_E and ϕ on to the sliding manifold σ in (6.1) in finite time t_{r_n} in the presence of bounded uncertainty ξ.

6.3.3 Boundedness of ϕ

Stability of ϕ_E doesn't guarantee the boundedness of ϕ which also needs to be ensured. We can devise a logic to bound ϕ: if $|\phi| \geq \phi_{max}$ then ϕ_E is forced to zero. In this case the UAV will keep turning towards the desired path with $\phi = \phi_{max}$ and try to minimize the cross track y and intercept course χ_E as quickly as possible. The dynamics of the system will be driven towards the sliding manifold σ in (6.1). Whenever a new ϕ_E is generated with a sense to reduce the magnitude of ϕ away from ϕ_{max}, the same will be passed on to the inner control loop and the guidance loop will become active again.

6.4 Flight Test Results

6.4.1 Implementation Issues

From implementation point of view, if we directly implement the control expression in (6.13), then the actuators will face heavy switching due to the *signum* function and may get damaged after a while. Due to this approximation, the real sliding occurs instead of ideal sliding i.e., the state trajectories are restrained to a small vicinity of the sliding manifold rather than σ exactly equal to zero. Therefore the expression for ϕ_E in (6.13) render the form

$$
\begin{aligned}
\phi_E = -\frac{g\tau}{V\gamma}\tan\phi + \frac{\tau}{\gamma}\dot{\chi}_R - \frac{\alpha\beta V\tau}{\gamma(1+\beta^2 y^2)}\sin\chi_E \\
- k\frac{\chi_E + \alpha\tan^{-1}(\beta y) + \gamma\phi}{|\chi_E + \alpha\tan^{-1}(\beta y) + \gamma\phi| + \epsilon} \\
+ \arctan\left(\frac{V\dot{\chi}_R}{g}\right)
\end{aligned}
\tag{6.28}
$$

Due to the approximation, it is acceptable to bound system trajectories within defined neighborhood of the sliding manifold. Gain reduction also affects the reachability condition that should be ensured to slide the system states trajectory in the neighborhood of sliding surface. In our case, for flight performance we target $|y| \leq 12$ m, $|\chi_E| \leq 1°$ and $\phi \leq 3°$, this implies $|\sigma| \leq 0.1354$, thus we selected $|\sigma| < 0.15$. In this case the width of the boundary layer will be 0.3. We selected $\epsilon = 0.3$ and for $\sigma = \pm 0.15$, yields $\frac{\sigma}{|\sigma|+\epsilon} = \pm 0.3333$. It can be implied that at the edges of the boundary layer, the actual gain delivered to the system is one third of the selected gain value. Negative definiteness of $\dot{W}$ must be ensured for the reduced effective gain. In our case, we have selected larger gain $'k'$ (3 times more than the minimum required) to ensure reachability condition in the neighborhood of sliding surface and this ensures $|\sigma| < 0.15$ with boundary layer approximation.

6.4.2 Parameter Selection

The sliding manifold parameters i.e., α, β and γ are selected first in accordance with the desired performance. The value for k is selected in accordance with the reachability condition in (6.22). The selected parameters are tabulated in 6.1

TABLE 6.1: Guidance Law Parameters

#	Parameter	Value
1	α	0.9
2	β	0.01
3	γ	0.1
4	k	0.95
5	τ	0.3
6	ϵ	0.3

6.4.3 Mission-1 Small cross track error

Figures 6.7 – 6.9 show the flight results of path following of UAV for a small lateral deviation of 200 m. In Figure 6.7, the time plots of track error y and intercept course χ_E are shown; the proposed scheme takes $\sim$ 15 sec to minimize the error from 200 m to 7 m. In the initial few seconds, χ_E is adequately large to reduce the lateral error y quickly. Thus, good performance is achieved and the track error is reduced smoothly to zero. The commanded bank error ϕ_E is shown in Figure 6.8 along-with the controller output δ_a. The maximum roll angle of the vehicle while following Mission-1 is less than 45°. The proposed 3-D sliding surface along with system states trajectory is shown in Figure 6.9. From these results it is clear that the designed framework provides good performance for small track errors.
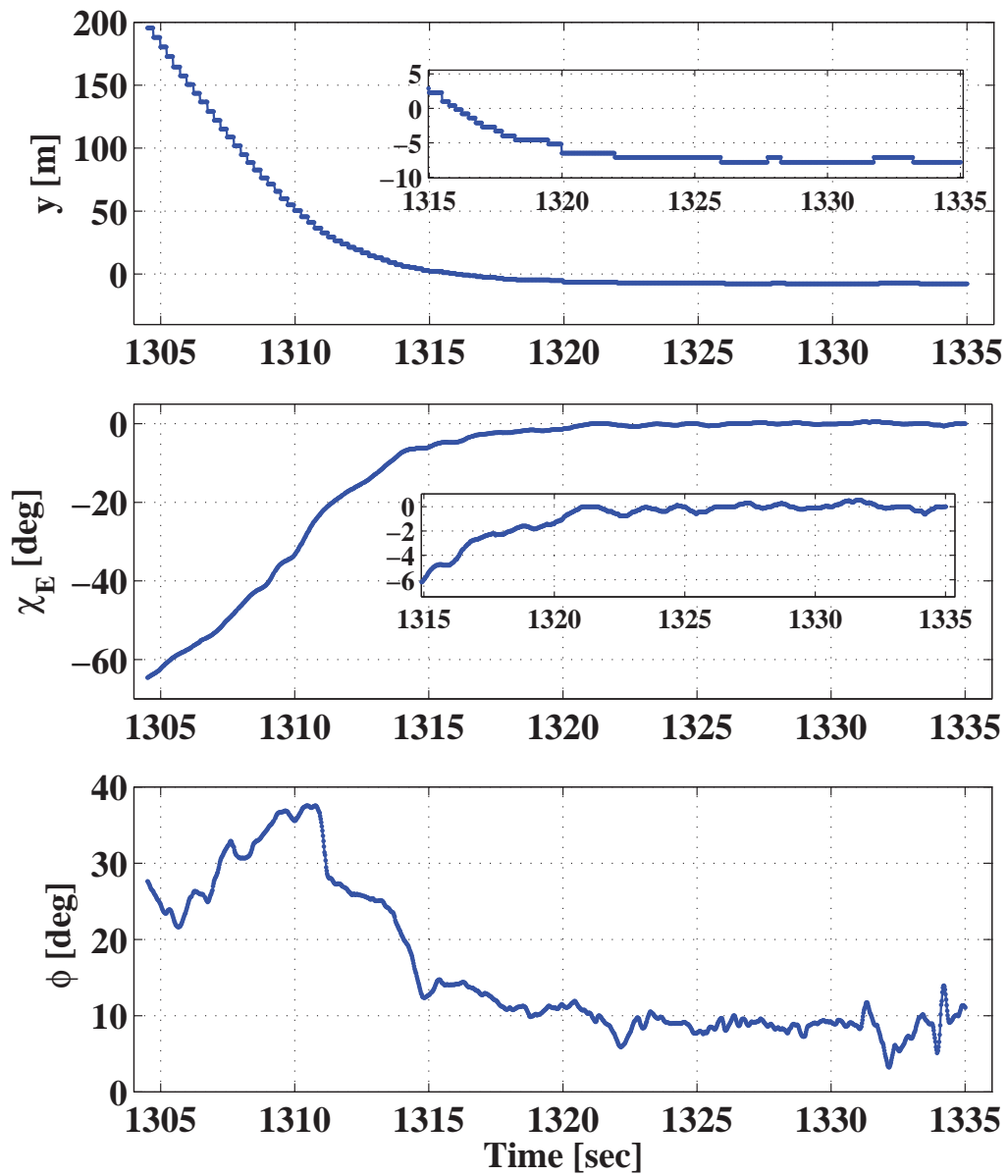
FIGURE 6.7: Cross Range y, intercept Course χ_E with corresponding ϕ for Mission-1
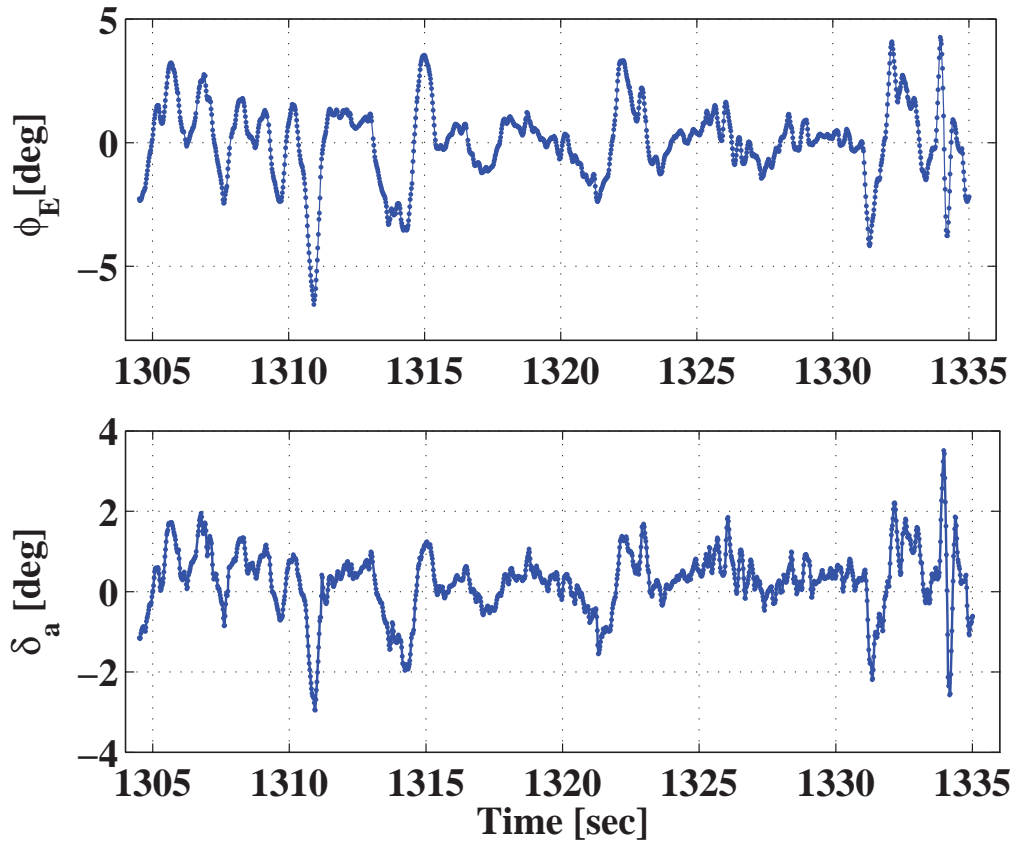
FIGURE 6.8: Commanded reference ϕ_E and control actuation δ_a for Mission-1

6.4.4 Mission-2 Large track error with sharp heading

Mission-2 demonstrates the flight results of the proposed scheme for following a straight segment with a large initial lateral deviation followed by a sharp heading change as shown in Figure 6.10 – Figure 6.13. The desired mission plan and the trajectory followed by the UAV is shown in Figure 6.10. The mission-2 is divided into three parts: a straight path $WP1 \rightarrow WP2$, a sharp turn (heading change of 133°), followed by another straight segment $WP2 \rightarrow WP3$. The key performance measure is the resulting miss distance from the path. For $WP1 \rightarrow WP2$, the guidance scheme is able to reduce the error y in the vicinity of 5 to 7 m from the initial deviation of 600 m with an intercept course χ_E of 145° as shown in Figure 6.10. It is followed by a sharp heading change to follow $WP2 \rightarrow WP3$

172
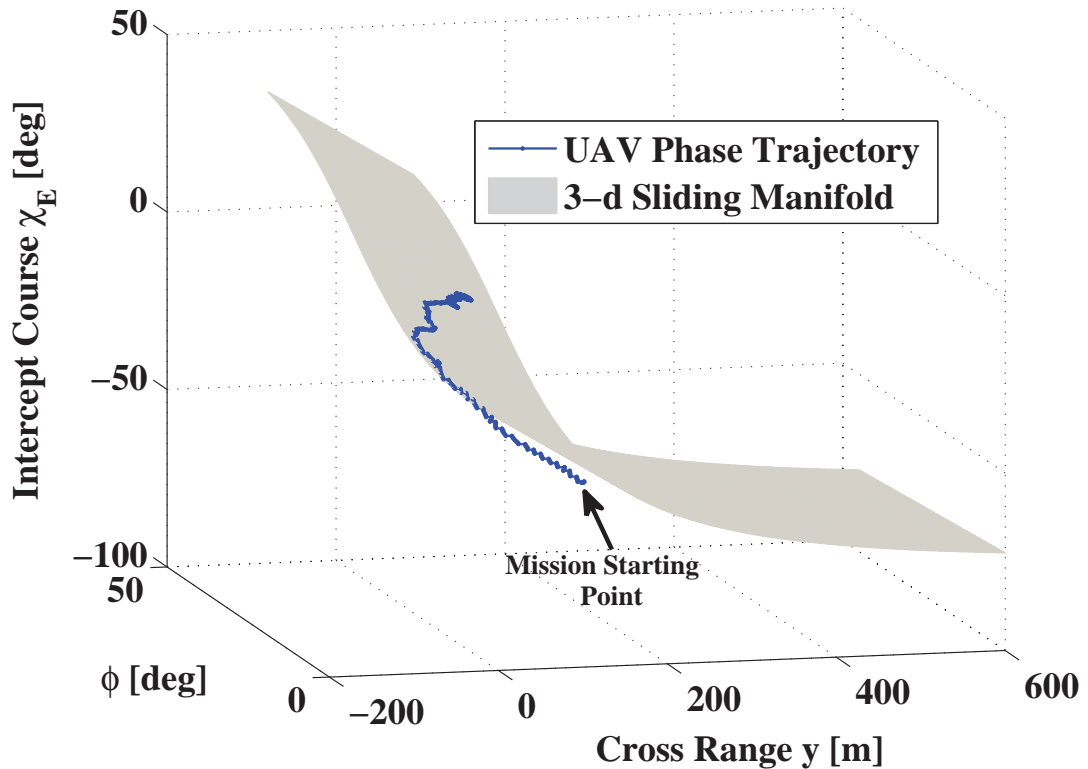
FIGURE 6.9: Phase portrait of UAV trajectories for Mission-1

with lateral deviation of 400 m, for this case also it is reduced to 6 to 7 m.

It is quite clear from the Figure 6.12 that the guidance reference commands are well behaved. Since the guidance algorithm generates reference commands based on the 3-D sliding manifold, the position of the states are attracted towards this manifold and then slide along to reach vicinity of zero (Figure 6.13). The corresponding results of the new design show both robustness and performance. The resultant control effort δ_a is shown in Figure 6.12 and it is evident that the control effort is within the desired limits. The control actuation i.e., aileron deflection well behaved and less than 5°.

6.4.5 Mission-3 Curved path

Figure 6.14 shows the 2-D scenario for following curved arcs by the guidance scheme, the reference trajectory is shown in dotted red, whereas the actual trajectory flown is shown in solid blue line. The proposed guidance scheme (Figure 6.14)

173
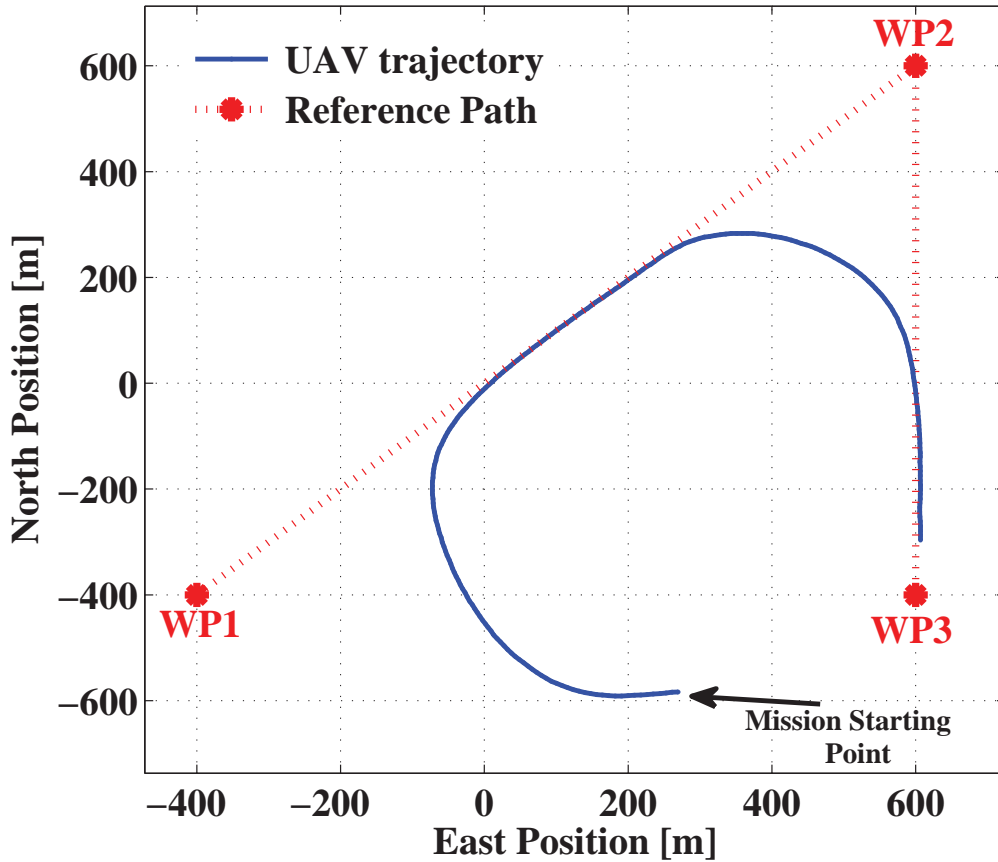
FIGURE 6.10: Mission-2 reference path and UAV trajectory

follow the same trend as that of the desired input profile with acceptable accuracy. Figure 6.15 shows the lateral error y and intercept course χ_E versus time, the error is maximum at the start of mission, however the guidance algorithm drives it down to less than 10 m quickly. The guidance output i.e., ϕ_E in Figure 6.16 keeps the vehicle bank angle well below the saturation limit of 45°. It is evident that the commanded values are accurately tracked by the control law, as these commands are generated based on the information of the autopilot loop.

In Figure 6.16, the nominal aileron deflection δ_a is well below the saturation limit of 5°. This shows the capability of the design in capturing the more realistic depiction of the actual plant. Figure 6.15 show the lateral error y, intercept course χ_E and roll angle ϕ for two different circular profiles. It can be seen that the profile representing the desired course with proposed design is followed quite

174
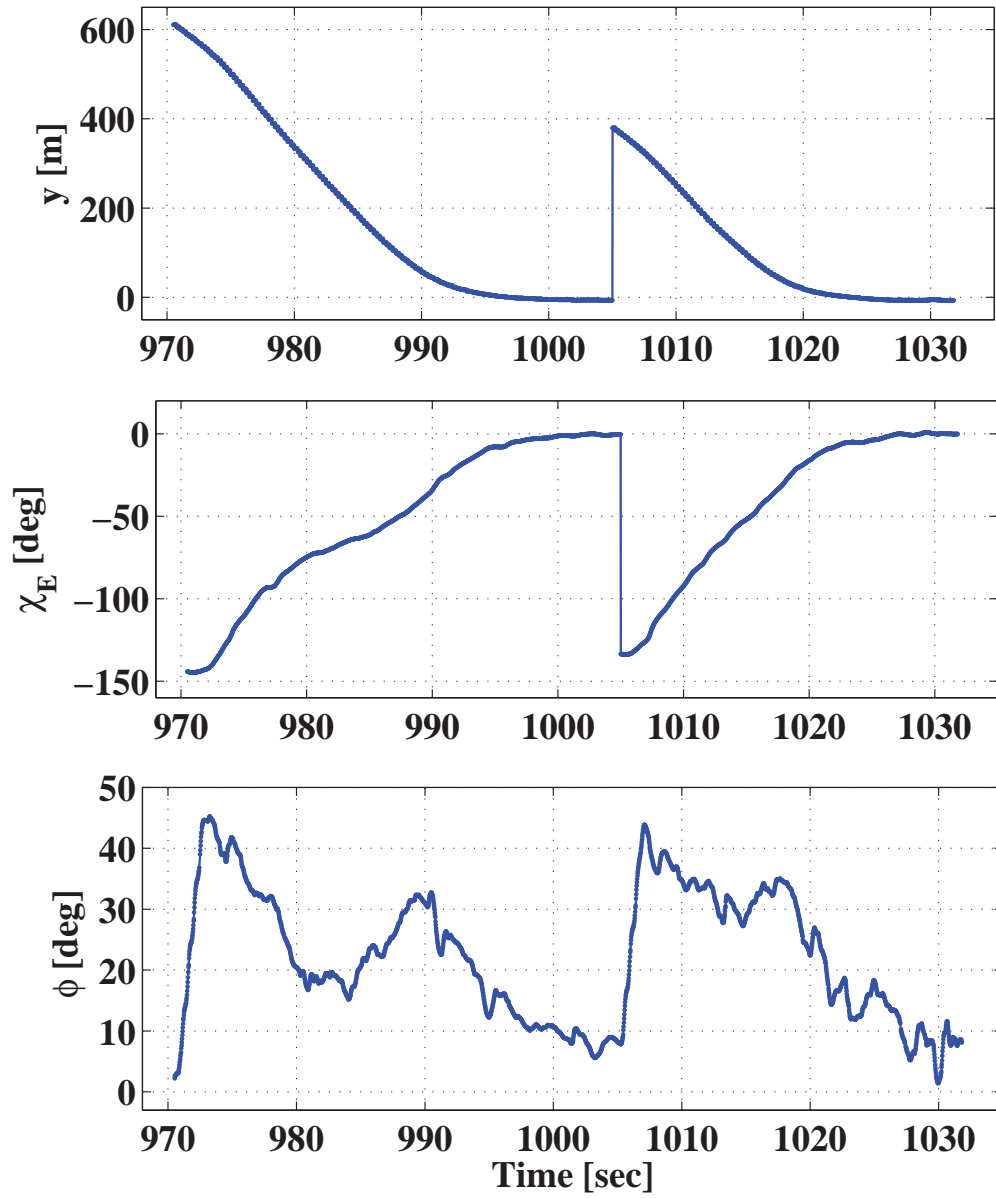
FIGURE 6.11: Cross Range y, intercept Course χ_E and corresponding ϕ for Mission-2
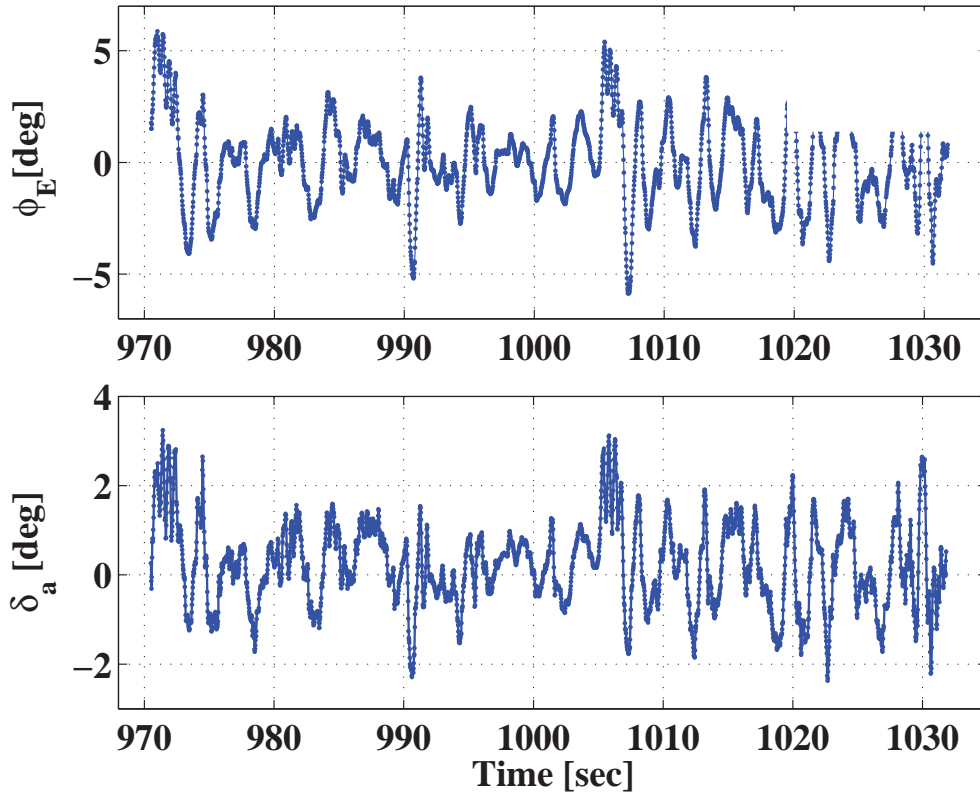
FIGURE 6.12: Commanded reference ϕ_E and control actuation δ_a for Mission-2

efficiently by the UAV. As seen in Figure 6.14 when the mission is changed to follow a different circle the UAV quickly adapts and change its course towards desired course and minimizes the error quickly. This implies that the proposed design provides prompt response to operator command while ensuring good performance and robustness against disturbances.

6.4.6 Mission-4 Loiter pattern

For a loiter mission, flight results are shown in Figure 6.17 – Figure 6.18. The desired path to follow (dotted red) and the actual flight path (solid blue) of the vehicle is shown in Figure 6.17. The origin is the take off point, the distance traveled towards north is denoted by North position, while distance traveled towards east is denoted as East position. At the corners for smooth transition, way-point switch algorithm is continuously active and when error y reduces to 300 m, it issues leg shift command. Thereafter the lateral error y is determined according to the next
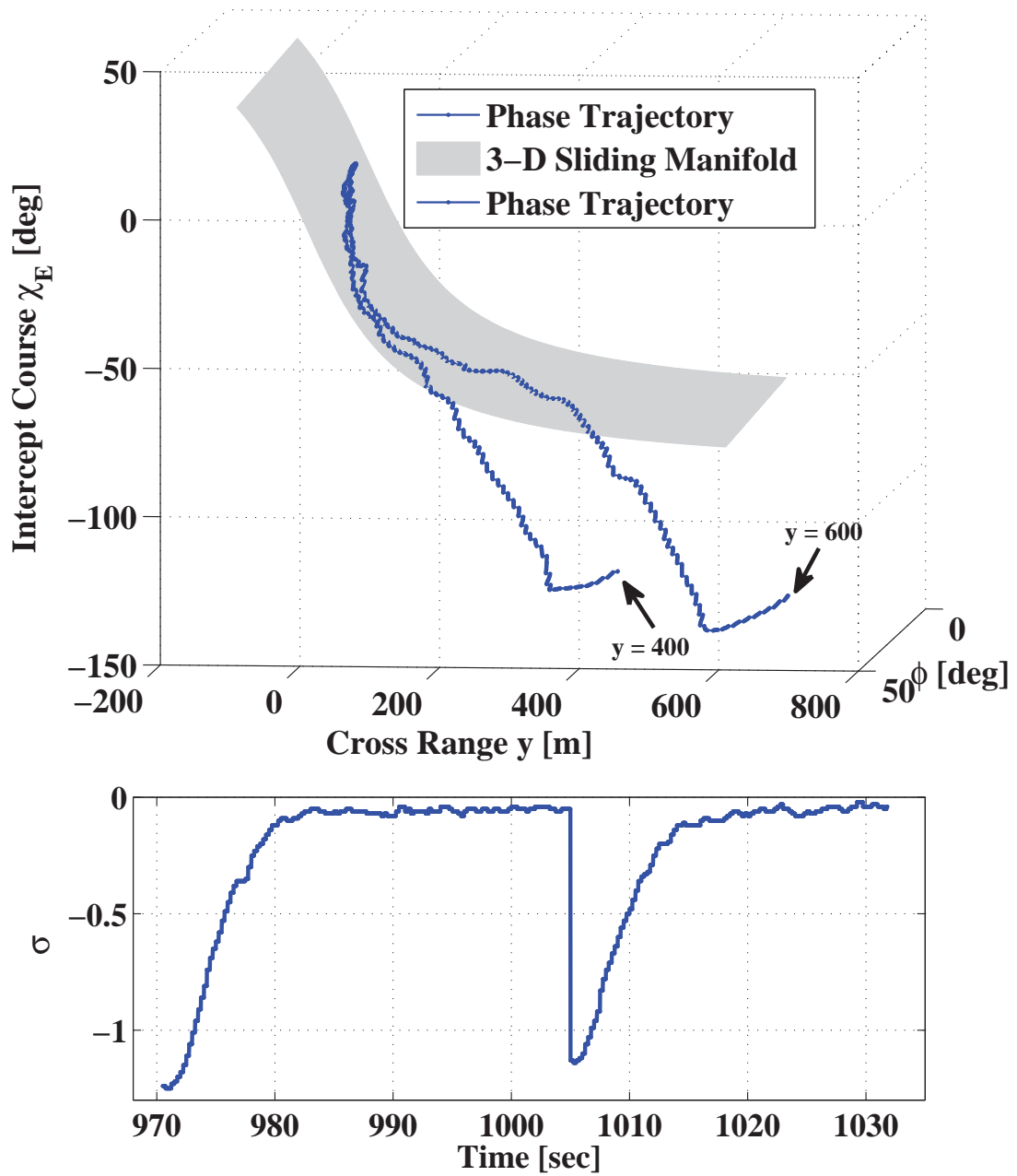
FIGURE 6.13: Phase portrait of UAV trajectories and sliding surface σ for Mission-2
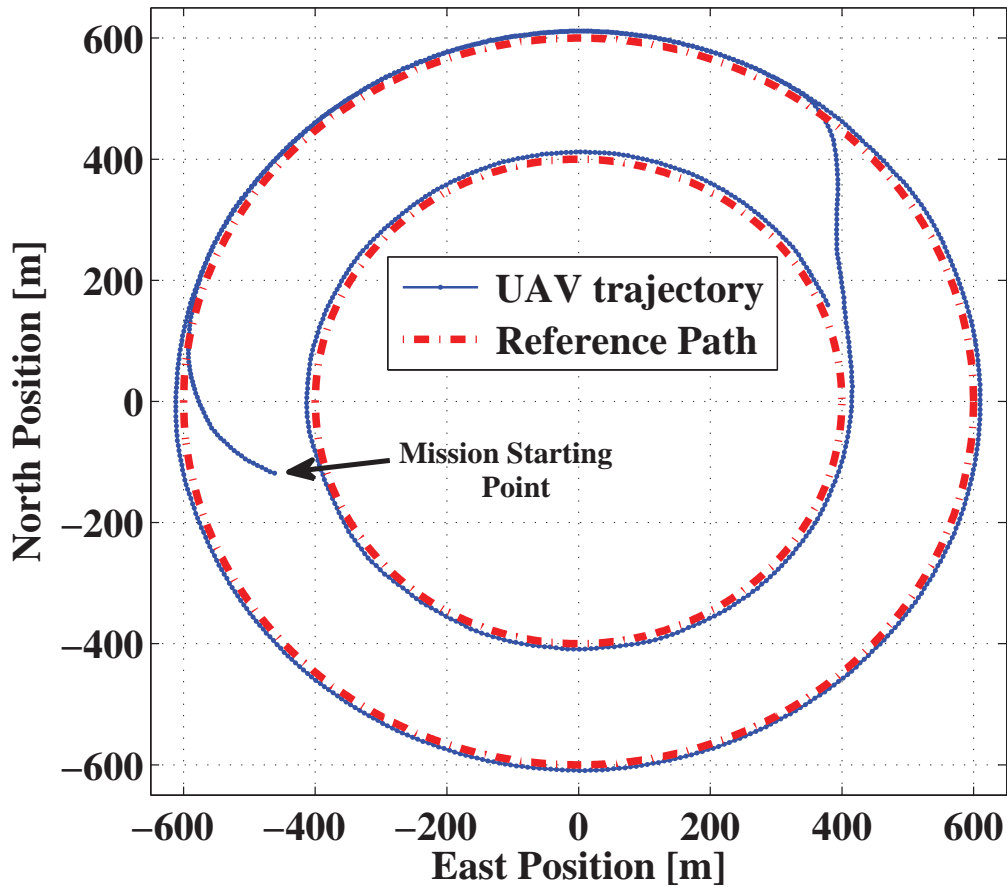
FIGURE 6.14: Mission-3 circular reference path and the UAV trajectory

reference leg of the mission and a smooth curve is flown inside the corner point by the vehicle. In this case also the proposed algorithm provides good performance. The algorithm generated the maximum commanded roll (reference) less than 42° for this mission. The proposed guidance algorithm was efficiently able to follow the complete loiter mission with lateral track steady state error of 6 m to 7 m. It is evident from these figures that the controller developed in (6.13) is able to provide cross track error and heading error regulation. In this case also the surface trajectory is brought to the vicinity of zero as in Figure 6.18 using (6.13).

6.4.7 Flight Comparison

A comparison study is given below for the proposed guidance scheme with existing algorithm in [55] with σ_z as nonlinear manifold. Flight results for approximately
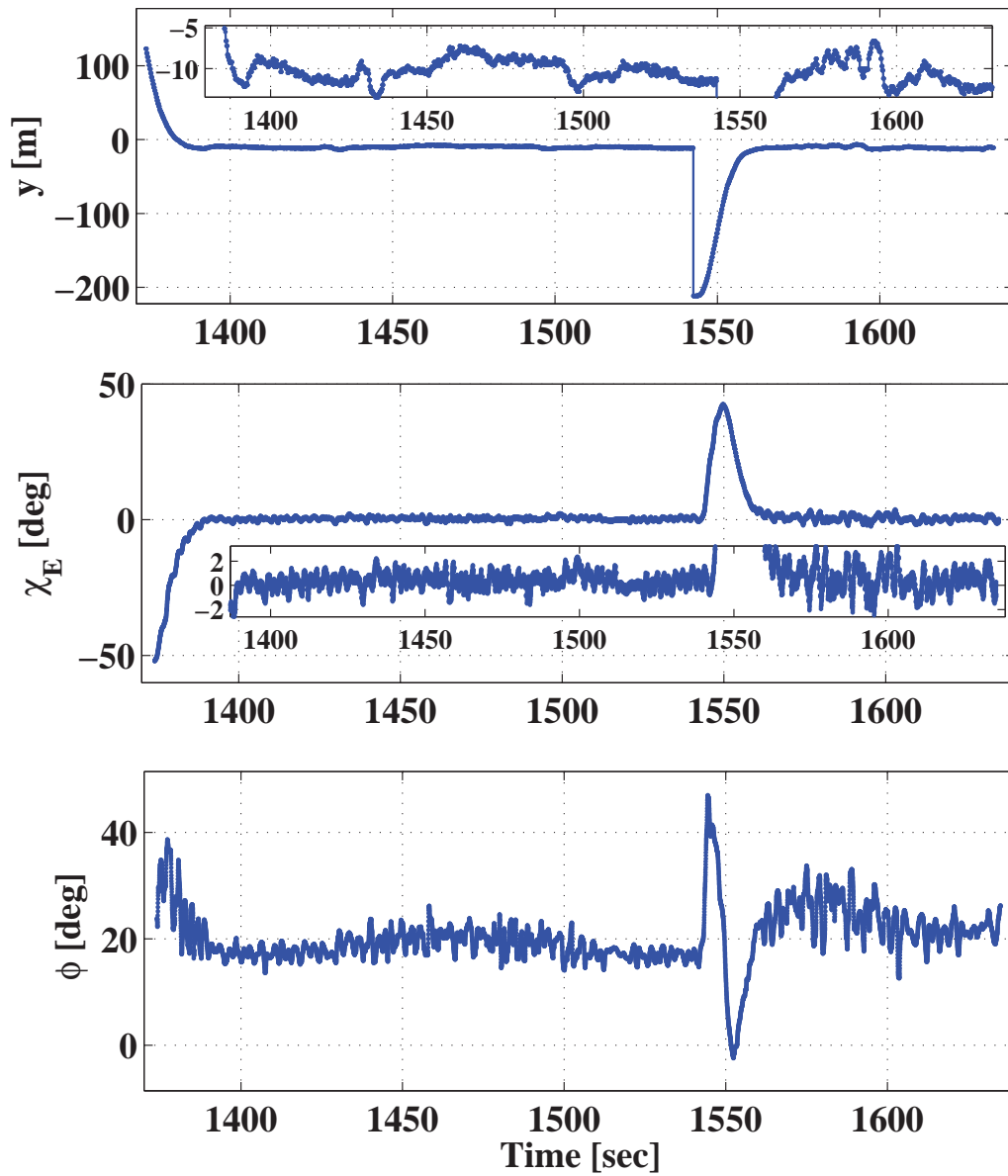
FIGURE 6.15: Cross Range y, intercept Course χ_E and roll angle ϕ for Mission-3
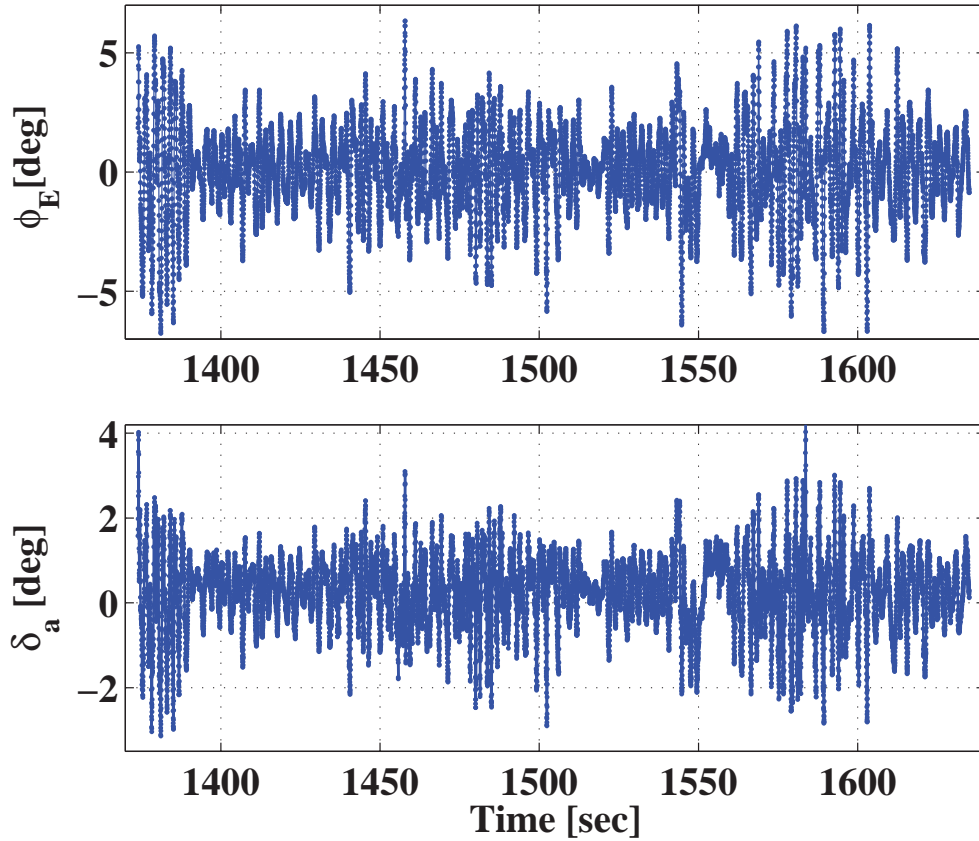
FIGURE 6.16: Commanded ϕ_E and aileron deflection δ_a for Mission-3

similar initial conditions are shown in Figure 6.19 and Figure 6.20. The sliding parameters are selected such that cross track error convergence is almost similar for both sliding manifolds.

For lateral track error of 300 m, results are shown in Figure 6.19 and Figure 6.20. The trajectory of the states i.e., lateral track error y, intercept course χ_E and corresponding ϕ with two different surfaces σ_z and σ are shown in Figure 6.19. The steady state cross track error for the two cases is not very different, yet with proposed σ it is a little smaller. For both the schemes, the roll angle ϕ is well below the maximum limit ϕ_{max}. The important aspect is the reaching time for both sliding manifolds. The proposed sliding manifold σ is capable of driving the states towards zero faster than the surface σ_z as evident from Figure 6.20 and Figure 6.21. The time taken by σ to reach the origin is ~6 sec and for the σ_z
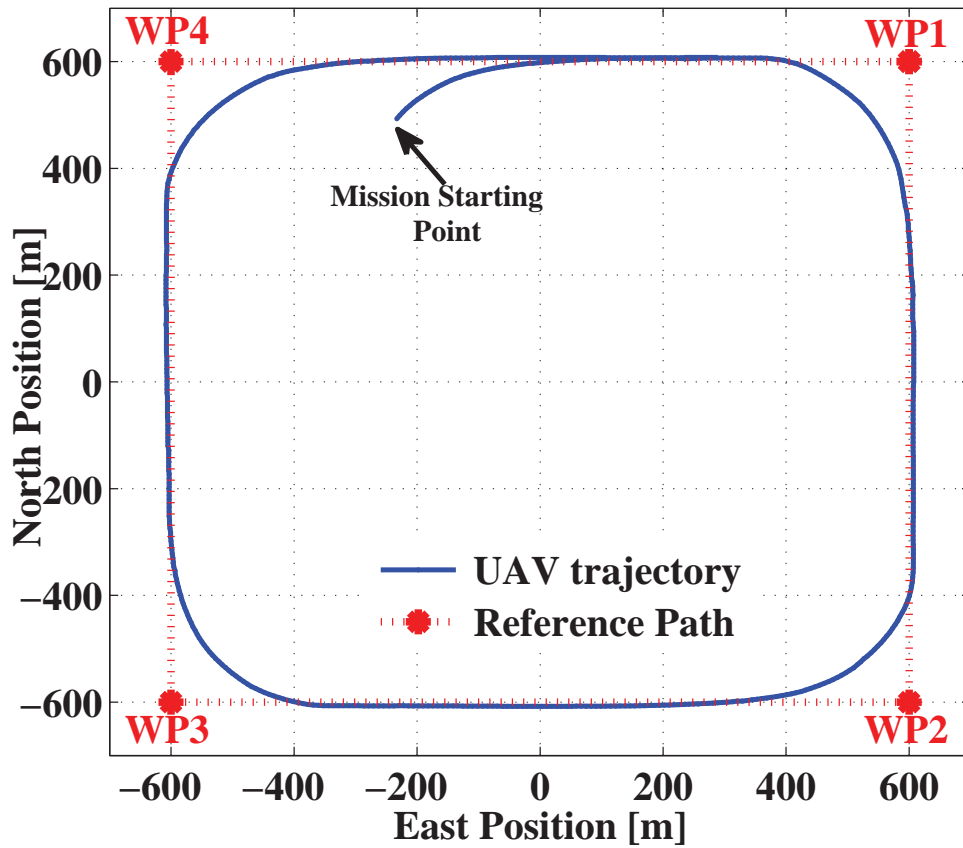
FIGURE 6.17: Mission-4 loiter reference path and the UAV trajectory

it is ∼14 sec. Thus we can say that design of SMC using σ is more robust for this application and less prone to disturbances and uncertainties. The trajectories will quickly reach the surface, thus restoring invariance property as evident from Figure 6.21.
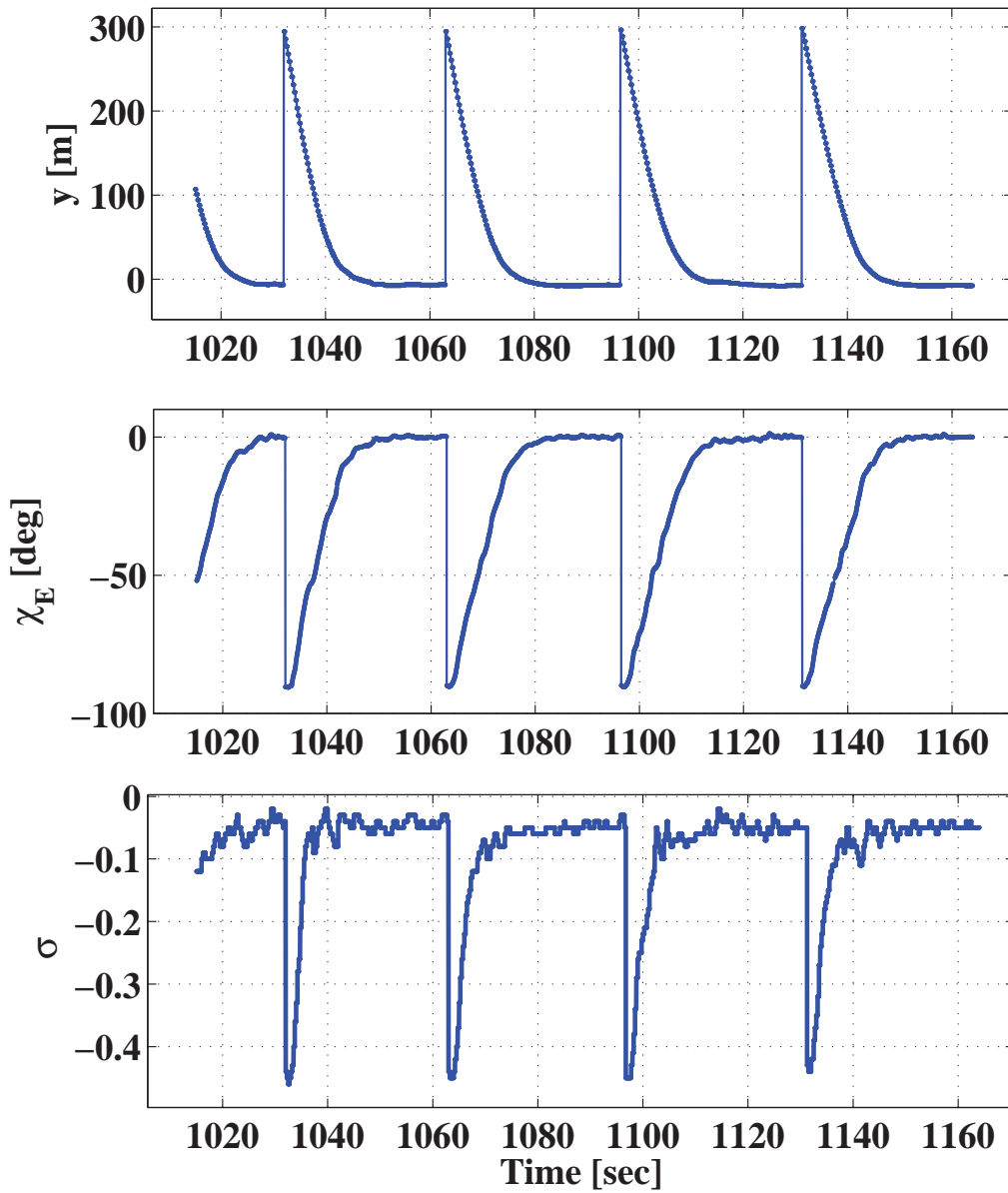
FIGURE 6.18: Cross Range y, intercept Course χ_E and sliding Surface s for Mission-4
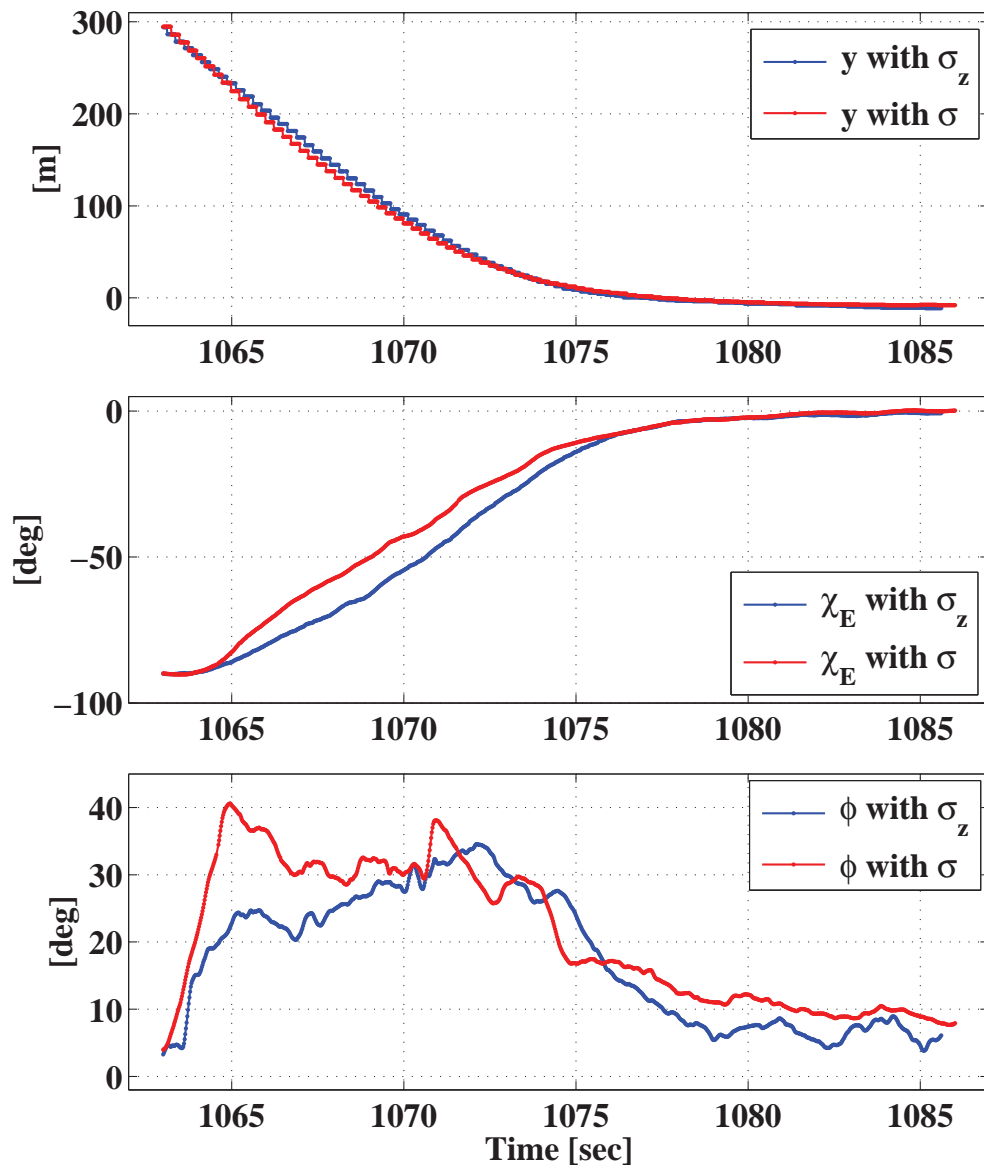
FIGURE 6.19: Flight data comparison of lateral error y, intercept course χ_E and ϕ with σ_z and σ
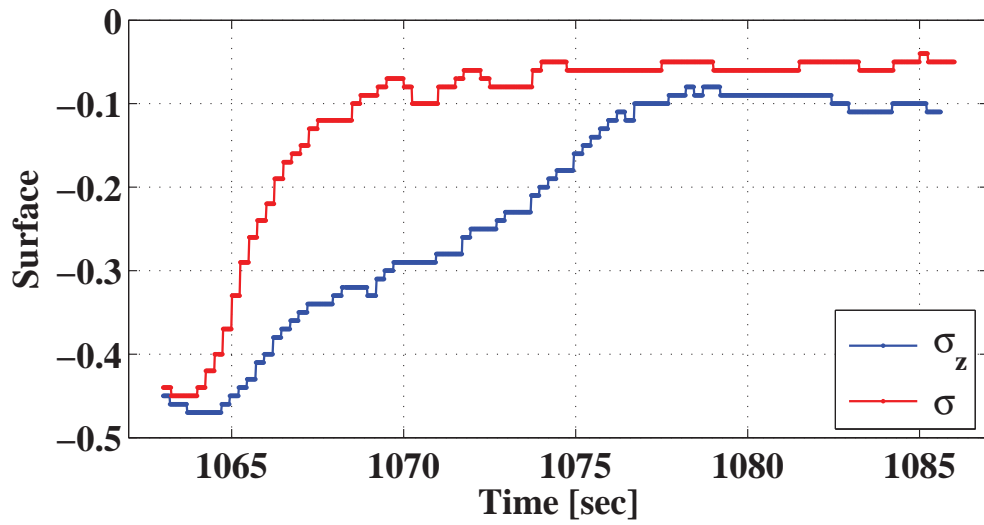
FIGURE 6.20: Flight data comparison of σ_z and σ
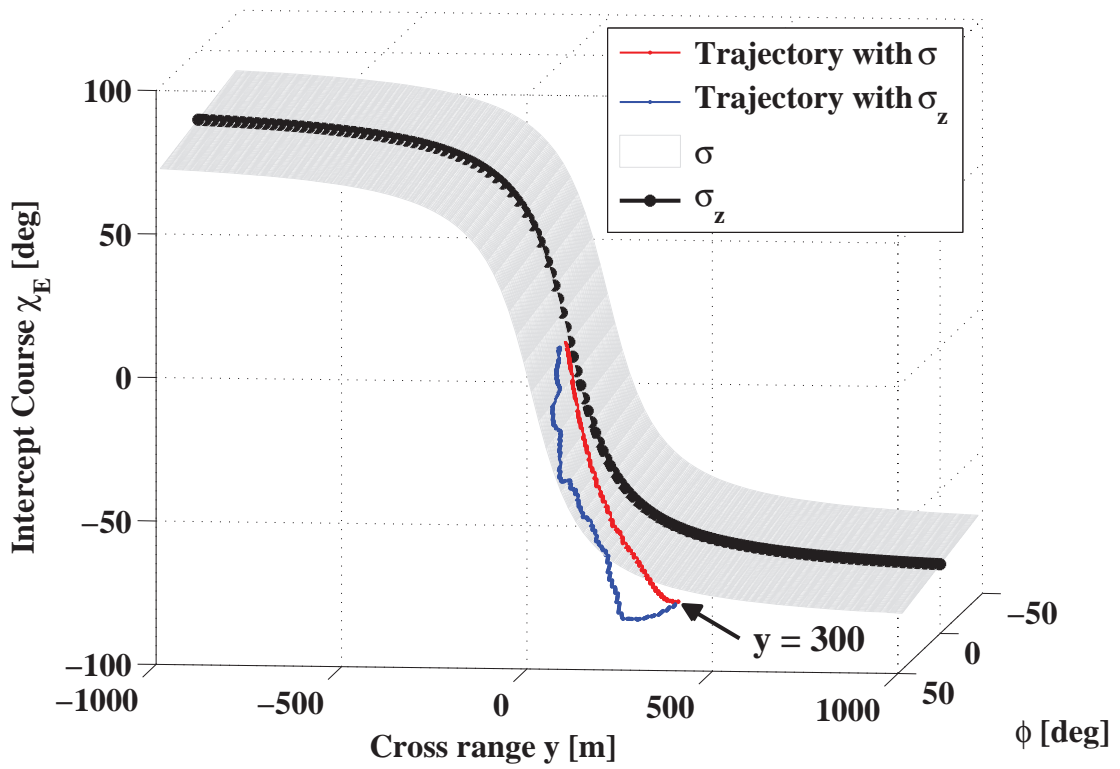
FIGURE 6.21: Flight data comparison of σ_z and σ

6.5   Conclusion

For ground track control of UAVs, a nonlinear path following scheme has been proposed and demonstrated. A novel solution was presented based on an inner-outer control structure with dynamical characteristics known to the outer loop. A 3-D nonlinear sliding manifold is proposed for lateral path following guidance of UAVs, which provides additional benefits compared to the existing 2-D manifolds in literature. For large and small lateral track errors, the proposed sliding manifold provides good performance. A feed forward term is included to the guidance law i.e., the additional bank required for better performance and accurate tracking of curved segments. Stability conditions are derived in terms of lower bound on the control gain and control boundedness is also ensured. The proposed sliding mode guidance law performs well in the presence of autopilot constraint, the control input channel does not saturate and good helmsman criteria is also met with designed stabilization function. As a result, the guidance solution presented is well suited for path following application for UAVs.

Chapter 7

CONCLUSION AND FUTURE WORK

In this dissertation, we focus on devising the path following strategies while considering the autopilot constraints in the presence of uncertainties and disturbances like wind. To achieve this goal, several studies for robust guidance and control systems are conducted using sliding mode theory, which include designing of guidance algorithms with high performance sliding manifolds, the designing of path following algorithms with autopilot dynamics in the loop, a new partially integrated guidance and control design and a novel robust sliding manifold for lateral path following applications. To demonstrate the effectiveness of the proposed algorithms, schemes are designed and tuned for research UAV scaled YAK-54 UAV for flight testing. However, the algorithms can be easily reconfigured for other UAVs to support research efforts associated with guidance and control of UAVs. The main contributions and results are summarized as follows.

7.1   Conclusion

- In **Chapter 3 "Nonlinear Sliding Manifolds"**

  Two novel nonlinear sliding surfaces are proposed, first to provide high performance and other with low computational complexity. The proposed manifolds provide additional benefits compared to existing manifolds in the literature. For lateral path following applications of UAVs, two new FOSMC guidance strategies are devised with the proposed manifolds. The manifolds' stability along with the existence of sliding mode and control boundedness is proved. We also demonstrate asymptotic Lyapunov stability of the nonlinear guidance law. The flight experiment analysis validates the proposed guidance framework and illustrates the effectiveness of the method. However, the analysis of the scheme shows that the framework relies on an assumption of

$\phi_{ref} \approx \phi$ in deriving the guidance law, which is later relaxed with HOSM based design.

- In **Chapter 4 "HOSM based Lateral Guidance with Autopilot Constraint"**

A robust nonlinear guidance framework using Higher order sliding mode control theory based on a nonlinear sliding surface is presented. The kinematic model was augmented with an extra state to incorporate the autopilot dynamics. Derivation of the guidance law with autopilot dynamics from ϕ_{ref} to ϕ resulted in a relative degree two problem for which the real twisting algorithm is used. Stability and control boundedness analysis for the proposed algorithm are performed. Flight performance of the algorithm is investigated for different cases of straight and curved path tracking. It is seen that the algorithm provides good performance driving the cross-track error to within a few meters. However the analysis of the designed framework suggests that with Partially Integrated guidance and control structure i.e., using the rate command as direct control instead of angular commands can speed up the response.

- In **Chapter 5 "Partially Integrated Guidance and Control (PIGC) Scheme"**

A path following guidance and control scheme is developed based on partially integrated guidance and control design which combines the benefits of both integrated guidance and control as well as the conventional guidance and control (two separate loops) design philosophies. The theoretical framework is based on path following in 2-D space using the SOSM real twisting algorithm for guidance, along with a SOSM super twisting algorithm for inner loop control. The guidance and control strategy effectively copes for the autopilot dynamics, and maintains performance for both small and large lateral errors. PIGC structure combined with manifold augmentation is exploited

here to provide faster convergence using angular rate commands. Experimental flight results for conventional two loop scheme and PIGC approach are compared to show that PIGC provides faster convergence of cross track error and intercept course towards zero. However, the PIGC scheme with HOSM reveals that due to higher relative degree of the system, more information is required and these measurements are noisy which has an adverse effect on the control channel. Therefore to incorporate autopilot dynamics an improved sliding surface should be designed, which should be the subject of future research.

- In **Chapter 6 "3-D Sliding Manifold for Lateral Guidance"**

  For ground track control of UAVs, a nonlinear path following scheme is proposed. A novel 3-D nonlinear sliding manifold is proposed for lateral path following guidance of UAVs which provides additional benefits compared to the existing 2-D manifold. Using the proposed 3-D nonlinear sliding manifold autopilot dynamics are incorporated into the guidance scheme. Further, FOSMC lateral design scheme is designed with the 3-D manifold. Control boundedness and stability conditions are derived in terms of lower and upper bound on the control gain. The proposed sliding mode guidance law performs well in the presence of autopilot constraint, the control input channel does not saturate and good helmsman criteria is also met with the designed stabilization function. Experimental flight results show the efficacy of the proposed scheme.

7.2 Future Research Directions

A number of potential avenues may be explored in the future work based on the contributions and results of this dissertation. In this section, we propose several possible directions.

- It will be interesting to design a lateral guidance scheme with FOSMC in which the sliding manifold is designed in a different form with relative degree

one with an aim to guarantee desired motion in the sliding mode and also incorporating the autopilot dynamics.

- One improvement is to devise an integrated guidance and control scheme by exploiting the synergy between guidance and control subsystems. An integrated guidance and control scheme may be explored which provides better realization of faster and slower dynamical variables besides providing an automated tuning criterion.

- The manifold coefficients are tuned for best performance, an optimization scheme based on work and energy principle may be devised to select these parameters. A criterion for the best selection yielding the minimum travel path may be explored.

- In all the strategies discussed, fixed controller gain is used satisfying reachability and control boundedness conditions. However, it can be made adaptive using adaptive sliding mode control, thus providing faster convergence as well as ensuring bounded control commands.

- An idea of fuzzy sliding mode control can be devised where the sliding manifolds are selected based on region of operation. A function between intercept course and lateral error can be realized by fuzzy system with fuzzy rules. In the systems with uncertainties, the discontinuous switching gain in conventional sliding mode control can also be replaced with fuzzy logic control to obtain a chatter free control input.

REFERENCES

[1] Foris A. Pappoullis. Cross track errors and proportional tuning rate guidance of marine vehicle. *Journal of Ship Research*, 38:123–132, 1994.

[2] G.M. Siouris. *Missile Guidance and Control Systems*. Springer, 2004.

[3] Marius Niculescu. Lateral track control law for Aerosonde UAV. In *39th AIAA Aerospace Sciences Meeting and Exhibit*, Reno, NV, USA, January 2001.

[4] S. Park, J. Deyst, and J.P. How. A new nonlinear guidance logic for trajectory tracking. In *AIAA Guidance, Navigation, and Control Conference and Exhibit*, pages 941–956, Providence, Rhode Island, USA, 16-19 August 2004.

[5] J.J. Deyst, J.P. How, and S. Park. Lyapunov stability of a nonlinear guidance law for UAVs. In *AIAA Atmospheric Flight Mechanics Conference and Exhibit*, San Francisco, CA, USA, 15-18 August 2005.

[6] W. Perruquetti and J.P. Barbot. *Sliding Mode Control In Engineering*. Automation and Control Engineering. CRC Press, 2002.

[7] A. Levant. Sliding order and sliding accuracy in sliding mode control. *International Journal of Control*, 58(6):1247–1263, 1993.

[8] R. Wise. *UAV Control and Guidance for Autonomous Cooperative Tracking of a Moving Target*. PhD thesis, Department of Aeronautics and Astronautics, University of Washington, 2006.

[9] Elisa Capello, Giorgio Guglieri, Paolo Marguerettaz, and Fulvia Quagliotti. Preliminary assessment of flying and handling qualities for mini-UAVs. 65(1-4):43–61, 2012.

[10] Raza Samar, Shakil Ahmed, and Muhammad Nzar. Lateral guidance & control design for an unmanned aerial vehicle. In 17th *IFAC World Congress Seoul, Korea*, volume 17, pages 4737–4742, 2008.

[11] M. Zamurad Shah, R. Samar, and A. I. Bhatti. Lateral control for UAVs using sliding mode technique. In 18th *IFAC World Congress Milano, Italy*, volume 18, pages 11121–11126, 2011.

[12] Rolf Rysdyk. Unmanned aerial vehicle path following for target observation in wind. *Journal of Guidance, Control, and Dynamics*, 29(5):1092–1100, Sep 2006.

[13] Navid Dadkhah and Brnice Mettler. Survey of motion planning literature in the presence of uncertainty: Considerations for UAV guidance. *Journal of Intelligent & Robotic Systems*, 65(1-4):233–246, 2012.

[14] T. Yamasaki and S.N. Balakrishnan. Sliding mode based pure pursuit guidance for UAV rendezvous and chase with a cooperative aircraft. In *American Control Conference (ACC)*, pages 5544–5549, June 2010.

[15] Jinyong Yu, Qingjiu Xu, and Yue Zhi. A TSM control scheme of integrated guidance/autopilot design for UAV. In *3rd International Conference on Computer Research and Development (ICCRD)*, volume 4, pages 431–435, March 2011.

[16] Isaac Kaminer, Antonio Pascoal, Eric Hallberg, and Carlos Silvestre. Trajectory tracking for autonomous vehicles: An integrated approach to guidance and control. *Journal of Guidance, Control, and Dynamics*, 21(1):29–38, Jan 1998.

[17] Takeshi Yamasaki, S.N. Balakrishnan, and Hiroyuki Takano. Integrated guidance and autopilot design for a chasing UAV via high-order sliding modes. *Journal of the Franklin Institute*, 349(2):531 – 558, 2012.

[18] T. Yamasaki, S. Balakrishnan, and H. Takano. Integrated guidance and autopilot for a path-following UAV via high-order sliding modes. In *American Control Conference (ACC)*, pages 143–148, june 2012.

[19] C. Charu and P. Radhakant. Partially integrated guidance and control of UAVs for reactive collision avoidance. Technical report, Department of Aerospace Engineering, Indian Institute of Science, October 2011.

[20] Radhakant Padhi and P. Rakesh. Formation flying of UAVs with dynamic inversion based partial integrated guidance and control. In *AIAA Guidance, Navigation, and Control Conference*, Portland, Oregon, Aug 2011.

[21] M. Breivik and T.I. Fossen. Principles of guidance-based path following in 2d and 3d. In *44th IEEE Conference on Decision and Control, and European Control Conference (CDC-ECC 05)*, pages 627–634, 2005.

[22] M. Ahmed and K. Subbarao. Nonlinear 3-D trajectory guidance for unmanned aerial vehicles. In *Proceedings of the 11th International Conference on Control, Automation, Robotics and Vision*, December 2010.

[23] C. Goerzen, Z. Kong, and B. Mettler. A survey of motion planning algorithms from the perspective of autonomous UAV guidance. *Journal of Intelligent and Robotic Systems*, 57(1-4):65–100, 2010.

[24] R. Samar, Shakil Ahmed, and Faisal Aftab. Lateral control with improved performance for UAVs. *IFAC Proceedings Volumes*, 40(7):37 – 42, 2007.

[25] N. Regina and M. Zanzi. UAV guidance law for ground-based target trajectory tracking and loitering. In *Proceedings of the IEEE Aerospace Conference*, pages 1–9, March 2011.

[26] R.A. Sasongko, J. Sembiring, H. Muhammad, and T. Mulyanto. Path following system of small unmanned autonomous vehicle for surveillance application. In 8th *Asian Control Conference (ASCC)*, pages 1259–1264, May 2011.

[27] Mehdi Golestani and Iman Mohammadzaman. PID guidance law design using short time stability approach. *Aerospace Science and Technology*, 43:71 – 76, 2015.

[28] Mehdi Golestani, Iman Mohammadzaman, and Ahmad Reza Vali. Finite-time convergent guidance law based on integral backstepping control. *Aerospace Science and Technology*, 39:370 – 376, 2014.

[29] Yeonsik Kang and J Karl Hedrick. Design of nonlinear model predictive controller for a small fixed-wing unmanned aerial vehicle. In *AIAA Guidance, Navigation, and Control Conference*, 2006.

[30] Kwangjin Yang, Salah Sukkarieh, and Yeonsik Kang. Adaptive nonlinear model predictive path tracking control for a fixed-wing unmanned aerial vehicle. In *AIAA Guidance, Navigation, and Control Conference*, Aug 2009.

[31] Eng-Kee Poh, Jian-Liang Wang, and Keck-Voon Ling. Near optimal tracking solution for input constrained UAV using MPC. In *Proceedings of the AIAA Guidance, Navigation, and Control Conference*, Aug 2010.

[32] Gonzalo Garcia and Shahriar Keshmiri. Nonlinear model predictive controller for navigation, guidance and control of a fixed-wing UAV. In *AIAA Guidance, Navigation, and Control Conference, Portland, OR*, pages 8–11, 2011.

[33] Prof Thrassos Panidis, Luca De Filippis, Giorgio Guglieri, and Fulvia B. Quagliotti. A novel approach for trajectory tracking of UAVs. *Aircraft Engineering and Aerospace Technology: An International Journal*, 86(3):198–206, 2014.

[34] R.W. Beard and T.W. McLain. *Small Unmanned Aircraft: Theory and Practice*. Princeton University Press, 2012.

[35] Derek R. Nelson, D. Blake, Barber Timothy, W. Mclain, and Randal W. Beard. Vector field path following for small unmanned air vehicles. In *IEEE Transactions on Control Systems Technology*, pages 5788–5794, 2006.

[36] D. A. Lawrence, E. W. Frew, and W. J. Pisano. Lyapunov vector fields for autonomous unmanned aircraft flight control. *Journal of Guidance Control and Dynamics*, 31(5):1220–1229, 2008.

[37] S.R. Griffiths. Vector-field approach for curved path following for miniature aerial vehicles. In *AIAA Guidance, Navigation, and Control Conference and Exhibit*, Keystone, Colorado, 21-24 August 2006.

[38] Eric W Frew, Dale A Lawrence, and Steve Morris. Coordinated standoff tracking of moving targets using lyapunov guidance vector fields. *Journal of Guidance, Control, and Dynamics*, 31(2):290–306, 2008.

[39] Zhenxing Zhang, Shihua Li, and Sheng Luo. Composite guidance laws based on sliding mode control with impact angle constraint and autopilot lag. *Transactions of the Institute of Measurement and Control*, 35(6):764–776, 2013.

[40] Yuri B. Shtessel, Ilya A. Shkolnikov, and Mark D.J. Brown. An asymptotic second-order smooth sliding mode control. *Asian Journal of Control*, 5(4):498–504, 2003.

[41] Yuri B. Shtessel, Ilya A. Shkolnikov, and Arie Levant. Smooth second-order sliding modes: Missile guidance application. *Automatica*, 43(8):1470 – 1476, 2007.

[42] T. Yamasaki, S.N. Balakrishnan, and H. Takano. Sliding mode based integrated guidance and autopilot for chasing UAV with the concept of time-scaled dynamic inversion. In *American Control Conference (ACC)*, pages 1598–1603, June 2011.

[43] T. Yamasaki, S.N. Balakrishnan, and H. Takano. Integrated guidance and autopilot for a path-following UAV via high-order sliding modes. In *American Control Conference (ACC)*, pages 143–148, 2012.

[44] Takeshi Yamasaki, S. N. Balakrishnan, and Hiroyuki Takano. Separate-channel integrated guidance and autopilot for automatic path-following. *Journal of Guidance, Control, and Dynamics*, 36(1):25–34, Dec 2012.

[45] I. Bayezit and B. Fidan. Distributed cohesive motion control of flight vehicle formations. *IEEE Transactions on Industrial Electronics*, 60(12):5763–5772, Dec 2013.

[46] Ony Arifianto and Mazen Farhood. Optimal control of a small fixed-wing UAV about concatenated trajectories. *Control Engineering Practice*, 40:113 – 132, 2015.

[47] B. Mettler, N. Dadkhah, and Z. Kong. Agile autonomous guidance using spatial value functions. *Control Engineering Practice*, 18(7):773 – 788, 2010. Special Issue on Aerial Robotics.

[48] Navid Dadkhah and Brnice Mettler. Control system design and evaluation for robust autonomous rotorcraft guidance. *Control Engineering Practice*, 21(11):1488 – 1506, 2013. Advanced Software Engineering in Industrial Automation (INCOM09).

[49] Hyunjin Choi and Youdan Kim. UAV guidance using a monocular-vision sensor for aerial target tracking. *Control Engineering Practice*, 22:10 – 19, 2014.

193

[50] Xian-Zhong Gao, Zhong-Xi Hou, Zheng Guo, Rong-Fei Fan, and Xiao-Qian Chen. Analysis and design of guidance-strategy for dynamic soaring with UAVs. *Control Engineering Practice*, 32:218 – 226, 2014.

[51] Sheng Sun, Di Zhou, and Wen tao Hou. A guidance law with finite time convergence accounting for autopilot lag. *Aerospace Science and Technology*, 25(1):132 – 137, 2013.

[52] R.W. Beard, J. Ferrin, and J. Humpherys. Fixed wing UAV path following in wind with input constraints. *IEEE Transactions on Control Systems Technology*, 22(6):2103–2117, Nov 2014.

[53] Liang Sun, R.W. Beard, and D. Pack. Trajectory-tracking control law design for unmanned aerial vehicles with an autopilot in the loop. In *American Control Conference (ACC)*, pages 1390–1395, June 2014.

[54] L. Sun and D. Pack. Controlling unmanned aerial vehicles with a pre-existing autopilot system in the loop. In *54th IEEE Conference on Decision and Control (CDC)*, pages 476–481, Dec 2015.

[55] M.Z. Shah, R. Samar, and A.I. Bhatti. Guidance of air vehicles: A sliding mode approach. *IEEE Transactions on Control Systems Technology*, 23(1):231–244, Jan 2015.

[56] M. Zamurad Shah, Raza Samar, and Aamer I Bhatti. Lateral track control of UAVs using the sliding mode approach: from design to flight testing. *Transactions of the Institute of Measurement and Control*, 37(4):457–474, 2015.

[57] D.T. McRuer, D. Graham, and I. Ashkenas. *Aircraft Dynamics and Automatic Control*. Princeton Legacy Library. Princeton University Press, 2014.

[58] J.C. Doyle, K. Glover, P.P. Khargonekar, and B.A. Francis. State-space solutions to standard H_2 and H_∞ control problems. *IEEE Transactions on Automatic Control*, 34(8):831 –847, aug 1989.

[59] P. L. D. Peres, J. C. Geromel, and S. R. Souza. H_∞ robust control by static output feedback. In *American Control Conference*, number 30, pages 620–621, june 1993.

[60] I. Yaesh and U. Shaked. Minimum entropy static output-feedback control with an H_∞ norm performance bound. *IEEE Transactions on Automatic Control*, 42(6):853–858, jun 1997.

[61] P. Apkarian and P. Gahinet. A convex characterization of gain-scheduled H_∞ controllers. *IEEE Transactions on Automatic Control*, 40(5):853–864, may 1995.

[62] J.F. Magni, S. Bennani, and J. Terlouw. *Robust flight control: a design challenge*. Lecture notes in control and information sciences. Springer, 1997.

[63] Richard J. Adams, James M. Buffington, and Siva S. Banda. Design of nonlinear control laws for high-angle-of-attack flight. *Journal of Guidance, Control, and Dynamics*, 17(4):737–746, Jul 1994.

[64] S. A. Snell, Dale F. Enns, and William L. Arrard. Nonlinear inversion flight control for a supermaneuverable aircraft. *Journal of Guidance, Control, and Dynamics*, 15(4):976–984, Jul 1992.

[65] R. Rysdyk and A.J. Calise. Robust nonlinear adaptive flight control for consistent handling qualities. *IEEE Transactions on Control Systems Technology*, 13(6):896–910, Nov 2005.

[66] Travis Kenneth Vetter. Sliding-mode control applied for robust control of a highly unstable aircraft. Master's thesis, University of California at Davis, 2002.

[67] S. Seshagiri and E. Promtun. Sliding mode control of F-16 longitudinal dynamics. In *American Control Conference*, pages 1770–1775, june 2008.

[68] M. Polas and A. Fekih. A multi-gain sliding mode based controller for the pitch angle control of a civil aircraft. In *42nd Southeastern Symposium on System Theory (SSST)*, pages 96–101, March 2010.

[69] N.K. Ure and G. Inalhan. Design of higher order sliding mode control laws for a multi modal agile maneuvering UCAV. In *2nd International Symposium on Systems and Control in Aerospace and Astronautics (ISSCAA)*, pages 1–6, Dec 2008.

[70] W. MacKunis, Z.D. Wilcox, M.K. Kaiser, and W.E. Dixon. Global adaptive output feedback tracking control of an unmanned aerial vehicle. *IEEE Transactions on Control Systems Technology*, 18(6):1390–1397, Nov 2010.

[71] P. Casau, D. Cabecinhas, and C. Silvestre. Hybrid control strategy for the autonomous transition flight of a fixed-wing aircraft. *IEEE Transactions on Control Systems Technology*, 21(6):2194–2211, Nov 2013.

[72] S. V. Emel'yanov. Theory of variable-structure control systems: Inception and initial development. *Computational Mathematics and Modeling*, 18(4):321–331.

[73] V. Utkin. Variable structure systems with sliding modes. *IEEE Transactions on Automatic Control*, 22(2):212–222, 1977.

[74] U. Itkis. *Control systems of variable structure*. A Halsted Press book. John Wiley & Sons, Incorporated, 1976.

[75] R.A. DeCarlo, S.H. Zak, and G.P. Matthews. Variable structure control of nonlinear multivariable systems: a tutorial. *Proceedings of the IEEE*, 76(3):212–232, mar 1988.

[76] J. Guldner Utkin, V.I. and J. Shi. *Sliding Mode Control in Electromechanical Systems*. Taylor & Francis. London, U.K, 1999.

[77] A.J. Koshkouei, K.J. Burnham, and A.S.I. Zinober. Dynamic sliding mode control design. *IEE Proceedings on Control Theory and Applications*, 152(4):392–396, July 2005.

[78] Arie Levant and L. Alelishvili. Integral high-order sliding modes. *IEEE Transactions on Automatic Control*, 52(7):1278–1282, July 2007.

[79] IgorM. Boiko. Chattering in sliding mode control systems with boundary layer approximation of discontinuous control. *International Journal of Systems Science*, 44(6):1126–1133, June 2013.

[80] J. A. Burton and A. S. I. Zinober. Continuous approximation of variable structure control. *International Journal of Systems Science*, 17(6):875–885, 1986.

[81] Jinkun Liu and Fuchun Sun. A novel dynamic terminal sliding mode control of uncertain nonlinear systems. *Journal of Control Theory and Applications*, 5(2):189–193.

[82] V.I. Utkin. *Sliding Modes in Control and Optimization*. Communications and Control Engineering. Springer Berlin Heidelberg, 2013.

[83] Arie Levant. Higher-order sliding modes, differentiation and output-feedback control. *International Journal of Control*, 76(9-10):924–941, 2003.

[84] Arie Levant. Universal single-input-single-output (siso) sliding-mode controllers with finite-time convergence. *IEEE Transactions on Automatic Control*, 46(9):1447 –1451, sep 2001.

[85] A. Levant. Sliding order and sliding accuracy in sliding mode control. *International Journal of Control*, 58(6):1247–1263, 1993.

[86] Leonid Fridman and Arie Levant. Higher order sliding modes as a natural phenomenon in control theory. In Franco Garofalo and Luigi Glielmo, editors, *Robust Control via Variable Structure and Lyapunov Techniques*, volume 217 of *Lecture Notes in Control and Information Sciences*, pages 107–133. Springer Berlin Heidelberg, 1996.

[87] Yuri B Shtessel, Leonid Fridman, and Alan Zinober. Higher order sliding modes. *International Journal of Robust and Nonlinear Control*, 18(4-5):381–384, 2008.

[88] C. Edwards and S. K. Spurgeon. *Sliding Mode Control: Theory and Applications*. Taylor and Francis, 1998.

[89] Y.B. Shtessel, I.A. Shkolnikov, and A. Levant. Guidance and control of missile interceptor using second-order sliding modes. *IEEE Transactions on Aerospace and Electronic Systems*, 45(1):110 –124, jan 2009.

[90] A. Levant, M. Taleb, and F. Plestan. Twisting-controller gain adaptation. In *50th IEEE Conference on Decision and Control and European Control Conference (CDC-ECC)*, pages 7015–7020, Dec 2011.

[91] Y. Shtessel, C. Edwards, L. Fridman, and A. Levant. *Sliding Mode Control and Observation*. Control Engineering. Springer New York, 2013.

[92] Michael Defoort, Thierry Floquet, Annemarie Kokosy, and Wilfrid Perruquetti. A novel higher order sliding mode control scheme. *Systems & Control Letters*, 58(2):102 – 108, 2009.

[93] Govert Monsees. *Discrete-time sliding mode control*. TU Delft, Delft University of Technology, 2002.

[94] B. Bandyopadhyay and S. Janardhanan. *Discrete-time Sliding Mode Control: A Multirate Output Feedback Approach*. Lecture Notes in Control and Information Sciences. Springer Berlin Heidelberg, 2005.

[95] M. Zamurad Shah, R. Samar, and S. Ussama Ali. Altitude controller design and flight demonstration for a research UAV. In 8th *Ankara International Aerospace Conference*, pages 10–12, Middle East Technical University, Ankara, Turkey, Sep 2015.

[96] B. Bandyopadhyay, F. Deepak, and K.S. Kim. *Sliding Mode Control Using Novel Sliding Surfaces*. Lecture Notes in Control and Information Sciences. Springer, Springer-Verlag Berlin Heidelberg, 2009.

[97] M. Zamurad Shah. *Guidance of Aerospace Vehicles: A sliding Mode Approach*. PhD thesis, Department of Electrical Engineering, Mohammad Ali Jinnah University, 2015.

[98] R. Padhi, P. R. Rakesh, and R. Venkataraman. Formation flying with nonlinear partial integrated guidance and control. *IEEE Transactions on Aerospace and Electronic Systems*, 50(4):2847–2859, October 2014.

[99] K.Y. Pettersen and E. Lefeber. Way-point tracking control of ships. In *Proceedings of the 40th IEEE Conference on Decision and Control*, volume 1, pages 940–945, 2001.

[100] Wilfred Perruquetti. From 1rst order to higher order sliding modes. Ecole Centrale de Lille, University Lecture, Available at `https://team.inria.fr/non-a/files/2012/06/Beamer_EEA10_douz.pdf` (11/2010).

[101] S Ussama Ali, Raza Samar, M Zamurad Shah, Aamer I Bhatti, and Khalid Munawar. Higher-order sliding mode based lateral guidance for unmanned aerial vehicles. *Transactions of the Institute of Measurement and Control*, Accepted for Publication, 2015.

[102] Syed Ussama Ali, Raza Samar, M. Zamurad Shah, Aamer I. Bhatti, Khalid Munawar, and Ubaid M. Al-Sggaf. Lateral guidance and control of {UAV}s using second-order sliding modes. *Aerospace Science and Technology*, 49:88 – 100, 2016.

[103] B.L. Stevens and F.L. Lewis. *Aircraft Control and Simulation*. Wiley, 2003.

Appendix A

YAK-54 UAV TEST PLATFORM

Flights were carried out with a research test platform, named as scaled YAK-54. The scaled YAK-54 UAV Figure A.1 is a fixed wing airplane designed for autonomous flying for long endurance $\approx$ 25 min to 30 min. The thrust generating unit of the scaled YAK-54 is a 50 cc gasoline engine DLE-55. It has a tractor configuration of thrust, with a JXR wooden propeller at the nose. The proposed nonlinear guidance and control scheme is implemented in flight control system of UAV. The structure of the UAV is modified to house sensors and a flight control system for autopilot controlled flight; the layout of the flight control system is shown in Figure A.3. The heart of the flight computer is a generic MPC-565 micro-controller based board with 6 serial ports for communication with ground terminal, data logger and on-board sensors .

Flight Control System Functionality

- Determination of attitude measurements, coordinates and motion parameters (angular rates, accelerations) from MEMS based AHRS (attitude and heading reference system).

- For altitude control, a low-cost pressure altitude sensor RC-AltPro-3 is used that outputs mean sea level altitude, along with the rate of climb/descent at an update rate of 10 Hz.

- Automatic-Manual Command: RC (remote control) receiver channel-7 is used for switching between manual and autopilot modes. Based on this signal, FCS decides to generate PWM signals for programmed automatic flight or to pass the PWM signals from remote for manual flight.

FIGURE A.1: Research Platform Yak-54

FIGURE A.2: Research platform scaled YAK-54 UAV

- Stabilization of pitch and roll angles.

- Telemetry of navigational and attitude data: Communication with the ground terminal is done through an RF modem which is connected to the flight computer through a serial port.

- Trajectory storage: The detailed flight data is stored in an on-board data logger at 115.2 kbps.

A.0.1 Servo Dynamics

For Guidance and Control design, servo dynamics is important specially when you are considering the inner loop control dynamics while the designing the guidance scheme. Therefore exact knowledge of how servo reacts to controller commands is important. In our case, we used HS5645MG as shown in Figure A.5. The servo dynamics is found experimentally. HS5645MG is an electromechanical PWM driven actuator. It is a low cost commercial standard actuator. The specification of HS5645MG actuator are as follows:

A.0.2 External Feedback Mechanism

A special fixture was designed and fabricated with provision of external POT for feedback acquisition mechanism. External POT of given parameters was used

- Resistance: 2 ± 0.4KΩ

- Power up voltage: ±15V

- Total Span: $340°\pm4°$
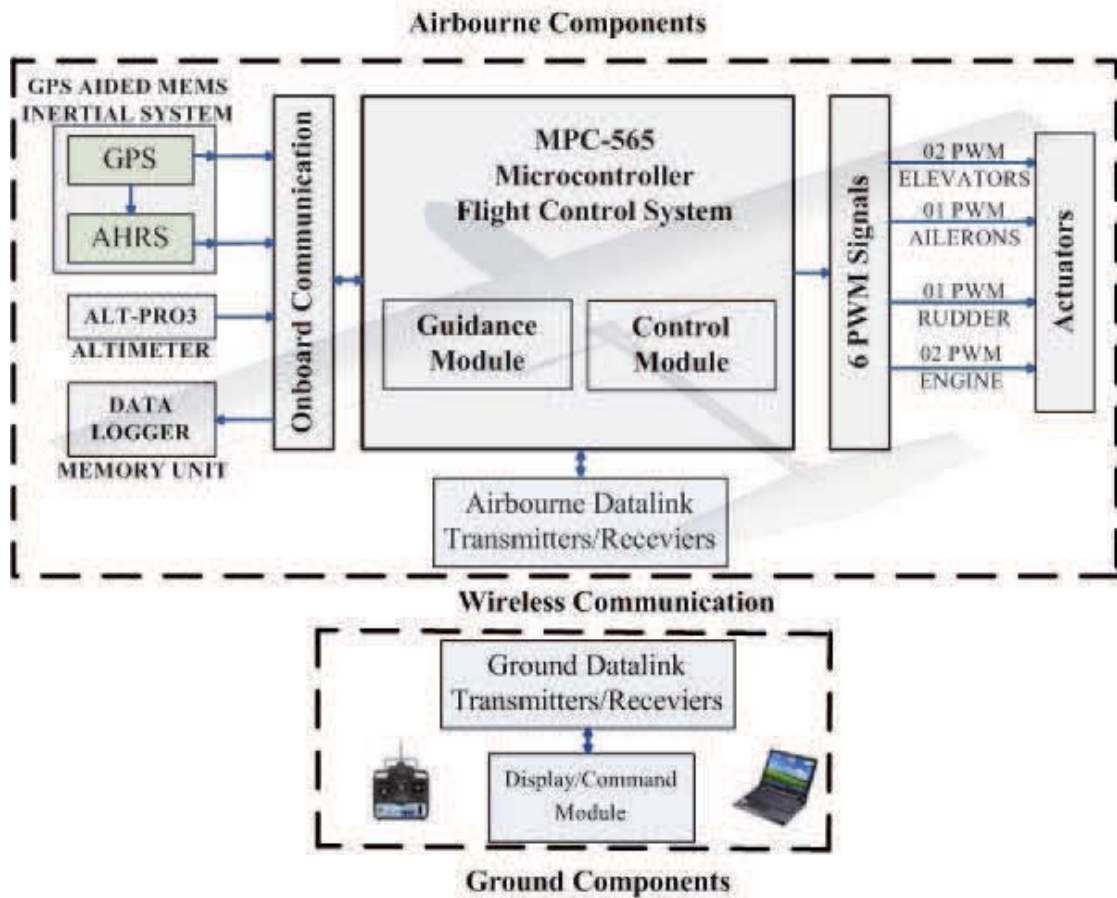
FIGURE A.3: Airborne and ground flight control components.
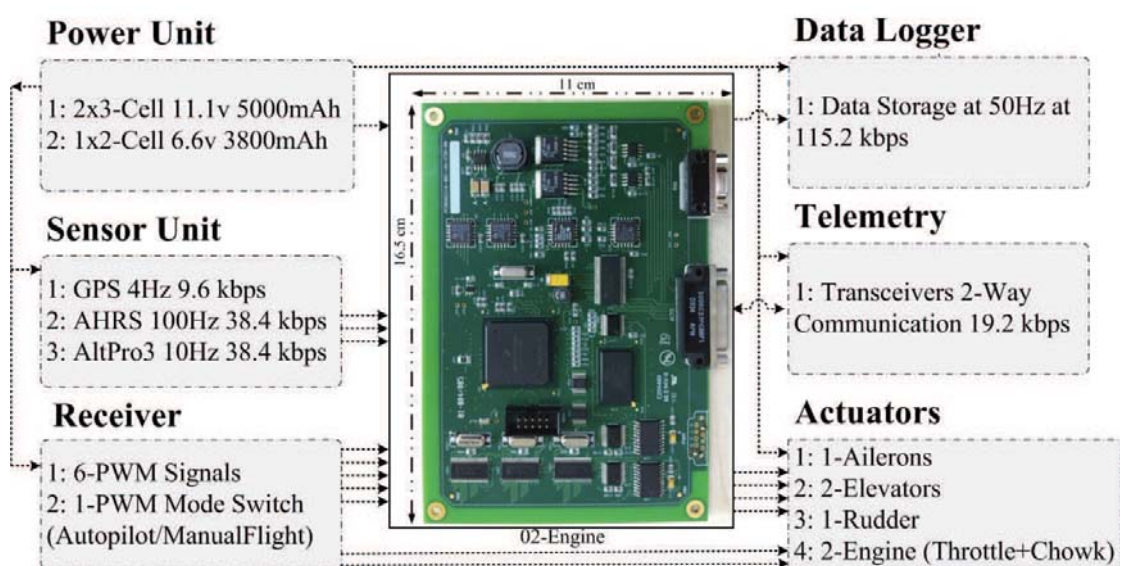
FIGURE A.4: Interfaces of flight control computer.

TABLE A.1: HS5645MG Servo Specification

Sr.	Parameter	Description
1.	Speed	0.18sec/60° at 6.0V
2.	Stall Torque	164.2 oz-in at 6.0V (1.16Nm)
3.	Length	1.59 inches (40.6mm)
4.	Width	0.77 inches (19.8mm)
5.	Height	1.48 inches (37.8mm)
6.	Weight	2.11 oz (60g)

FIGURE A.5: External feedback acquisition mechanism

The fixture along with provision of external POT feedback is shown in the figure below:

For the estimation of transfer function of HS5645MG actuator various tests were conducted under no load and load conditions. The said actuator accepts PWM signal as input, however for frequency and time domain analysis it was required that command and feedback were in analog form. The following table describes the relation between PWM signals, analog voltage command and the corresponding deflection of actuator.

Sr.	Voltage	Pulse Width (ms)	Degrees(°)
1.	0	1.5	0
2.	+10	2	+50
3.	-10	1	-50
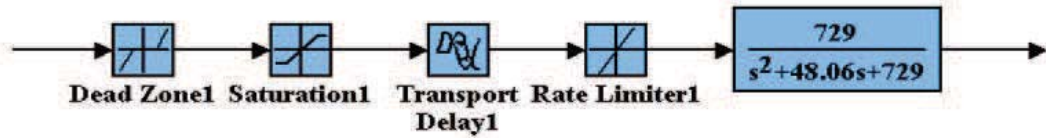
Figure A.6: Mathmatical Model for Servo HS5645MG

Proposed Mathematical Model The results of extensive testing (No-load tests 15 times, Load tests 26 times) were analyzed thoroughly. It was concluded that the system's response best fits the experimental data at 1V (5°) under load and no load conditions using average values of ξ and w_n. After through testing and analysis following model of HS5645MG was proposed.

- Voltage 2 Deg: 5°/V (5°/0.048ms)

- Saturation: $\pm 50°$

- Delay at 1V & 0.19 Nm (1Kg): 23msec

- Dead Zone: $\pm 0.1°$

- Rate Limit: 500°/sec

Transfer function of HS5645MG actuator was evaluated as

$$S(s) = \frac{729}{s^2 + 48s + 729} \tag{A.1}$$

Frequency domain and time domain responses of the actuator system with the proposed transfer function are shown in Figure A.7 and Figure A.8 respectively.
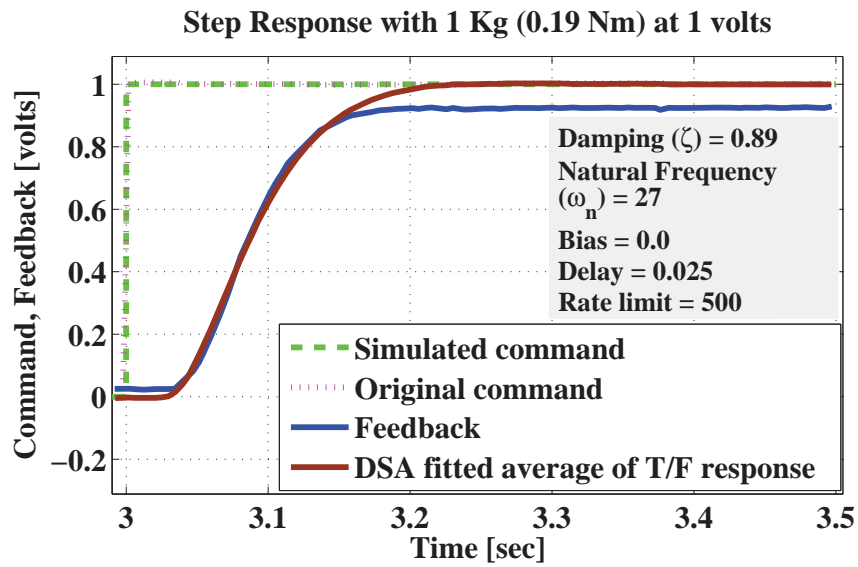
FIGURE A.7: Time Domain Plots with Proposed Transfer Function & Rate Limit
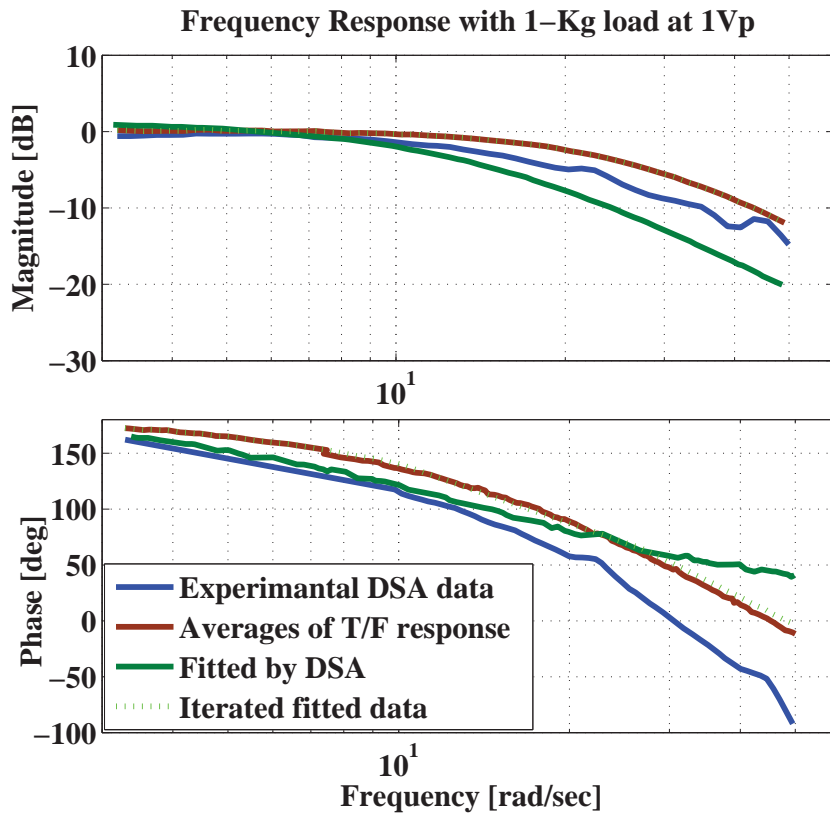
FIGURE A.8: Frequency Domain Plots with Proposed Transfer Function & Rate Limit

A.1 Sensors

Two sensors modeled are altimeter (RC-ALTPro3) and AHRS with built in GPS module. The alt-pro3 outputs data at 10Hz. A sample output is

$$RCALT, +00531, +023, 490, +0351, +0497 * CS$$

where altitude above ground is 53.1m, ROC 2.3 m/sec, battery voltage is 4.9volts, temperature is 53.1 deg and MSL altitude is 490.7m. The AHRS data is a 36 bytes packet sent every 10msec.

TABLE A.3: AHRS Packet Data

Parameters	Size (each)	Update Rate
Roll, Pitch, Yaw angles	2 Bytes	100Hz
Roll, Pitch, Yaw angular rates	2 Bytes	100Hz
North, East, Down Velocity	2 Bytes	100Hz
Latitude, Longitude	4 Bytes	4Hz
Altitude	2 Bytes	4Hz
Header and Checksum	8 Bytes	100Hz

A.2 Conclusion

The YAK-54 test platform provides state of the art solution for research of new guidance and control algorithms. These schemes can be easily implemented in FCS of the platform, to have a better insight of physical limitations of the designed theoretical ideas.

Appendix B

LATERAL AUTOPILOT CONTROL DESIGN

B.1 Lateral Control Loop Design

B.1.1 Lateral Control Model

In order to design a controller for any physical system, it is necessary to first obtain the equations of motion for that system including identification of states and control variables. In case of UAVs, the lateral modes are excited with the aileron control surface implying control input vector $U = [\delta_a]$. For the lateral state-space equations of UAVs, the state vector is given by $X = [\phi, p, r, \beta]^t$. Assuming that the longitudinal states are zero (i.e., $\theta = q = u = \alpha = w = 0$) and in the absence of wind, we have the following equations for lateral plane of UAVs [103]:

$$\dot{\phi} = p \tag{B.1}$$

$$\dot{p} = \frac{I_z \bar{L}}{I_x I_z - I^2_{xz}} + \frac{I_{xz} N}{I_x I_z - I^2_{xz}} \tag{B.2}$$

$$\dot{r} = \frac{I_{xz} \bar{L}}{I_x I_z - I^2_{xz}} + \frac{I_x N}{I_x I_z - I^2_{xz}} \tag{B.3}$$

$$\dot{\beta} = \frac{1}{m} \cos \beta C_Y \bar{q} S - (g'_o) \sin \phi \tag{B.4}$$

Side-force coefficient is given by C_Y, it is created due to side slipping motion i.e., $\beta \neq 0$

$$C_Y = C_{Y_\beta} \beta + C_{Y_{\delta_a}} \delta_a + (C_{Y_p} p + C_{Y_r} r) \frac{b}{2V} \tag{B.5}$$

The moments acting on the lateral plane of the UAV is defined in terms of dimensionless aerodynamic coefficients, $\bar{L}$ is the rolling moment and N is the yawing moment as

$$\bar{L} = \bar{q} S b \left(C_{l_\beta} \beta + C_{l_{\delta_a}} \delta_a + \left(C_{l_p} p + C_{l_r} r \right) \frac{b}{2V} \right) \tag{B.6}$$

$$N = \bar{q} S b \left(C_{n_\beta} \beta + C_{n_{\delta_a}} \delta_a + \left(C_{n_p} p + C_{n_r} r \right) \frac{b}{2V} \right) \tag{B.7}$$

where $\bar{q}$ is the dynamic pressure calculated as $\bar{q} = \frac{1}{2} \rho V^2$. We can now formulate the control task i.e., to generate a smooth control actuation command δ_a to track

ϕ_{ref}. The control function δ_a is treated as an input to the UAV inner loop for aerodynamic surface deflections for stabilizing the lateral autopilot system.

B.1.2 1st Order SMC design

In this formulation, it is required that the vehicle should track the commanded ϕ_{ref} generated by the outer guidance loop for generating the required lateral accelerations. The control loop generates the necessary control surface deflections δ_a to track the reference commands. Design of SOSM super twisting algorithm is performed to track the desired angle via a linear switching manifold with the following expression:

$$s_a = C_s \left(\phi - \phi_{ref} \right) + p \tag{B.8}$$

where the constants $C_s \in \Re$, $C_s > 0$ is required for a stable manifold [6]. The inner loop takes the desired roll angle as an input and generates the necessary aileron deflections. The time derivatives of the switching surface in (B.8) along the vehicle dynamics becomes

$$\dot{s}_a = C_s \dot{\phi} + C_s \dot{\phi}_{ref} + \dot{p} \tag{B.9}$$

under the assumption of constant bank angle command

$$\dot{s}_a = C_s p + \dot{p} \tag{B.10}$$

using (B.2) and (B.6) the expression for $\dot{p}$ renders the following form

$$\begin{aligned}
\dot{p} =& C_3 \bar{q} S b C_{l_{\delta_a}} \delta_a + C_4 \bar{q} S b C_{n_{\delta_a}} \delta_a \\
& + C_3 \left\{ \bar{q} S b \left(C_{l_\beta} \beta + \left(C_{l_p} p + C_{l_r} r \right) \frac{b}{2V} \right) \right\} \\
& + C_4 \left\{ \bar{q} S b \left(C_{n_\beta} \beta + \left(C_{n_p} p + C_{n_r} r \right) \frac{b}{2V} \right) \right\}
\end{aligned} \tag{B.11}$$

where

$$C_3 = \frac{I_z}{I_x I_z - I^2_{xz}}, C_4 = \frac{I_{xz}}{I_x I_z - I^2_{xz}} \tag{B.12}$$

If we simplify the expression of $\dot{p}$ in (B.11) and separate the terms which are directly influenced by δ_a we can write

$$\dot{p} = a_{1_\delta} \delta_a + \eta_p \tag{B.13}$$

where

$$a_{1_\delta} = C_3 \bar{q} S b C_{l_{\delta_a}} + C_4 \bar{q} S b C_{n_{\delta_a}} \tag{B.14}$$

and

$$
\begin{aligned}
\eta_p =& C_3 \bar{q} S b \left(C_{l_\beta} \beta + \left(C_{l_p} p + C_{l_r} r \right) \frac{b}{2V} \right) \\
&+ C_4 \bar{q} S b \left(C_{n_\beta} \beta + \left(C_{n_p} p + C_{n_r} r \right) \frac{b}{2V} \right)
\end{aligned}
\tag{B.15}
$$

solving (B.10) with $\dot{p}$ as in (B.13)

$$
\dot{s}_a = C_s p + a_{1_\delta} \delta_a + \eta_p
\tag{B.16}
$$

For equivalent control we need to put $\dot{s} = 0$, and derive the expression for $\delta_{a_{eq}}$

$$
\delta_{a_{eq}} = \frac{-C_s p - \eta_p}{a_{1_\delta}}
\tag{B.17}
$$

And in order to make the control law robust a discontinuous term is added and the final expression of the control law becomes $\delta_a = \delta_{a_{eq}} - K \operatorname{sgn}(s)$

$$
\delta_a = \frac{-C_s p - \eta_p}{a_{1_\delta}} - K \operatorname{sgn}(s)
\tag{B.18}
$$

B.1.2.1 Reachability Condition

The control must be designed such that it drives the state trajectories toward the sliding surface, and once achieved, maintains that sliding motion. The attractivity of the sliding surface can be expressed by the condition

$$
s\dot{s} < 0
\tag{B.19}
$$

The aforementioned condition is referred to as the reachability condition. To check for the reachability condition, let us take the following Lyapunov candidate function

$$
W = \frac{1}{2} s_a s_a^2
\tag{B.20}
$$

The derivative of W is given as

$$
\dot{W} = s_a \dot{s}_a
\tag{B.21}
$$

Now if there exist unknown bounded uncertainty η in the plant model, the expression of $\dot{s}$ becomes

$$
\dot{s}_a = C_s p + a_{1_\delta} \delta_a + \eta_p + \eta
\tag{B.22}
$$

The expression for $\dot{W}$ along system states in (B.22)

$$
\dot{W} = s \left\{ C_s p + a_{1_\delta} \delta_a + \eta_p + \eta \right\}
\tag{B.23}
$$

Substituting the control (B.18) in (B.23)

$$\dot{W} = s\left\{C_s p + a_{1_\delta}\left(\frac{-C_s p - \eta_p}{a_{1_\delta}}\right.\right. \tag{B.24}$$
$$\left.\left. - K\operatorname{sgn}(s)\right) + \eta_p + \eta\right\}$$

$$\dot{W} = s\left\{\frac{-K\operatorname{sgn}(s)}{a_{1_\delta}} + \eta\right\} \tag{B.25}$$

$\dot{W}$ will be negative definite if

$$K \geq a_{1_\delta}\eta \tag{B.26}$$

As our control input in (B.18) with K constrained as above, the reachability condition ($s\dot{s} < 0$) is satisfied during controlled flight envelope. Hence for any initial condition, with the above selected control gain K, the state trajectory will always be directed toward the sliding surface, and once acquired, shall subsequently remain on it.

Besides the inherent flaw of chattering in 1st order SMC, the design scheme discussed in Section B.1.2 encouraged the authors to design a new control design strategy in which transient performance is the same but it requires less information in its implementation. In order to implement the 1st order SMC controller (B.18) in flight control computer of UAV the extra data required is the side slip angle β. So either you measure this quantity from sensor or design an observer. In both the ways cost and computational complexity is increased. The new design control strategy provides same measures of performance and robustness against uncertainties without an extra input of β. Secondly, as the senor output is noisy the more inputs from sensors into the control design will cause the control channel to be noisy, for the 1st order SMC the noise induced into the control channel is twice then the super twisting controller. One may argue that how these flaws are removed in SOSM STA, the reason can be understood by the explicit power of STA design, it simply does not need measurement of $\dot{s}_a$ from which you derive the $\delta_{a_{eq}}$, it inherently accounts for the dynamics of $\dot{s}_a$ and derives the states to equilibrium point be generating adequate δ_a.

B.1.3 Super Twisting Algorithm

The control loop generates the necessary control surface deflections to track the commanded bank angle. Design of SOSM super twisting algorithm is performed to track the desired angle via a linear switching manifold with the following expression:

$$s_a = C_s\left(\phi - \phi_{ref}\right) + p \tag{B.27}$$

where the constants $C_s \in \Re$, $C_s > 0$ is required for a stable manifold [6]. Since δ_a is the control input therefore comparison of (B.16) with (2.36) gives:

$$a(t,x) = C_s p + \eta_p \qquad (B.28)$$

$$b(t,x) = a_{1_\delta} \qquad (B.29)$$

where η_p and a_{1_δ} are given in (B.14) and (B.15). SMC based super twisting controller is designed for generating the control input δ_a based on ϕ_{ref} (desired bank angle) ϕ (bank angle) and p (roll rate). Using (2.37), the control effort can be written as:

$$\delta_a = -\lambda |C_s (\phi - \phi_{ref}) + p|^\gamma$$
$$\mathrm{sgn}(C_s (\phi - \phi_{ref}) + p) + u_1$$

$$\dot{u}_1 = \left\{ \begin{array}{ll} -\delta_a & |\delta_a| > U_S \\ -K\,\mathrm{sgn}(C_s (\phi - \phi_{ref}) + p) & |\delta_a| \le U_S \end{array} \right\} \qquad (B.30)$$

B.1.3.1 Existence of 2-sliding mode

For k_s, i.e., the minimum bound on (B.29):

$$k_s = \frac{\rho V_{min}^2 Sb}{2} \left(C_3 C_{l_{\delta_a}} + C_4 C_{n_{\delta_a}} \right) \qquad (B.31)$$

For K_S, i.e., the maximum bound on (B.29):

$$K_S = \frac{\rho V_{max}^2 Sb}{2} \left(C_3 C_{l_{\delta_a}} + C_4 C_{n_{\delta_a}} \right) \qquad (B.32)$$

Now in order to satisfy the conditions (2.39), (2.40), (2.41) and (2.42) we must derive the expressions for $\dot{a}(t,x)$ and $\dot{b}(t,x)$ which renders the form as

$$\dot{a}(t,x) = C_s \dot{p} + \dot{\eta}_p \qquad (B.33)$$

with

$$\begin{aligned}\dot{\eta}_p =& \frac{\gamma V Sb}{2} \left(C_3 C_{l_\beta} + C_4 C_{n_\beta} \right) \left(V\dot{\beta} + 2\dot{V}\beta \right) \\ &+ \frac{\gamma Sb^2}{4} \left(C_3 C_{l_p} + C_4 C_{n_p} \right) \left(V\dot{p} + p\dot{V} \right) \\ &+ \frac{\gamma Sb^2}{4} \left(C_3 C_{l_r} + C_4 C_{n_r} \right) \left(V\dot{r} + r\dot{V} \right) \end{aligned} \qquad (B.34)$$

For the lateral plane the condition (2.39), renders the form as

$$\gamma U_S < \left| \frac{C_s p + \eta_p}{C_3 \bar{q} S b C_{l_{\delta_a}} + C_4 \bar{q} S b C_{n_{\delta_a}}} \right| \tag{B.35}$$

To derive the value of C to satisfy (2.40) of our control design in (B.30) takes the form as

$$C \geq |C_s \dot{p} + \dot{\eta}_p| + U_S |K_S| \tag{B.36}$$

TABLE B.1: Lateral Directional Derivatives (rad^{-1})

C_{Y_p}	0.0194	C_{Y_r}	0.2531
C_{l_β}	-0.0220	C_{l_p}	-0.5858
C_{l_r}	0.0743	C_{n_β}	0.1052
C_{n_p}	-0.0387	C_{n_r}	-0.2890
C_{Y_β}	-0.2707	$C_{l_{\delta_a}}$	0.3707
$C_{n_{\delta_a}}$	-0.0088	$C_{n_{T_\beta}}$	-0.0045

First the sliding surface s_a parameter C_s is selected based on required performance. Here C_s is chosen as 5 to provide rapid convergence of the error to zero i.e., $\phi \to \phi_{ref}$, to achieve good performance. Values of $|a(t,x)|$ and $|b(t,x)|$ calculated for the scaled YAK-54 are 13.3680 and 487.9116, respectively. The upper bound of $|\dot{a}(t,x)|$ is computed as 182.4847, and for $|\dot{b}(t,x)|$ it is 184.6152; from these values we can now select C as 192.1511. Magnitude of the maximum control effort δ_a is selected as 5° for our application. Computed values of k_s and K_S (upper and lower bounds on $b(t,x)$) are 320.76 and 487.9116, respectively. We can now choose the gains K, γ and λ satisfying inequalities (2.38), (2.39), (2.40) and (2.42). We choose K, γ and λ as 1.75, 0.35 and 0.55 respectively, these satisfy all the above conditions and hence a 2-sliding mode will exist for the inner loop with $s_a = \dot{s}_a = 0$. The control u enters the segment $[-U_S, U_S]$ in finite time and stays there, i.e., $\delta_a = [-5°, 5°]$.

B.2   Simulation Results
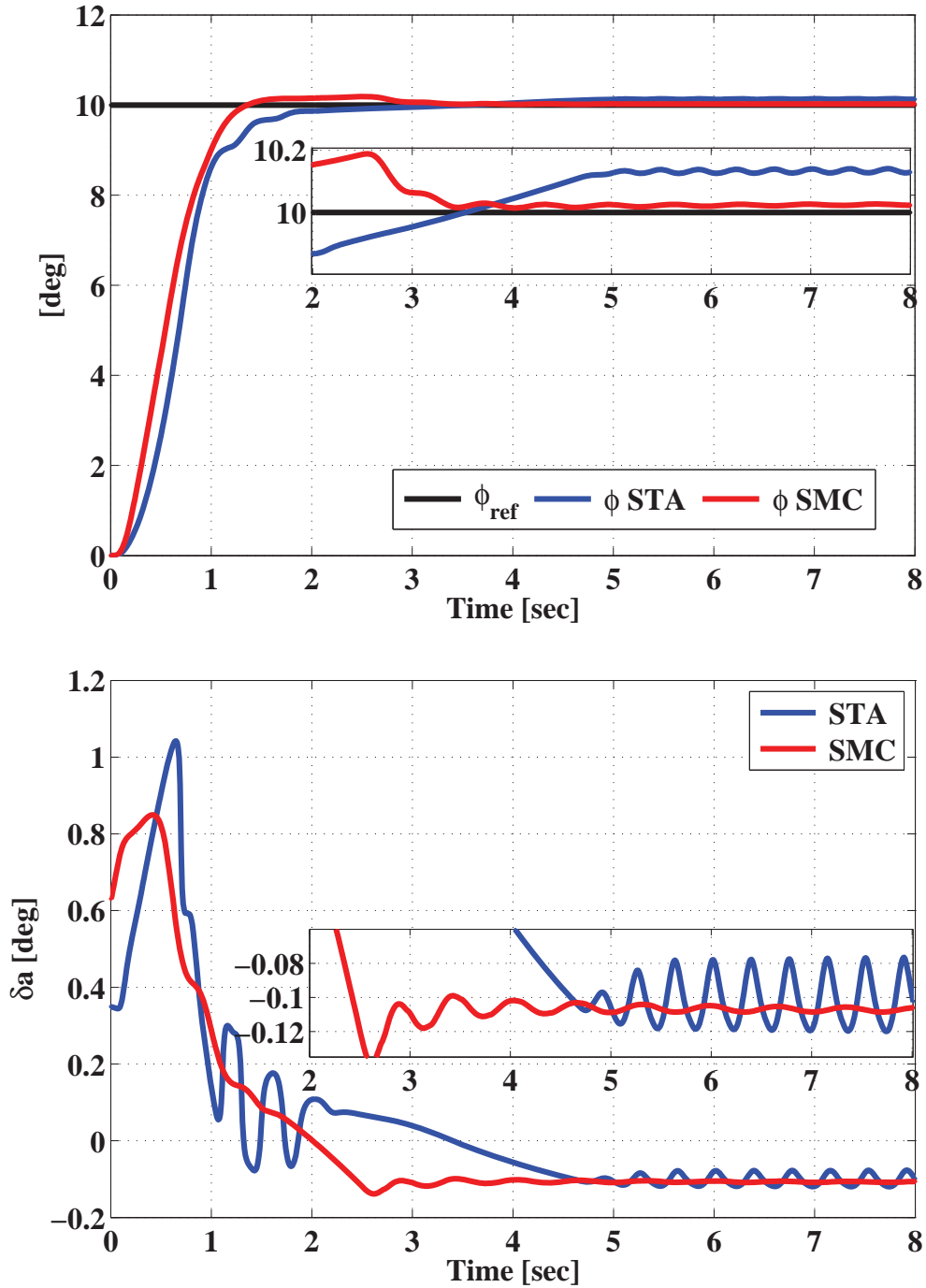
FIGURE B.1: Roll Angle ϕ and control actuation δ_a with 1st Order Sliding
Mode and 2nd Order Super Twisting Algorithm
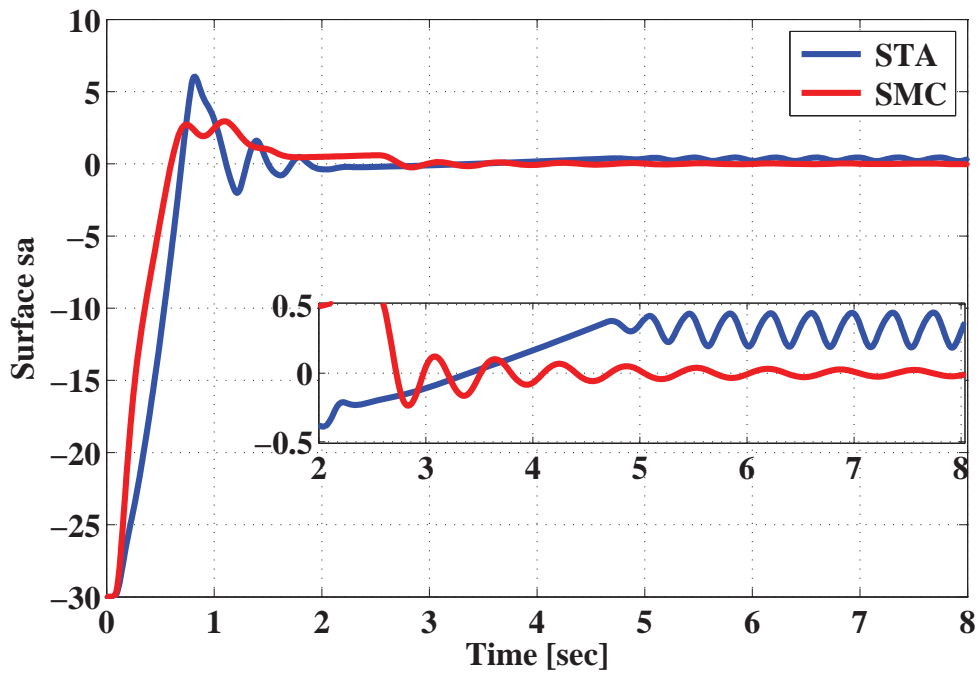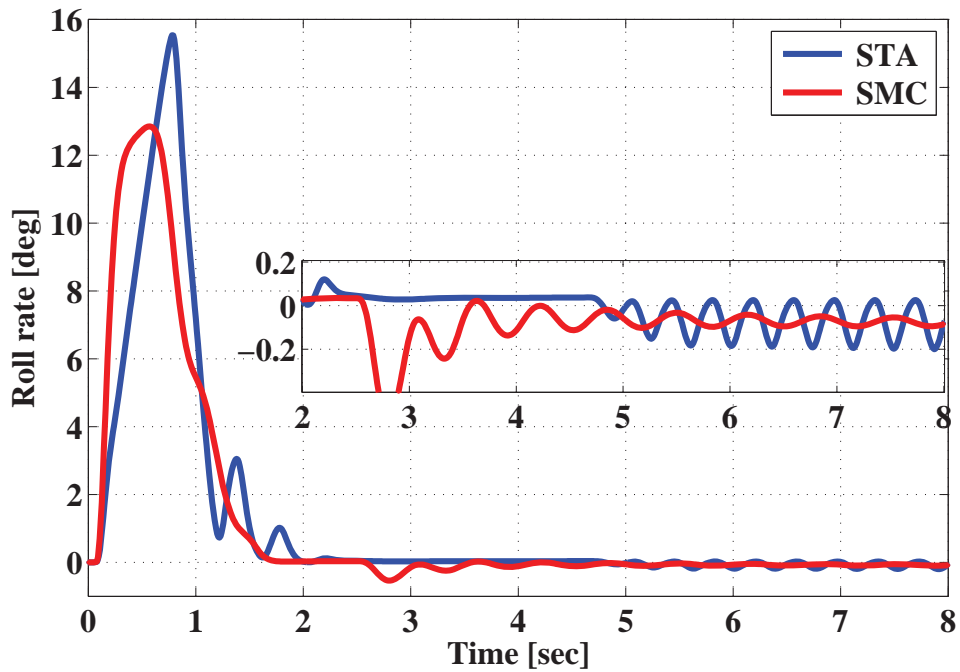
FIGURE B.2: Roll Rate p and surface convergence s_a with 1st Order Sliding Mode and 2nd Order Super Twisting Algorithm

The objective of the simulation was to show that the designed controllers were successful in stabilizing the angular rates and angular position. We now discuss the simulations and compare the results of sliding mode controller 1st - order SMC and super twisting algorithm. The input to the system is desired reference roll

angle i.e., 10° in our case. Simulation results for following the reference input in the absence of any disturbances or parametric uncertainties are shown in Figure B.1 and Figure B.2. From Figure B.1, it is evident that the reference input is followed by both controllers closely. Considerable chattering can be observed in Figure B.1 for the case of 1st order SMC design. The reaching time can be further improved for the 1st - order SMC case but this will further degrade the control channel.

As we earlier said, chattering excites the high-frequency unmodelled dynamics, degrades performance of the system, cause actuator wear, and even result in instability. In order that chattering be avoided, we must consider the qualities of HOSM. The HOSM offers a way to retain transient performance of ideal SMC and achieve zero steady-state error, without having chattering in the control input, and this is readily inferred from Figure B.1. Figure B.2 shows the roll rate p. The super twisting controller provides appearance of a 2-sliding mode, the state trajectories are attracted in finite time, i.e., $s_a = 0$ as can be seen from Figure B.2. Higher order sliding mode, i.e the super twisting controller provides much superior performance as compared to 1st order sliding mode control law. The effectiveness of the super twisting technique in avoiding chattering was also highlighted. Lastly, before we summarize our results in this section, we briefly mention that all our simulations have concentrated on the design of control inputs δ_a in controlling the roll angle ϕ and roll rate q for attaining the desired lateral motion. From implementation point of view it has been observed that SOSM STA design is more suitable to be implemented in FCS of YAK-54 UAV for flight experiments.